

LASER INTERFEROMETRY FOR LISA AND SATELLITE GEODESY MISSIONS

Katharina-Sophie Isleif





# LASER INTERFEROMETRY FOR LISA AND SATELLITE GEODESY MISSIONS

---

Von der QUEST-Leibniz-Forschungsschule  
der Gottfried Wilhelm Leibniz Universität Hannover  
zur Erlangung des Grades

**Doktorin der Naturwissenschaften**  
Dr. rer. nat.

genehmigte Dissertation von

**M. Sc. Katharina-Sophie Isleif**  
geboren am 01. Juli 1989  
in Langenhagen, Deutschland

2018

REFERENT Prof. Dr. Karsten Danzmann  
Universität Hannover

KORREFERENT Apl. Prof. Dr. Gerhard Heinzl  
Universität Hannover

KORREFERENT Prof. Dr. Guido Müller  
University of Florida

SUPERVISORS Prof. Dr. Karsten Danzmann  
Apl. Prof. Dr. Gerhard Heinzl  
Dr. Jeffrey Livas  
Dr. Oliver Gerberding

TAG DER PROMOTION 16. Mai 2018



**Leibniz Universität Hannover**  
Institut für Gravitationsphysik  
Callinstr. 38, 30167 Hannover, Germany



**Albert-Einstein-Institut (AEI)**  
Max-Planck Institut für Gravitationsphysik  
Callinstr. 38, 30167 Hannover, Germany

in collaboration with



**European Space Agency (ESA)**  
European Space Research and Technology Centre (ESTEC)  
Keplerlaan1, Noordwijk, The Netherlands



**Deutsches Zentrum für Luft- und Raumfahrt (DLR)**  
Bundesministerium für Wirtschaft und Technologie  
(Project Ref. No. 50 OQ 0601)



**National Aeronautics & Space Administration (NASA)**  
Goddard Space Flight Center  
8800 Greenbelt Rd, Greenbelt, MD 20771, USA



**National Institute of Standards & Technology (NIST)**  
100 Bureau Drive Gaithersburg, MD 20899, USA



**University of Glasgow (UoG)**  
Institute for Gravitational Research  
University Avenue, Glasgow G12 8QQ, Scotland



**Deutsche Forschungsgemeinschaft (DFG)**  
Sonderforschungsbereich (SFB) 1128 Relativistic Geodesy and  
Gravimetry with Quantum Sensors (geo-Q)



# ABSTRACT

The development and investigation of laser interferometry concepts for performing precise length measurements at frequencies below 1 Hz is the main topic of this thesis. These concepts are quintessential for space-based measurements of gravitational waves or the Earth gravity field. For the Laser Interferometer Space Antenna (LISA) and future satellite geodesy missions, various interferometer types have been studied between 2014 and 2018 at the Albert Einstein Institute (AEI) in Hannover as a part of the work presented here.

The first part of this thesis presents conceptual design studies of phase reference distribution systems (PRDSs) for LISA. The usage of *Telescope Pointing* is the baseline mechanism for the current LISA design and implies the need for a light-exchanging backlink connection between two rotating optical benches within one satellite. Different backlink implementations are presented and analyzed, the final choice however remains one of the last open questions for the LISA optical metrology. A test-bed for comparing three backlinks with each other in a single, so-called *Three-Backlink interferometer (TBI)* experiment, has been simulated and a detailed noise estimation, including a critical stray light analysis, is presented. A free-beam connection between two moving set-ups was established by which the full functionality of the experimental environment was validated. The design of the TBI has been completed and the experiment, consisting of two rotating quasi-monolithic optical benches, is currently under construction. The full experiment will enable to test the performance of LISA backlink candidates with a precision of  $1 \text{ pm}/\sqrt{\text{Hz}}$  in a relevant environment.

The second part of this thesis describes alternative interferometer techniques for reducing the complexity of optical set-ups, while modern digital signal processing is applied for recovering the desired phase information. The simplifications in the optical part enables multi-channel operation and multi-degree of freedom readout, which is required for future gradiometers in satellites consisting of six or more test masses. An experiment simulating such a test mass readout with only a single optical component has been established. Interferometric readout noise levels of  $1.0 \text{ pm}/\sqrt{\text{Hz}}$  at 100 mHz were achieved by using *deep frequency modulation interferometry (DFMI)*, a novel technique developed as part of this thesis.

KEYWORDS: gravitational physics, laser interferometry, space application



# KURZZUSAMMENFASSUNG

Die Entwicklung von Laserinterferometern für präzise Längenänderungsmessungen im 1 mHz-Frequenzbereich ist das Kernthema dieser Arbeit. Diese finden Anwendung in der Detektion von Gravitationswellen und der Messung des Erdschwerefeldes aus dem Weltraum. Verschiedene Interferometerkonzepte wurden für die Laser Interferometer Space Antenna (LISA)- und zukünftige geodätische Missionen innerhalb der hier dargestellten Arbeit am Albert-Einstein-Institut (AEI) in Hannover zwischen 2014 und 2018 untersucht.

Der erste Teil dieser Arbeit befasst sich mit einer Designstudie über unterschiedliche Phasenreferenzverteilungssysteme (PRDSs) für LISA. Das derzeitige Design sieht das sogenannte *Telescope Pointing* als Basis-Mechanismus vor, wodurch eine *Backlink*-Verbindung zwischen zwei rotierenden optischen Bänken innerhalb eines Satelliten benötigt wird. Die Laser werden hiermit zwischen den beiden Interferometern ausgetauscht. Eine konkrete Realisierung dieses Backlinks ist eine der letzten offenen Fragen für das optische Design von LISA. Das sogenannte *Drei-Backlink Interferometer (TBI)* wurde speziell entworfen und dient als Testumgebung, in welcher drei Backlinks in einem einzelnen Aufbau miteinander verglichen werden. Optische Simulationen und eine Vorhersage möglicher Rauschquellen werden in dieser Arbeit präsentiert. Eine Freistrah-Verbindung zwischen zwei rotierenden Bänken wurde bereits untersucht und es konnte gezeigt werden, dass die experimentelle Infrastruktur voll funktionsfähig ist. Das Design des Drei-Backlink Experiments ist abgeschlossen und es wird derzeit konstruiert.

Der zweite Teil dieser Arbeit beschreibt alternative Interferometertechniken um die Komplexität optischer Aufbauten zu reduzieren. Moderne digitale Verarbeitungssysteme werden benutzt, um die gewünschte Phaseninformation zurückzugewinnen. Eine Vereinfachung der Optik ermöglicht den Betrieb mehrerer Kanäle gleichzeitig und die Auslesung vieler Freiheitsgrade. Diese Techniken werden in zukünftigen Satelliten-Gradiometern benötigt, um die Bewegung mehrerer Testmassen zu bestimmen. Dies wurde in einem optischen Aufbau mit nur einer einzelnen optischen Komponente simuliert. Mit tiefen Laserfrequenzmodulationen (DFMI), einer im Rahmen dieser Arbeit entwickelten Methode, konnte eine Messgenauigkeit von unter  $1.0 \text{ pm}/\sqrt{\text{Hz}}$  bei 100 mHz erreicht werden.

SCHLAGWORTE: Gravitationsphysik, Laserinterferometrie, Weltraumanwendung





# OVERVIEW

An introduction to high-precision laser interferometry for satellite missions is given in Chapter 1. Two different fields of application of the same separate this document into two main parts:

The first part addresses the investigation of alternative backlink concepts for the space-based gravitational wave observatory LISA. Chapter 2 gives an introduction to phase references and motivates the experimental investigation of alternative backlink schemes for LISA. The optical layout of the so-called *Three-Backlink interferometer (TBI)*, an experiment to compare different backlink implementations, is simulated and the results are described in Chapter 3. The experimental infrastructure for this experiment is presented in Chapter 4. Results of a free-beam pre-experiment are shown in Chapter 5, together with the construction status of the TBI.

The second part of this thesis focuses on alternative multi-degree of freedom test mass interferometry concepts, using optical phase shifting techniques for generating quasi-heterodyne signals in compact, cm-scale set-ups, so-called optical heads. Chapter 6 motivates the development of multi-channel interferometry based on application examples and provides an introduction to *deep frequency modulation interferometry (DFMI)*. The optical designs for a reference Mach-Zehnder interferometer (MZI) and a so-called *Test Mass in the Middle (TMitM)* experiment, emulating the readout of a test mass from two sides, are simulated and shown in Chapter 7. The experimental infrastructure for testing DFMI is shown in Chapter 8. Detailed experimental results are given in Chapter 9.

Chapter 10 concludes this thesis and presents a summary and outlook for both parts.



# CONTENTS

<b>Abstract</b>	<b>vii</b>
<b>Kurzzusammenfassung</b>	<b>ix</b>
<b>Overview</b>	<b>xi</b>
<b>List of Acronyms</b>	<b>xix</b>
<b>List of Figures</b>	<b>xxvi</b>
<b>List of Tables</b>	<b>xxvii</b>
<b>1 Introduction</b>	<b>1</b>
1.1 Gravitational wave detection . . . . .	1
1.2 Satellite geodesy missions . . . . .	5
1.3 Laser interferometry . . . . .	7
1.3.1 Heterodyne phase readout . . . . .	9
1.3.2 Contrast and heterodyne efficiency . . . . .	12
1.3.3 Longitudinal pathlength signal . . . . .	13
1.3.4 Differential wavefront sensing . . . . .	14
1.3.5 Differential power sensing . . . . .	15
1.3.6 Tilt-to-length coupling . . . . .	16
<b>I Towards the LISA backlink:   The Three-Backlink interferometer</b>	<b>17</b>
<b>2 Phase reference distribution systems</b>	<b>19</b>
2.1 Laser Interferometer Space Antenna . . . . .	20
2.1.1 In-Field Pointing . . . . .	22
2.1.2 Telescope Pointing . . . . .	23
2.2 Prior fiber backlink experiment . . . . .	24

2.3	Spurious light beams and signals . . . . .	26
2.3.1	Categories . . . . .	26
2.3.2	Coupling into the phase measurement . . . . .	28
2.3.3	Occurrence and dynamics in optical set-ups . . . . .	30
2.3.4	Influence of focusing lenses in front of photodiodes . . . . .	32
2.3.5	Mitigation strategies . . . . .	34
2.4	Backlink designs and spurious beam limitations . . . . .	36
2.4.1	Fiber backlinks . . . . .	36
2.4.2	Free-beam backlinks . . . . .	41
2.4.3	Backlink suggestions for LISA and the TBI . . . . .	42
<b>3</b>	<b>Optical simulations</b>	<b>45</b>
3.1	Three-Backlink interferometer design . . . . .	46
3.2	Power budget and fundamental noise sources . . . . .	50
3.3	Spurious light suppression . . . . .	51
3.4	Phase error of remaining ghost beams . . . . .	52
3.5	Tilt-to-length coupling . . . . .	54
3.6	Free-beam backlink . . . . .	58
3.6.1	Pathlength noise . . . . .	58
3.6.2	Optical signals . . . . .	58
3.6.3	DWS coupling coefficients of the free-beam . . . . .	62
3.7	Three-Backlink construction plan . . . . .	65
3.7.1	Template . . . . .	65
3.7.2	Construction order . . . . .	66
<b>4</b>	<b>Experimental infrastructure</b>	<b>73</b>
4.1	Laser preparation . . . . .	73
4.1.1	Laser stabilization . . . . .	75
4.1.2	High voltage amplifier design . . . . .	76
4.2	Vacuum set-up . . . . .	78
4.2.1	Photodiode mount . . . . .	79
4.2.2	Faraday mount . . . . .	80
4.2.3	Temperature sensors . . . . .	81
4.3	Phasemeter and electronics . . . . .	83
4.3.1	Free-beam control . . . . .	84
4.3.2	Rotary stage control . . . . .	86
4.4	Planned experiments . . . . .	86
4.4.1	Non-reciprocal backlink phase noise . . . . .	88
4.4.2	Non-reciprocity of the Faraday rotator . . . . .	90
4.4.3	Backscatter measurements of various fibers . . . . .	92

4.4.4	Dynamic range suppression of balanced detection . . . . .	93
<b>5</b>	<b>Experimental work and results</b>	<b>95</b>
5.1	Free-beam experiment . . . . .	96
5.1.1	Optical set-up . . . . .	96
5.1.2	Alignment of the free-beam backlink . . . . .	96
5.1.3	Rotation of two benches relative to each other . . . . .	98
5.1.4	DWS coupling coefficients . . . . .	100
5.1.5	Steering mirror control loop . . . . .	101
5.1.6	Long term phase measurements . . . . .	103
5.1.7	Thermal measurement results . . . . .	106
5.1.8	Beam dumps characterization . . . . .	108
5.2	Status of the Three-Backlink interferometer . . . . .	109
5.2.1	Laser modulation bench . . . . .	109
5.2.2	Monolithic fiber output couplers . . . . .	110
5.2.3	Monolithic set-up . . . . .	110
<b>II</b>	<b>Deep frequency modulation interferometry: Advanced optics for space applications</b>	<b>113</b>
<b>6</b>	<b>Multi-channel interferometry</b>	<b>115</b>
6.1	Test mass interferometry . . . . .	116
6.2	Deep frequency modulation interferometry . . . . .	119
6.2.1	Theory . . . . .	120
6.2.2	Signal processing . . . . .	123
6.2.3	Optical head design . . . . .	125
6.3	Alternative interferometer techniques . . . . .	128
6.3.1	Digitally enhanced interferometry . . . . .	128
6.3.2	Deep phase modulation interferometry . . . . .	131
6.4	Comparison and applications of interferometer techniques . . . . .	132
6.4.1	Test mass interferometry . . . . .	132
6.4.2	Laser preparation . . . . .	133
6.4.3	Stray light suppression in a Michelson interferometer . . . . .	134
6.4.4	Identification of stray light sources . . . . .	135
6.4.5	Simultaneous measurements of multiplexed optical signals . . . . .	135
6.4.6	Absolute distance measurements . . . . .	136
<b>7</b>	<b>Optical simulations</b>	<b>137</b>
7.1	Mach-Zehnder reference interferometer . . . . .	138
7.1.1	Optical design . . . . .	138

7.1.2	Ghost beams . . . . .	140
7.1.3	Tilt-to-length coupling by wedged components . . . . .	140
7.1.4	Performance for a static interferometer misalignment . . . . .	142
7.2	Test Mass in the Middle experiment . . . . .	146
7.2.1	Prism-interferometry . . . . .	146
7.2.2	Optical design . . . . .	149
7.2.3	Ghost beams . . . . .	151
7.2.4	Test mass displacement . . . . .	153
7.2.5	Test mass tilt couplings . . . . .	155
<b>8</b>	<b>Experiment preparation</b>	<b>161</b>
8.1	Frequency tunable laser sources . . . . .	161
8.1.1	Rapidly tunable external cavity diode laser . . . . .	162
8.1.2	Eternal™ SlowLight Laser from Orbits Lightwave . . . . .	166
8.2	Front-end electronics . . . . .	166
8.2.1	Photoreceiver . . . . .	166
8.2.2	Low-pass filter . . . . .	167
8.3	Data acquisition . . . . .	167
8.3.1	Measured transfer function . . . . .	170
8.4	Laser preparation . . . . .	171
8.4.1	Amplitude stabilization . . . . .	172
8.4.2	Frequency stabilization . . . . .	174
8.4.3	Modulation index stabilization . . . . .	176
8.5	Test mass control . . . . .	176
8.6	Interferometer construction . . . . .	178
8.6.1	Reference Mach-Zehnder interferometer . . . . .	178
8.6.2	Test Mass in the Middle experiment . . . . .	180
<b>9</b>	<b>Results</b>	<b>185</b>
9.1	First proof-of-principle measurement . . . . .	186
9.1.1	Experiment description . . . . .	187
9.1.2	Optical signals . . . . .	188
9.1.3	Time domain analysis of frequency modulation linearity . . . . .	188
9.1.4	Phase performance of DFM . . . . .	190
9.1.5	Residual amplitude fluctuations . . . . .	191
9.1.6	Laser frequency noise correction . . . . .	193
9.2	Frequency stabilization via balanced readout . . . . .	195
9.2.1	Experiment description . . . . .	196
9.2.2	Measured frequency stability . . . . .	197
9.3	Test Mass in the Middle experiment . . . . .	199

9.3.1	Experiment description . . . . .	200
9.3.2	Frequency stabilization . . . . .	201
9.3.3	Readout noise limitations . . . . .	202
9.3.4	Modulation depth stabilization . . . . .	203
9.3.5	Effect of refractive index changes . . . . .	205
9.3.6	Test mass stabilization and increased tilt-to-length coupling	206
9.3.7	Test mass readout performance . . . . .	209
<b>10</b>	<b>Summary and outlook</b>	<b>213</b>
10.1	Three-Backlink interferometer . . . . .	213
10.2	Deep frequency modulation interferometry . . . . .	216
10.3	Future test mass readout with DFMI . . . . .	218
	<b>Bibliography</b>	<b>221</b>
	<b>Appendix</b>	<b>233</b>
<b>A</b>	<b>Three-Backlink parameters</b>	<b>233</b>
<b>B</b>	<b>Deep frequency modulation</b>	<b>237</b>
B.1	Analytic calculation of interferometer signals . . . . .	237
B.2	Data demodulation . . . . .	239
<b>C</b>	<b>Prism coatings</b>	<b>241</b>





# LIST OF ACRONYMS

<b>ADC</b>	analog-to-digital converter
<b>AEI</b>	Albert Einstein Institute
<b>AFG</b>	Arbitrary Function Generator
<b>aLIGO</b>	advanced LIGO
<b>ALO</b>	additional local oscillator
<b>AML</b>	left actuator mirror
<b>AMR</b>	right actuator mirror
<b>AOES</b>	Department of Atmospheric, Oceanic, and Earth Sciences
<b>AOI</b>	angle of incident
<b>AOM</b>	Acoustic-Optical modulator
<b>AOMFBL</b>	AOM fiber backlink
<b>AR</b>	anti-reflecting
<b>ASCII</b>	American Standard Code for Information Interchange
<b>BL</b>	backlink
<b>BPSK</b>	binary phase shift keying
<b>BS</b>	beam splitter
<b>BW</b>	bandwidth
<b>CAD</b>	computer-aided design
<b>CFBL</b>	cavity fiber backlink
<b>CMM</b>	coordinate measurement machine
<b>CPN</b>	common phase noise
<b>CTE</b>	coefficient of thermal expansion
<b>DAC</b>	digital-to-analog converter
<b>DAQ</b>	data acquisition
<b>DI</b>	digital interferometry
<b>DEHeI</b>	digitally enhanced heterodyne interferometry
<b>DEHoI</b>	digitally enhanced homodyne interferometry
<b>DFBL</b>	direct fiber backlink
<b>DFM</b>	deep frequency modulation
<b>DFMI</b>	deep frequency modulation interferometry
<b>DFT</b>	Discrete Fourier Transform
<b>DLR</b>	German Aerospace Center/Deutsches Zentrum für Luft- und Raumfahrt

<b>DoF</b>	degree of freedom
<b>DPM</b>	deep phase modulation
<b>DPS</b>	differential power sensing
<b>DuT</b>	device under test
<b>DWS</b>	differential wavefront sensing
<b>ECDL</b>	external cavity diode laser
<b>EN</b>	electronic noise
<b>EOAM</b>	electro-optical amplitude modulator
<b>EOM</b>	electro-optical modulator
<b>ESA</b>	European Space Agency
<b>FBBL</b>	free-beam backlink
<b>FFT</b>	Fast Fourier Transform
<b>FIFBL</b>	Faraday isolator fiber backlink
<b>FIOS</b>	fiber injection optical subassembly
<b>FMA</b>	fiber mount assembly
<b>FMCW</b>	frequency modulated continuous wave
<b>FPGA</b>	Field-programmable gate array
<b>FS</b>	fiber splitter
<b>FSFBL</b>	frequency separated fiber backlink
<b>GOCE</b>	Gravity field and steady-state Ocean Circulation Explorer
<b>GPS</b>	Global Positioning System
<b>GRACE</b>	Gravity Recovery and Climate Experiment
<b>GRACE-FO</b>	Gravity Recovery and Climate Experiment Follow-On
<b>GRS</b>	gravitational reference sensor
<b>HR</b>	high-reflective
<b>HV</b>	high-voltage
<b>IFE</b>	Institute for Geodesy/Institut für Erdmessung
<b>InGaAs</b>	indium gallium arsenide
<b>JPL</b>	Jet Propulsion Laboratory
<b>KAGRA</b>	Kamioka Gravitational Wave Detector
<b>LD</b>	laser diode
<b>LFN</b>	laser frequency noise
<b>LIGO</b>	Laser Interferometer Gravitational-Wave Observatory
<b>LISA</b>	Laser Interferometer Space Antenna
<b>LISO</b>	LInear Simulation and Optimization
<b>LO</b>	local oscillator
<b>LPF</b>	LISA Pathfinder
<b>LTP</b>	LISA Technology Package
<b>MC</b>	measurement computing
<b>MI</b>	Michelson interferometer
<b>MLI</b>	multilayer insulation
<b>MOSA</b>	moving optical sub-assembly
<b>MZI</b>	Mach-Zehnder interferometer
<b>NASA</b>	National Aeronautics and Space Administration

<b>NCO</b>	numerically controlled oscillator
<b>NI</b>	National Instruments
<b>NIST</b>	National Institute of Standards and Technology
<b>NPRO</b>	non-planar ring oscillator
<b>NSF</b>	noise shape function
<b>NTC</b>	Negative Temperature Coefficient
<b>OB</b>	optical bench
<b>OEC GmbH</b>	Opto-Electronic Components
<b>OH</b>	optical head
<b>op-amp</b>	Operational amplifier
<b>OPD</b>	optical pathlength difference
<b>PA</b>	phase accumulator
<b>PAAM</b>	point ahead angle mechanism
<b>PBS</b>	polarizing beam splitter
<b>PC</b>	personal computer
<b>PCI</b>	Peripheral Component Interconnect
<b>PD</b>	photodiode
<b>PEEK</b>	polyether ether ketone
<b>PER</b>	polarization extinction ratio
<b>PFBL</b>	Polarization Fiber backlink
<b>PL</b>	pathlength
<b>PLL</b>	phase-locked loop
<b>PI</b>	Physik Instrumente
<b>PID</b>	proportional integral derivative
<b>PIR</b>	phase incremental register
<b>PM</b>	polarization-maintaining
<b>PRN</b>	pseudo-random noise
<b>PRDS</b>	phase reference distribution system
<b>PTC</b>	Positive Temperature Coefficient
<b>PZT</b>	piezoelectric transducer
<b>QPD</b>	quadrant photodetector
<b>QPSK</b>	quadrature phase shift keying
<b>REF</b>	reference
<b>RF</b>	radio frequency
<b>RIN</b>	relative intensity noise
<b>RMBL</b>	reflector in the middle backlink
<b>RTL</b>	left rotation table
<b>RTR</b>	right rotation table
<b>RX</b>	received
<b>SBFT</b>	single-bin Fourier transform
<b>S/C</b>	spacecraft
<b>SED</b>	single element photodiode
<b>SFB</b>	Collaborative Research Center/Sonderforschungsbereich
<b>Si</b>	silicon

<b>SLB</b>	spurious light beam
<b>SLS</b>	spurious light signal
<b>SM</b>	single-mode
<b>SN</b>	shot noise
<b>SoC</b>	System-on-a-Chip
<b>SSE</b>	sum of squared errors
<b>SSQ</b>	sum of squares
<b>SuK</b>	Schäfter und Kirchhoff
<b>SW</b>	software
<b>TBI</b>	Three-Backlink interferometer
<b>TDI</b>	time delay interferometry
<b>THD</b>	third harmonic distortion
<b>TIA</b>	transimpedance amplifier
<b>TM</b>	test mass
<b>TMitM</b>	Test Mass in the Middle
<b>TS</b>	thermal stability
<b>TSH</b>	thermal shielding
<b>TTL</b>	tilt-to-length
<b>TX</b>	transmitted
<b>US</b>	United States
<b>USB</b>	Universal Serial Bus
<b>USO</b>	ultra-stable oscillator
<b>UV</b>	ultra-violet
<b>VAC</b>	vacuum chamber
<b>Virgo</b>	Europe-based gravitational wave detector
<b>VOA</b>	variable optical attenuator

# LIST OF FIGURES

1.1	Sketch of gravitational wave polarizations and the event GW150914.	2
1.2	LISA and its expected gravitational wave sources. . . . .	3
1.3	The LPF satellite and the measured acceleration sensitivity. . . . .	4
1.4	Earth’s gravity field fluctuations measured by GRACE. . . . .	5
1.5	Homodyne interferometry: Optical set-up and readout. . . . .	8
1.6	Heterodyne interferometry: Optical set-up and readout. . . . .	10
1.7	Phasor diagram showing the $IQ$ -demodulation scheme. . . . .	11
1.8	Differential wavefront sensing on a QPD. . . . .	15
2.1	Illustration of the LISA orbits. . . . .	20
2.2	Sketch of the LISA optical bench and the MOSA. . . . .	21
2.3	Telescope vs. In-Field Pointing. . . . .	23
2.4	Set-up of the prior fiber backlink experiment. . . . .	24
2.5	Phase noise of the prior fiber backlink experiment. . . . .	25
2.6	A selection of spurious beam sources. . . . .	27
2.7	Vector representation showing the influence of a spurious signal. . . . .	29
2.8	ABCD matrix formalism for a ghost beam backreflected from a lens. . . . .	33
2.9	Vector representation showing balanced detection. . . . .	35
2.10	Overview of optical designs for various PRDSs. . . . .	37
2.11	Implementation of selected backlinks on the LISA optical bench. . . . .	44
3.1	Simulated optical layout of the TBI. . . . .	48
3.2	Horizontal pathlength signal of the TBI. . . . .	55
3.3	Vertical pathlength signal of the TBI. . . . .	57
3.4	Horizontal DWS, DPS and heterodyne efficiency of the TBI. . . . .	59
3.5	Vertical DWS, DPS and heterodyne efficiency of the TBI. . . . .	60
3.6	DWS offsets for horizontal and vertical signals over misalignment. . . . .	61
3.7	Spot size and condition number over lens position in the FBBL. . . . .	64
3.8	3D model of one TBI bench and drawing of the template. . . . .	66
3.9	Steps 2-8 from the construction of the TBI plan. . . . .	68
3.10	Steps 9-14 from the construction of the TBI plan. . . . .	70

4.1	Laser frequency stabilization of the TBI. . . . .	74
4.2	Transfer function and phase noise of the laser frequency stabilization. . . . .	76
4.3	Measured NPRO PZT impedances and the equivalent circuit model. . . . .	77
4.4	Sketch of the vacuum chamber prepared for the TBI. . . . .	78
4.5	Photographs of photodiode mounts. . . . .	79
4.6	Thermally compensated mount for the Faraday rotator. . . . .	80
4.7	Circuit diagram of a Wheatstone bridge and thermistor response. . . . .	82
4.8	Phase readout and front- and back-end electronics. . . . .	83
4.9	Photographs of steering mirrors and rotary stages. . . . .	84
4.10	Control loop diagram for the steering mirror stabilizations. . . . .	85
4.11	Occurring phase noise illustrated for the DFBL. . . . .	87
4.12	Experiment for measuring the non-reciprocity of the Faraday rotator. . . . .	91
5.1	Layout and photograph of the free-beam pre-experiment. . . . .	97
5.2	Time series of rotation tables and the in-loop DWS signals. . . . .	98
5.3	Phase oscillation measured during co-rotating benches. . . . .	99
5.4	Time series of the steering mirror actuation signals. . . . .	101
5.5	Linear spectral densities of DWS error signals. . . . .	102
5.6	Phase noise of the free-beam pre-experiment and $\pi$ -measurement. . . . .	104
5.7	Non-reciprocal phase signal combination of the free-beam pre-experiment. . . . .	105
5.8	Absolute temperatures and noise measured in vacuum during rotation. . . . .	107
5.9	Optical set-up of the laser preparation in the cleanroom. . . . .	109
5.10	Construction process of the TBI. . . . .	111
6.1	Optical bench of LISA Pathfinder. . . . .	116
6.2	Definition of TM displacement, yaw, pitch and roll angle. . . . .	117
6.3	Set-up for deep frequency modulation interferometry (DFMI). . . . .	121
6.4	Bessel functions and amplitudes for first $n = 10$ harmonics. . . . .	122
6.5	Possible MI constellations for DFM test mass readouts. . . . .	126
6.6	Possible MZI constellations for DFM test mass readouts. . . . .	127
6.7	Set-up for digital interferometry (DI). . . . .	128
6.8	Set-up for deep phase modulation (DPM) interferometry. . . . .	131
6.9	Optical test mass readout with alternative interferometer techniques. . . . .	132
6.10	Laser preparation by using alternative interferometer techniques. . . . .	134
6.11	Stray light suppression experiment with a locked MI. . . . .	135
7.1	2D IfoCAD drawing of the reference MZI. . . . .	139
7.2	Pathlength signal over beam jitter in the MZI. . . . .	141
7.3	TTL coupling in the MZI for different wedge angles. . . . .	142
7.4	Horizontal signals for lens misalignments. . . . .	143

7.5	Horizontal signals for lens misalignments. PD1 is re-aligned. . . . .	144
7.6	Horizontal signals for misalignments of BS2. . . . .	145
7.7	Isosceles prism for one-component interferometry. . . . .	146
7.8	2D sketch of the TMitM generated with IfoCAD. . . . .	150
7.9	Spot sizes in the TMitM over lens positions. . . . .	151
7.10	2D ray propagation of the ghost beam through the prism. . . . .	152
7.11	Simulated signals of the TMitM over test mass displacement. . . . .	154
7.12	Horizontal signals of the TMitM over test mass yaw tilt. . . . .	156
7.13	Horizontal pathlength of the TMitM over test mass yaw tilt. . . . .	157
7.14	Optimized horizontal pathlength for yaw tilts. . . . .	158
7.15	Vertical signals of the TMitM over test mass pitch tilts. . . . .	160
8.1	Tunable ECDL and Eternal™ SlowLight laser. . . . .	162
8.2	Littrow and Littman-Metcalf configuration of an ECDL. . . . .	163
8.3	Characterization measurements of the TLB 6700. . . . .	164
8.4	Schematic of a second order Sallen-Key low-pass filter. . . . .	167
8.5	Pictures of the DAQ card and the DFM phasemeter. . . . .	168
8.6	Measured transfer functions of the DFM DAQ system. . . . .	169
8.7	Optical set-up of the DFM laser preparation. . . . .	170
8.8	Schematic of a variable gain amplifier and offset circuit. . . . .	171
8.9	Time series and transfer function of the DFM amplitude stabilization. . . . .	173
8.10	Relative intensity noise spectrum of the ECDL laser. . . . .	174
8.11	Control loop diagram for the DFM laser stabilization. . . . .	175
8.12	Transfer functions of the DFM frequency stabilization. . . . .	176
8.13	Control loop diagram of the three-axis test mass stabilization. . . . .	177
8.14	3D CAD model of the reference MZI and template. . . . .	179
8.15	Construction of the reference MZI. . . . .	182
8.16	Construction of the TMitM experiment. . . . .	183
9.1	Sketch of the DFM experimental set-up at NIST. . . . .	186
9.2	DFM photodiode signals and the FFTs. . . . .	187
9.3	DFM time series showing the modulation non-linearity. . . . .	189
9.4	Phase noise of the DFM experiments measured at NIST. . . . .	190
9.5	DFM time series showing residual amplitude noise and timing errors. . . . .	192
9.6	Phase noise corrected by LFN. . . . .	194
9.7	Photographs of the frequency-stabilization experiment. . . . .	195
9.8	Sketch of the frequency-stabilization experiment. . . . .	196
9.9	Frequency noise measured in the reference MZI. . . . .	197
9.10	Temperature noise during the frequency-stabilization experiment. . . . .	198
9.11	Sketch of the full TMitM experimental set-up. . . . .	199

9.12	Photographs of the TMitM. . . . .	200
9.13	Laser frequency noise stabilization with DFMI. . . . .	201
9.14	Electronic and optical phase noise combinations of MZI/TMitM. . .	203
9.15	Modulation depth noise stabilization with DFMI. . . . .	204
9.16	Measuring coupling coefficients of the test mass control loop. . . . .	206
9.17	Test mass tilt noise with feedback control. . . . .	207
9.18	Test mass phase noise with stabilizations. . . . .	209
9.19	Singular test mass phase noise measured with stabilizations. . . . .	210
9.20	Temperature drifts during test mass readout measurement. . . . .	211
9.21	Time series data of the TMitM and MZI. . . . .	212
10.1	Final 3D model of the TBI experiment. . . . .	215
10.2	Torsion pendulum as test facility for multi-channel interferometry. .	217
10.3	3D model of a monolithic frame design for prism-interferometers. . .	218
10.4	A re-worked one-component interferometer design without ghost beam.	219
10.5	Multi-core fiber for DWS measurements. . . . .	220
C.1	Reflectivities of the prism coatings. . . . .	241



# LIST OF TABLES

2.1	List of spurious beams, separated by their categories . . . . .	31
2.2	Beat note separation of ghost beams in the FSFBL. . . . .	39
2.3	Beat note separation of ghost beams in the AOMFBL. . . . .	41
2.4	Estimated phase errors for the different backlink candidates. . . . .	43
3.1	List of components used in the TBI on one bench. . . . .	47
3.2	Laser power distribution in the TBI and its fundamental noise limit. . . . .	50
3.3	Simulated residual ghost beam powers in the TBI . . . . .	53
4.1	Laser offset frequencies of the TBI laser preparation. . . . .	75
6.1	Comparison of alternative interferometer techniques. . . . .	133
7.1	Spot size radii of the prism beams. . . . .	148
8.1	Comparison of deep frequency tunable laser sources. . . . .	165
9.1	AOIs in the prism for different environment. . . . .	205
A.1	Beam parameter for the alignment process of the TBI plan. . . . .	233
A.2	Component positions of the left TBI bench. . . . .	234
A.3	Component positions of the right TBI bench. . . . .	235



” *A chapter about the observation of smallest changes in displacement and acceleration with high precision laser interferometry.*

Today’s laser interferometry is able to sense length variations with very high precision over large distances and long timescales. It is an outstanding technology for measuring relative displacement, motion or acceleration changes between satellites, test masses or other targets. The measurement of spurious forces at low frequencies, like small effects from gravity variations, with ground-based detectors is limited due to environmental disturbances. The demand for laser interferometry in space is therefore growing worldwide and international scientists are working on improved measurement systems. Two possible applications of space interferometry are the detection of gravitational waves and satellite geodesy. Depending on the individual mission design both, inter- and intra-satellite interferometry, are used. The interferometer concepts investigated and described in this thesis focus on the intra-satellite interferometry as it is used for example for measuring the motion of free-floating test masses within a spacecraft (S/C).

In this chapter, the two main applications are motivated, namely gravitational wave observatories and geodesy missions. They are introduced based on prior, successfully performed missions, currently planned missions and future concepts promising improved scientific results. At the end of this chapter an introduction to laser interferometry is given, explaining the fundamentals of distance measurements and optical signals.

## 1.1 Gravitational wave detection

Gravitational waves were predicted by Albert Einstein’s General Theory of Relativity in 1915 [Ein16]. They are ripples in spacetime that are caused by accelerated massive objects. They propagate as waves through spacetime at the speed of light almost without being attenuated. Perpendicular to their propagation direction

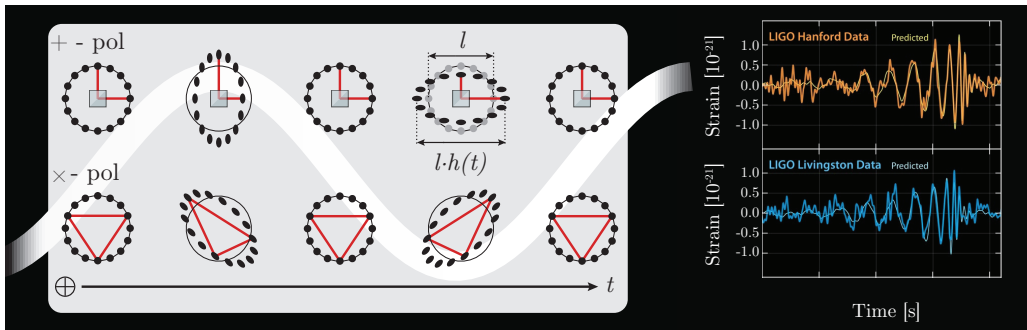
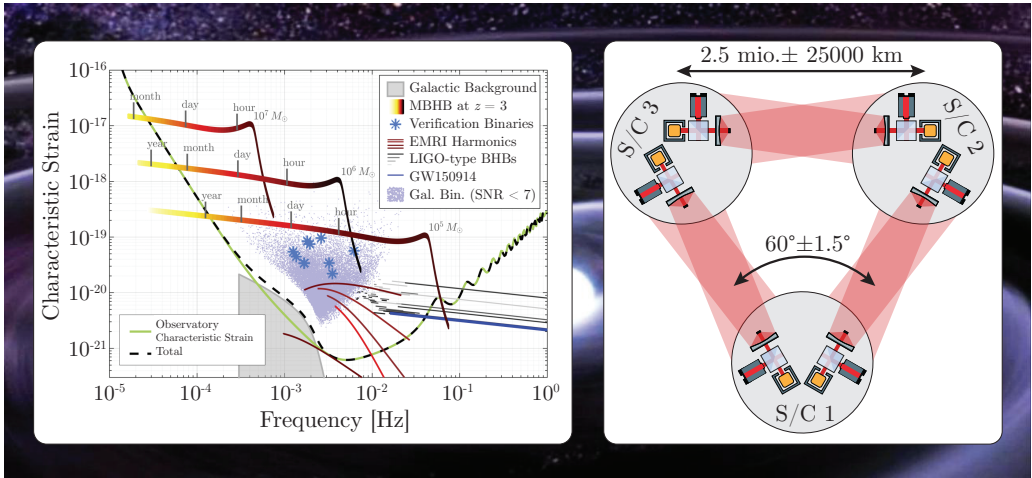


Fig. 1.1.: Sketch of the influence of a gravitational wave with two polarizations, 'plus' and 'cross', on an assembly of test masses, arranged in a circular constellation, with laser interferometry in-between. The length change induced by the gravitational wave depends on its strain,  $h(t)$ , and causes an interferometric phase signal [SS09]. Also shown are the results of the event GW150914, the first direct detection of a gravitational wave [Abb+16].

they stretch and compress spacetime in two polarization directions, as illustrated in Figure 1.1. Similar to the description of other waves, e.g. electromagnetic waves, gravitational waves have an amplitude, usually denoted as strain,  $h(t)$ , which describes the induced relative changes in spacetime. Gravitational waves passing through the Earth have typically strains of below  $h(t) = 1 \cdot 10^{-20}$  which makes a direct detection of the caused spacetime deformations very challenging [Dan+17]. High precision laser interferometry is the tool of choice for sensing smallest distance changes between two test objects, as it can be used for gravitational wave detection [SS09]. A network of such sensitive devices exist on ground and consist of the Laser Interferometer Gravitational-Wave Observatories (LIGOs) in Hanford, Washington United States (US), and Livingston, Louisiana US [BW99], the Europe-based gravitational wave detector (Virgo) near Pisa, Italy [Ace+07] and GEO600 in Hannover, Germany [Wil+02]. Under construction is a cryogenic variant, Kamioka Gravitational Wave Detector (KAGRA), in Gifu Prefecture, Japan, a project of the Institute for Cosmic Ray Research of the University of Tokyo [Som12]. LIGO India is also under construction and will be set up in Aundh in Hingoli district of Maharashtra [Unn13].

100 years after Einstein's prediction, the first direct detection of gravitational waves was measured by the two ground-based advanced LIGO (aLIGO) detectors. The results of the groundbreaking discovery, originating from a pair of merging black holes on September 14 2015, are shown in Figure 1.1 [Abb+16]. This discovery was rewarded the Nobel Prize in Physics in 2017, shared by Rainer Weiss, Kip Thorne and Barry Barish. By direct detections of gravitational waves, astronomers can deduce detailed information about the origin of the source by monitoring the amplitude, phase and frequency of the wave [Sch99]. This new field



**Fig. 1.2.:** Selected gravitational wave sources are shown on the left for the Laser Interferometer Space Antenna (LISA) measurement band together with the expected LISA sensitivity. A possible LISA three-arm configuration is shown on the right with six laser links established between three spacecraft (S/C). Image credits: [Dan+17], [NASb].

of gravitational wave astronomy complements the existing observations that are based on electro-magnetic radiation and neutrino detection. The first detected event GW150914 [Abb+16] shows that also dark objects, or new, yet unknown objects, can be revealed since gravitational waves are caused by all massive objects in the universe [Ein16]. A further event, GW170814, was a first three-detector observation by the two LIGO detectors and Virgo [Abb+17]. With three detectors the gravitational wave parameters, especially the sky position, can be defined about 10 times more precise than with a two-detector observation. A network of ground-based observatories, located all over the Earth, would significantly improve gravitational wave astronomy [Abb+17]. But also other detector classes are relevant for future gravitational wave astronomy. While large ground-based laser interferometers detect gravitational waves in the audio frequency band between 10 Hz and 10 kHz, so-called pulsar-timing arrays are able to deduce waves at very low frequencies from about  $1 \cdot 10^{-8}$  Hz to  $1 \cdot 10^{-9}$  Hz [Hob+10]. A large frequency regime between these two measurement bandwidths is unfilled which motivates space-based gravitational wave detectors.

The Laser Interferometer Space Antenna (LISA) will allow us to directly detect gravitational waves from astrophysical sources radiating in the frequency band from 0.1 mHz to 1 Hz as illustrated in Figure 1.2 [Dan+17]. Extreme mass ratio inspirals, supermassive black holes and binary neutron stars can be detected and future detections on ground of e.g. black hole binaries (BHBs) can be predicted in advance by LISA [Ses16; aC13; DR03]. LISA has recently been chosen by the European

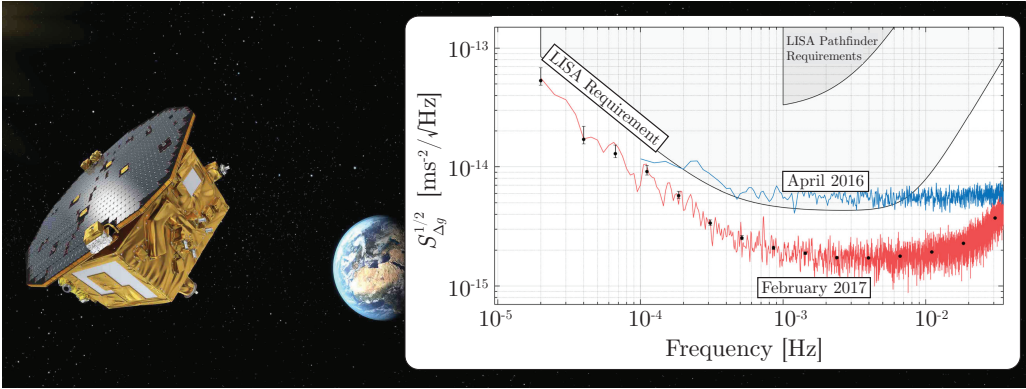


Fig. 1.3.: Picture of the LISA Pathfinder (LPF) satellite and the measured acceleration sensitivity. Image Credit: ESA-C.Carreau and [Arm+18].

Space Agency (ESA) as L3 mission [Dan+17]. As shown in Figure 1.2, it will consist of three S/C forming a cartwheel formation that follows the Earth around the sun. For the measurement of gravitational waves at mHz frequencies, very long interferometer arms of several 1 Gm are needed, which can only be realized in space. Longer detector arms leads to more precise strain measurements for the same displacement noise. LISA will have an arm length of  $2.5 \cdot 10^6$  km, corresponding to 8.3 s time-of-flight, with  $60^\circ$  angles between them. Due to solar system celestial mechanics, the satellite constellation is disturbed and the interferometer arm length will vary by 1 % and the angles by about  $\pm 1.5^\circ$  with an annual period [Fol01; Xia+10]. For compensating the breathing angles the current baseline includes two moving optical sub-assemblies (MOSAs) per S/C, articulating the full payload and retaining the interferometric contrast [Sch+14a]. This mechanism is called *Telescope Pointing*. An alternative approach using a single optical bench and an actuation of the tertiary telescope mirror is called *In-Field Pointing* and is also under investigation [Liv+17; Bru+17]. The readout of free-floating test masses is performed relative to the local optical benches similar to the interferometry in LISA Pathfinder (LPF) [Arm+16; Hei+04].

LPF was a technology demonstrator for LISA, carrying the so-called LISA Technology Package (LTP). One LISA arm is shrunk to fit into a single satellite that is shown in Figure 1.3. The payload of one LPF satellite consists of two test masses and one optical bench in-between. The acceleration of the two test masses along one axis is measured relative to each other with four heterodyne interferometers in total. The drag-free control of the S/C and the reliability of various components like capacitive sensors, micro-Newton thrusters and the optic and laser itself are also tested for LISA. The LPF satellite was launched in 2015 and operated between March 2016 and July 2017. The mission demonstrated a

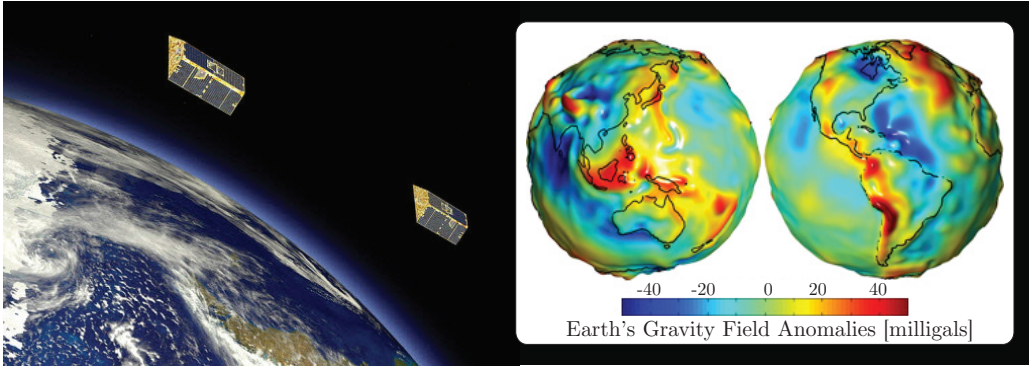


Fig. 1.4.: Earth's gravity field fluctuations measured by Gravity Recovery and Climate Experiment (GRACE). Image Credits: [ESA18] and [NASA].

remarkable low acceleration noise below the LPF requirement, even achieving the LISA requirement. The final performance of LPF is shown in Figure 1.3. With this knowledge the LISA mission concept can be revised and relevant issues learned by LPF can be adapted in LISA [Anz+05].

## 1.2 Satellite geodesy missions

The Earth's gravity is a gravitational acceleration acting on objects, or test masses, due to the mass distribution of the Earth. The standard gravity is by definition  $9.80665 \text{ m/s}^2$ , this is the nominal average of gravity at the surface. The actual gravity field depends on the location on Earth where it can be influenced by various effects, like tides [Han+04], climate, melting ice [VW13], earth quakes [Che+07], water reservoirs [Lon+13] and more. Figure 1.4 shows the Earth's gravity field as an equipotential surface map of the Earth. This map demonstrates how geoid measurements offer details of how mass, especially water, is moving on our planet [See03]. Locally placed gravimeters on ground cannot be used to map the Earth completely. Another way to probe the global gravity field is to measure the gravitational acceleration acting on satellites, which are orbiting the Earth. Satellites can bridge large distances over a relatively short time. With this satellite geodesy, a complete map of the Earth can be measured and weekly-variations of the Earth's gravitational potential can be sensed. The main working principle of satellite geodesy is that the relative motion between two or more test masses is tracked continuously by orbiting the Earth. Since the satellites follow almost drag-free orbits, the test masses are only influenced by the Earth's gravitational field, in the ideal case. Several satellite missions have used this principle of acceleration measurements to scan the Earth's gravitational field [Che+05].

The Gravity Recovery and Climate Experiment (GRACE) was a joint mission of National Aeronautics and Space Administration (NASA) and German Aerospace Center/Deutsches Zentrum für Luft- und Raumfahrt (DLR) that measured the relative motion between two satellites with a microwave-ranging link between them. GRACE, shown in Figure 1.4, started measuring the Earth's gravitational field on March 17 2002, with two satellites separated by about 220 km in an altitude of around 500 km. The pair of satellites, cycling the Earth, are affected in their speed by the mass distribution of the Earth. A higher mass concentration accelerates the leading satellite away from the trailing satellite. Once the trailing satellite passes the gravity anomaly this one is now pulled towards the leading satellite. By measuring the distance changes between the two satellites, the Earth's gravitational field for this mass contribution can be determined. A microwave-ranging link performs the precise length change measurement between the satellites. Each satellite is armed with an accelerometer, located at the satellite's center of mass, that is used to measure all non-gravitational accelerations of the satellite, e.g. the atmospheric drag. This ensures that only accelerations caused by the Earth gravity are considered. The exact sky position within a few cm is determined by Global Positioning System (GPS) receivers. With these techniques the GRACE mission provided data that can be used to construct maps from the averaged Earth's gravity field with a monthly period [Tap+04]. In 2018, the Gravity Recovery and Climate Experiment Follow-On (GRACE-FO) will be launched. The GRACE-FO satellites are an improved rebuild of the GRACE ones. In addition to the microwave-ranging the inter-satellite distance will be measured with laser interferometry to achieve an improved sensitivity of  $80 \text{ nm} / \sqrt{\text{Hz}}$  relative distance change. For this purpose LISA-technology, like the laser and interferometer techniques, is used along with the LISA phasemeter. Thus, the LISA-technology for inter-satellite ranging will already be tested to some degree within the GRACE-FO mission [She+12; Sch+14a]. Time-dependent gravity changes can be measured with this two-satellite system. The height of 500 km, at which the GRACE satellites are orbiting the Earth, limits however the accuracy of the absolute gravitational potential measurement.

The Gravity field and steady-state Ocean Circulation Explorer (GOCE) satellite measured the Earth's gravity field with three pairs of gradiometers within a single satellite that cycled the Earth in a lower orbit of about 255 km. This delivers gravity gradient measurements which can be used to determine the reference shape of the Earth, the so called geoid, with an accuracy of 1 cm and the anomalies in the gravity field with an accuracy of  $1 \cdot 10^{-5} \text{ m/s}^2$  [Dri+03; Dri+06]. The combination of time-dependent GRACE data and high-accuracy GOCE data provides the best estimation for the Earth gravity field. The GOCE mission was launched on 17 March 2009 and cycled the Earth until 2013. To overcome the problem of air drag, an ion propulsion system was used for compensation. The three gradiometers



consist of six test masses in a cross-shaped constellation. Gravitational gradients along three perpendicular axes were measured with this architecture by using an electrostatic readout.

Owing to the huge success of these missions, new technology development for future missions is highly demanded such that the measurements of the gravitational field can be continued with even higher precision, like the ones that will be performed by GRACE-FO. It has shown that one can greatly benefit from time-variable gravity field measurement for studying the Earth's gravitational potential. For this purpose, the potential of space-based laser gradiometry is analyzed in Hannover within a Collaborative Research Center/Sonderforschungsbereich (SFB), together with geodesists from the Institute for Geodesy/Institut für Erdmessung (IFE) who investigate future gravity field missions using an architecture based on GOCE. Parameters for potential future GOCE-like missions are simulated. Starting from the requirements for the different sensors, an estimation of the final achievable precision is achieved, together with an estimation of the spatial resolution of the recovered gravity field models. Simulations have shown that future gradiometers will reach a sensitivity of  $1 \cdot 10^{-4} \text{ E}/\sqrt{\text{Hz}}$  at frequencies between 0.5 mHz and 10 mHz, equivalent to  $1 \cdot 10^{-13} \text{ s}^{-2}/\sqrt{\text{Hz}}$  [Dou+17b; Dou+17a; Dou+17c]. As a comparison, the maximum Earth's gravity gradient is around 3.08 E in vertical direction, the horizontal one is around 1.54 E. Gravity anomalies, for example in mountainous areas, can increase this number to several 100 E [Wik16]. This improved sensitivity can only be achieved by replacing the capacitive readout, as it has been used in GOCE, by an optical one. LPF has demonstrated that an acceleration noise down to  $1 \cdot 10^{-13}$  to  $1 \cdot 10^{-14} \text{ ms}^{-2}/\sqrt{\text{Hz}}$  can be measured between two test masses. This is one to two orders of magnitude below the strain sensitivity achieved in the GOCE mission. The long term goal is then the development of a multi-test mass sensor system as central sensor for future geodesy missions.

### 1.3 Laser interferometry

For the detection of any kind of gravity changes, either caused by gravitational waves or for the determination of the Earth gravity field, a precise distance measurement between test masses is required, which can be done by laser interferometry. Typically, interferometric length measurements use lasers with a near infrared wavelength,  $\lambda = 1064 \text{ nm}$ , that allows very precise measurement of relative displacement variations according to

$$\Delta l = \frac{\varphi}{2\pi} \cdot \lambda. \quad (1.1)$$

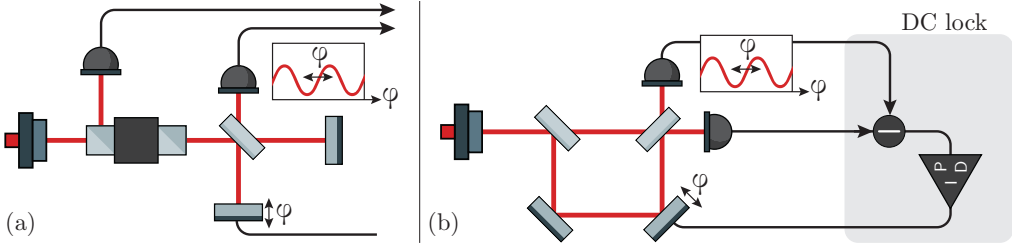


Fig. 1.5.: Shown is a classic homodyne interferometer that interferes two beams with the same frequency in a Michelson interferometer (MI) (a) and a Mach-Zehnder interferometer (MZI) (b). The detector monitors a DC amplitude that depends on the phase between the two interferometer arms. The output directly delivers the desired phase information.

Here,  $\varphi$  is the optical phase which is measured by an interferometer as for example the ones shown in Figure 1.5. The interferometric phase can be converted directly into the length measurement by using the above relation. Another advantage of laser interferometry is the high frequency stability of the laser sources in comparison to others. Typical laser stabilities, described by laser frequency noise (LFN), used for LISA interferometry are on the order  $100 \text{ kHz}/\sqrt{\text{Hz}}$  at  $1 \text{ mHz}$  for free-running lasers. Stabilized lasers show a remaining LFN of about  $30 \text{ Hz}/\sqrt{\text{Hz}}$ . Since the laser's frequency,  $f$ , and its phase are both related to each other any frequency deviations also couple into the phase of a single beam via

$$\varphi(t) = 2\pi \int_0^t f(t - \tau) dt, \quad (1.2)$$

makes the frequency stability of laser sources to a demanding issue. Here,  $\tau$  is the time interval according to the propagated pathlength,  $l = c_0 \cdot \tau$ , with the speed of light in vacuum  $c_0$ . While LFN cancels out for two interfering beams propagating through two equal arms, an enhanced phase noise is measured in unequal arm length interferometers. The amount of LFN coupling depends, in first order, linearly on the travel time difference,  $\Delta\tau$ , and is described in the following by the approximation for low frequencies,

$$\tilde{\nu}(\Delta\tau) = 2\pi \tilde{f} \Delta\tau = \frac{2\pi \tilde{f} \Delta l}{c_0}, \quad (1.3)$$

$$[\tilde{\nu}] = \text{rad}/\sqrt{\text{Hz}}.$$

In ground-based gravitational wave observatories one uses massive end mirrors that are suspended sophisticatedly to reduce the impact of external forces. The displacement of the mirrors is read out optically with homodyne interferometry as depicted in Figure 1.5. A single laser beam is split on a beam splitter, travels

along two arms to two end mirrors where it is reflected. Both beams travel back to the beam splitter that guides them to a detector on which both beams overlap and interfere with each other. The laser frequency is the same for both beams, this is why the interferometer is called homodyne. Only the phases, accumulated in both arms, differs for the beams. The laser power on the two beam splitter output ports will fluctuate depending on the differential phase. With modified homodyne interferometry, very low detection noise levels can be achieved when powerful laser beams and massive, suspended mirrors are used, like it is done in LIGO or Virgo. This technique however is not able to operate over multiple fringes where phase signals, that are larger than  $2\pi$  rad, can be tracked. While in LIGO and Virgo the test mass mirror positions are being kept very stable, space missions have free-floating test masses within a satellite whose positions are driven by residual forces, like gravity fluctuations, and celestial dynamics causing Doppler shifts in the order of 1 to 10 MHz. They require therefore a certain dynamic range for the interferometric phase measurement that exceeds the capabilities of homodyne detection. Observatories in space use therefore heterodyne interferometers to measure the distance between free-floating test masses over a long baseline.

### 1.3.1 Heterodyne phase readout

Figure 1.6 shows a typical optical set-up of a heterodyne interferometer. The interference of two beams can be described by the superposition of two electromagnetic waves whose propagation can be described by

$$\vec{E}_i(x, y, z, t) = \vec{g}_i(x, y, z)E_i \sin[\omega_i t + \varphi_i]. \quad (1.4)$$

It contains an electric field amplitude,  $E_i$ , an oscillating term including the laser frequency,  $\omega_i = 2\pi f_i$ , and phase,  $\varphi_i$ , and a geometrical term  $\vec{g}_i$  that depends on the optical properties of the beam, like the polarization and mode. The polarization describes the direction of the oscillation of the electric field and is always perpendicular to the propagation direction. At a recombination beam splitter two electromagnetic waves, here referred as measurement,  $\vec{E}_m$ , and reference beam,  $\vec{E}_r$ , can be superimposed by vector addition, resulting in the following field intensity on a photodiode (PD),

$$I_{\text{tot}}(x, y, z, t) = \frac{c_0 \varepsilon_0 n}{2} \left| \sqrt{\frac{1}{2}} \vec{E}_m(x, y, z, t) + \sqrt{\frac{1}{2}} \vec{E}_r(x, y, z, t) \right|^2. \quad (1.5)$$

Here, the intensity is given for a square-law detector for a power reflectivity of  $r = 0.5$  for the recombining beam splitter. The speed of light is given by  $c_0 = 299\,792\,458$  m/s, the vacuum permittivity is  $\varepsilon_0 = 8.85 \cdot 10^{-12}$  F/m and the

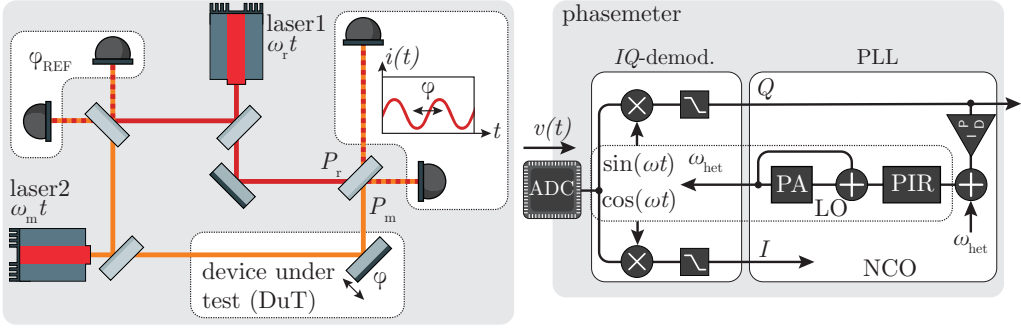


**Fig. 1.6.:** In a heterodyne interferometer two laser beams with different frequencies are recombined which results in an AC signal on the detector. A demodulation scheme is required to extract the desired phase information of the sinusoidal signal. Here shown is a typical  $IQ$ -demodulation principle with an extension of a phase-locked loop (PLL). The PLL consists of a proportional integral derivative (PID)-controller that amplifies the quadrature signal. The actuator signal is used to numerically control the local oscillator. For this purpose a phase incremental register (PIR) is used for the storage of the current frequency and the phase accumulator (PA) for the actual phase.

refractive index  $n$  from the medium. The integration over the active area from the photodiode leads to the following received optical power,

$$P_{\text{tot}}(t) = \frac{c_0 \varepsilon_0 n}{2} [P_m + P_r + 2|\langle E_m, E_r \rangle| \cos(\omega_{\text{het}} t + \varphi(t))] = \frac{i_{\text{PD}}(t)}{R_{\text{PD}}}, \quad (1.6)$$

which depends on the fields of measurement and reference beam,  $|\langle E_m, E_r \rangle| = \sqrt{P_m P_r} \eta$ , with the laser powers,  $P_m$  and  $P_r$ , of measurement and reference beam and the heterodyne efficiency  $\eta$ . The heterodyne frequency, or beat note, is  $\omega_{\text{het}} = \omega_m - \omega_r$  and the interferometric phase is given by  $\varphi = \varphi_m - \varphi_r$ . With this, the detector output changes from a pure balanced DC readout to a signal with an AC part that oscillates with a frequency. This beat note corresponds to the frequency difference of measurement and reference beam by neglecting all frequency terms of higher order. The generated photocurrent,  $i_{\text{PD}}$ , is then given by the multiplication of the total power with the photodiode responsivity  $R_{\text{PD}}$ , typically on the order of 0.7 A/W. Equation (1.6) is further simplified by separating the individual parts into DC and AC [Ger14]. The resulting photocurrent can therefore be expressed by

$$i_{\text{PD}}(t) = i^{\text{DC}} [1 + \kappa \cos(\omega_{\text{het}} t + \varphi(t))] = i^{\text{DC}} + i^{\text{AC}}(t), \quad (1.7)$$

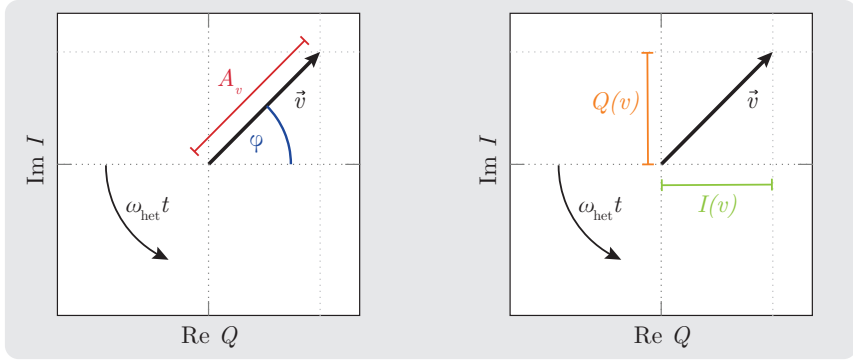


Fig. 1.7.: Phasor diagram in the frame rotating with the angular frequency  $\omega_{\text{het}}$ . Shown is the  $IQ$ -demodulation scheme based on a signal given in Equation (1.9). The projection into complex amplitudes can be used to extract phase and amplitude.

with the contrast  $\kappa$ . In the following we will define the amplitude,  $A$ , of an interference signal as

$$A = \frac{2|\langle E_m, E_r \rangle|}{P_m + P_r} = \kappa \cdot i^{\text{DC}}. \quad (1.8)$$

For ground-based observatories, one uses homodyne interferometry and, thus, with  $\omega_{\text{het}} = 0$ , the photodiode DC output directly depends on the desired phase information. LISA will be operated using a heterodyne interferometer scheme with beat notes in the MHz frequency range. The reason for this are the arm length fluctuations in the interferometer constellation which produce a Doppler shift of the laser frequency. A dedicated frequency plan is used to ensure that the heterodyne beat note is always in the detection bandwidth between 5 MHz and 25 MHz. According to Equation (1.6), the photodiode output power contains the phase information, but also the heterodyne frequency  $\omega_{\text{het}}$ . An  $IQ$ -demodulation, as illustrated in Figure 1.7, is used to extract the phase of the beat note. A transimpedance amplifier (TIA) converts the photocurrent into a voltage as

$$v(t) = A_v [\cos(\omega_{\text{het}}t + \varphi(t))], \quad (1.9)$$

with the amplitude  $A_v$ . Only the AC signal is considered for simplification since the DC part does not contain any phase information. The quadratures for the in-phase component and complex amplitude component can be determined by

multiplying the signal with cosine and sine at the desired frequency  $\omega$ , usually  $\omega_{\text{het}}$ , from which the phase needs to be extracted,

$$I = v(t) \cdot \cos(\omega t) \approx \frac{1}{2} A_v \cos(\varphi(t)), \quad (1.10)$$

$$Q = v(t) \cdot \sin(\omega t) \approx \frac{1}{2} A_v \sin(\varphi(t)). \quad (1.11)$$

In the last step a demodulation frequency of  $\omega = \omega_{\text{het}}$  and a low-pass filter for frequencies above  $2\omega_{\text{het}}$  are assumed. The interference signal amplitude and phase are then recovered by

$$A_v = 2\sqrt{I^2 + Q^2}, \quad (1.12)$$

$$\varphi(t) = \arctan\left(\frac{Q}{I}\right). \quad (1.13)$$

These steps are integrated into an electronic readout system, the phasemeter, which is a Field-programmable gate array (FPGA)-based device with integrated analog-to-digital converters (ADCs) [Ger14]. This principle is applied to all interferometric measurements in LISA, and has been used for LISA Pathfinder and on ground-based experiments for technology development. To achieve a large dynamic phase range, as required for space interferometry, the  $IQ$ -demodulation is extended by a phase-locked loop (PLL) that controls the demodulation frequency,  $\omega_{\text{het}}$ , and its phase to track the optical signal. This scheme is illustrated in Figure 1.6 on the right. The frequency of a local oscillator (LO) is actuated on by the feedback control system to keep the complex quadrature small. The phase difference between incoming signal and LO is minimized. The LO is therefore also called numerically controlled oscillator (NCO). The information about the optical phase is transferred from  $Q$  into the actuation signal, controlling the LO phase, which can be read out digitally. The  $I$  quadrature provides a value that is proportional to the optical amplitude, if the control loop is locked (see Equation (1.12)).

### 1.3.2 Contrast and heterodyne efficiency

A comfortable tool to measure the quality of an optical signal in heterodyne detection is the contrast,  $\kappa$ , which is in general determined by the ratio of measured photocurrent,  $i$ ,

$$\kappa = \frac{i_{\text{max}} - i_{\text{min}}}{i_{\text{max}} + i_{\text{min}}} = \frac{P_{\text{max}} - P_{\text{min}}}{P_{\text{max}} + P_{\text{min}}} \quad (1.14)$$

with the peak values,  $i_{\text{max}}$  and  $P_{\text{max}}$ , and the minimum values  $i_{\text{min}}$  and  $P_{\text{min}}$  of current or optical power. The contrast can also be defined as the amplitude of the

optical signal divided by the mean power,  $\bar{P} = P_m + P_r$ . Equation (1.6) can now be reformed and the expression becomes

$$P_{\text{tot}}(t) = \frac{c_0 \varepsilon_0 n}{2} (P_m + P_r) \left( 1 + \frac{2|\langle E_m, E_r \rangle|}{P_m + P_r} \cos(\omega_{\text{het}} t + \varphi(t)) \right) \quad (1.15)$$

$$\propto \bar{P} (1 + \kappa \cos(\omega_{\text{het}} t + \varphi(t))) \quad (1.16)$$

with the contrast,

$$\kappa = \frac{2|\langle E_m, E_r \rangle|}{P_m + P_r}, \quad (1.17)$$

which is now given by an expression that depends on the properties of the optical fields of measurement and reference beam [Sch17]. The electrical fields can be rewritten by the optical powers and the overlap of the phase-fronts and polarization. This is called heterodyne efficiency,  $\eta$ , and given by

$$|\langle E_m, E_r \rangle| = \sqrt{\eta P_m P_r}. \quad (1.18)$$

The relation between contrast and heterodyne efficiency can therefore be derived from Equations (1.17) and (1.18) and shows that these two quantities differ only by a scaling factor that depends on the powers of the two laser beams entering the detector,

$$\kappa = 2 \frac{\sqrt{P_m P_r}}{P_m + P_r} \sqrt{\eta}. \quad (1.19)$$

### 1.3.3 Longitudinal pathlength signal

As mentioned earlier in this chapter, length changes can be measured with high accuracy by heterodyne phase readout. According to Equation (1.1) we can define a longitudinal pathlength signal,  $l$ , as

$$l = \frac{\lambda}{2\pi} \varphi = \frac{1}{k} \varphi \quad (1.20)$$

with the wavenumber  $k = 2\pi/\lambda$ . This relation is simply applicable for single element photodiodes (SEDs), where the phase information is extracted from the argument of the complex amplitude as shown in Equation (1.13). Many experiments use quadrant photodetectors (QPDs) that consist of four active segments which are spatially separated from each other by a  $\mu\text{m}$ -slit. An illustration of such a QPD sensor is shown in Figure 1.8. Each segment, labelled A, B, C and D, senses different AC and DC currents. The phases and amplitudes measured by each one depends on the optical laser power, the beam position and angle, and the overlap between the two impinging beams. For each of these segments the phase and

amplitude of the individual photocurrents must be extracted. According to the heterodyne phase readout, the  $IQ$ -demodulation scheme is applied to each segment and the complex amplitudes are computed for each one individually. To get the overall phase signal of a QPD, the complex amplitudes are combined which can be done in different ways [Wan+12b].

The so-called *LISA Pathfinder longitudinal signal* has been used in this thesis for the analysis of the optical simulations. This calculation provides a longitudinal pathlength (PL) signal which is very close to the one calculated on a SED. This scheme is also used in the LPF phasemeter. The complex amplitudes of the different segments are summed up and the calculation of the argument of this complex number provides the phase. The longitudinal pathlength can then be determined via

$$l = \frac{1}{k} \operatorname{atan2} \left( \frac{Q_A}{I_A} + \frac{Q_B}{I_B} + \frac{Q_C}{I_C} + \frac{Q_D}{I_D} \right). \quad (1.21)$$

In the data analysis of optical experiments we use typically the so-called *averaged phase longitudinal signal*, where the argument of each segment is calculated first and then summed up and divided by the number of channels,

$$\begin{aligned} l &= \frac{1}{4k} \left[ \operatorname{atan2} \left( \frac{Q_A}{I_A} \right) + \operatorname{atan2} \left( \frac{Q_B}{I_B} \right) + \operatorname{atan2} \left( \frac{Q_C}{I_C} \right) + \operatorname{atan2} \left( \frac{Q_D}{I_D} \right) \right] \\ &= \frac{\varphi_A + \varphi_B + \varphi_C + \varphi_D}{4k} = \frac{\varphi_{\text{QPD}}}{k}. \end{aligned} \quad (1.22)$$

This approach is easily implementable in experimental set-ups in which the phase information is directly available. In case that the beams are not centered on the QPD and do not hit one of the segments, the phase of this segment would still contribute to the optical pathlength signal which is why this definition may cause some unexpected results [Sch17].

### 1.3.4 Differential wavefront sensing

In addition to the measurement of relative distance changes, an interferometer can also be used to measure beam pointing variations. The technique to do so is called differential wavefront sensing (DWS) and is applied in many interferometers in LISA. It is a very useful tool for the readout of test mass tilt since it provides very sensitive angle measurements that can achieve 1 nrad-precision in the tilt sensing. The reason for this high accuracy is that the actual wavefront tilt between two beams is measured by using QPDs. Each segment monitors a different phase according to the wavefront difference. The predicted DWS signal depends on various parameters, like the profile of the beams, the waist position or other beam parameters, and the detector geometry. Using a QPD with the segments A, B, C



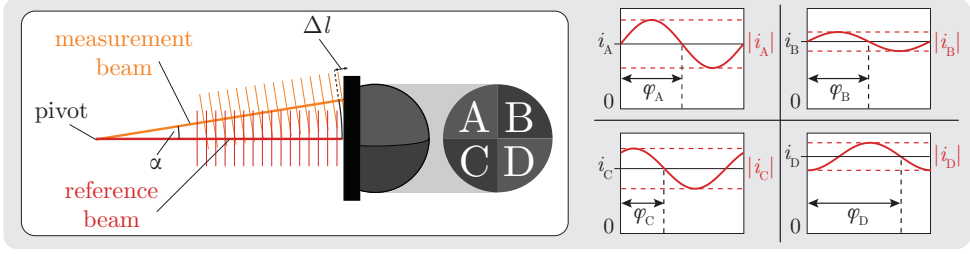


Fig. 1.8.: Differential wavefront sensing on a quadrant photodetector (QPD). Each segment, A, B, C, D, shows a different photocurrent, depending on the impinging beam powers, overlap and position. The measurement beam is tilted around a pivot point by an angle  $\alpha$ ,  $\Delta l$  is the resulting additional distance travelled by the measurement beam. This is also referred to as geometrical tilt-to-length (TTL) coupling. Picture based on [Ger14].

and D, as illustrated in Figure 1.8, the actual optical tilt in horizontal and vertical direction can be determined by the combination of the individual phase signals,

$$\Psi_{\text{DWS}} = \frac{1}{2}(\varphi_A + \varphi_C) - \frac{1}{2}(\varphi_B + \varphi_D) \quad (1.23)$$

$$\Theta_{\text{DWS}} = \frac{1}{2}(\varphi_A + \varphi_B) - \frac{1}{2}(\varphi_C + \varphi_D). \quad (1.24)$$

Here,  $\Psi_{\text{DWS}}$  measures the yaw angle, and therefore the horizontal tilt, and  $\Theta_{\text{DWS}}$  senses angle fluctuations along the pitch angle, thus vertical tilts [Wan+12b]. The optical simulation tool IfoCAD weights the phase information of each segment with the amplitude of the heterodyne signal. This makes the evaluation more robust for phase jumps.

### 1.3.5 Differential power sensing

In order to detect differential power fluctuations the averaged optical power,  $\bar{P}$ , of different QPD segments are compared with each other. For a beam that is not centered on the QPD, each segment measures a different amount of power. It is therefore possible to determine the position of the beam centroid and potential beam walk on the detector by so-called differential power sensing (DPS). The normalized QPD signal is determined by the following expressions

$$\Psi_{\text{DPS}} = \frac{\bar{P}_B + \bar{P}_D - \bar{P}_A - \bar{P}_C}{\bar{P}_A + \bar{P}_B + \bar{P}_C + \bar{P}_D}, \quad (1.25)$$

$$\Theta_{\text{DPS}} = \frac{\bar{P}_A + \bar{P}_B - \bar{P}_C - \bar{P}_D}{\bar{P}_A + \bar{P}_B + \bar{P}_C + \bar{P}_D}, \quad (1.26)$$

for measuring beam walks in horizontal,  $\Psi_{\text{DPS}}$ , and vertical,  $\Theta_{\text{DPS}}$ , directions [Wan+12b].

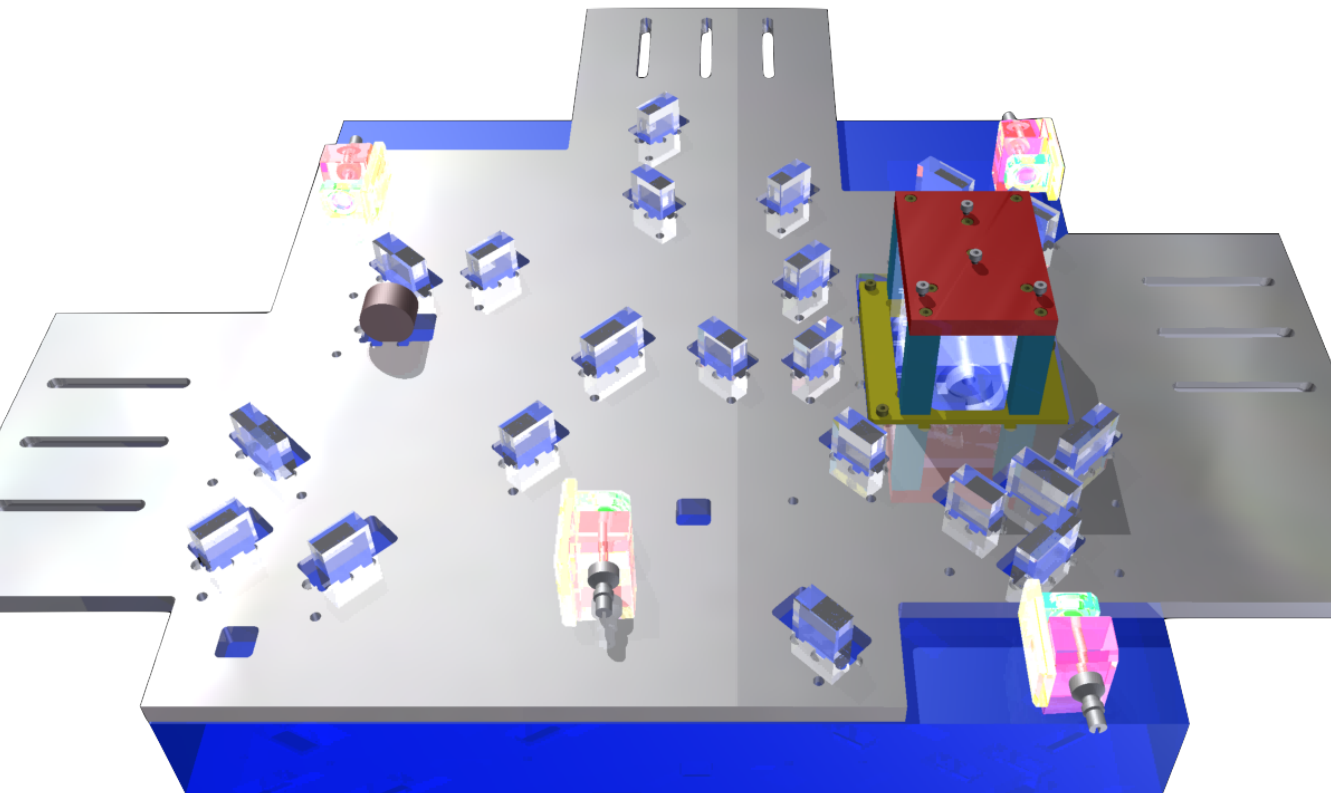
### 1.3.6 Tilt-to-length coupling

Interferometers are often limited in their displacement performance by tilt-to-length (TTL) coupling, an effect that occurs when an optical component is tilted and produces a longitudinal pathlength change on the detector as shown in Figure 1.8. The underlying mechanisms are not only geometrical in nature, where a tilted beam propagates a longer distance to the test mass due to the enhanced lever arm. Other mechanisms can also increase the TTL coupling. A list of the same can be found in [Sch17] and [Chw+16]. Beam parameters, like different wavefront curvatures between the two detected beams, wavefront errors or beam offsets, as well as the detector geometry, can cause non-geometrical TTL coupling [Sch17; Wan+12b]. These effects must also be considered in interferometers and will be measured by monitoring the longitudinal pathlength changes in dependency on beam tilts. A typical mitigation strategy for unwanted TTL coupling in experimental set-ups is the usage of imaging systems. Those can be used to suppress geometrical TTL coupling and beam walk on the detector. Prior optical simulations and proof-of-principle experiments have shown that the coupling can be reduced sufficiently in LISA interferometry with dedicated imaging systems [Sch17; Chw+16]. In both parts of this thesis, the TTL coupling is estimated by optical simulations performed with the C++ library IfoCAD. The influence of lenses, integrated in the interferometers, is investigated to estimate the amount of TTL coupling in any interferometer design.

# Part I

---

Towards the LISA backlink:  
The Three-Backlink interferometer





# PHASE REFERENCE DISTRIBUTION SYSTEMS

” *An introduction to LISA, a catalogue of backlink schemes and the current understanding of ghost beams.*

The current baseline for LISA is to use *Telescope Pointing* for compensating angular fluctuations in the satellite constellation. This mechanism implies the usage of two movable optical benches within one satellite and, thus, a flexible optical connection between those. A backlink connection, or also known as phase reference distribution system (PRDS), is used for this purpose. It exchanges light bi-directionally between two, spatially separated, optical set-ups. Such an optical connection has a certain property, called non-reciprocity, which is the pathlength difference between two counter-propagating beams along this backlink. If a light beam sees in both propagation directions the exact same pathlength, or pathlength changes, the backlink is called reciprocal. The absolute pathlength is not crucial, it is common mode for both directions, but the differential phase noise must reach the LISA requirement of  $1 \text{ pm}/\sqrt{\text{Hz}}$  [aC13].

In this chapter, the current baseline architecture of the LISA optical bench is introduced and the mechanisms of *In-Field Pointing* and *Telescope Pointing* are compared with each other. Based on the results of the prior fiber backlink experiment [Fle+17], that are shortly summarized in the subsequent section, a catalogue of spurious beams is developed. Various sources for each class of spurious beams have been studied and their influence on the phase measurement is estimated by using a simplified model for the underlying coupling mechanism. The strategies to mitigate, or to prevent, phase errors caused by spurious beams are presented and their applicability on the LISA optical bench is discussed. In the last section of this chapter alternative backlink candidates are envisaged. Both, fiber-based as well as free-beam variants are discussed and their potential limitations are studied. Three of them are chosen to be experimentally compared to each other in the so-called Three-Backlink interferometer (TBI). These three candidates show the highest potential to be implementable in LISA.

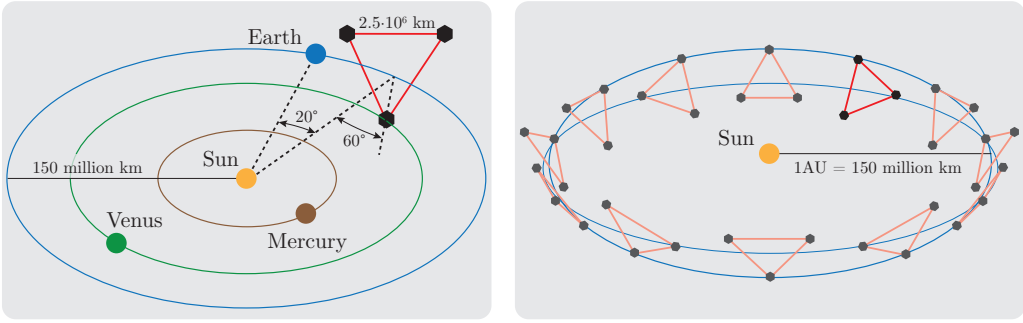


Fig. 2.1.: Illustration of the LISA orbits. The three-satellite constellation follows the Earth around the sun by about  $20^\circ$ , the angle measured to the ecliptic is  $60^\circ$ . Due to external forces from astronomical objects, the triangle legs and angles vary periodically over one year [aC13].

## 2.1 Laser Interferometer Space Antenna

LISA consists of three spacecraft (S/C) in an equilateral triangular formation which are optically connected with each other by laser links over a distance of  $2.5 \cdot 10^6$  km. LISA will follow the Earth around the sun with a distance of about  $50 \cdot 10^6$  to  $65 \cdot 10^6$  km. An illustration of the LISA orbit is depicted in Figure 2.1. The Earth-trailing heliocentric orbit is a tradeoff between keeping the breathing angles and the range rate between the S/C minimal, while it must be ensured that the constellation is close enough to Earth to keep the communication running. The depicted orbit will lead to vertex angle fluctuations in the LISA-triangle on the order of  $\pm 1.5^\circ$  and to arm length changes of 1%, generating Doppler shifts between the S/C of about  $\pm 5$  MHz [aC13; Xia+10].

Along the three sides of the satellite constellation differential optical pathlength changes between free-falling test masses are measured with heterodyne interferometry. The long travel time of 8.3s and the divergence of the laser beam enlarges the spot size and limits the received laser power. Instead of conventional passive reflections by means of interferometer end mirrors, each S/C transmits a reprocessed high power laser beam which is offset phase-locked to the received weak beam. Telescopes are used in each arm for further improving the laser power levels of the received and transmitted beams at each S/C. The relative displacement measurement between two test masses is divided into three parts: The displacement measurements between test mass and optical bench at both ends of a LISA arm and then the distance measurement between the satellites. The optical bench connects all three interferometers with each other as shown in Figure 2.2a. The science interferometer measures the beat note between one of the local lasers, the transmitted (TX) beam, and the received (RX) laser from the distant S/C. It

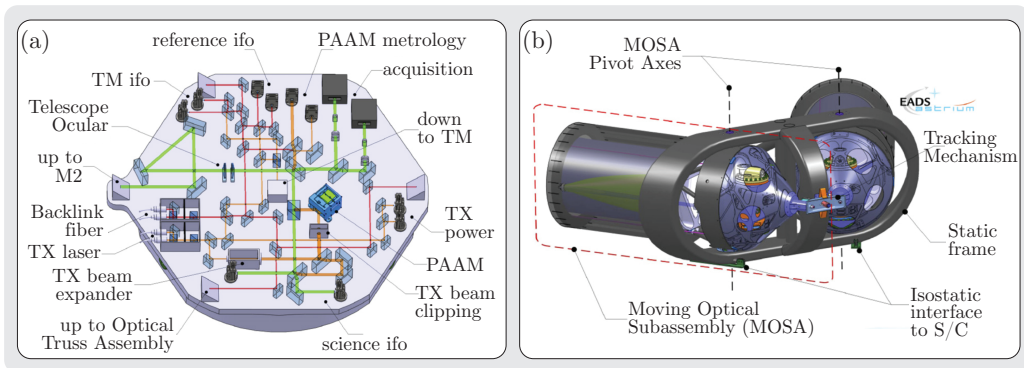


Fig. 2.2.: Sketch of the LISA optical bench, shown in (a), and its actuation device, the moving optical sub-assembly (MOSA), shown in (b). To overcome the breathing angle of  $\pm 1.5^\circ$  per year the MOSA will actuate on the full optical payload. Image credit: [Sal+09].

measures distance changes and pointing to the other satellite and contains the gravitational wave signal. It is the most difficult interferometer in LISA because it must operate with very low optical power, variable beam pointing and laser frequency noise (LFN) accumulated over  $2.5 \cdot 10^6$  km long arms. The test mass interferometer measures the heterodyne beat note between TX laser and a reference beam, a local oscillator (LO), that is provided locally by a second laser source. Since LISA requires heterodyne frequencies in the MHz band to track the phases over multiple fringes, these two lasers are offset phase-locked to each other, an adequate stabilization also reduces the LFN of one master laser in the constellation. The test mass interferometer measures the displacement and tilt of the test mass relative to the optical bench. The reference interferometer, or PRDS, measures the beat note between the TX and the LO beams directly without test mass motion. For the case of *Telescope Pointing*, and thus two optical benches that are rotating against each other, the LO for the reference interferometer is provided by the backlink connection. Also proposed for some LISA designs are further auxiliary interferometers for measuring the point ahead angle mechanism (PAAM) and the stability of the telescope (optical truss) [Sal+09; aC13].

The calculation of the overall performance requirement for LISA depends on various noise contributions. Optical noise, readout noise, digitization noise or post-processing noise are only a few of them. Furthermore, the influence of a gravitational wave on the measurement of differential test mass motions is very tiny. For detecting gravitational waves with strengths on the order of  $h(t) \approx 10^{-22}$

relative displacement changes of  $\Delta L = 1.25 \text{ pm}/\sqrt{\text{Hz}}$  must be measured at mHz frequencies over the distance of  $L = 2.5 \cdot 10^6 \text{ km}$  according to

$$\frac{\Delta L}{L} = \frac{h(t)}{2}. \quad (2.1)$$

One assumes that each part of the overall metrology system contributes less than  $1 \text{ pm}/\sqrt{\text{Hz}}$  in the LISA measurement band from  $f = 0.1 \text{ mHz}$  to  $1 \text{ Hz}$ , multiplied by a noise shape function (NSF) defined as

$$\text{REQ}(f) = 1 \text{ pm}/\sqrt{\text{Hz}} \cdot \text{NSF}(f) = 1 \text{ pm}/\sqrt{\text{Hz}} \sqrt{1 + \left(\frac{2.8 \text{ mHz}}{f}\right)^4}. \quad (2.2)$$

This means all parts of the metrology system must show a displacement level that is below  $1 \text{ pm}/\sqrt{\text{Hz}} \cdot \text{NSF}(f)$ . This guarantees an overall single arm sensitivity of about  $10 \text{ pm}/\sqrt{\text{Hz}}$  in the LISA science measurement, dominated by about 6 to  $8 \text{ pm}/\sqrt{\text{Hz}}$  of shot noise. The  $1 \text{ pm}/\sqrt{\text{Hz}}$  noise is equivalent to an optical phase noise of about  $6 \text{ } \mu\text{rad}/\sqrt{\text{Hz}} \cdot \text{NSF}(f)$  for an assumed wavelength of  $1064 \text{ nm}$  [aC13; Dan+17].

LFN limits the readout of the S/C separations in LISA's science interferometer because it enters the phase measurement due to the large arm length mismatches. This effect is suppressed in data post-processing by time delay interferometry (TDI) [TD05; Ott+12], which forms linear combinations of the local and the inter-S/C phase measurements from different arms with time-delayed versions of themselves. For this purpose a precise phase comparison between the two local lasers, TX and LO, is required. Depending on the mission design of either using *In-Field* or *Telescope Pointing*, the performance of this PRDS, or backlink, is critical.

### 2.1.1 In-Field Pointing

So-called *In-Field Pointing* is one of two possibilities to compensate the breathing angle in LISA. This is a mechanism that uses an actuator in the telescope design for steering one of the telescope mirrors, as schematically shown on the right in Figure 2.3. This scheme keeps the laser beam collinear to the LISA arms. With this architecture only one optical bench and test mass per satellite is required and the optical reference measurement between TX laser and LO can be performed directly on a single optical bench. The second test mass is used for redundancy if an optical readout is done for both test mass axis, or it also allows single test mass architectures. This method requires however an actuation mirror that can be tilted over a large angle of about  $30^\circ$ , depending on the required magnification of the LISA telescope. Since the actuation mirror is placed in LISA's sensitive path,



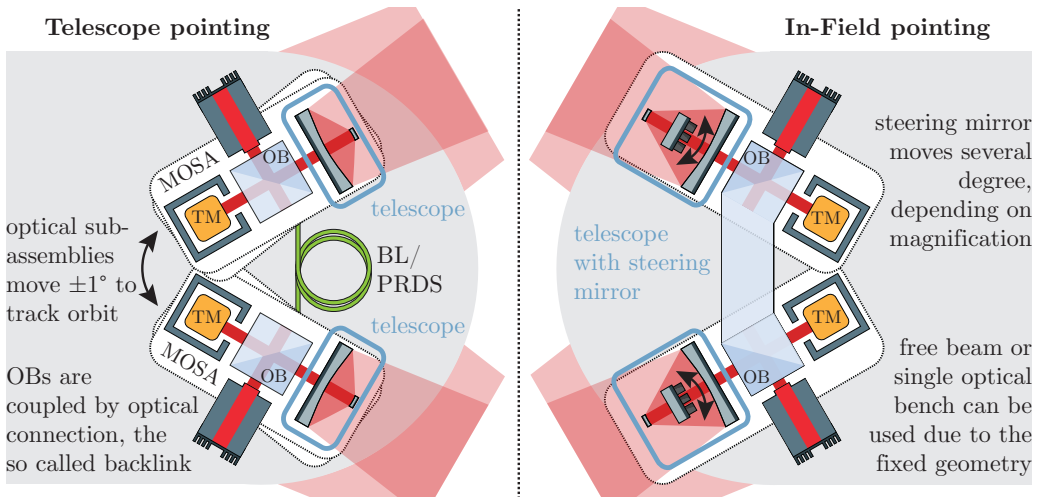


**Fig. 2.3.:** Telescope vs. In-Field Pointing. Telescope pointing is foreseen as baseline for LISA to compensate the breathing angle fluctuations. The In-Field pointing mechanism is considered as alternative. Picture is based on [Liv+17].

containing the gravitational wave signal, it must show a pathlength stability of  $1 \text{ pm} / \sqrt{\text{Hz}}$  for the full angle range. Optical simulations investigated at NASA's Goddard Space Flight Center in Maryland, US, have shown that the optical design of the LISA telescope has a high stray light contribution. With an actuation mirror inserted into the telescope optics, the stray light beams undergo high dynamics, which directly couple into the phase measurement [Liv+13]. Colleagues at Airbus are investigating the In-Field Pointing method in an experiment as an alternative to *Telescope Pointing* for LISA [Liv+17; Bru+17].

### 2.1.2 Telescope Pointing

The second scheme for compensating the breathing angle uses the so-called *Telescope Pointing* mechanism. This scheme is currently proposed as baseline concept for LISA. Each satellite contains two optical benches, mounted to the back of a telescope along with a gravitational reference sensor (GRS). The optical benches (OBs) are equipped with a local TX laser beam, such that the full optical payload, including telescope and GRS, can independently follow the RX beam for each arm and can point to the distant S/C. This technique ensures the preservation of full contrast within the inter-S/C interferometry by actuating each OB via a moving optical sub-assembly (MOSA), as depicted in Figure 2.2b. A sketch of the Telescope Pointing mechanism is shown in Figure 2.3. As consequence of implementing both, Telescope Pointing and TDI in LISA, some challenges appear. The exchange of the TX beams is required to perform a phase reference

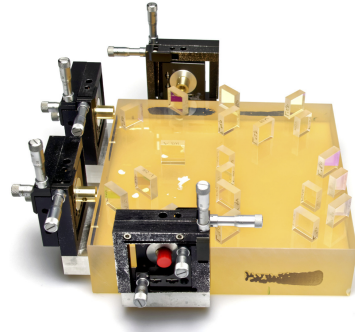
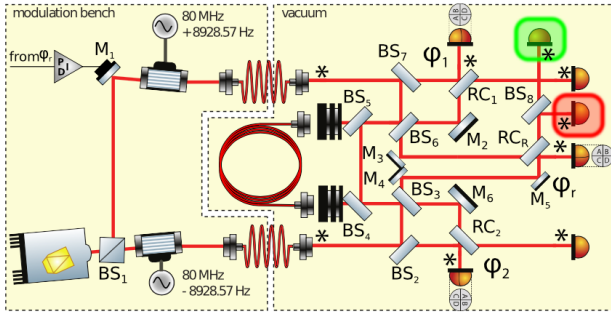


Fig. 2.4.: The optical set-up of the prior fiber backlink experiment at the AEI, investigated by Roland Fleddermann et al. [Fle+17]. A sketch of the experimental set-up including laser modulation bench outside the vacuum chamber is depicted on the left. A photograph of the fiber backlink experiment’s optical bench is shown on the right. Image credit: [Fle+17].

measurement. This is the-so called backlink, or PRDS, which must show a non-reciprocal phase noise of  $1 \text{ pm}/\sqrt{\text{Hz}}$  [aC13]. Since an additional laser frequency is required on each of the two benches, which is used as LO for the local interferometry, the backlink laser beam is typically used for this purpose, providing a few mW of laser power and a frequency difference between 5 MHz and 25 MHz. Establishing such a bi-directional link between two actuated benches requires either a flexible optical connection via fiber or a type of steered free-beam set-up, compensating the motion of the MOSAs [Ste+09; Isl+17; Fle+17]. Another problem is the harness of more than 100 cables which must be continuously moved.

## 2.2 Prior fiber backlink experiment

The non-reciprocity of a straightforward, direct fiber backlink has been demonstrated in previous experiments. A fiber connection was compared to a stable reference path implemented on a single optical bench. A sketch of the optical set-up is shown in Figure 2.4. One laser beam is split and separated into two paths on a modulation bench where the beams are frequency shifted relative to each other by  $80 \text{ MHz} + 9 \text{ kHz}$  and  $80 \text{ MHz} - 9 \text{ kHz}$ . The laser light is sent via two fibers into a vacuum system where the quasi-monolithic set-up of the fiber backlink experiment was installed. Two adjustable fiber output couplers are used to inject the two TX beams onto the optical set-up. The lasers propagate through a backlink fiber in opposite directions, clockwise and counter-clockwise. They are interfered afterwards with the other TX beams. These two interferometers measure the phase behavior of the clockwise and counter-clockwise propagation

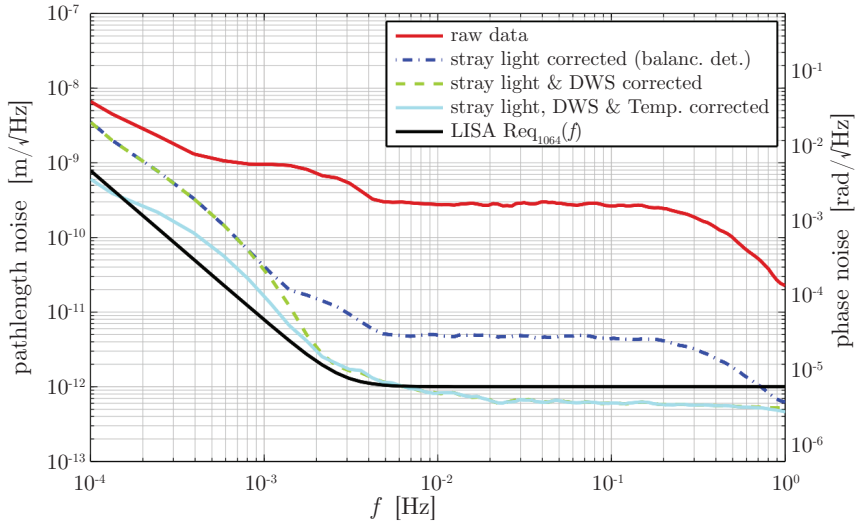


Fig. 2.5.: Pathlength performance of the fiber backlink’s non-reciprocity measured in the prior experiment [Fle+17].

direction of the backlink fiber. An additional interferometer is used as reference to eliminate the differential phase noise between the lasers, only the non-reciprocity of the backlink remains in the signal combination [Fle+17].

Figure 2.5 shows the final achieved non-reciprocity performance as phase spectral densities measured by the fiber backlink experiment. The results show that in addition to DWS post-corrections for beam pointing fluctuations and subtraction of some unexplained temperature coupling, the fiber backlink requires a balanced detection scheme (see Section 2.3.5) to reduce the phase noise caused by parasitic ghost beams. While an active length stabilization of the backlink fiber, or attenuation stages behind the injection fiber collimators, reduce the ghost beam coupling [Hen13], these measures are not sufficient to achieve the required non-reciprocity and must be improved by balanced detection. The reason for the high amount of ghost beam coupling is the direct optical connection between two fiber output couplers and the backlink fiber itself. Something like a low-finesse cavity is generated between the two fiber couplers. The so generated parasitic beat notes couple into all local interferometers. The usage of this backlink on the LISA optical bench would require balanced detection to be applied in each interferometer that uses the same TX or LO beam. In order to achieve the performance with this correction scheme, two orders of magnitude of phase noise must be suppressed by balanced detection in each one.

Within the work of the prior fiber backlink experiment the amount of backscatter from a fiber and its interface has also been measured. The main noise source of

ghost beams is assumed to be Rayleigh scattering inside the fiber itself, a scatter effect that is generated over the whole fiber length. While the backscatter from lens and fiber coupler was measured to be 0.1 ppm and about 1 ppm, the Rayleigh scattering showed backreflections on the order of 4 ppm per meter [Fle12]. This number is likely to increase in flight due to radiation damage in the fiber core to yet unknown values. It is unclear if the in-flight performance can achieve the redundancy implications and the noise characteristics in comparison to alternative schemes. The noise suppression level of balanced detection required in LISA depends directly on the ghost beam powers which are driven by the amount of fiber backscatter. Suppressing more than two orders of magnitude with balanced detection has not yet been demonstrated, and even the use of normalized balanced detection, as shown by Fleddermann et al. [Fle+17], might be limited by other sources of low-frequency amplitude drifts, leading to additional constraints on the stability, or readout, of the signal amplitudes. For this purpose phase references with less ghost beam coupling are intended to be studied for supporting the trade-off solutions for the LISA optical bench design. Furthermore, the behavior of the backlink connections under periodic disturbances, as it is expected for LISA due to the motion of the MOSAs, will be investigated by using two separate optical benches in future backlink experiments. As part of this thesis the TBI has been designed for the purpose to test backlink alternatives.

## 2.3 Spurious light beams and signals

In order to understand the current limitations of the prior backlink experiment and other optical set-ups, a study of spurious light beams and their influence on the phase measurement is given by this section. In the following we define spurious light beams (SLBs) as main category for stray light and ghost beams. Those travel in interferometers, but are not foreseen as nominal beams for the interference [Wu03]. The measurement and reference beams, as introduced in Section 1.3.1, are both referred to as nominal beams in this context. These are used to generate the desired interferometer signal. Spurious beams create often unwanted spurious light signals (SLSs) by interfering with one of the nominal beams, or among each other. Competitive interferometers are generated in both cases which disturbs the phase measurement when the SLS enters the photodetectors.

### 2.3.1 Categories

Based on the individual SLB properties and origins, we will distinguish between the three following categories: Ghost beams that are caused by secondary reflections, scattered light that is generated by surface contaminations and stray light that is

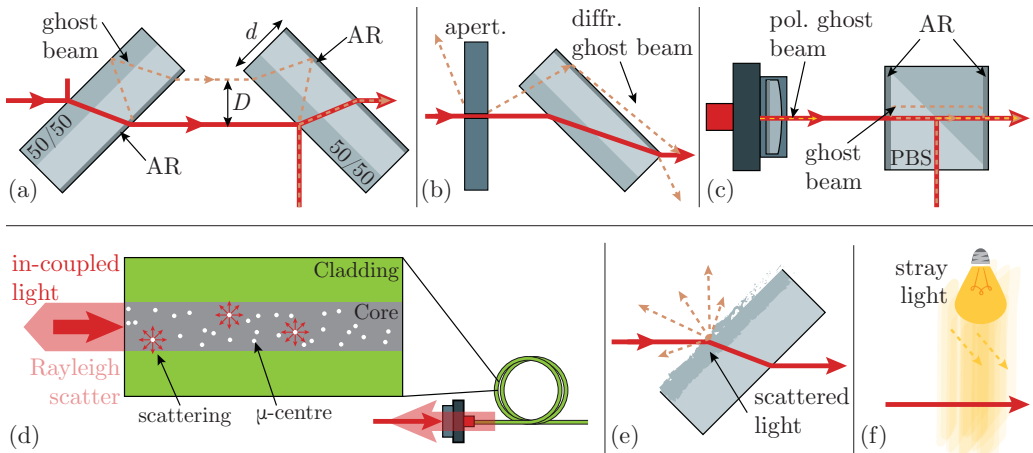


**Fig. 2.6.:** Ghost beams are caused by reflections at secondary surfaces, typically anti-reflecting (AR)-coated. A ghost beam reflected under an AOI of  $45^\circ$  is shown in (a) and under  $0^\circ$  in (c). Diffracted ghost beams are caused by clipping effects that are shown in (b). Ghost beams of spurious polarization are illustrated in (c). Fiber ghost beams are caused by Rayleigh scattering inside the fiber which is shown in (d). Scattered light and stray light is shown in (e) and (f), respectively.

induced by external light sources. An overview of this catalogue is illustrated in Figure 2.6 where a selection of possible sources and origins is shown.

*Ghost beams* travel collinear, or parallel, in the same interferometer axes, as shown in Figure 2.6a. They have often a mode that is similar to the one of the nominal beams, which makes them critical for the phase measurement. The ghost beam (highlighted light red in Figure 2.6a) can be projected by two subsequent components onto a propagation direction that is collinear to the direction of the nominal beam (red). This makes the two beams undistinguishable from each other and both couple into the phase performance. The low power reflectivity of about a thousandth of an AR coating (equivalent to  $1/30$  in amplitude) already contributes to the interferometric phase measurement if the ghost beam enters the detector.

*Diffracted ghost beams* are generated by clipping effects and can be avoided by the interferometer design. Diffraction can however also appear from spurious beams, like ghost beams, that were initially caused by any other effect. Those might be misaligned such that they do not hit the apertures and optical components accurately and therefore cause diffracted ghost beams. Examples for possible resulting beam propagations are shown in Figure 2.6b.

*Ghost beams of spurious polarization* can also disturb the interferometric phase measurement. Polarization components, as shown in Figure 2.6c, have typically an extinction ratio of only  $0.1\%$  when taking the finite polarization axis alignment in real interferometers into account. Thin-film polarizers provide higher extinction

ratios, but their usage leads to other challenges, like wavefront distortion and backreflections. Also other optical components can slightly change the polarization due to effects like reflections, refractions or diffractions. The resulting state contains a remaining part of 'wrong' polarization. A competitive interferometer is generated and influences the heterodyne readout.

*Fiber ghost beams* are caused by fiber backreflections or backscatter. Spurious beams that propagate back to a fiber interface are coupled into the fiber. A part of the light is directly reflected, while the coupled light generates Rayleigh scattering, as illustrated in Figure 2.6d. This is assumed to be the limiting noise source of the prior fiber backlink experiment. The so-generated fiber ghost beam is not spatially distinguishable from the nominal beam. Thermal fluctuations or density fluctuations change the refractive index inside the fiber and will additionally drive the dynamics of the ghost beam. For this reason fiber ghost beams often limit the phase measurements in a non-linear matter.

*Scattered light*, as it is expected being generated by the LISA telescope, is caused by contaminations, scratches, or dust on component surfaces and non-perfect coatings as illustrated in Figure 2.6e. Especially optical components that are used for actuation purposes, like beam-steering, generate scattered light with high dynamics. Due to the motion of the mirror, the reflected beam moves along the component surface. The scattered light differs in frequency for each reflection point on the mirror if the surface is not perfect. This produces a phase disturbance that is continuously changing.

*Stray light* denotes light coming from external sources like lamps or the sun. An illustration is shown in Figure 2.6f. The influence of stray light on the phase measurement is negligible compared to other spurious beams since the mode overlap and the light power are assumed to be low enough for the applications discussed here.

### 2.3.2 Coupling into the phase measurement

A representation of optical signals in the complex plane by using the decomposition in amplitude and phase, as illustrated in Figure 2.7, shows intuitively the coupling of the so-called small-vector-noise. This describes the influence of a spurious signal on a nominal, non-contaminated signal. The non-contaminated signal is the desired interferometer signal, generated by the recombination of the measurement and reference beam (see Section 1.3.1). The spurious light signal (SLS) is the recombination of a spurious light beam (SLB) and any other beam. The actually measured signal is described by the vector addition of these two. Both, amplitude and phase measurement, are disturbed in a certain way, depending on the small

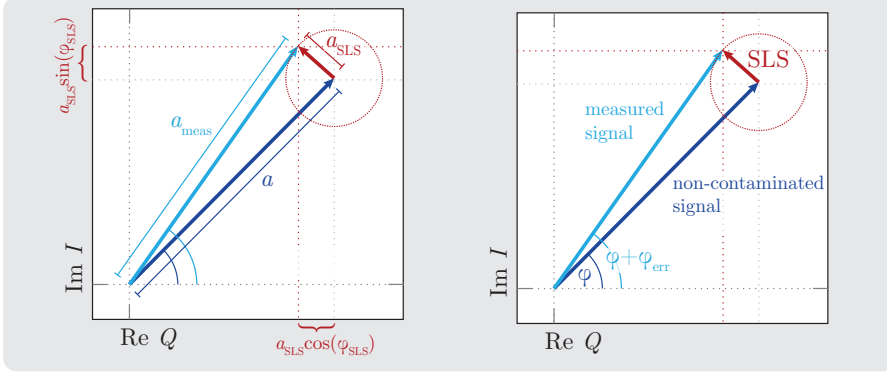


**Fig. 2.7.:** Vector representation of a spurious signal ( $a_{\text{SLS}}$ ) influencing the actual signal, ( $a$ , phase  $\varphi$ ). The sum of these two vectors provides the vector of the measured signal which has the phase  $\varphi + \varphi_{\text{err}}$ , while  $\varphi_{\text{err}}$  is the disturbance introduced by the spurious light signal (SLS).

vectors's phase and amplitude. By using trigonometric relations, the accumulated phase error,  $\varphi_{\text{err}}$ , can be calculated by

$$\tan(\varphi_{\text{err}}) = \frac{a_{\text{SLS}} \sin(\varphi_{\text{SLS}})}{a + a_{\text{SLS}} \cos \varphi_{\text{SLS}}}, \quad (2.3)$$

where  $a_{\text{SLS}}$  and  $\varphi_{\text{SLS}}$  are the amplitudes and phases of the spurious signal, and  $a$  and  $\varphi$  are the corresponding parameters for the nominal, non-contaminated, interference signal. Here,  $\varphi = 0$  is assumed for simplicity's sake. Under the assumption that the amplitude of the disturbance is small in comparison to the actual signal,  $a_{\text{SLS}} \ll a$ , the expression in Equation (2.3) can be further simplified,

$$\varphi_{\text{err}} = \frac{a_{\text{SLS}}}{a} \cdot \sin(\varphi_{\text{SLS}}) \approx \frac{a_{\text{SLS}}}{a} \cdot \varphi_{\text{SLS}} \leq \frac{a_{\text{SLS}}}{a}, \quad (2.4)$$

also taking into account that the phase error is small,  $\varphi_{\text{err}} \ll 1$ , as well as the phase difference, such that  $\sin x \approx x$ . The last step results from a spurious signal that is in-phase to the nominal signal, thus  $\varphi_{\text{SLS}} - \varphi = 0, \pi, 2\pi, \dots$ . This expression can be extended for any values for  $\varphi \neq 0$  with  $\varphi_{\text{SLS}} \mapsto \varphi_{\text{SLS}} - \varphi$ . By including multiple,  $n$ , spurious signals we can expand Equation (2.4) to

$$\varphi_{\text{err}} = \frac{1}{a} \sum_i^n a_{\text{SLS},i} \cdot \sin(\varphi_{\text{SLS},i} - \varphi) \approx \frac{1}{a} \sum_i^n a_{\text{SLS},i} \cdot (\varphi_{\text{SLS},i} - \varphi) \leq \frac{1}{a} \sum_i^n a_{\text{SLS},i}. \quad (2.5)$$

The phase error only depends on the amplitude ratios of the nominal interference signal,  $a = \sqrt{\eta P_{\text{meas}} P_{\text{ref}}}$  and the spurious interference,  $a_{\text{SLS},i} = \sqrt{\eta_i P_{\text{SLB},i} P_x}$ , with  $P_x = \{P_{\text{meas}}, P_{\text{ref}}, P_{\text{SLB},j}\}$ ,  $j \neq i$ . Here,  $P_{\text{meas}}$  and  $P_{\text{ref}}$  are the optical powers of



measurement and reference beam, and  $P_{\text{SLB}}$  the power of the spurious light beam. The according heterodyne efficiencies are given by  $\eta$ . A SLS can be compound by forming all possible combinations of beams entering the same detector. The beat note of some of these combinations might not contribute to the phase error because they differ from the nominal one and are therefore not being detected by the heterodyne readout. The largest contribution to the phase error is otherwise expected from SLBs interfering with one of the nominal beams. The resulting phase error is enlarged due to the strong laser power of the nominal beam. Only the interference with one nominal beam is critical, here we assume the interference with the measurement beam. The interference with the reference beam is shifted to DC. With this assumption Equation (2.4) can be rewritten in terms of power,

$$\varphi_{\text{err}} \approx \frac{\sqrt{\eta_{\text{SLS}} P_{\text{SLB}} \cdot P_{\text{meas}}}}{\sqrt{\eta P_{\text{meas}} \cdot P_{\text{ref}}}} \cdot \varphi_{\text{SLS}} = \sqrt{\frac{\eta_{\text{SLS}} P_{\text{SLB}}}{\eta P_{\text{ref}}}} \cdot \varphi_{\text{SLS}}, \quad (2.6)$$

$$\approx \frac{\sqrt{P_{\text{SLB}} \cdot P_{\text{meas}}}}{\sqrt{P_{\text{meas}} \cdot P_{\text{ref}}}} = \sqrt{\frac{P_{\text{SLB}}}{P_{\text{ref}}}}. \quad (2.7)$$

Interferences among spurious beams can also produce significant phase errors that are critical for high-precision interferometry. For example, if one detects  $P_{\text{meas}} = P_{\text{ref}} = 1 \text{ mW}$  optical laser powers for the measurement and reference beam, the spurious beams power must be below  $6 \cdot 10^{-9} \text{ W}$  to reach an interferometric readout sensitivity of  $1 \text{ pm}/\sqrt{\text{Hz}}$ . For a spurious beam interfering with one of the  $1 \text{ mW}$  nominal beams, its optical power must be even less than  $3.6 \cdot 10^{-14} \text{ W}$ .

By using optical simulation tools that offer ray tracing capabilities and integration methods for signal and mode overlap calculations, detailed estimations about the influence of multiple SLSs can be made. The dynamics of the small vector, that couple non-linearly and to effects like frequency up-conversion of out-of-band signals, are however not easily implementable in simulations, like IfoCAD, and could increase the phase error even beyond the upper limits given by Equation (2.7). The non-linear coupling prevents a spectral noise model, making time series simulations necessary for an exact prediction.

### 2.3.3 Occurrence and dynamics in optical set-ups

A summary of spurious beams, that are expected to occur eventually in optical set-ups, are listed in Table 2.1. This table has been developed in cooperation with Jeffrey Livas from the NASA's Goddard Space Flight Center in the US. It shows among others the individual source of origin for each category. For example, the TBI will consist of bonded components, like mirrors and beams splitters, metal mounted components that are partly adjustable, as used for lenses or photodiodes,



**Tab. 2.1.:** List of spurious beams, separated by their categories. For each component we assume an estimated dynamical behaviour in dependency on the mounting. In relation to this, a model is given with which the phase error can be determined for any spurious light beam (SLB). This model contains for each case individually either the estimation of optical power,  $P$ , ray tracing, beam overlap, phase dynamics or all of these must be considered together.

category	compon.	noise source origin	dynamic	model	phase error [rad]
ghost beams	bonded	2nd refl.	$\ll 1$ pm	$P$ , rays	$\sqrt{\frac{P_{\text{SLB}}}{P_{\text{ref}}}}$
	metal mounted	2nd refl.	$\ll 1$ nm	$P$ , rays, overlap, dynamics	$\sqrt{\frac{\eta_{\text{SLS}} P_{\text{SLB}}}{\eta P_{\text{ref}}}} \varphi_{\text{SLS}}$
	fibers	fiber scatter	thermal, angle jitter, stress		
		test mass	2nd refl.	1 nm	
diffracted	Isolator, aperture	diffraction, clipping	$\ll 1$ nm	$P$ , rays	$\sqrt{\frac{P_{\text{SLB}}}{P_{\text{ref}}}}$
p-pol.	fiber	fast axis coupling	thermal, acoustic, coupling pointing	no model used	unknown
	FIOS	FIOS misalignm., birefringent lens			
scattered light	bonded	dust, surface roughness, scratches, coating quality	$\ll 1$ pm	$P$ , rays	$\sqrt{\frac{P_{\text{SLB}}}{P_{\text{ref}}}}$
	metal mounted		$\ll 1$ nm	$P$ , rays, overlap, dynamics	$\sqrt{\frac{\eta_{\text{SLS}} P_{\text{SLB}}}{\eta P_{\text{ref}}}} \varphi_{\text{SLS}}$
	steering mirrors	thermal, steering			
		test mass		1 nm	
stray light	external	lamp			$\sqrt{\frac{P_{\text{SLB}}}{P_{\text{ref}}}} 10^{-6}$

and components that are actually moving, like steering mirrors. Optical fibers, for injecting the laser light to the vacuum chamber, are also used in combination with fiber injection optical subassemblies (FIOSs). All of them can generate spurious beams. Due to their individual stability, the influence on the phase error varies between them. It is assumed that bonded components have a high displacement stability on the order of  $1 \text{ pm}/\sqrt{\text{Hz}}$ , while the dynamics of other components, like metal mounted ones, steered ones and fiber-based ones, are much higher on the order of  $1 \text{ nm}/\sqrt{\text{Hz}}$  and, in some cases, thermally driven additionally.

We assume two simplified models by which the phase errors caused by ghost beams can be approximated at stable and less stable components, respectively. The first model uses only the results of ray tracing techniques that determine the number of spurious beams entering a detector and the amount of optical laser power of each of them, based on Equation (2.7). This model can be solved manually without optical simulation tools. It is therefore easily applicable without huge processing powers and delivers a worst case phase error estimation. For some cases this model delivers too pessimistic results which leads to over-complex, unrealistic interferometer designs and stability constraints. Therefore, a second model is used that includes also the mode overlap,  $\eta_{\text{SLS}}$ , and the dynamic behavior,  $\varphi_{\text{SLS}}$ , described by Equation (2.6). This model is only applied to selected spurious beams, whose power exceeds the tolerable upper limit. Since the calculation of the mode overlap is elaborate, it is not proposed to apply this model to each spurious beam. The optical simulation tool IfoCAD can be used for the signal computation. It numerically integrates over the detector surface and estimates the optical signal properties, like the heterodyne efficiency. In combination with an estimation of the expected dynamics,  $\varphi_{\text{SLS}}$ , this model provides more realistic results. Spurious beams, that were previously classified to be crucial for the overall interferometer performance, can eventually be excluded.

Two other categories of spurious beams, shown in Table 2.1, are not described by a model or an analytic solution. Since IfoCAD does not support polarization effects to the required degree, ghost beams of spurious polarization cannot be analyzed in this context. The influence of stray light on the phase error is assumed to be negligible. They have often very low optical powers and a vanishing mode overlap when they finally reach the detector, or are incoherent or have different frequencies. For this reason we relax the phase error for these categories by an arbitrary factor of six orders of magnitude.

#### 2.3.4 Influence of focusing lenses in front of photodiodes

In general, focusing lenses are used in front of the photodiodes to achieve an adequate beam diameter on the active area and for adjusting the beam in the

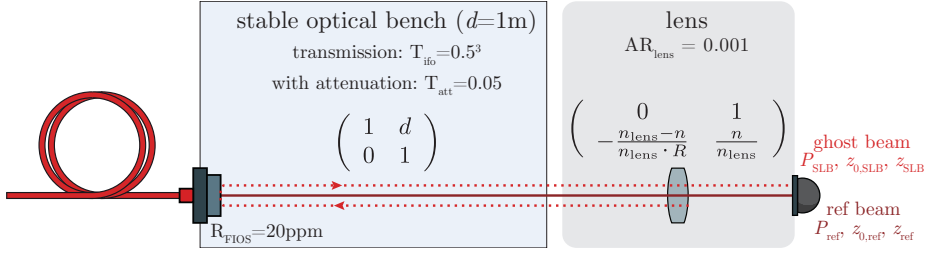


**Fig. 2.8.:** Illustration of a ghost beam backreflected from a focusing lens. The influence on the phase error can be estimated by using the ABCD matrix analysis for gaussian beams that are used to determine the divergence of the ghost beam due to the lens.

center of the diode. This implementation causes some unwanted backreflections from the AR-coatings, which are re-entering the interferometer. Since the lenses are typically not angled with respect to the interferometer axis to avoid lens errors, the ghost beams propagate back to the FIOSs, or any other surface under almost  $0^\circ$ . This generates a subsequent backreflection and ghost beams propagate towards the photodiodes. The ray propagation of this example is shown in Figure 2.8. Since the lens will generate a non-collimated backreflection, the mode overlap of ghost beam and nominal beam is assumed to be low. For estimating the actual influence, the contrast is determined according to equation [WH14]

$$\kappa = \frac{2 \cdot A_p \cdot \sqrt{z_{0,SLB} \cdot z_{0,ref}}}{\sqrt{(z_{0,SLB} + z_{0,ref})^2 + (z_{SLB} - z_{ref})^2}} = 1.021 \cdot 10^{-7} \quad (2.8)$$

with the constant factor,  $A_p = 2 \cdot \sqrt{(P_{SLB} \cdot P_{ref})} / (P_{SLB} + P_{ref})$ , the Rayleigh range of the ghost beam,  $z_{0,SLB}$ , and of the reference beam,  $z_{0,ref}$  and the distance from the individual waist in direction of propagation for each beam,  $z_{SLB}$  and  $z_{ref}$ . An ABCD matrix analysis for Gaussian beams is used to calculate the propagation of a beam with  $500 \mu\text{rad}$  waist size, a waist position of 20 cm and a wavelength of 1064 nm. The lens has a focal length of 25.4 mm, an AR-coating reflectivity of 0.001 and a refractive index of 1.449 63. The propagation delay between ghost beam and reference beam is 1 m. The ghost beam power is calculated by using the beam splitting ratios of the interferometer, here three 50/50 beam splitters and one attenuation beam splitter with 95 % reflectivity. We assume a fiber backscatter of the order of 20 ppm. The estimated value for the contrast, given by Equation (2.8), is equivalent to the phase error according to Equation (2.6). We can expect that ghost beams from lenses generate phase errors on the order of  $0.1 \mu\text{rad}/\sqrt{\text{Hz}}$  and are likely negligible in our application. We also discarded clipping effects due to the high divergence, which will further limit the effective ghost beam power.

### 2.3.5 Mitigation strategies

Several mitigation strategies can be used to reduce the induced phase errors by ghost beams. Especially interferometers which are designed in advance and quasi-monolithically bonded afterwards promise high spurious beam suppressions.

- **High quality optical components**

The usage of optical components with high quality can improve the interferometric phase performance. High-reflective mirrors, AR-coatings and the surface quality can be optimized such that secondary reflections and scattered light can be attenuated.

- **Beam dumps/apertures**

The easiest way to reduce spurious beams is the usage of beam dumps. Thick components, as illustrated in Figure 2.6a, generate a parallel shifted ghost beam with respect to the nominal beam. The shift is about

$$D = d \cdot \sin(\text{AOI}) \cdot \left( 1 - \frac{\cos(\text{AOI})}{\sqrt{n^2 - \sin^2(\text{AOI})}} \right) = 2.2 \text{ mm} \quad (2.9)$$

for an angle of incident (AOI) of  $45^\circ$ , vacuum,  $n_0 = 1$  and components made of fused silica with a refractive index of  $n = 1.44963$  and a thickness of  $d = 7 \text{ mm}$ . The resulting ghost beam can be blocked by a beam dump that is inserted between the two optical components.

- **Wedged components**

A wedge angle at the secondary surface produces a ghost beam that leaves the interferometer under an angle. A tilt of optical components leads to the same effect. These ghost beams can be dumped later on.

- **Attenuation stages**

The ratio of nominal power to spurious power can be improved by attenuation stages. It implies that the spurious beam passes the attenuation stage more often than the nominal beam. The usage of attenuation stages requires very high initial laser powers. An attenuation of 0.1 % power transmission for example improves the power ratio by a factor of  $1 \cdot 10^{-6}$ . The phase error, which depends on the square-root of the power, is only improved by a factor of  $1 \cdot 10^{-3}$ , while the initial laser power is reduced by the same factor. Since the LISA telescope requires the major part of the light power a beam splitter with a reflectivity of about 0.95 will be used. This already acts as attenuation stage for ghost beams coming from the local interferometry. Stray light from the telescope is not attenuated.

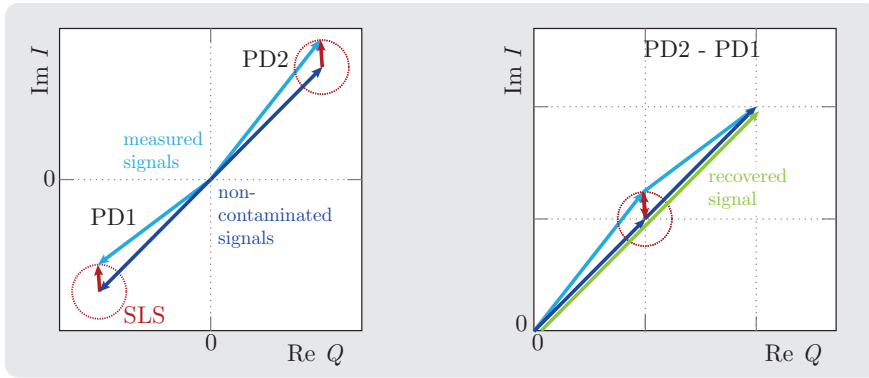


**Fig. 2.9.:** Vector representation of balanced detection. The optical signals of redundant photodiode measurement are subtracted from each other whereby the phase error caused by ghost beams can be eliminated to some degree.

- **Off-axis interferometry**

Off-axis interferometers, like the test mass readout in LPF where the beam hits the surface under an angle, can be used to prevent ghost beams in traveling back to the laser source.

- **Fiber length stabilization**

This implementation reduces the dynamical behavior of fiber ghost beams.

- **Polarization optics**

Parasitic interferometers of different polarization can be reduced by polarization components, like a polarizing beam splitters (PBSs) behind each FIOS. Polarization encoding can also be used for on-axis MIs. The change of the polarization state via Faraday isolators, or via half-waveplates in combination with PBS, separates in-bound and out-bound beams from each other. This ensures that no light travels back to the laser source where it is reflected back into the interferometer. Thin film polarizers in front of the photodiodes are often used due to their high polarization extinction ratios. However, the limited polarization extinction ratio of these components produce ghost beams of 'wrong' polarization which generate interferometers competitive to the nominal one.

- **Balanced detection**

Balanced detection is a post-correction method that can be applied to the phase data if a redundant PD at the second output port of the recombining beam splitter is also read out. The vector plane depicted in Figure 2.9 represents a signal on two redundant PDs that is contaminated by a small vector. If the SLS has been interfered with one of the beams before it reaches

the recombination beam splitter, it is split by half and accumulates a phase shift of  $\pi$  for one of the ports. The small vector in Figure 2.9 has therefore the same sign for both PDs. The subtraction of the two measured signals is illustrated on the right of Figure 2.9. The spurious beam is common mode and vanishes in the signal combination, the actual signal is recovered. This technique can always be applied if the two redundant beam splitter output ports are accessible and the phasemeter, or data acquisition system, provides enough channels and processing capabilities. Earlier experiments have shown that balanced detection is able to improve the phase performance by about two orders of magnitude which works only well if the ghost beam is collinear with respect to the nominal beams [Fle+17]. Ghost beams interfering at the recombination beam splitter and not before cannot be subtracted by this method.

## 2.4 Backlink designs and spurious beam limitations

In the following, a list of some selected possible backlink candidates for LISA are shown. Conversations with Guido Müller from the University of Florida, Jeffrey Livas from the NASA’s Goddard Space Flight Center in the US and Ewan Fitzsimons from the Astronomy Technology Centre in UK had a helpful outcome to the content of this section. The optical layout of each candidate is shown on a two-bench set-up. Some components are inherited in each layout that are derived from the current LISA optical bench design. These are polarizing components in the first place, which are in principle parts of the fiber output coupler devices, and a 95% beam splitter, which is used on the LISA optical bench for sending most of the TX light to the telescope. It serves as single-component attenuation stage in the backlink interferometers. For each implementation an estimation of the expected phase errors is given. The calculation is based on Equation (2.7), thus we only use the ratio of the estimated optical laser powers while the heterodyne efficiency is assumed to be 1 and the fiber backscatter is on the order of 20 ppm (5 m fiber length with 4 ppm/m).

### 2.4.1 Fiber backlinks

The *prior direct fiber backlink (DFBL)* experiment is shown in Figure 2.10a, here depicted for a two-bench scenario as it would be implemented in the TBI. The TX beam, with a frequency  $f_1$ , is injected on the left bench, the TX’ beam, with a frequency of  $f_2$ , on the right bench respectively. Both are coupled into the backlink fiber and are guided via this connection to the adjacent bench where they serve as LO. Due to the fiber coupling a ghost beam is generated by Rayleigh

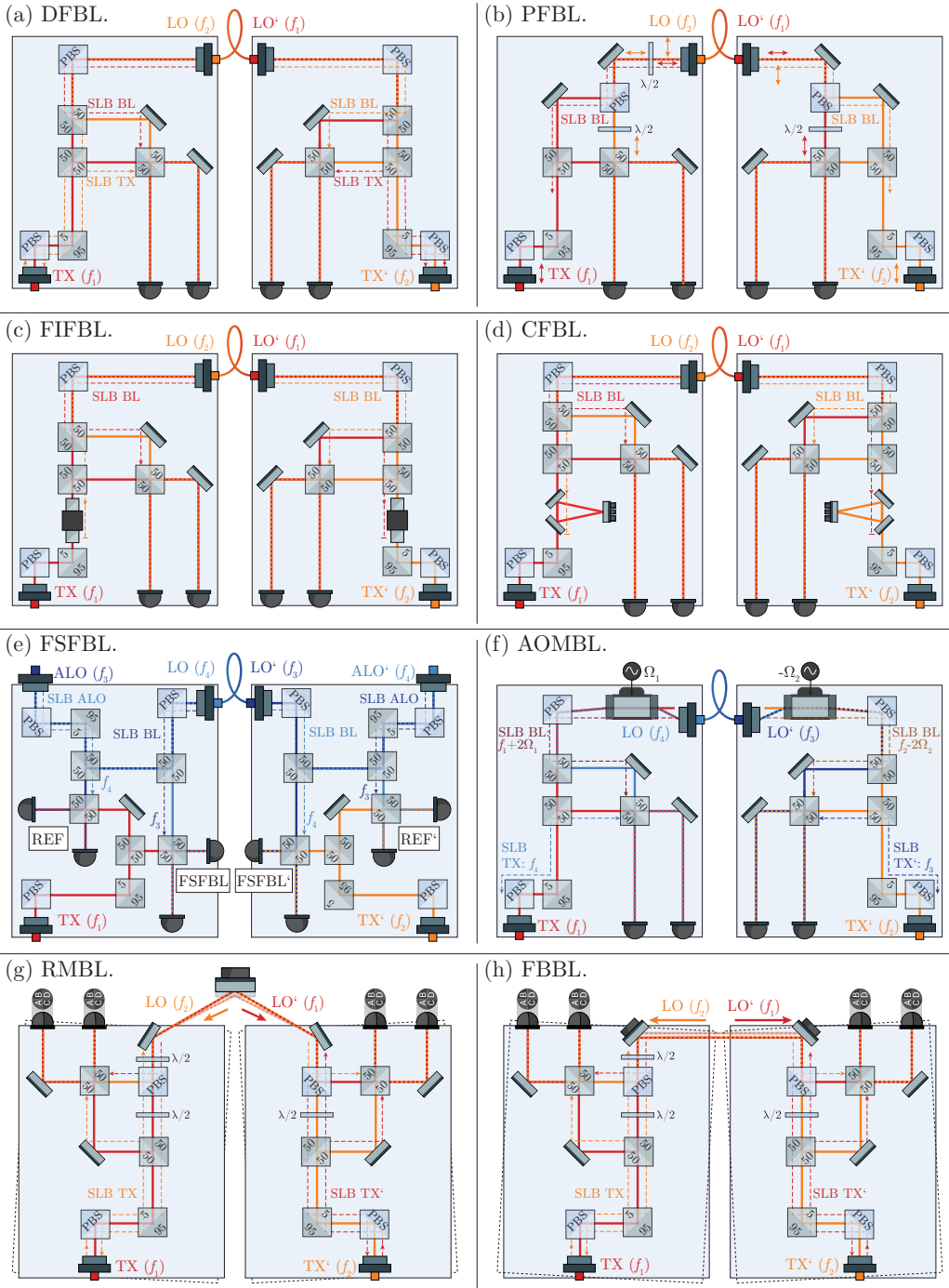


Fig. 2.10.: Overview of optical designs of various PRDSs. The backscatter from the backlink connection generates ghost beams that are named SLB BL, while the backscatter from the TX fiber is named SLB TX and SLB ALO for the one from the additional local oscillator (ALO) injection fiber, respectively.

scattering. It interferes with the LO beam and generates therefore a signal with the beat note  $f_1 - f_2$ . The LO is required for local interferometry, but it also propagates to the TX FIOS where another ghost beam is generated. This one interferes with the TX beam which leads again to a spurious signal with the beat note  $f_1 - f_2$ . An additional interference among the two ghost beams is produced by the recombination beam splitter, whose phase error cannot be subtracted via balanced detection. Due to the very low laser powers of these ghost beams the expected phase error is only about  $0.25 \mu\text{rad}$ . The interferences generated by the SLB TX and TX beam, producing a phase error of  $110 \mu\text{rad}$ , and by the SLB backlink (BL) and LO beam ( $2.2 \text{mrad}$ ), have a much higher influence on the phase error (see Table 2.4). The SLB TX will not only limit the direct fiber backlink interferometer itself, but also all other interferometers which are implemented on the same bench and also use the TX beam. The backscatter from the backlink fiber, SLB BL, will only disturb the DFBL itself in the TBI-experiment. On the LISA optical bench, it will contaminate all interferometers using the LO beam.

Figure 2.10b shows a direct fiber connection with polarization encoding, called *Polarization Fiber backlink (PFBL)*. The in-bound and out-bound light, traveling through the backlink fiber, is separated from each other based on polarization. This concept was initially proposed by Christian Diekmann [Die13] and is able to reduce the ghost beam powers from both occurrences, the backlink fiber and injection fiber. The resulting phase error scales with the square-root of the extinction ratio of the polarizing components and is given in Table 2.4. To achieve an adequate ghost beam suppression, such that the LISA requirement can be achieved, the polarizing beam splitter must show an extinction ratio of better than  $1 \cdot 10^{-6}$  in power for both, vertical and horizontal polarization. The backlink fiber however needs to deal with two different polarizations in this design. Backlink light is guided along the fast and slow axis of the fiber, depending on the propagation direction. Whether the propagation along the two perpendicular fiber axes is reciprocal within the required LISA specifications is not proven yet. The polarization-maintaining (PM) fiber itself has already a limited extinction ratio.

A further evolved DFBL is shown in Figure 2.10c and is called *Faraday isolator fiber backlink (FIFBL)*. It uses the polarization changing properties of a Faraday rotator to prevent the LO from propagating to the TX injection fiber. It decreases the influence of ghost beams coming from the injection fiber, SLB TX, but not the SLBs of the BL. The suppression rate depends on the extinction ratio of the polarizing beam splitters, that belong to the Faraday rotator, and the accuracy of the polarization change due to the Faraday crystal. The phase error induced from ghost beams from the injection fiber can be reduced by a factor that is determined by the square-root of the extinction rate of the Faraday isolator,  $\sqrt{\text{ISO}_{\text{extc}}}$ , as shown in Table 2.4. It has been shown that the extinction ratio of a Faraday



**Tab. 2.2.:** Beat note separation of ghost beams in the frequency separated fiber backlink (FSFBL), once shown for four different sidebands. Shown are two cases: In the first one, all four lasers are frequency shifted with respect to each other. In the second case, both TX lasers have the same frequency,  $f_1 = f_2$ .

interferometer	$f_1 > f_2 > f_3 > f_4$			$f_1 = f_2$		
	nominal beat	SLS beats		nominal beat	SLS beats	
REF	$f_1 - f_3$	$f_3 - f_4$	$f_1 - f_4$	$f_1 - f_3$	$f_3 - f_4$	$f_1 - f_4$
REF'	$f_2 - f_4$	$f_3 - f_4$	$f_2 - f_3$	$f_1 - f_4$	$f_3 - f_4$	$f_1 - f_3$
FSFBL	$f_1 - f_4$	$f_3 - f_4$	$f_1 - f_3$	$f_1 - f_4$	$f_3 - f_4$	$f_1 - f_3$
FSFBL'	$f_2 - f_3$	$f_3 - f_4$	$f_2 - f_4$	$f_1 - f_3$	$f_3 - f_4$	$f_1 - f_4$

isolator is below  $1 \cdot 10^{-6}$ , sufficient for our application [Win17]. The usage of a Faraday isolator is not proposed being used in the LISA mission. It is surrounded by a strong magnet magnetic field that will significantly influence the motion of the free-floating test masses within the satellite. Suppression techniques can be used to decouple the test mass motion from magnetic field gradients. One could add compensating magnetics in the satellite, other shielding techniques or increase the distance between magnet and test mass.

Figure 2.10d shows the *cavity fiber backlink (CFBL)*, an alternative design of a fiber-based backlink with a mode-cleaning cavity implemented behind the injection fiber. The cavity has a narrow bandwidth and is matched to the laser frequency of the injected TX beam,  $f_1$ , for the left bench. It filters therefore the LO beam with frequency  $f_2$ , which comes from the BL fiber. The phase error induced by ghost beams from the injection fiber, SLB TX, can be reduced by a factor that is determined by the square-root of the extinction rate of the cavity,  $\sqrt{\text{CAV}_{\text{extc}}}$ . Ghost beams from the backlink, SLB BL, cannot be removed or filtered. Due to the triangular cavity shape, direct backreflections from the cavity itself can be avoided. An additional cavity however increases the complexity of the LISA optical bench and requires further locking electronics, readouts and sidebands for stabilizing the cavity length. A dedicated error signal for actuating the piezoelectric transducer (PZT) end mirror of the cavity is also needed.

A further proposed PRDS is the *frequency separated fiber backlink (FSFBL)*. It eliminates the direct ghost beam influence of both, the injection fibers and the BL fiber. While the schemes mentioned before reduce only the ghost beam powers, the FSFBL eliminates completely the coupling of all fiber ghost beams due to fiber reflections and scattering of the first order. By shifting their frequencies away from the actual beat note frequency the heterodyne readout is not influenced by those. A possible layout is depicted in Figure 2.10e. For the frequency separation a further laser source is required per bench. It provides a laser beam with a frequency that is offset-shifted with respect to the frequency of the TX,  $f_1$ , as well as to the one of

the TX' beam,  $f_2$ . These beams will be named as additional local oscillators, ALO and ALO', on the left and right bench, respectively, with the frequencies  $f_3$  and  $f_4$ . These ALOs are used for the light exchange between the two benches. A further interferometer per bench is required due to the additional laser injection. These reference interferometers measure the phase stability between the TX and the ALO on both benches. Ghost beams of first order of fiber backscatter interfere to signals with uncritical beat notes which are shown in Table 2.2. Second order fiber ghost beams are generated when a beam is backreflected subsequently from both FIOSs. Firstly, from the BL fiber interface, secondly from the ALO fiber output coupler. These second order ghost beams have the same frequency as the initially injected ALO beam, but the power level is very low. Without attenuation stages also behind the ALO FIOS, this backreflection of second order exceeds the tolerable power levels in this backlink design. In Table 2.4 the corresponding remaining phase error is depicted. The usage of a beam splitter with 0.05 relative power reflectivity decreases the ratio to  $0.25 \cdot 10^{-6}$  rad. This is about a factor of 4 below the LISA requirement. The FSFBL is a promising candidate for the LISA PRDS. It only consists of commercial well-known optical components, which is advantageous if one compares it with the FIFBL design. Even by implementing a further reference interferometer on the optical benches, only two additional photodiodes are required for this scheme. The usage of balanced detection, as required for the DFBL, requires one additional photodiode in each LISA interferometer, not counting further redundant ones. The additional laser source on-board the satellite is a disadvantage considering further electronics that are required for stabilizing the amplitude and frequency of the same. The optical bench gets more complex and the power consumption for operating two more lasers per S/C increases. One could use Acoustic-Optical modulator (AOM)s instead for generating additional frequencies. The LISA payload design however would not be simplified significantly in comparison to additional laser sources. Additional laser frequencies however might reduce the complexity of the LISA frequency plan. The same handles the inter-satellite MHz-frequencies which vary due to the Doppler shift between the moving satellites. This plan can be modified if additional laser sidebands are available on-board, which can be tuned more freely [Bar15].

A similar suppression technique as introduced for the FSFBL, is used in the *AOM fiber backlink (AOMFBL)*. Figure 2.10f shows a possible implementation of an AOM integrated in the design of a fiber-based PRDS. The AOMs uses the acousto-optic effect to shift the laser frequencies of the TX beams before they are coupled into the backlink fiber. The frequency shifts have a different sign such that the absolute offset is kept in the detection bandwidth. A ghost beam passing the AOM twice, collects the same frequency shift twice with the same sign. It is therefore shifted out of the detection bandwidth and interfered to signals with

**Tab. 2.3.:** Beat note separation of beams in the AOM fiber backlink (AOMFBL). The frequencies  $\Omega_1$  and  $\Omega_2$  are introduced by the AOMs. Three SLSs appear. Two are caused by ghost beams from the backlink fiber, having different frequencies. The last one is generated from the TX fiber and not frequency shifted.

interferometer	$f_1 > f_2$ and nominal beat	$f_4 = f_2 - \Omega_2 + \Omega_1$ and $f_3 = (f_1 + \Omega_1 - \Omega_2)$ SLS beats		
AOMFBL	$f_1 - f_4$	$f_1 - f_4$	$f_1 - (f_1 + 2\Omega_1)$	$f_4 - (f_1 + 2\Omega_1)$
AOMFBL'	$f_2 - f_3$	$f_2 - f_3$	$f_2 - (f_2 - 2\Omega_2)$	$f_3 - (f_2 - 2\Omega_2)$

uncritical heterodyne frequencies, which are shown in Table 2.3. Ghost beams from the TX fiber however are not frequency shifted and produce a phase error of about  $100 \mu\text{rad}$ . Since the Gaussian beam quality suffers from the acousto-optic effect, the heterodyne efficiency in the interferometers and the coupling efficiency into the fibers could drop. Unknown is the thermal behavior of the AOM, leading to a significant heat source on the optical bench. Also the electro-magnetic crosstalk between two of these devices must be investigated.

#### 2.4.2 Free-beam backlinks

The backlink alternatives proposed in the recent section are only fiber-based PRDS. The *reflector in the middle backlink (RMBL)* is the first free-beam candidate that is shown in Figure 2.10g. The beam propagation and the set-up are identical to the ones used in the PFBL. This scheme however excludes the fiber from the backlink connection by which ghost beams, caused by backlink Rayleigh scattering, are eliminated. It is therefore an attractive alternative. To compensate the angular variations between the two rotating optical benches, a mirror is placed in the bisectrix of the optical benches such that the preservation of heterodyne efficiency in the local interferometry is ensured via the law of reflection. The rotation point of both optical benches is required to be at the laser reflection point on the mirror surface. A translational actuation must be applied on the reflector in the middle if the rotation axis is not stable during the rotation of  $\pm 1.5^\circ$ . Even though the RMBL provides an optical set-up with less complexity in comparison to similar fiber set-ups, the alignment of the reflector and the actuation of the MOSAs are very challenging. The redundancy of this PRDSs also needs to be developed. The reflector position is at a fixed point between the benches. A secondary, redundant reflector cannot be placed at the same position, which is why the motion of the benches must be changed by switching between the redundant schemes. To prevent the occurrence of ghost beams in this BL implementation, polarization optics are used to separate in-bound and out-bound light from each other. This leads to a significant additional suppression of TX backreflections. Only the accuracies of

the extinction ratios of these components will cause secondary power reflections and, thus, a beam propagating towards the injection FIOS.

A further fiber-free implementation is depicted in Figure 2.10h. The so called *free-beam backlink (FBBL)* uses two actuator mirrors in a closed feedback control loop to compensate the bench rotation in horizontal direction, and potential wobbles in vertical direction. The beam propagation of the TX beams on the optical benches is identical to the ones in the PFBL or the RMBL. The active control loop requires error signals that are provided by two QPDs, measuring DWS signals. To decouple the motion of the actuator mirrors from each other, imaging lenses are required. With these, a certain degree of decoupling in the control loops can be achieved and the usage of DWS signals enables high gain feedback control. In order to suppress ghost beams, polarizing optics are installed in the free-beam (see RMBL). Free-beam solutions however have a much higher dynamic behavior due to the backlink actuation. This could potentially increase and up-convert the stray light coupling in the detection bandwidth.

### 2.4.3 Backlink suggestions for LISA and the TBI

Each backlink proposed in this chapter deals with its own challenges. The decision for a PRDS for LISA is a trade-off between the complexity of the optics, the amount of ghost beam suppression and the application of post-corrections. Without any stabilizations, post-correction or balanced detection, the DFBL will not achieve the desired performance, even by integrating an attenuation system. Evolved versions of the DFBL, like the integration of a Faraday isolator in the FIFBL, polarizing optics as in the PFBL or a cavity in the CFBL design, achieve an improvement if the regarding components have an extinction ratio,  $\text{PBS}_{\text{extc}}$ ,  $\text{ISO}_{\text{extc}}$ ,  $\text{CAV}_{\text{extc}}$ , of better than  $1 \cdot 10^{-6}$  in power. Very likely is a combination of two different BL alternatives to achieve the desired performance. E.g. the implementation of a Faraday isolator behind the TX fiber output coupler and an AOM in front of the BL FIOS would eliminate both ghost beam sources. These backlink combinations however would increase the complexity of the LISA optical bench. The polarizing BLs, both fiber-based and free-beam, as well as the FSFBL, have by design a low ghost beam coupling and can potentially meet the requirement with less optical complexity. A full trade-off for LISA will also need to take additional complexities into account, like the potential suppression of telescope stray light with a frequency swap or the integration and testing complexities of the payload. A frequency swap in the telescope would lead to a science interferometer using the RX and LO beams, instead of the RX and TX beams.

The Three-Backlink interferometer (TBI) serves as test-bed for LISA PRDSs. It will be used to test three independent backlink implementations against each

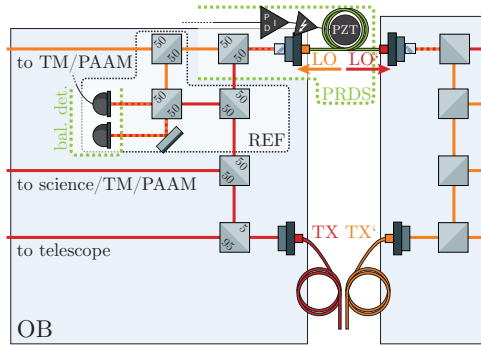
**Tab. 2.4.:** Overview of spurious light beams (SLBs) occurring in the different backlink (BL) implementations. The estimated phase error is calculated via Equation (2.7) for each backlink interferometer for three different scenarios: Firstly, SLB from the TX fiber that interferes with the TX beam. Secondly, SLB from the BL fiber that interferes with the LO. Thirdly, the interference among these two SLB beams. A fiber backscatter of 20 ppm, an attenuation ratio of  $r_{\text{att}} = 0.05$  and a heterodyne efficiency of 1 is assumed.

backlink	interfering beams		phase error [rad]
DFBL	SLB TX	TX	$1.1 \cdot 10^{-4}$
	SLB BL	LO	$2.2 \cdot 10^{-3}$
	SLB TX	SLB BL	$0.25 \cdot 10^{-6}$
PFBL /	SLB TX	TX	$\sqrt{\text{PBS}_{\text{extc}}} \cdot 1.1 \cdot 10^{-4}$
RMBL /	SLB BL	LO	$\sqrt{\text{PBS}_{\text{extc}}} \cdot 4.4 \cdot 10^{-3}$
FBBL	SLB TX	SLB BL	$\text{PBS}_{\text{extc}} \cdot 0.5 \cdot 10^{-6}$
FIFBL	SLB TX	TX	$\sqrt{\text{ISO}_{\text{extc}}} \cdot 1.1 \cdot 10^{-4}$
	SLB BL	LO	$2.2 \cdot 10^{-3}$
	SLB TX	SLB BL	$\sqrt{\text{ISO}_{\text{extc}}} \cdot 0.25 \cdot 10^{-6}$
CFBL	SLB TX	TX	$\sqrt{\text{CAV}_{\text{extc}}} \cdot 1.1 \cdot 10^{-4}$
	SLB BL	LO	$2.2 \cdot 10^{-3}$
	SLB TX	SLB BL	$\sqrt{\text{CAV}_{\text{extc}}} \cdot 0.25 \cdot 10^{-6}$
FSFBL	SLB BL	LO	$0.25 \cdot 10^{-6}$
REF	SLB ALO	ALO	$0.25 \cdot 10^{-6}$
	–	–	
AOMFBL	SLB TX	TX	$1.1 \cdot 10^{-4}$
	SLB BL	LO	–
	SLB TX	SLB BL	–

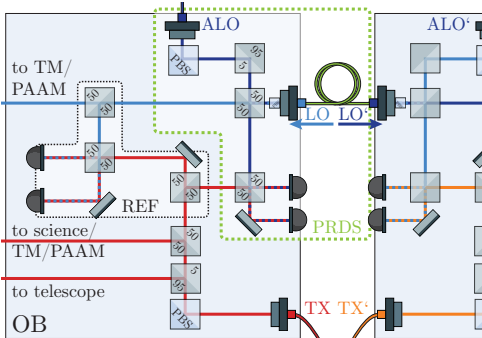
other within a single set-up. Two spatially separated optical benches are rotatable against each other by  $1.5^\circ$ , a similar amount of rotation is expected for LISA. We decided to implement a direct fiber backlink in the TBI. Due to the results from the prior fiber backlink experiment, this interferometer can be used as reference. The two alternative schemes are the FSFBL and the FBBL. Both show an adequately low ghost beam contribution. Since the DFBL would spoil all other backlink interferometers by ghost beams from the TX fiber, we integrate in the TBI a Faraday isolator in the TX path. A LISA optical bench design for each of the three TBI backlinks is given in Figure 2.11a.

An evolved version of the direct fiber backlink (not depicted here), proposed by Guido Müller and his working group in Florida, might also be a promising PRDS alternative. Only a few nW of optical laser power for the fiber backlink path is used. The LO provides even enough power to keep the shot noise level below  $1 \text{ pm}/\sqrt{\text{Hz}}$  for the reference interferometer, using balanced detection, and for the adjacent

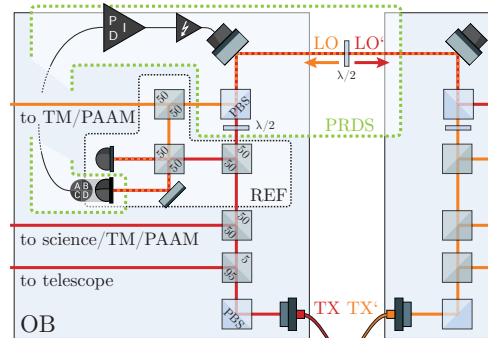
bench. An additional FIOS on each bench provides a high-power LO beam for the test mass and other LISA interferometers. This additional laser injection requires again a further reference interferometer. The advantage of this implementation is the need for balanced detection in only one LISA interferometer. The ghost beam influence in other interferometers is sufficiently low due to the low-power link. This implementation could also be tested within the TBI experiment by attenuating the power of the DFBL.



(a) Backlink ghost beams are not eliminated, which is why balanced detection and/or a fiber length stabilization is required for the LISA OB.



(b) The frequency separated fiber backlink with two ALOs for shifting spurious beat notes to other frequencies.



(c) A free-beam link completely eliminates the backlink fiber and reduces ghost beams via polarization encoding.

**Fig. 2.11.:** Overview of the three backlinks and their implementation on the LISA optical bench. The TX beam of each bench is used as LO on its counterpart, respectively, enabling heterodyne interferometry in the science, test mass (TM), and point ahead angle mechanism (PAAM) interferometers as well as in the PRDS.

# OPTICAL SIMULATIONS

” *Results of optical simulations containing the layout, ghost beam analysis and the decoupling strategy for the control loop DWS signals of the Three-Backlink interferometer.*

The TBI experiment provides a side-by-side comparison of two alternative backlink candidates, the frequency separated fiber backlink and the free-beam backlink, with respect to the direct fiber backlink, equipped with a Faraday isolator. The respective limitations of each backlink can be investigated and a trade-off study for the LISA optical bench design can be supported by this experiment. In addition, the TBI experiment is to be conducted in a more representative environment than the previous one since it will be operated by two optical set-ups that are rotatable against each other by  $\pm 1.5^\circ$ . With the integration of three backlinks in a single experiment, and eight interferometric measurements, the TBI is one of the most complex quasi-monolithic interferometers ever built at the AEI and it requires a careful design of the optical layout.

In this chapter the final optical layout of the TBI is demonstrated, which has been developed by optical simulations performed with the C++ library IfoCAD. Based on this design the influence of fundamental noise sources is estimated, the phase error of remaining ghost beams is analyzed and optical signals, that show among others the TTL coupling for each backlink, are numerically calculated for the TBI. Additional simulations are performed only for the free-beam link. The results of the optical signals are demonstrated in order to estimate the longitudinal pathlength noise which is induced by the free-beam connection. In addition, the DWS signals are calculated and the coupling matrix, describing the relation between actuator mirror motion and sensor signal, is determined. The knowledge about this coupling mechanism is essential for the operation of the free-beam backlink which is actively controlled by using a feedback system for compensating the bench rotation. Parts of this chapter have already been published in [Isl+18].

### 3.1 Three-Backlink interferometer design

The TBI experiment consist of two, mirror-symmetrical optical benches which are almost equally equipped by several optical components. Figure 3.1 depicts the design of the TBI as a technical drawing which was, to a large degree, produced by a simulation based on IfoCAD. Four lasers, the transmitted beams TX and TX', along with the additional local oscillators ALO and ALO', are fed via fibers to two optical benches, each having a size of 270 mm  $\times$  270 mm  $\times$  36 mm. The fibers are mounted on quasi-monolithic ultra stable FIOSs [Kil+16; Sch15]. These FIOSs are also used for connecting the backlink fibers to the optical benches. In the simulation, each FIOS produces a laser beam with a waist size radius of 0.5 mm and a waist position of 25 cm, measured from the FIOS front. The laser output powers are 320 mW for the TX beams and 160 mW for the ALOs. All lasers are frequency shifted with respect to one another to allow for a unique heterodyne detection in each interferometer. The frequencies of the two TX beams are  $f_1$  and  $f_2$ , the ALOs have frequencies of  $f_3$  and  $f_4$ . Four interferometers per bench measure the phase performance of the direct fiber backlink (DFBL), frequency separated fiber backlink (FSFBL) which, in turn, requires an additional reference (REF) interferometer, and the free-beam backlink (FBBL). A complete list of components of the left bench can be found in Table 3.1. Due to the mirror symmetry of the experiment the list of components for the right bench is identical, with the mere addition of a prime in its notation. In total, the experiment requires 8 monolithic FIOSs, 16 deflection mirrors, 24 beam splitters with a splitting ratio of 50 %, 4 attenuation beam splitters with a reflectivity of 95 %, 2 actuation mirrors, 12 polarizing beam splitters, 16 lenses, 3 half-wave plates (potentially 2 quarter-wave plates instead of 1 half-wave plate), 2 Faraday rotators, 74 beam dumps, 18 photodiodes and 2 quadrant photodiodes. All interferometers are equipped with two photodiodes, the secondary ones being redundant or used for balanced detection. Two additional photodiodes per bench are used for monitoring amplitude fluctuations and can be used as error signals for an amplitude stabilization that will be set up by means of analog electronics. One of the photodiodes in the FBBL and FBBL' interferometers is a QPD providing the error signals for the steering mirror control loops.

The absolute optical pathlength difference for each interferometer is listed in Table 3.2. The largest arm length mismatch is given by the FBBL interferometers and is about 720 mm, leading to LFN-levels of  $1.5 \mu\text{rad}/\sqrt{\text{Hz}}$  assuming frequency stabilities of about  $100 \text{ Hz}/\sqrt{\text{Hz}}$ . For the fiber-to-fiber coupling in the DFBL we simulated an optical pathlength of 411.21 mm and for the FSFBL about 368.87 mm.



Tab. 3.1.: List of components used in the TBI on one bench.

dynamic	component	$R$	AR	description
fiber	fios1, fios4	20 ppm [Fle12]		FIOS for TX and ALO laser injection
	fios2, fios3	20 ppm [Fle12]		FIOS for backlink fiber DFBL and FSFBL
bonded	OB	–	–	optical bench (OB), Clearceram HS, Ohara, with a CTE of $1 \cdot 10^{-8}/K$
	m1-m8	0.999	0.001	deflection mirror (M)
	bs1-bs5, bs9, bs10	0.5	0.001	beam splitter for TX and ALO laser power splitting
	bs6, bs8, bs11, bs12	0.5	0.001	recombining beam splitter (BS) for DFBL, FBBL, FSFBL, REF
	bs7	0.5	0.001	BS for laser power splitting of TX
	att1, att2	0.95	0.001	attenuation BS for spurious light of fios1 and fios4
	pbs1	0.99	0.001	PBS, polarization cleaning after fios1 & for the Faraday rotator
	pbs2-pbs4	0.99	0.001	PBS, polarization cleaning after fios2, fios3, fios4
	pbs5	0.99	0.001	PBS, polarizing beam separation for the FBBL
	pbs6	0.99	0.001	isolating PBS for the Faraday rotator
metal mounted	RTL/RTR			rotary table, left & right, Newport (URS50BPPV6)
	AML/AMR	0.999	0.001	gold-coated, PI actuation mount (S-334), 50 mrad tip/tilt range
	l1	0.01	0.01	imaging lens $f = 25.4$ mm for the actuation loop
	l2-l8	0.01	0.01	focusing lens $f = 25.4$ mm
	hwp1	0.01	0.01	$\lambda/2$ for the FBBL light
	qwp2	0.01	0.01	$\lambda/4$ for FBBL, qwp2 & qwp2' or a single $\lambda/2$
	hwp3	0.01	0.01	$\lambda/2$ behind the Faraday rotator
	Faraday rotator	30 dB	0.01	eliminates backreflections from fios1, Qi Optik (FI-1060-3SC LO)
	bd1-bd37	0.0001	0.01	beam dumps, KG5, for 2 mm $T \ll 0.01$ %
	pd1	0.01	0.01	power monitor for TX, Pacific Silicon (PC50)
	pd2	0.01	0.01	power monitor for ALO, Pacific Silicon (PC50)
	pd3-pd9	0.01	0.01	SED; Roithner (LAPD-1-09-17-TO46) InGaAs
	qpd1	0.01	0.01	QPD for the FBBL, OEC GmbH (GAP1000Q) InGaAs
	polarizer	T=0.80	yes	thin film polarizer, CODDIX, (colorPol VISIR CW02, laminated for DWS ( $\lambda/4$ ) and non-laminated ( $3\lambda$ ), PER 100000:1)

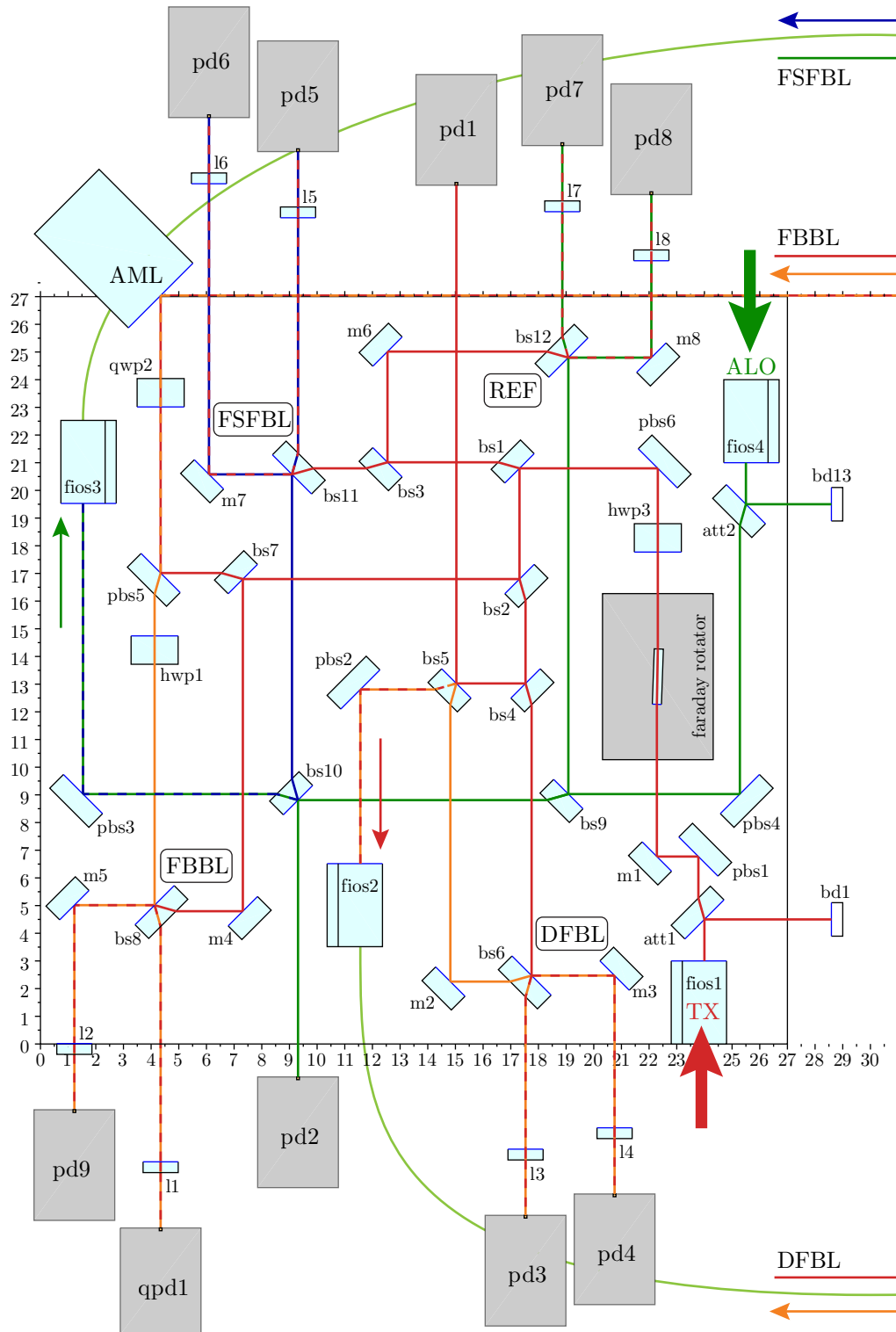
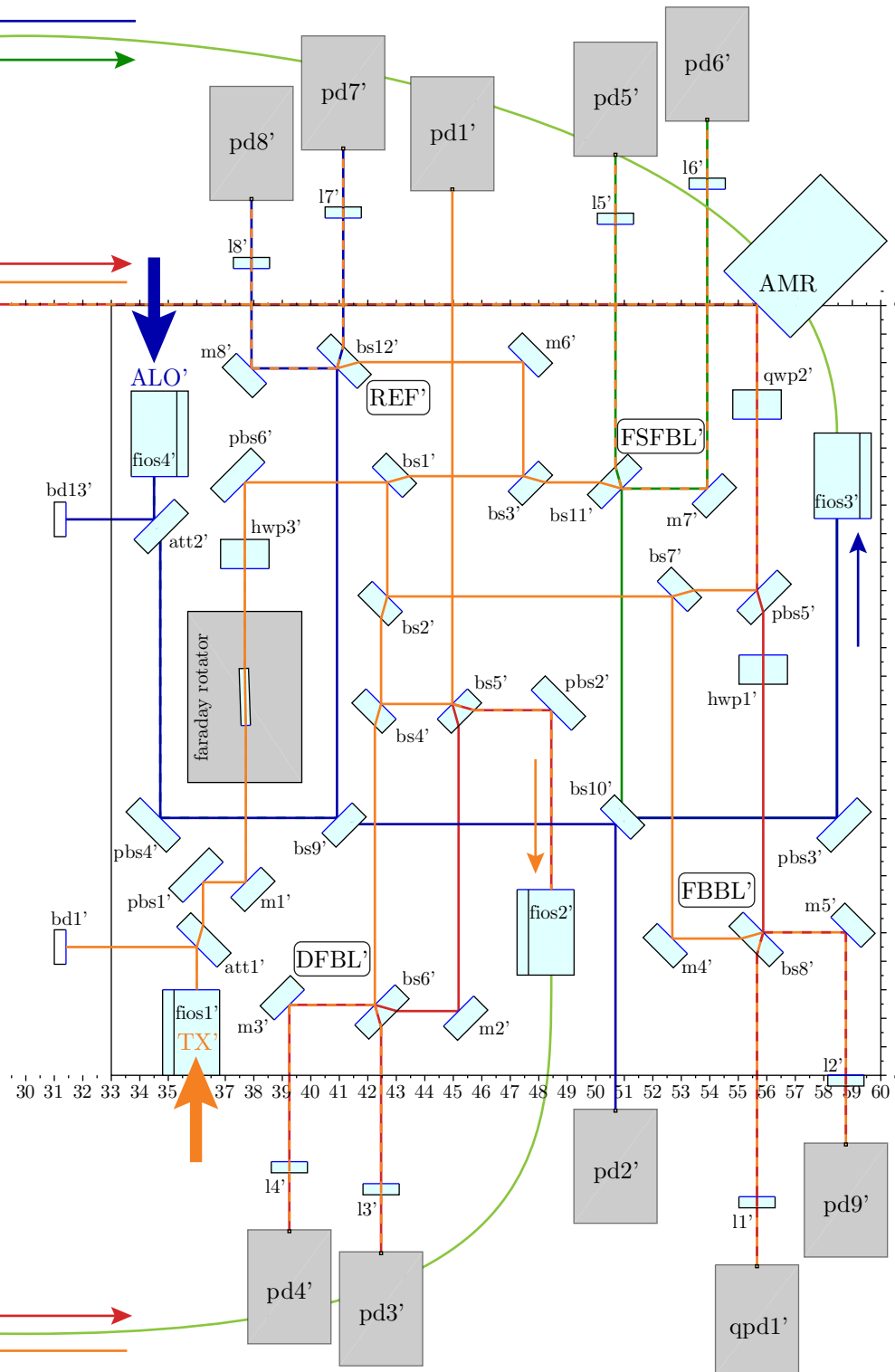


Fig. 3.1.: Optical layout of the Three-Backlink interferometer (TBI).



**Tab. 3.2.:** Laser power distributions in the interferometers of the DFBL, the FSFBL and its REF and the FBBL for an input laser power of 320 mW for the TX beams and 160 mW for the ALO. The coupling efficiency for the fiber-to-fiber couplings of the backlink connections is assumed to be 70 %. The pathlength (PL) noise contribution due to shot noise (SN) is calculated by using Equation (3.1), due to electronic noise (EN) by Equation (3.2) and due to relative intensity noise (RIN) by Equation (3.3).

inter-ferometer	laser power [mW]		het. eff.	pathlength noise $\delta s$ [m/ $\sqrt{\text{Hz}}$ ]				PL [mm]
	meas.	ref.		SN	EN	RIN	total	
DFBL	0.17	0.99	0.986	6.68e-15	4.66e-15	6.77e-15	1.81e-14	210
FSFBL	0.35	1.98	0.999	4.70e-15	2.32e-15	6.73e-15	1.38e-14	52
REF	1.98	1.99	0.999	2.57e-15	9.68e-16	4.79e-15	1.70e-14	84
FBBL	0.99	0.99	0.890	3.84e-15	2.05e-15	5.08e-15	1.10e-14	720

### 3.2 Power budget and fundamental noise sources

The overall laser power budget of the TBI and the influence of fundamental noise sources, like shot noise (SN), electronic noise (EN) and relative intensity noise (RIN), on the expected pathlength noise, is calculated in the following. Due to the usage of attenuation beam splitters behind the injection FIOSs these noise sources could limit the optical performance in the end. The attenuation stage for the TX beam has a value representative of the LISA optical bench architecture. The attenuation ratio of 95 % of the beam splitter behind the ALO FIOS in the TBI is a trade-off between achieving an adequate ghost beam suppression, while keeping the input laser power as low as possible, which makes it energy efficient and thus attractive for space applications. The laser power on the photodiodes should be kept above the fundamental noise limits of SN, EN, and RIN. All of these can disturb the pathlength measurement sensitivity in dependence on the laser power by the factors  $\delta s_{\text{SN}}$ ,  $\delta s_{\text{EN}}$  and  $\delta s_{\text{RIN}}$  [Trö+12],

$$\delta s_{\text{SN}} = \frac{\lambda}{2\pi} \sqrt{\frac{q_e(P_{\text{meas}} + P_{\text{ref}})}{R\eta P_{\text{meas}}P_{\text{ref}}}}, \quad (3.1)$$

$$\delta s_{\text{EN}} = \frac{\lambda}{\pi} \frac{n_{\text{el}}}{R\sqrt{\eta P_{\text{meas}}P_{\text{ref}}}}, \quad (3.2)$$

$$\delta s_{\text{RIN}} = \frac{\lambda}{2\pi} \frac{n_{\text{RIN}}(P_{\text{meas}} + P_{\text{ref}})}{\sqrt{2\eta P_{\text{meas}}P_{\text{ref}}}}, \quad (3.3)$$

with the wavelength  $\lambda = 1064$  nm, the photodiode responsivity  $R \approx 0.7$  A/W, the heterodyne efficiency  $\eta$ , the laser powers of measurement and reference beam,  $P_{\text{meas}}$  and  $P_{\text{ref}}$ , the elementary charge,  $q_e = 1.6 \cdot 10^{-19}$  A s, the electronics noise of each segment of a quadrant photodiode,  $n_{\text{el}} = 4 \cdot 10^{-12}$  A/ $\sqrt{\text{Hz}}$ , and the relative

intensity noise of both beams,  $n_{\text{RIN}} = 2 \cdot 10^{-8} / \sqrt{\text{Hz}}$ . The combined pathlength noise can be determined by the square-root of the quadratic sum of the single noise sources since they are uncorrelated [Trö+12],

$$\delta s_{\text{tot}} = \sqrt{\delta s_{\text{SN}}^2 + \delta s_{\text{EN}}^2 + \delta s_{\text{RIN}}^2}, \quad (3.4)$$

and gives a value for the fundamental limit for the pathlength measurement performance. Table 3.2 shows the power of measurement and reference beam, the heterodyne efficiency on the photodiode, determined by means of IfoCAD, and the equivalent pathlength noise for each interferometer in the TBI. The largest combined pathlength noise is  $0.018 \text{ pm} / \sqrt{\text{Hz}}$ , two orders of magnitude below the requirement of  $1 \text{ pm} / \sqrt{\text{Hz}}$ .

### 3.3 Spurious light suppression

The suppression of spurious light beams in the TBI requires various methods to ensure that each backlink is able to achieve  $1 \text{ pm} / \sqrt{\text{Hz}}$  phase performance and that it does not interact with other interferometers via spurious beams. The suppression methods that are applied in the TBI are the usage of attenuation stages, Faraday rotators, polarizers, waveplates, frequency shifting, eventually a dynamic range reduction via fiber length stabilization, the usage of beam dumps and apertures and potentially post-correction methods like balanced detection.

All backlink implementations profit from the attenuation beam splitters placed behind each TX and ALO FIOS. Only 5 % of the light is used in the interferometer, equivalent to LISA, where most of the optical power is sent to the telescope. For the ALO laser the splitting ratio can be matched to the desired ghost beam extinction ratio. The attenuation beam splitter only reduces ghost beams from the injection fiber since it attenuates the spurious beams twice in comparison to the nominal beam that passes the stage only once. The backlink, on the other hand, is a bi-directional light exchange that decreases the nominal and SLB beam powers by the same factor. The signal to ghost beam ratio can therefore not be improved with intentional attenuation.

To eliminate ghost beams originating from the DFBL, the integration of a Faraday rotator is unavoidable. The Faraday is placed behind the TX output coupler and before the laser separation. In general, only the DFBL requires the Faraday rotator, but potential pathlength noise introduced by the Faraday's non-linear crystal itself, that might be thermally driven, is common mode in all interferometers if the Faraday is placed before the laser separation and, thus canceling out in the signal combination required for the calculation of the non-reciprocity. The thermal stability of the mounting of the rotator is crucial for the

dynamic behavior of eventual ghost beams from this component. The design of a thermally compensated mount is required (Section 4.2.2).

The out-bound and in-bound light, that is exchanged between the two benches in the free-beam backlink, is separated by polarization. The remaining ghost beam influence of the free-beam backlink depends on the extinction properties of the polarizing optics. For the fiber-based backlinks polarizing beam splitters behind each fiber output coupler are used to clean the polarization. The polarization-separation method however cannot be used for the direct fiber backlink implementation due to the non-uniform behavior of a PM optical fiber when comparing the propagation in the fiber's slow and fast axes. Thin film polarizers are installed in front of the photodiodes to further clean the polarization of the interfered signals [Fle12; Fle+17; Die13; Deh+12].

Beat notes caused by spurious beams in the FSFBL are shifted to different frequencies by using additional local oscillator beams. Only those ghost beams reflected at both FIOSs, i.e. the ALO and the backlink FIOS, contribute to the phase error in the measurement performance.

Beam dumps (baffles) for high power ghost beams and beam stops for all other ghost beams are used to prevent these beams from traveling in parallel to the actual beams. Beam stops are made of an infrared filter glass that only transmits 0.01% of the light for a material thickness of 2 mm. They are produced with vertical wedge angles at the front and back surfaces and anti-reflecting coatings, reflecting all residual beams outside the critical plane.

Not included in the simulation but relevant for the experiment is the usage of angled photodiodes, since they produce ghost beams via backreflection which would otherwise enter the interferometer plane. In addition, thin film polarizers are often used in front of them to reduce the influence of competitive interferometers with other polarizations. Those must also be angled with respect to the interferometer plane (Section 4.2.1).

### 3.4 Phase error of remaining ghost beams

Even though most of the spurious beams are blocked, some residual ghost beams remain in the TBI, which are listed in Table 3.3. The beams are distinguished based on their absolute frequency. All remaining ghost beams are caused by backreflections of the fibers or fiber interfaces. Not included are polarizing effects, meaning that the Faraday rotator and the polarizing beam splitter in the FBBL, pbs5, are not considered in the IfoCAD simulation. Their influence on the ghost beam suppression is therefore not included and the power budget listed in Table 3.3 are expected being lower than declared. For the optical simulation we assume a fiber backscattering of 20 ppm. The phase errors for the worst case scenario, based

**Tab. 3.3.:** Residual ghost beam powers in the TBI calculated for a fiber backscatter of 20 ppm. The beam powers on each photodiode (pd) are estimated using IfoCAD. The polarizing beam splitter in the FBBL and the Faraday rotator provide an additional ghost beam power suppression which is not yet included in this table.

PD	beam	frequency	power [mW]	description
pd3/4 (DFBL)	TX	$f_1$ (TX)	0.99	signal's reference beam
	DFBL	$f_2$ (TX')	0.17	signal's measurement beam
	TX	$f_1$ (TX)	$4.94 \cdot 10^{-6}$	SLB from fios2 (DFBL)
	DFBL	$f_2$ (TX')	$\ll 1.35 \cdot 10^{-10}$	SLB from fios1 (TX), Faraday not incl.
	FBBL	$f_2$ (TX')	$\ll 1.92 \cdot 10^{-10}$	SLB from fios1 (TX) via FBBL, Faraday not incl.
pd5/6 (FSFBL)	TX	$f_1$ (TX)	1.98	signal's reference beam
	FSFBL	$f_4$ (ALO')	0.35	signal's measurement beam
	FSFBL	$f_4$ (ALO')	$2.16 \cdot 10^{-14}$	2nd order SLB from fios4 & fios3 (ALO & FSFBL)
	DFBL	$f_2$ (TX')	$\ll 2.69 \cdot 10^{-10}$	SLB from fios1 (TX), Faraday not incl.
	FBBL	$f_2$ (TX')	$\ll 3.84 \cdot 10^{-10}$	SLB from fios1' (TX') via FBBL, Faraday not incl.
	ALO	$f_3$ (ALO)	$9.91 \cdot 10^{-6}$	SLB from fios3 (FSFBL)
pd7/8 (REF)	TX	$f_1$ (TX)	1.98	signal's reference beam
	ALO	$f_3$ (ALO)	1.99	signal's measurement beam
	DFBL	$f_2$ (TX')	$\ll 2.69 \cdot 10^{-10}$	SLB from fios1 (TX), Faraday not incl.
	FSFBL	$f_4$ (ALO')	$4.34 \cdot 10^{-9}$	SLB from fios4 (ALO)
	FBBL	$f_2$ (TX')	$\ll 3.84 \cdot 10^{-10}$	SLB from fios1' (TX') via FBBL, Faraday not incl.
qpd1/pd9 (FBBL)	TX	$f_1$ (TX)	0.99	signal's reference beam
	FBBL	$f_2$ (TX')	0.99	signal's measurement beam
	FBBL'	$f_1$ (TX)	$\ll 4.80 \cdot 10^{-11}$	SLB from fios1' (TX'), Faraday & FBBL pol. not incl.
	FBBL	$f_2$ (TX')	$\ll 1.92 \cdot 10^{-10}$	SLB from fios1 (TX), Faraday & FBBL pol. not incl.
	DFBL	$f_2$ (TX')	$\ll 1.34 \cdot 10^{-10}$	SLB from fios1 (TX), Faraday not incl.
	DFBL'	$f_1$ (TX)	$\ll 3.37 \cdot 10^{-11}$	SLB from fios1' (TX') via FBBL, Faraday not incl.

on Equation (2.7), are shown, and some of them are highlighted, which will be discussed in the following.

The direct fiber backlink is disturbed by a ghost beam from the TX laser that is reflected by the DFBL fiber and its interface (highlighted red in Table 3.3). The phase error produced by this ghost beam is on the order of  $2 \cdot 10^{-3}$  rad. Since no further suppression methods can be used for this ghost beam this will be the dominating noise source. A fiber length stabilization, suppressing the ghost beam dynamics, could improve the phase performance such that the requirement could be achieved. However, the post-correction method balanced detection can also be applied for the DFBL.

The second critical ghost beam occurs in the free-beam backlink due to two fiber backscatter actions, first from the ALO fiber and then the same beam is again backreflected by the FSFBL fiber (highlighted green in Table 3.3). The estimated phase error is  $\varphi_{\text{err}} = 5 \cdot 10^{-7}$  rad, which meets the requirement of  $6 \mu\text{rad}$ . Here, one should note that an attenuation of 95 % is already included in this calculation. Frequency dependent noise projection is not possible without detailed knowledge about the phase dynamics of the signal and ghost beam. Since this ghost beam travels collinear to its nominal beam having the same frequency it only affects the nominal beam's amplitude and phase and does not interfere with it to a spurious signal having the critical beat note. Since this ghost beam enters the photodetector by the same port as its nominal beam at the same frequency, it might influence the measurement and cannot be subtracted via balanced detection.

For remaining ghost beams of  $2 \cdot 10^{-10}$  mW laser power, (e.g. the ghost beam that is highlighted blue), the phase error of  $3 \cdot 10^{-5}$  rad is above the requirement. Therefore, the Faraday rotator must attenuate the ghost beam power by two orders of magnitude to achieve a further phase error suppression of one order of magnitude. The extinction ratios of the TBI Faraday rotators have been measured and showed a sufficient suppression [Win17]. Other ghost beams have a different frequency such that they do not disturb the phase measurement.

### 3.5 Tilt-to-length coupling

The TTL coupling to be expected in the TBI is analyzed on the basis of simulation results gained for the FBBL. Here, the left actuator mirror (AML) was rotated once horizontally (yaw,  $\Psi$ ), and once vertically (pitch,  $\Theta$ ), by  $\pm 150 \mu\text{rad}$  to simulate a beam tilt in the FBBL interferometers. Simulations have shown that similar results are also achieved for the other interferometers, by inducing beam tilts at equivalent positions. For the sake of simplicity, only the results of one backlink interferometer, the FBBL, are shown. The optical pathlength is calculated for two QPDs, one on the left bench and the other one on the right. Due to the



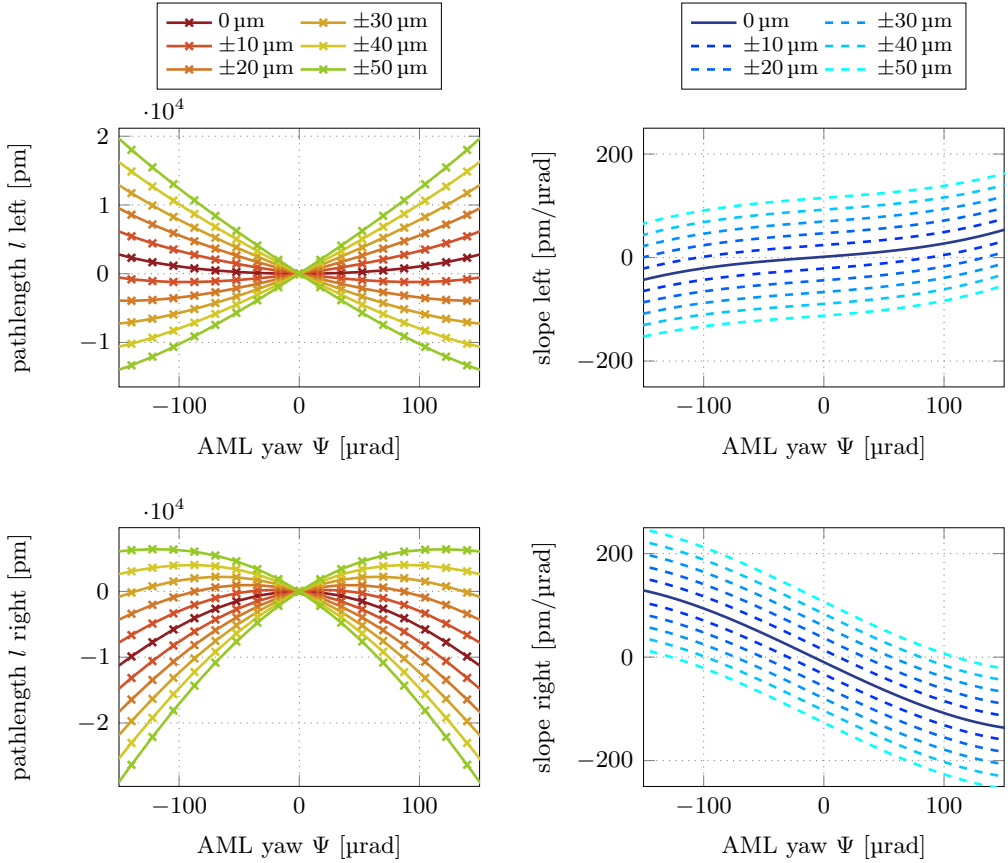


**Fig. 3.2.:** Horizontal pathlength signal of the TBI, left and right QPD for  $\pm 150$   $\mu$ rad tilt of the AML. With focusing lens having a focal length of  $f = 25.4$  mm, placed in 21 mm distance to the QPD. The recombination beam splitter of the FBBL, BS8, was misaligned laterally by  $\Delta_{BS8}$  in 10  $\mu$ m steps.

mirror-symmetry of the two optical benches, the simulation shows identical results for a rotation of only the right actuator mirror (AMR), the only exception given by a permuted QPD signal response. In front of the QPDs lenses with  $f = 25.4$  mm focal length are installed in a distance of 21 mm with respect to the photodiodes. To calibrate the longitudinal pathlength data an absolute value has been subtracted for each measurement such that the longitudinal pathlength crosses the x-axis for  $0^\circ$  beam tilt.

Figure 3.2 shows the resulting pathlength signals on both QPDs while the left actuator mirror is tilted horizontally by  $-150$  to  $150$   $\mu$ rad. The various plots show results for different interferometer misalignments. For this, the recombination beam splitters, BS8 and BS8', of the two interferometers, FBBL and FBBL', are shifted

each in lateral direction from 0 to  $\pm 50 \mu\text{m}$ . For a perfectly aligned interferometer the trend of the simulated pathlength noise over the induced tilt angle is shown in the two plots by the dark red curve. A polynomial model of fourth order is used to fit the data. By increasing the misalignment of the beam splitter up to  $50 \mu\text{m}$  only the linear part of the polynomial trend is enhanced by almost four orders of magnitude for both detectors, from  $0.012 \text{ pm}/\mu\text{rad}$  to  $110 \text{ pm}/\mu\text{rad}$ . For both QPDs the corresponding slopes, and therefore the TTL couplings, given by the derivation of the according model, are shown on the right of Figure 3.2. The enhancement of the linear trend, which was observed before, is visible here as an increase of the ordinate-intercept. For small tilt angles between  $\pm 50 \mu\text{rad}$  the slope can be approximated by only a linear trend. For a perfectly aligned interferometer the maximum TTL coupling is  $7 \text{ pm}/\mu\text{rad}$ , on the left (in other words on the local bench), and  $50 \text{ pm}/\mu\text{rad}$ , on the right (the far) bench. With an induced misalignment of  $10 \mu\text{m}$ , an accuracy that is typically achievable during construction, we already reach maximum coupling coefficients of around  $20 \text{ pm}/\mu\text{rad}$  and  $80 \text{ pm}/\mu\text{rad}$ , while the distant detector shows a worse coupling, validating the expectation that the TTL coupling depends on the absolute pathlength between tilt point and detector. The beam tilt noise requirement concerning the FIOSs to achieve a displacement stability of  $1 \text{ pm}/\sqrt{\text{Hz}}$  can be derived from these values and is  $50 \text{ nrad}/\sqrt{\text{Hz}}$  for  $20 \text{ pm}/\mu\text{rad}$ , and  $12.5 \text{ nrad}/\sqrt{\text{Hz}}$  assuming a worst case of  $80 \text{ pm}/\mu\text{rad}$  TTL coupling. In dependency on the actual, absolute pathlength and the static misalignment of the individual TBI interferometers the coupling could even be larger. However, since the FBBL interferometer contains the largest optical pathlength these results may already show an upper limit of the TTL coupling that should be expected in each measurement performed with the TBI.

For the estimation of the vertical TTL coupling in the TBI the AML is tilted along its pitch angle by  $\pm 150 \mu\text{rad}$ , static misalignments between  $0 \mu\text{rad}$  and  $50 \mu\text{rad}$  are induced by vertical tilts of recombination beam splitters BS8 and BS8'. Figure 3.3 shows the equivalent pathlength signals on the two QPDs, on the left and right bench. A polynomial function of fourth order is used to fit the data. The corresponding slope is derived from the model and extrapolates the expected TTL coupling, the plots are shown on the right of Figure 3.3. A similar behavior as already shown for the horizontal TTL coupling is also observed here. The shape of the model stays constant, only the linear part changes and produces a shift of the slope along the ordinate of at most  $16 \text{ pm}/\mu\text{rad}$ , which is equivalent to a beam noise requirement of  $62 \text{ nrad}/\sqrt{\text{Hz}}$  (for  $50 \mu\text{rad}$  misalignment). However, the overall TTL coupling is almost one order of magnitude below the coupling that was simulated for the horizontal case. Even though the FIOS constraints concerning vertical beam pointing fluctuations are relaxed in comparison to the horizontal TTL coupling, any static vertical misalignment introduced by bonding

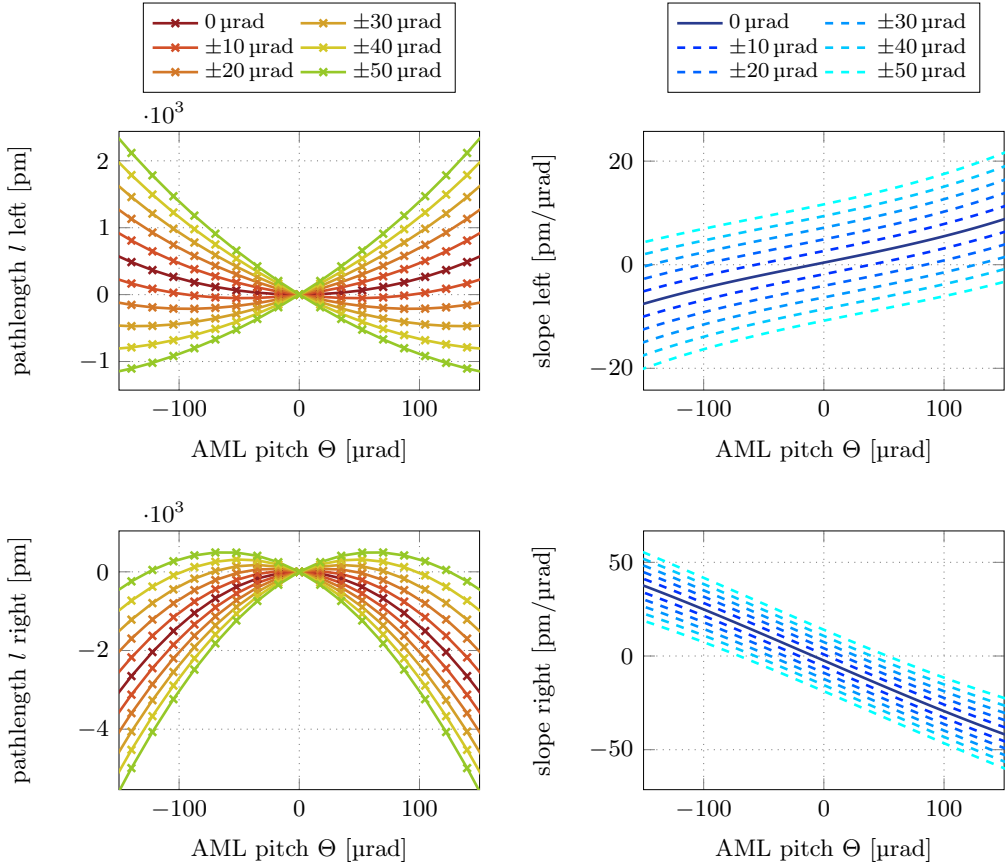


**Fig. 3.3.:** Vertical pathlength signal of the TBI, left and right QPD for  $\pm 150 \mu\text{rad}$  tilt of the AML. With focusing lens having a focal length of  $f = 25.4 \text{ mm}$ , placed in  $21 \text{ mm}$  distance to the QPD. The recombination beam splitter of the FBBL, BS8, was tilted vertically by  $\Delta_{\text{BS8}}$  in  $10 \mu\text{rad}$  steps.

components cannot be compensated for afterwards. These components have typically a perpendicularity between optical surface and ground surface that is better than  $2''$ , which is equivalent to  $10 \mu\text{rad}$ . For this case of misalignment the expected TTL coupling in the range from  $-50 \mu\text{rad}$  to  $50 \mu\text{rad}$  is about  $4 \text{ pm}/\mu\text{rad}$  on the left bench and below  $20 \text{ pm}/\mu\text{rad}$  on the right bench. The expected TTL coupling due to vertical misalignment is expected to be a factor of four below the horizontal TTL coupling and therefore negligible, if one assumes that the beam pointing fluctuations caused by FIOS jitter or residual steering mirror noise are similar for both directions.

## 3.6 Free-beam backlink

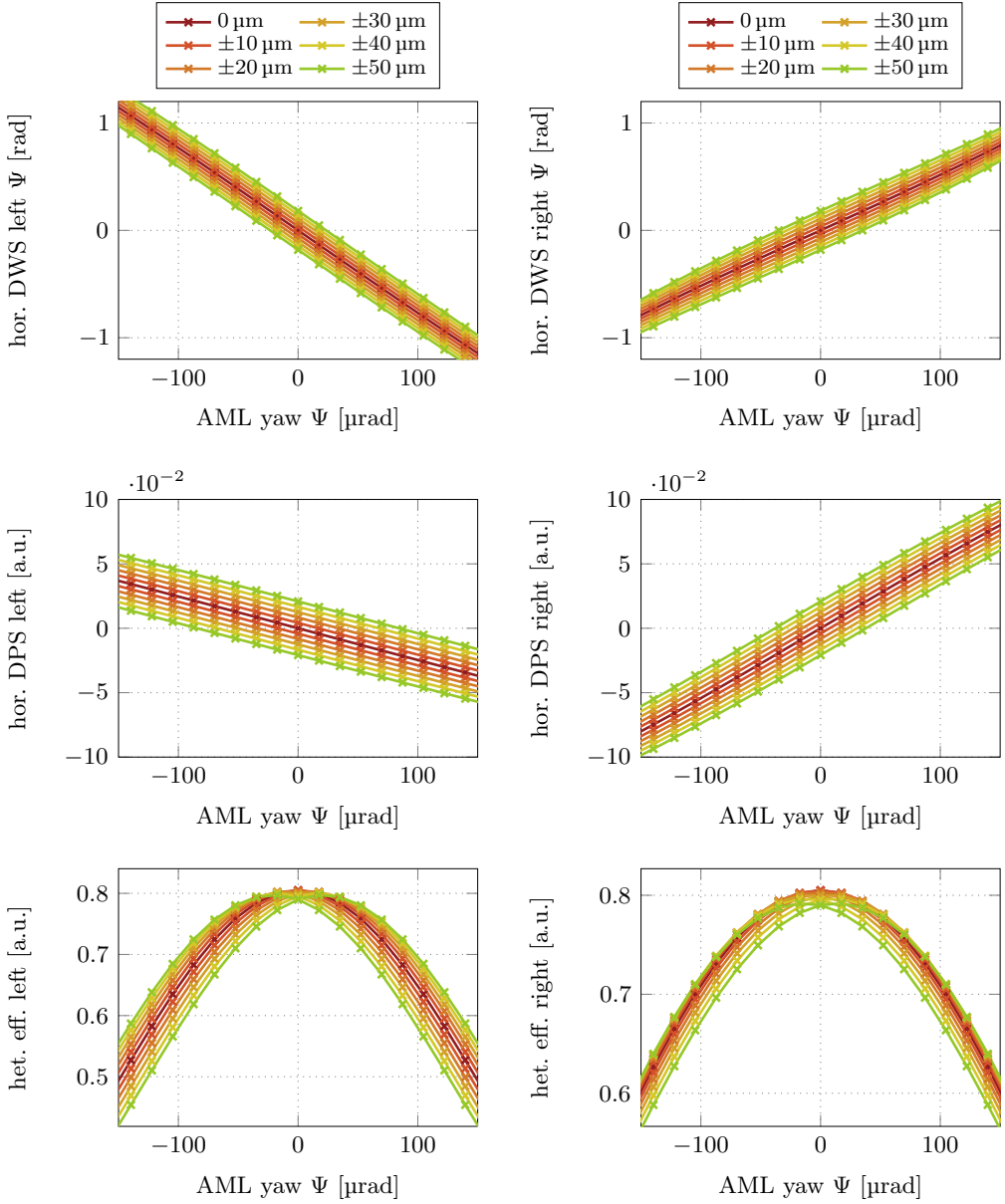
The implementation of the FBBL in the TBI requires additional support from two steering mirrors, AML and AMR, that are compensating the bench rotation. Results from IfoCAD simulations help to predict the detector signals on the QPDs. The expected pathlength noise is estimated for the free-beam link and a DWS noise requirement for the control loops can be approximated from these results. The coupling coefficients are derived from the DWS signals for both steering mirrors and each axes, horizontal and vertical. The decoupling of the two coupled control loop systems can be optimized with imaging systems, or simply lenses.

### 3.6.1 Pathlength noise

The simulation results from the latter Section 3.5 are used to determine the pathlength noise that is caused by the actuation of the free-beam link. The free-beam backlink uses two actuator tip-tilt mirrors to compensate the beam pointing of incoming and outgoing beam that is caused by the bench rotation. The actuator mirrors can only be actuated in two degrees of freedom (DoF), namely horizontal and vertical, for compensating the rotation and a possible wobble caused by the rotary stages. The simulation of baseplate rotations around each center reveals a pathlength change of 17.2 mm for a rotation of  $1.5^\circ$ . The DWS signals calculated by IfoCAD indicate that a decoupling of the remote and far steering mirror tilt-sensing, which is crucial for establishing closed-loop control, can be realized by simply placing the focusing lenses in front of the QPDs. For a misalignment of  $\Delta_{BS8} = 10 \mu\text{rad}$  the coupling from steering mirror angle into interferometric pathlength is  $20 \text{ pm}/\mu\text{rad}$ , according to the results shown in Figure 3.2, resulting in a beam tilt noise requirement of  $50 \text{ nrad}/\sqrt{\text{Hz}}$ . Assuming a DWS coupling coefficient of  $4000 \text{ rad}/\text{rad}$  (see the following sections) this results in a DWS noise requirement of  $0.2 \text{ mrad}/\sqrt{\text{Hz}}$ . A static misalignment and the stability of the photodiode assemblies might also influence the pathlength noise. By re-adjusting the lenses the couplings can be reduced. Post-corrections can also be applied in case of insufficient closed-loop suppression of the steering mirror control if the DWS sensing noise is below the requirement.

### 3.6.2 Optical signals

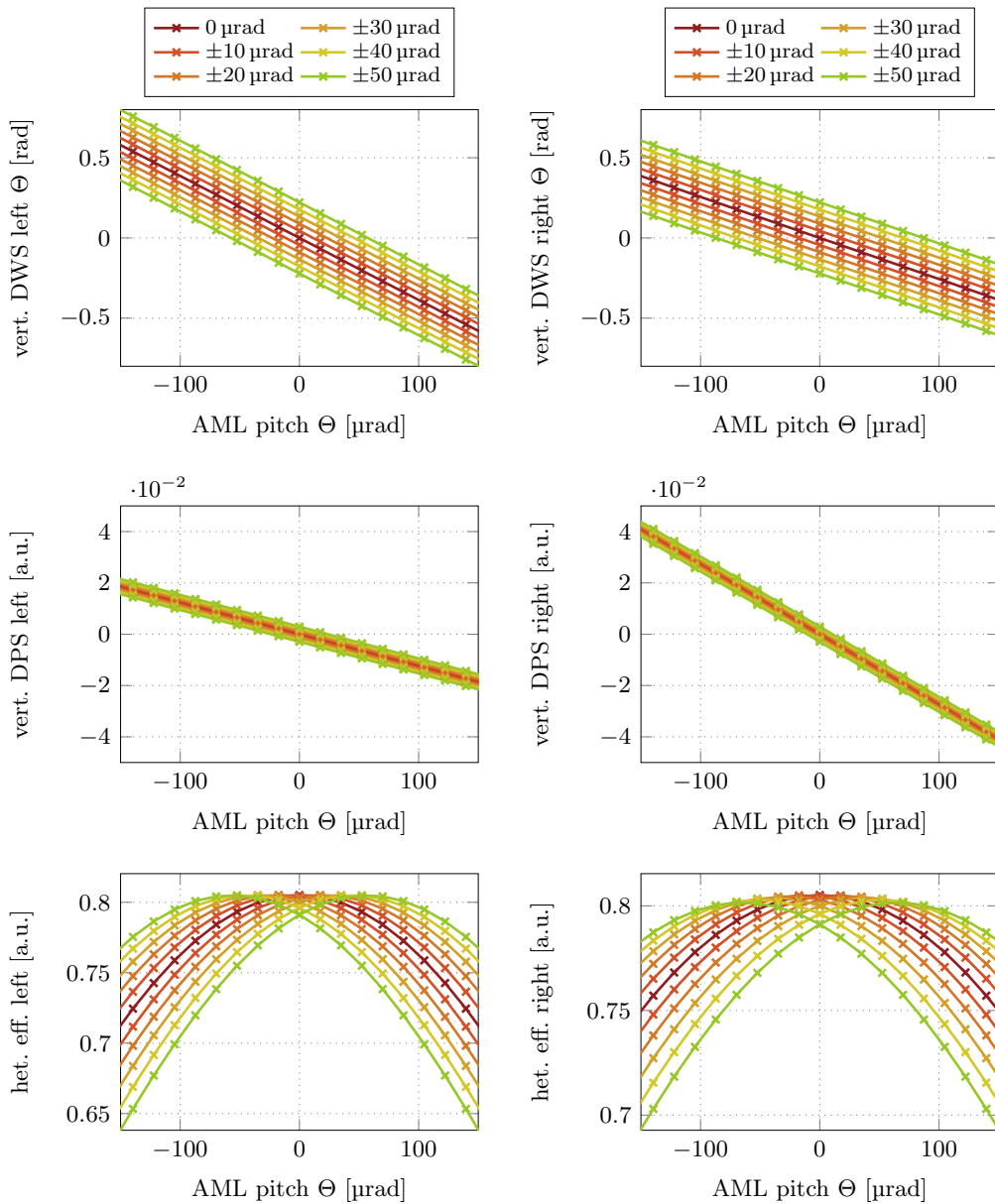
The actuation of the free-beam link requires in total four feedback loops to control each mirror in both axes. Two QPDs, one per bench, are used as sensor. Since each sensor detects the motion of both steering mirrors, the two horizontal control loops, and the two vertical ones respectively, are coupled with each other. Figure 3.4 shows the photodiode response for the left and right QPD by tilting the steering



(a) Horizontal DPS, DWS and heterodyne efficiency on the left QPD.

(b) Horizontal DPS, DWS and heterodyne efficiency on the right QPD.

**Fig. 3.4.:** Signals of the TBI, left and right QPD for  $\pm 150 \mu\text{rad}$  horizontal tilt of the AML. With focusing lenses having a focal length of  $f = 25.4 \text{ mm}$ , placed in  $21 \text{ mm}$  distance to the QPD. The recombination beam splitters of the FBBL, BS8 and BS8', were shifted laterally by  $\Delta_{\text{BS8}}$  in  $10 \mu\text{m}$  steps.



(a) Vertical DPS, DWS and heterodyne efficiency on the left QPD.

(b) Vertical DPS, DWS and heterodyne efficiency on the right QPD.

**Fig. 3.5.:** Signals of the TBI, left and right QPD for  $\pm 150 \mu\text{rad}$  vertical tilt of the AML. With focusing lenses having a focal length of  $f = 25.4 \text{ mm}$ , placed in 21 mm distance to the QPD. The recombination beam splitters of the FBBL, BS8 and BS8', were tilted vertically by  $\Delta_{\text{BS8}}$  in 10  $\mu\text{rad}$  steps.

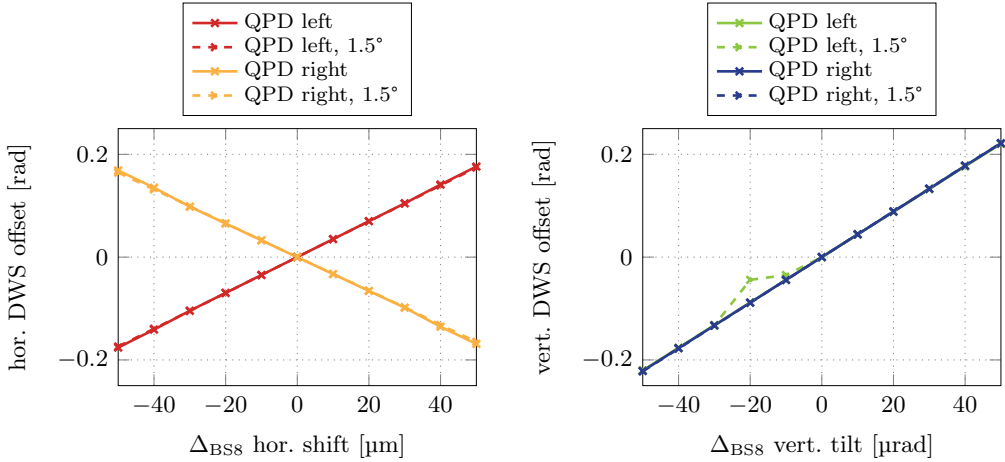


Fig. 3.6.: DWS offsets for horizontal and vertical QPD signals that are caused by component misalignments. The plots shown here are based on the DWS simulation results from Figures 3.4 and 3.5.

mirror AML horizontally. Similar results are shown for an induced vertical tilt in Figure 3.5. Plotted are the signals of DWS, DPS and heterodyne efficiency over the mirror motion of  $\pm 150 \mu\text{rad}$ . Each signal shows a significant dependency on the mirror tilt and is therefore a candidate to be used as error signal for the control loops. The heterodyne efficiency drops only by a factor of two, from around 80 % down to 40 %, and the dependency shows a quadratic behavior which excludes this signal from being used as error signal. Both, the DWS and DPS response show a linear trend with zero-crossing which is why they are both useable as error signal. As indicated by the results shown in Figures 3.4 and 3.5 the DWS signal has a higher gain factor in comparison to the DPS signal. The DPS sensing gain for 2 mW optical power on the QPD is  $0.49 \mu\text{W}/\mu\text{rad}$  for the left, and  $1.06 \mu\text{W}/\mu\text{rad}$  for the right bench. To reach a  $1 \mu\text{rad}/\sqrt{\text{Hz}}$  sensor noise, relative optical amplitude changes on the order of  $2.45 \cdot 10^{-4}$  must be detected. Therefore, the absolute amplitudes of the individual beams must also be stable enough within this order of magnitude. In comparison to this, the DWS signal has a high gain factor of more than 5000 rad/rad to convert the measured DWS phase into an optical phase. Therefore, a measurable DWS accuracy of 5 mrad is sufficient for achieving a sensor noise level of  $1 \mu\text{rad}/\sqrt{\text{Hz}}$ .

Both signals, DWS and DPS in Figures 3.4 and 3.5, show a non-negligible influence if a static misalignment is applied on one of the interferometer components. This is implemented in the simulation by adding lateral shifts up to  $\pm 50 \mu\text{m}$  to the positions of the recombination beam splitters of the FBBL, BS8 and BS8', for

analyzing the horizontal dependency. Vertical tilts up to  $\pm 50 \mu\text{rad}$  are applied to the same components for estimating the vertical dependency. The assembly of lens and photodiode is re-adjusted after misalignment with respect to one of the interfering beams. Figures 3.4 and 3.5 show that the slope of the linear trends, also referred to as coupling factor, is barely influenced in either of the two directions, whereas an offset shifts the linear trend along the ordinate. The amount of offset depends linearly on the misalignment, as shown in Figure 3.6, and leads to DWS, or DPS, signals whose zero-crossing is not anymore at the initial mirror orientation of  $0 \mu\text{rad}$ . Depending on the amount of misalignment the locking point of the control loop would be influenced in this way. A typically achievable positioning accuracy of  $10 \mu\text{m}$ , or  $10 \mu\text{rad}$ , would cause an offset error of  $35 \text{mrad}$  in the horizontal DWS signal and about  $44 \text{mrad}$  in the vertical axis. Including a bench rotation of  $-1.5^\circ$  to the left set-up and  $1.5^\circ$  to the right set-up the DWS and DPS signals do not change significantly, neither do their offsets.

### 3.6.3 DWS coupling coefficients of the free-beam

From the simulation results given in the previous section, the DWS coupling coefficients for the free-beam control loop can be calculated by determining the slope of the DWS plots shown in Figures 3.4 and 3.5. The relation between horizontal (yaw) DWS signals,  $\Psi_{\text{DWS}}$ , and a horizontal mirror motion is given by the following equation,

$$\begin{pmatrix} \Psi_{\text{DWS, left}} \\ \Psi_{\text{DWS, right}} \end{pmatrix} = \underbrace{\begin{pmatrix} K1_{\Psi\Psi} & K2_{\Psi\Psi} \\ K3_{\Psi\Psi} & K4_{\Psi\Psi} \end{pmatrix}}_{K_{\Psi\Psi}} \cdot \begin{pmatrix} \Psi_{\text{AML}} \\ \Psi_{\text{AMR}} \end{pmatrix}, \quad (3.5)$$

and equivalently for the vertical (pitch) DWS signals and a vertical mirror motion,

$$\begin{pmatrix} \Theta_{\text{DWS, left}} \\ \Theta_{\text{DWS, right}} \end{pmatrix} = \underbrace{\begin{pmatrix} K1_{\Theta\Theta} & K2_{\Theta\Theta} \\ K3_{\Theta\Theta} & K4_{\Theta\Theta} \end{pmatrix}}_{K_{\Theta\Theta}} \cdot \begin{pmatrix} \Theta_{\text{AML}} \\ \Theta_{\text{AMR}} \end{pmatrix}. \quad (3.6)$$

Here,  $\Psi_{\text{AML}}$  and  $\Psi_{\text{AMR}}$  are the horizontal tilt for the left and right actuator mirror, called AML and AMR, and, analogously,  $\Theta_{\text{AML}}$  and  $\Theta_{\text{AMR}}$  are the vertical tilt of AML and AMR. The coupling of mirror tilt into DWS signal is described by the matrices  $K_{\Psi\Psi}$  and  $K_{\Theta\Theta}$ , for horizontal and vertical direction. Here, we assume no significant cross-coupling between vertical and horizontal tilts and DWS signals.



In order to implement a control scheme for the free-beam backlink, Equations (3.5) and (3.6) need to be solved for the vectors  $(\Psi_{\text{AML}}, \Psi_{\text{AMR}})$ ,

$$\begin{pmatrix} \Psi_{\text{AML}} \\ \Psi_{\text{AMR}} \end{pmatrix} = \frac{1}{\det(K_{\Psi\Psi})} \begin{pmatrix} K4_{\Psi\Psi} & -K3_{\Psi\Psi} \\ -K2_{\Psi\Psi} & K1_{\Psi\Psi} \end{pmatrix} \cdot \begin{pmatrix} \Psi_{\text{DWS,left}} \\ \Psi_{\text{DWS,right}} \end{pmatrix}, \quad (3.7)$$

and  $(\Theta_{\text{AML}}, \Theta_{\text{AMR}})$ ,

$$\begin{pmatrix} \Theta_{\text{AML}} \\ \Theta_{\text{AMR}} \end{pmatrix} = \frac{1}{\det(K_{\Theta\Theta})} \begin{pmatrix} K4_{\Theta\Theta} & -K3_{\Theta\Theta} \\ -K2_{\Theta\Theta} & K1_{\Theta\Theta} \end{pmatrix} \cdot \begin{pmatrix} \Theta_{\text{DWS,left}} \\ \Theta_{\text{DWS,right}} \end{pmatrix}. \quad (3.8)$$

Thus the coupling matrices are required to be invertible and, beyond that, well-conditioned. A diagonal matrix represents a completely decoupled control system but is not achievable in experimental set-ups. The so-called condition number of a matrix can be used to determine the quality of specific coupling matrices. This number measures how much an output value of a system, here the DWS signal in the feedback control loop, can change for a small change in the input arguments, meaning the actuation of the mirrors. It directly delivers information about how sensitive the system is to changes or disturbances in the input. For a normal matrix  $K$  the condition number can be calculated by

$$\text{cond}(K) \geq \frac{\|\lambda_{\max}(K)\|}{\|\lambda_{\min}(K)\|} \quad (3.9)$$

where  $\lambda_{\max}$  and  $\lambda_{\min}$  are the largest and smallest eigenvalues of  $K$ . If  $K$  is unitary, the condition number is 1 and the system is optimally conditioned [CF88]. The ratio of two coupling coefficients,

$$\text{decpl}(K) = \frac{|k_{ii}|}{|k_{ij}|} \quad (3.10)$$

can be used as approximation to determine the decoupling factor of the system. Here,  $k_{ii}$  are the diagonal entries of  $K$ ,  $k_{ij}$  are the off-diagonal ones. This factor increases for well-conditioned systems and is therefore inversely proportional to the condition number.

For the TBI first simulations have shown that the condition number of the system for the FBBL control loop of the horizontal direction is about 15.0, which is equivalent to a decoupling factor of about 1.1. A simple decoupling can already be achieved due to the implementation of different lever arms through which the beam is propagating towards the two QPDs on the left and right bench. With the current optical layout, as shown in Figure 3.1, we already achieve condition numbers of 5.2 and 5.7 for the horizontal,  $K_{\Psi\Psi}$ , and vertical,  $K_{\Theta\Theta}$ , system. By

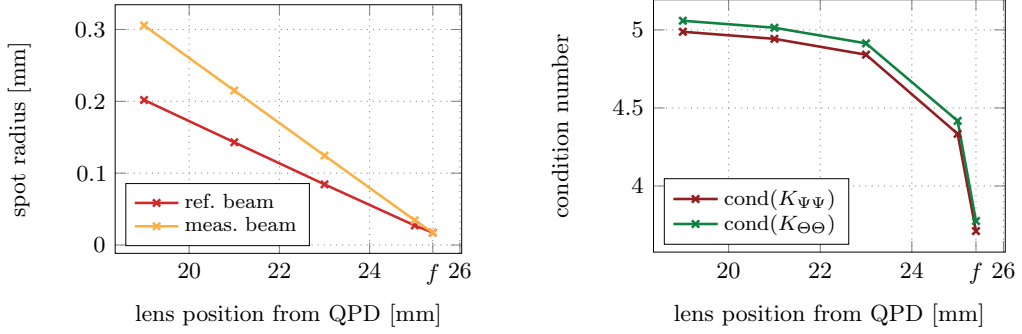


Fig. 3.7.: Influence of the focusing lens position with respect to the QPD position in the FBBL of the TBI. Shown are the achievable spot size radii of measurement (meas.) and reference (ref.) beam on the left QPD and the condition numbers for the horizontal,  $K_{\Psi\Psi}$ , and vertical,  $K_{\Theta\Theta}$ , coupling matrices.

simply inserting lenses (with 25.4 mm focal length) in front of the QPDs, which are required anyhow to achieve an adequate spot size on the small active area of the QPD (1 mm diameter), the decoupling of the system can be further influenced.

Simulation results, showing the achievable spot size radii and condition numbers, are demonstrated in Figure 3.7 for various lens positions. The lens position is measured relatively to the QPD position. One can conclude from these plots that the smaller the spot size the larger is the decoupling factor, therefore a minimum condition number of about 3.7 is achieved if the QPD is positioned in the focal length of the lens,  $f = 25.4$  mm. But the resulting spot size radii of about  $17\ \mu\text{m}$  are too small with regard to the gap size between the QPD segments of about 10 to  $20\ \mu\text{m}$ . Typically a distance of about 21 mm is desired to achieve spot size radii on the order of 0.21 mm and 0.14 mm, depending on the different arm lengths. For this constellation a horizontal condition number of  $\text{cond}(K_{\Psi\Psi}) = 4.9427$ , and a vertical condition number of  $\text{cond}(K_{\Theta\Theta}) = 5.0138$ , can be achieved. The system is therefore improved by 5% (horizontal) and 12% (vertical) in comparison to the TBI without lenses. Additionally, the usage of focusing lenses as decoupling mechanism for the FBBL shows no significant dependency on the actual bench orientation, which is advantageous for our application. The coupling coefficients and the resulting condition number of the horizontal DWS signal were simulated for different bench rotations from  $0^\circ$  to  $1.5^\circ$ . The left set-up was rotated in negative direction, while the right bench is counter-rotating in the opposite, positive direction. Thus, the absolute angle between the two benches changes from 0 to  $3.0^\circ$ . The horizontal coupling coefficients of  $K_{\Psi\Psi}$  only change by at most 1.6%, the vertical coupling coefficients of  $K_{\Theta\Theta}$  change by only 1.5% maximum for this amount of bench rotation. Thus the maximum deviation in the condition number is about 5%,

measured in the horizontal DWS signal. These coupling fluctuations in dependency on the bench rotation are tolerable for our application, but other effects, like misalignment in real set-ups, could reduce the decoupling. But as indicated before even a static misalignment induced at one of the interferometer components does not change the slope of the DWS signals significantly, as shown in Figures 3.4 for yaw and in Figure 3.5 for pitch angles. The effect of a misalignment included in the simulation, induced at beam splitter BS8, is much smaller than the one caused by bench rotation and can therefore be neglected. Even though the fluctuations could be enhanced in an experimental set-up due to some unknown effects, the actual coupling coefficients can be measured for various bench orientations and are then used to calibrate and optimize the system. In the end, we expect to measure coupling coefficients on the order of 7600 rad/rad and 5200 rad/rad for the horizontal direction, and 3900 rad/rad and 2600 rad/rad for the vertical one.

### 3.7 Three-Backlink construction plan

The TBI will be constructed on two optical benches made of the glass ceramic Clearceram HS that has a very low coefficient of thermal expansion (CTE) ( $1 \cdot 10^{-8}/\text{K}$ ). The optical components will be installed to the glass plate by adhesive-bonding with an ultra-violet (UV) epoxy Optocast 3553-LV-UTF, which leads to a quasi-monolithic set-up that has a high temperature insensitivity and therefore meets the desired interferometric stability [Sch+09; Deh+12]. Other bonding techniques, like hydroxide catalysis bonding or optical contacting, provide optical set-ups that are potentially even more stable, but the construction process however is more challenging, stressful and time consuming, which is why we decided to use adhesive bonding for experiments on ground, but hydroxide catalysis bonding for space applications. The components on the optical bench are specifically manufactured with optical surfaces, having a perpendicularity of better than  $2''$ , such that an adequate vertical alignment is ensured.

#### 3.7.1 Template

From the IfoCAD simulations the exact position and orientation of each component on the two optical benches can be extracted (see Tables A.2 and A.3 in the Appendix). The corner points of each one is written into data files, as well as the positions for bearing balls, by which the components will later be positioned. These data points are imported into AutoDesk Inventor and a template is constructed around them. Figure 3.8 shows the Inventor model of the template on top of the left bench of the TBI. The 3D model of the optical bench is generated by running a Python script on the IfoCAD-viewer output file by which a FreeCAD model is

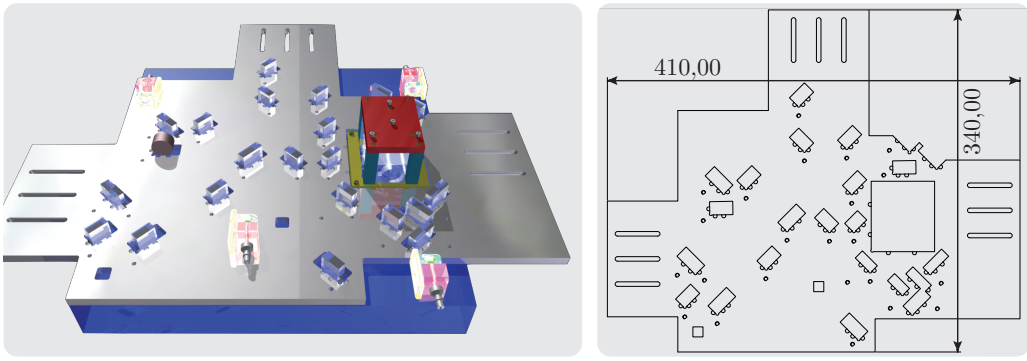


Fig. 3.8.: One bench of the TBI is shown on the left as 3D CAD model. The template drawing is shown on the right.

created which can then be imported into the AutoDesk Inventor project. Here, we use a 6 mm aluminum plate 410 mm  $\times$  340 mm as template with pockets for each component, holding slots and holes for bearing balls. With these precise positioning spheres, having a diameter of 4 mm, the components can be adjusted via Three-Point adjustment within the template pockets. Some threaded holes are distributed all over the template where posts can be mounted. An elastic band around a post and the optical component holds the component with a small amount of force in its position while the glue is cured. The template is precision-milled by an external manufacturer, called PROTLABS. The accuracy ensured by the manufacturer is below 100  $\mu\text{m}$ , but expected to be around a few 10  $\mu\text{m}$ .

Only uncritical components will be bonded by means of the template. For recombining beam splitters, fiber coupling and fiber injection higher positioning accuracies are necessary which can be achieved by other techniques, like using a beam measurement technique that was developed in-house and uses the coordinate measurement machine (CMM) and a QPD as sensor [Sch+14b]. The template design is based on the construction plan, which is demonstrated in the subsequent section, which is why some FIOSs in Figure 3.8 are omitted by the template.

### 3.7.2 Construction order

The construction of the TBI in the cleanroom is subdivided into several, individual steps. The high complexity of the set-up makes the organization challenging. This is why the construction was planned and simulated in advance to ensure that the optical components and FIOSs can be placed and aligned in sequence without blocking the next steps of the construction process. In the following, the plan for the construction in the cleanroom of the left bench is shown. This plan might need modifications due to unforeseen challenges occurring during the construction, some

of which are described in Section 5.2. The optical bench is placed into a box that has micrometer screws by which the baseplate can be shifted or held in its position. The set-up is fixed on the optical bench of the CMM. The IfoCAD beam directions are also required during construction and are listed in Table A.1 (Appendix).

### **1. Template alignment**

The template is installed above the optical bench and fixed to the optical table. The parallelism between the surfaces of optical bench and template is measured with the CMM. With height adjustment screws a tilt of the template can be minimized. Afterwards, the optical bench is aligned with respect to the template by shifting its lateral position with the micrometer screws. According to the Inventor models the relative position between optical bench and template is adjusted. The coordinate system, measured with the CMM by scanning the template sides and the top baseplate surface, serves as reference frame for the following construction steps.

### **2. 1st batch template-assisted positioning. Metal components**

Once the optical bench and template are well-aligned to each other, three metal components are glued with a two-component epoxy to the baseplate by using template-assisted positioning. The components are the mount of the Faraday rotator, and two waveplate mounts, hwp1 and hwp3. The duration for this step is at least 24 h due to the long curing time of the two-component epoxy. This is also the reason why as many components as possible should be glued within one step.

### **3. 2nd batch template-assisted positioning. Optical components**

The first set of optical components can be glued after the epoxy is cured. With template-assisted alignment six optical components are being positioned, without laser light on the optical bench yet. The two attenuation beam splitters for the TX and ALO beam, att1, att2, have a reflectivity of 95%. One mirror, m1, is glued and three polarizing beam splitters, pbs1, pbs4 and pbs5. The curing duration for each component with UV glue is about 3 min. The remaining optical components, slated for template-assisted bonding in step 7, can also be glued in this step. Only the gluing of pbs6, the components that are critical for the interference and some deflection mirrors whose positions are too close to some FIOSs, is not yet allowed.

### **4. Construction of fios1 (TX beam)**

Fios1 is assembled directly on the optical bench. The template is still present on top of the optical bench during this procedure which is why it has notches to provide alignment space for the FIOS construction tool. The propagation

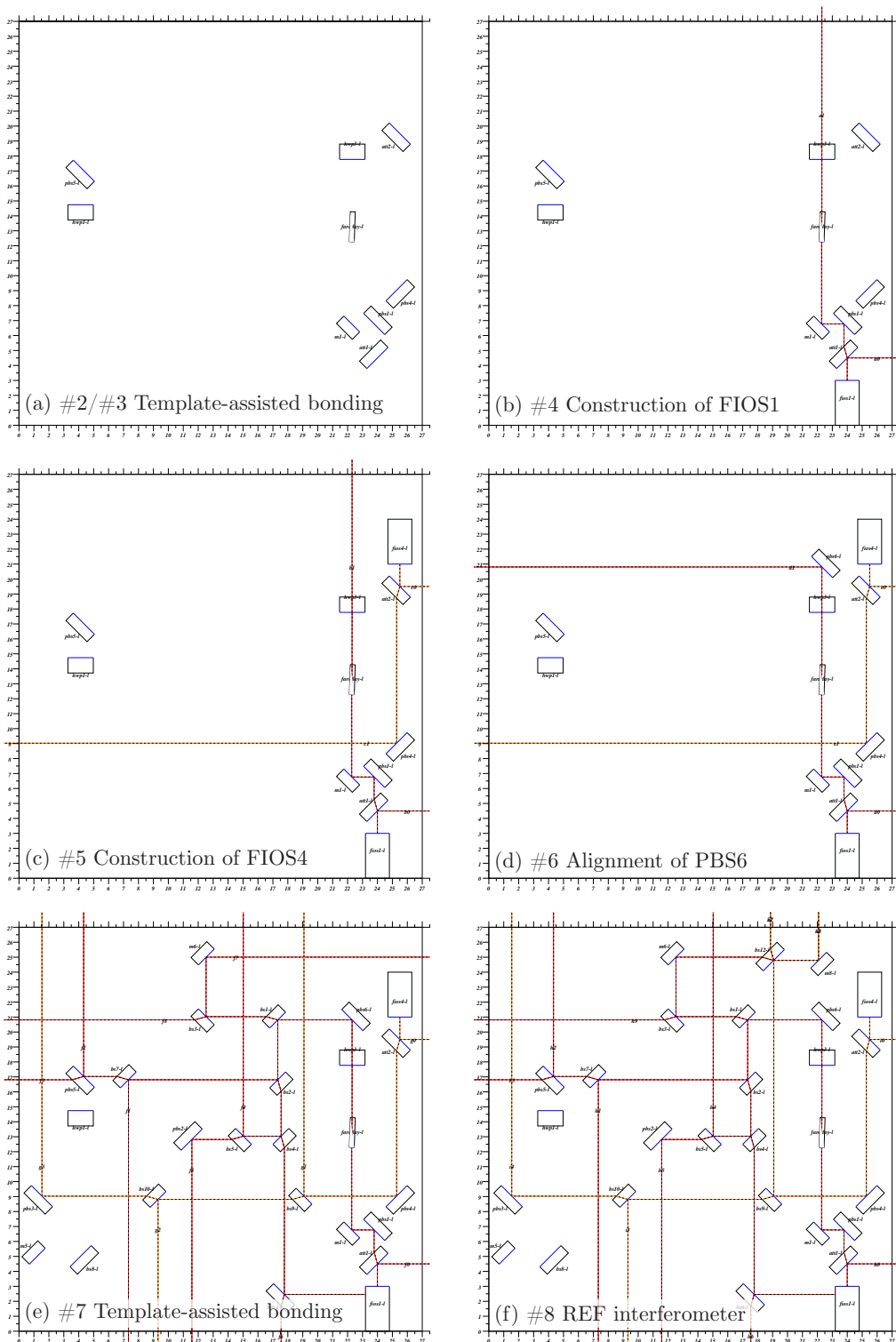


Fig. 3.9.: Steps 2-8 from the construction of the TBI plan.

direction of beam a0, reflected by the first optical component, att1, is measured with the CMM to adjust the FIOS position roughly. Afterwards, it must be ensured that the beam propagates without diffraction through the Faraday crystal. Behind the Faraday the beam profile and propagation height is measured and compared to the simulation results for beam a1. A horizontal tilt of beam a1 can be compensated for later on with pbs6, while a vertical misalignment of the beam, which can be caused by a misalignment of the Faraday crystal inside the housing, cannot be compensated for afterwards. The height of beam a1 is measured over a large distance and adjusted by aligning fios1 and the tilt of the Faraday itself. If the beam propagates in parallel to the optical bench surface within  $<10\ \mu\text{rad}$  and within  $<10\ \mu\text{m}$  around the nominal 15 mm beam height, the Faraday mount is fixed with locking screws and the FIOS is glued.

### **5. Construction of fios4 (ALO beam)**

Fios4, providing the ALO beam on the optical bench, is also constructed directly on the optical bench with the FIOS alignment tool. The template is still attached to the set-up. The beams c0 or c1 are used to determine the beam propagation with the CMM relative to the template. pbs6 is not glued yet, otherwise the FIOS construction tool would not fit into the set-up. After fios4 is properly aligned within  $10\ \mu\text{rad}$  horizontal and vertical tilt, it is glued to the baseplate.

### **6. Alignment of pbs6 via pointing fingers**

Beam d1 is aligned horizontally with respect to the template via the adjustment of the polarizing beam splitter pbs6. This step compensates for any tilt of the TX beam that was caused by passing through the Faraday crystal. pbs6 can be adjusted by using a pointing fingers alignment tool. The beam propagation of d1 is measured with the CMM with respect to the template and should be aligned within  $10\ \mu\text{m}$  and  $10\ \mu\text{m}$ . The component is glued by means of UV epoxy.

### **7. 3rd batch template-assisted positioning**

The remaining, uncritical optical components are glued to the optical bench with template-assisted positioning. Two mirrors (m5, m6), ten beam splitters (bs1 - bs10), and two polarizing beam splitters (pbs2, pbs3), are glued with UV epoxy onto the baseplate. The orientation of each component can be controlled with the TX and ALO beams. The template is removed after this step. The recombination components, bs12, m2, bs11, m4, are placed by means of the pointing fingers, followed by their associated deflection mirrors m8, m3, m7 (see following steps).

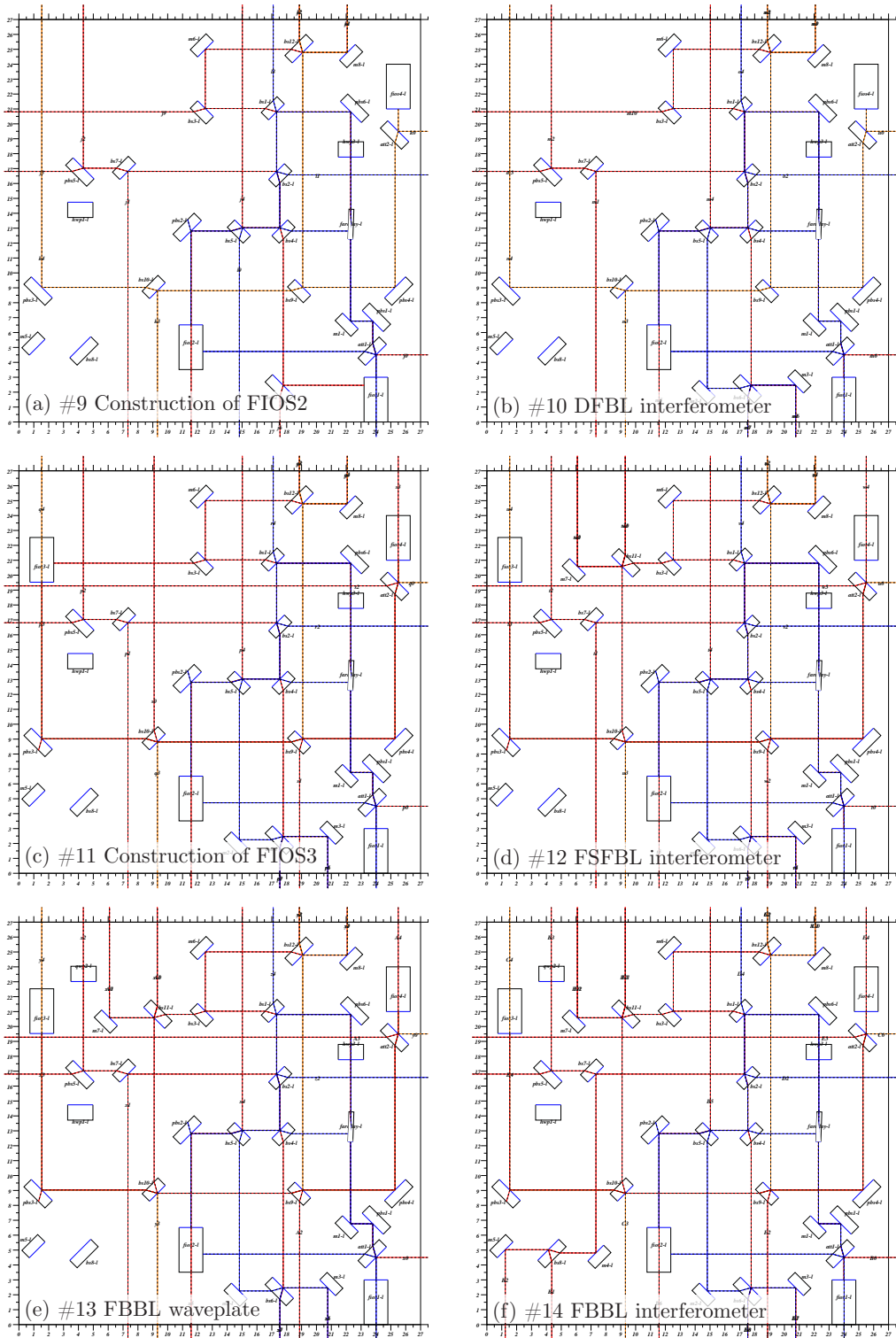


Fig. 3.10.: Steps 9-14 from the construction of the TBI plan.



### **8. Contrast in REF interferometer: alignment of bs12 (and m8)**

The recombining beam splitter bs12 is aligned manually using the pointing fingers alignment tool while monitoring the contrast of the interference signal between TX and ALO. Afterwards the deflection mirror m8 can be placed by hand. This mirror is only used to redirect the interference signal from the second beam splitter output port off of the optical bench.

### **9. Construction of fios2 (DFBL)**

Fios2 is constructed directly on the optical bench. With the construction tool, it is aligned such that most of the TX beam, l0, is coupled into its fiber. Different alignment approaches might be helpful for this step. First, laser light can be guided to fios2 via a fiber connection. The collimated beam is measured on the optical bench and the FIOS can be adjusted by measuring its out-going beam which must show an identical propagation direction as beam l0. Second, the coupling into fios2 can be measured simultaneously. By optimizing the amount of backreflection the coupling efficiency of the TX beam into fios2 can be maximized. The FIOS is then glued with UV epoxy.

### **10. Contrast in DFBL interferometer: alignment of m2**

For the alignment of the DFBL interferometer the mirror m2 is used, since the recombination beam splitter was already glued in batch 3. For this purpose, light from the second path of the laser preparation is sent to fios2. By monitoring the contrast of the interference signal between the out-going light from fios2 and the TX beam m2 is aligned with the pointing fingers assembly. After curing, the deflection mirror m3 can be placed by hand and glued. Mirror m3 could also not be positioned with the template still on due to its close proximity to fios1.

### **11. Construction of fios3 (FSFBL)**

Fios3 is constructed directly on the optical bench. The procedure is identical to the one of fios2, which is described in step 9. The TX beam is again coupled into the fiber and the coupling efficiency is either monitored by the backreflection of the Faraday in the laser preparation or the out-going beam from fios3 is measured with the CMM and compared to beam s0. After achieving a high coupling efficiency the FIOS can be glued.

### **12. Contrast in FSFBL interferometer: alignment of bs11**

For the alignment of the FSFBL interferometer the recombination beam splitter bs11 is adjusted by the pointing fingers assembly. The procedure is similar to the interferometer alignment for the DFBL described in step 10. One beam path from the laser preparation is sent to fios3, the other path is

sent to the ALO output coupler fios4. The contrast of the interference signal between the out-going light from fios3 and the ALO is monitored and the beam splitter bs11 is adjusted according to this signal. After curing bs11, the deflection mirror m7 can be placed by hand and glued.

### 13. Mount for hwp2

With two-component epoxy the mount for hwp2 is glued by hand adjustment on the optical bench. A half-waveplate is inserted into the mount. This step must only be done for one of the two benches, since only one half-waveplate is required for the polarization encoding in the FBBL.

### 14. Contrast in FBBL interferometer. Alignment of BL beam and m4

The alignment of the FBBL interferometer is the most challenging one, since any misalignment in this path produces enhanced TTL coupling in the phase measurements. In addition, a reference beam, simulating the free beam coming from the adjacent bench, must be aligned in advance. For this purpose, the out-going FBBL beam, B3, is coupled into an adjustable fiber collimator which is placed somewhere on the CMM breadboard. A large optical distance is advantageous since the beam propagation direction can be measured with higher accuracy along longer beam paths. The second beam path of the laser preparation is connected via fiber to the adjustable fiber collimator. With the CMM, the direction of the in-bound and out-bound light from the adjustable fiber collimator is measured. By adjusting the fiber collimator the out-bound light is aligned collinearly to beam B3, but traveling in opposite direction. The half-waveplate hwp2 rotates the polarization of the light coming from the fiber collimator to p-polarization such that it is transmitted by the polarizing beam splitter pbs5. The beam directions of B1 and B2 can also be measured as reference for the beam direction after pbs5, and in addition the amount of backreflection from the Faraday in the laser preparation shows how much light is actually coupled in by the TX beam. The interferometer alignment is done by mirror m4. Since the interferometer must be aligned with high accuracy, the detection of contrast is not sufficient. As shown by IfoCAD simulations, the contrast changes only by a few 0.1 % over tilts on the order of 20  $\mu$ rad. The TTL coupling, on the other hand, shows a high dependency on the misalignment and requires an accuracy of better than at least 10  $\mu$ rad and 10  $\mu$ m, which is not achievable with contrast detection. For this reason the propagation directions of the two interfering beams must again be measured with the CMM which is able to reach these accuracies. Mirror m4 is glued with UV epoxy afterwards and the first bench is completed.

# EXPERIMENTAL INFRASTRUCTURE

” *An experimental characterization of the  
Three-Backlink interferometer environment  
and the free-beam link control loops.*

To probe the noise influences in the TBI down to the LISA requirements an experimental infrastructure is required that provides all laser beams, including desired stabilizations, a representative environment, and the phase readout and control electronics. These parts of the experiment have been implemented and they will be described in this chapter. Since the TBI experiment will be set up on two separate optical benches, which rotate relatively to each other, this operation is tested within some pre-investigation. First experimental results of a free-beam laser link between two optical set-ups that are co-rotating by about  $\pm 1^\circ$  are presented. It is set up on two carbon breadboards and used to test the functionality of the rotary stages and the control loop for the steering mirrors. The work of this chapter is partly based on the experimental description published [Isl+18] and in the bachelor’s and master’s thesis of Lea Bischof [Bis15; Bis18].

## 4.1 Laser preparation

The laser frequency locks and fiber coupling are placed outside the vacuum chamber on an optical table, as shown in Figure 4.1. We supply four single sideband lasers beams, with nominal wavelengths of 1064.5 nm, to the TBI with constant frequency offsets between them and power levels of 320 mW for the TX beams and 160 mW for the ALOs reaching the TBI. The lasers are placed outside the vacuum chamber and will be connected to the experiment via 12 m fiber feedthroughs. Four Mephisto NPRO lasers from Coherent, formerly Innolight, are used, two with 1 W nominal output power, and two with 500 mW, serving as TX laser sources, and ALO respectively, for the TBI experiment. In the laser preparation set-up the light of each laser is first collimated with a 200 mm focal length lens. A combination of

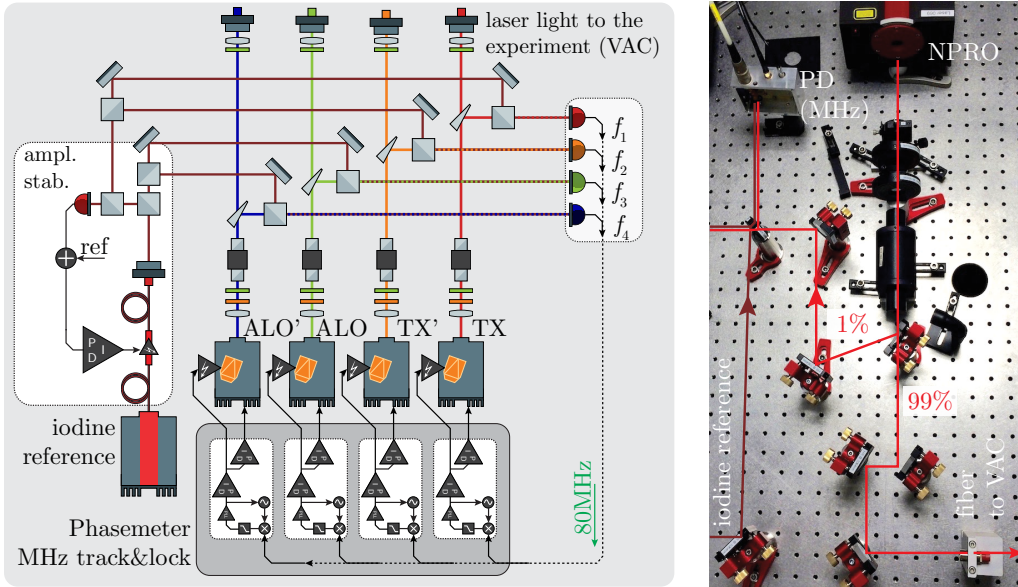


Fig. 4.1.: Scheme and photograph of the set-up of the laser frequency stabilization for the Three-Backlink interferometer. Four Mephisto non-planar ring oscillators (NPROs) are stabilized to an iodine-stabilized laser with MHz offset frequencies. 99 % of the light is guided to the fiber.

half-waveplate and quarter-waveplate ensures a properly aligned polarization of the beam. With these components, the propagation through the Faraday isolator is aligned such that the beam is not diffracted. An uncoated wedge reflects only a minor part, of about 1%, of the laser light. Due to the Brewster angle, the amount of reflectivity can be adjusted via the AOI independently for each laser beam. The low-power path is used for the reference interferometer in the laser preparation that detects the beat note between each laser and an iodine-stabilized laser. An iodine-stabilized laser source, Prometheus from Coherent (Innolight), is fed via a fiber onto the table. The outgoing collimated beam is split into four equivalent beam paths and guided to the interferometers by propagating nearly the same distance to each recombination beam splitter. The pathlengths for the four individual laser sources, which are measured from the wedge to the interferometer, are also matched within 5 cm. The light from the high-power paths of the NPROs is coupled into fibers that guide the light to the vacuum chamber. Imaging systems and half-waveplates in front of the commercial fiber collimators enhance the coupling efficiency. Here, the optical pathlengths measured from the wedge to the coupling are also matched for the laser beams [Bis15].

**Tab. 4.1.:** Offset frequencies between the single lasers used in the TBI laser preparation. Four lasers are used and named as TX, TX', ALO and ALO' in the TBI experiment. The frequency offset between TX and TX' laser is  $f_0 = 9.765\,625$  kHz. The frequency values below and above the diagonal are identical and we define  $f_M = 80\text{ MHz}/2^4 + 80\text{ MHz}/2^5 = 7.5$  MHz.

	TX	TX'	ALO	ALO'	iodine [MHz]
TX	-	9.765 625 kHz	68.359 375 kHz	107.421 875 kHz	7.500 000 000
TX'	$f_0$	-	58.593 75 kHz	97.656 250 kHz	7.509 765 625
ALO	$7 \cdot f_0$	$6 \cdot f_0$	-	39.062 50 kHz	7.568 359 375
ALO'	$11 \cdot f_0$	$10 \cdot f_0$	$4 \cdot f_0$	-	7.607 421 875
iodine	$f_M + 0 \cdot \frac{80\text{ MHz}}{2^{13}}$	$f_M + 1 \cdot \frac{80\text{ MHz}}{2^{13}}$	$f_M + 7 \cdot \frac{80\text{ MHz}}{2^{13}}$	$f_M + 11 \cdot \frac{80\text{ MHz}}{2^{13}}$	-

#### 4.1.1 Laser stabilization

Assuming a maximal arm length difference between each interferometer on both optical benches of the TBI of less than 1 cm, the common frequency stability of the lasers should be better than  $30\text{ kHz}/\sqrt{\text{Hz}}$  between 1 mHz and 1 Hz. We achieve this by offset-phase locking the NPRO lasers to the iodine-stabilized reference laser with an offset frequency of about 7.5 MHz. The iodine stabilization provides frequency noise below  $100\text{ Hz}/\sqrt{\text{Hz}}$  at the desired frequencies. The exact offset for each laser is slightly shifted, such that their heterodyne beat notes are at 9.76 kHz, 39.06 kHz, 58.59 kHz, 68.36 kHz, 97.66 kHz and 107.42 kHz, as shown in Table 4.1. Later backlink experiments might require MHz beat notes, which can easily be achieved by this implementation. Operational amplifier (op-amp)-based single element photoreceivers are used to detect the MHz frequencies. They provide an AC output, and a DC-coupled part that contains a low drift op-amp (AD8629). The photoreceiver front-electronic is based on a design from Germán Fernández Barranco and uses indium gallium arsenide (InGaAs) diodes (LAPD-1-09-17-TO64) with 1 mm diameter. The laser frequencies are chosen such that both phasemeters, the one for the MHz frequency locks and the one for the kHz readout, sampling at 80 MHz, can optimally resolve them and that there are no coinciding harmonics below fourth order. The phasemeter for the laser stabilization consists of an FPGA, an ADC and a digital-to-analog converter (DAC) card. The implementation of the heterodyne readout is based on a PLL-phasemeter which is typically used for reading out MHz frequencies (see Section 1.3.1), like required for the LISA-phasemeter. The phase locking (PID-controller) is realized digitally with an algorithm implemented in the FPGA [McN05; Die+09; Ger+15]. The same photoreceivers and phasemeter are also used in the Hexagon experiment [Sch18]. Actuation signals are converted into analog voltages modulating the laser crystals via a piezoelectric transducer (PZT) for fast frequency changes and the crystal

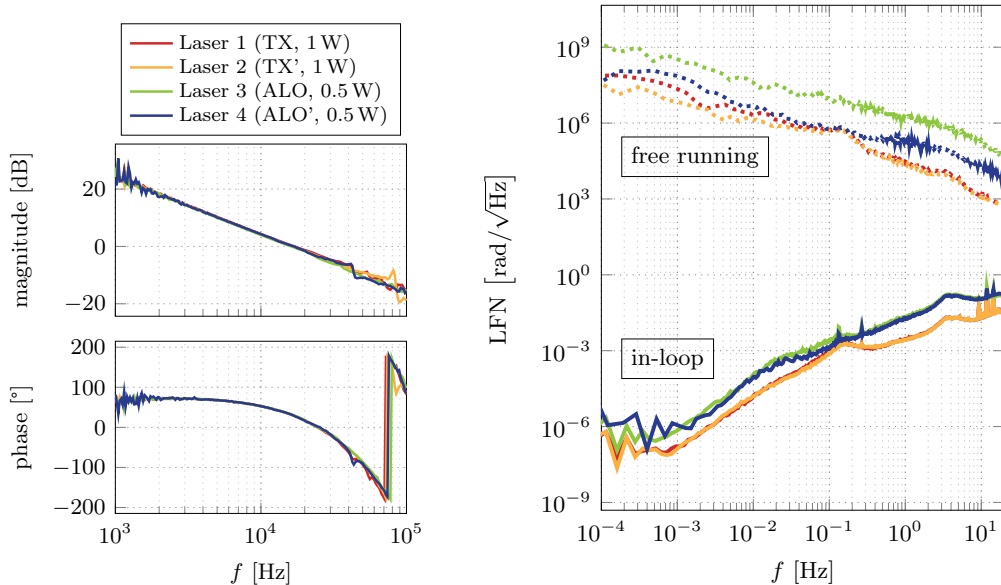


Fig. 4.2.: Measured transfer functions (left) and phase noise spectral densities (right) of the laser frequency stabilization. Shown are the transfer functions measured for all four NPRO lasers being locked to an iodine reference laser. The frequency noise spectrum is shown with (in-loop signals) and without feedback control loop.

temperature for slow changes. The transfer functions for each laser frequency lock are shown in Figure 4.2. Each feedback control loop achieves a unity-gain frequency of 17 kHz and a phase margin of  $30^\circ$  and they have already been operated continuously over several months.

To maintain constant power levels in the TBI, we also established analog amplitude stabilizations actuating on fiber-based amplitude modulators. A prototype amplitude stabilization has been tested for the iodine reference laser. A power pick up photodiode monitors amplitude fluctuations to be compared against a stable reference current. An analog feedback circuit provides the actuation signal for the fiber-based amplitude modulator. We measured a unity-gain frequency of 2.2 kHz with a phase margin of  $44^\circ$ . Four copies of this amplitude control will be implemented for the TBI with photodiode sensors inside the vacuum chamber [Bis15].

#### 4.1.2 High voltage amplifier design

The integration of a high-voltage (HV) amplifier could further improve the long-term stability of the laser frequency locks by actuating the PZT loop with a larger voltage range. An optimal HV amplifier design depends mainly on one of the

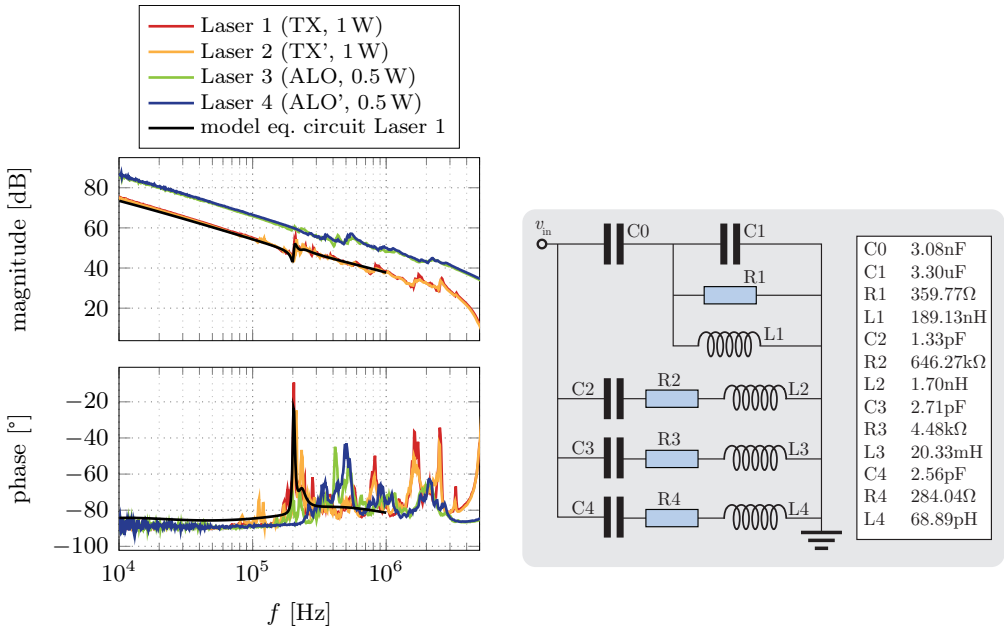


**Fig. 4.3.:** Measured transfer functions of the NPRO PZT impedances for the four Mephisto lasers for the frequency range from  $1 \cdot 10^4$  to  $1 \cdot 10^6$  Hz. The equivalent circuit model is fitted to one of the 1 W lasers. A sketch of the equivalent electrical circuit is shown on the right.

laser's PZT properties, its capacitance and resonances, which can be determined by measuring the PZT impedance over frequency. Figure 4.3 shows the measured transfer functions of all four NPRO PZT capacitances. A model, based on the electric equivalent circuit shown in Figure 4.3 on the right, is used to fit the data by using the software tool LInear Simulation and Optimization (LISO) by Gerhard Heinzl for simulating analog electronic circuits. Here, we show the model result for one of the 1 W lasers in the frequency range from 10 to 1000 kHz. The value of the capacitor  $C_0$  is the capacitance of the laser PZT. The parallel circuit constructed by  $C_1$ ,  $R_1$  and  $L_1$  describes a notch, which is the valley in the fit function. The three series circuits,  $(C_2, R_2, L_2) - (C_4, R_4, L_4)$ , produce the resonance peaks. Figure 4.3 shows also a list of the fitted parameters. The desired capacitance of the laser PZT is determined by this model and is about 3.1 nF. Further LISO simulations have shown that the capacitance is similar for each laser. From this value a dedicated two channel HV amplifier has been designed by Gerhard Heinzl and Iouri Bykov, together with a HV power supply circuit providing  $\pm 100$  V output voltages. The HV power supply uses an input voltage of 12 V and provides two outputs, one with 100 V, from 30 to 150 V, and one with  $-100$  V, from  $-30$  to  $-150$  V. Two 2-channel amplifiers are used for the PZT control of all four lasers. Each channel

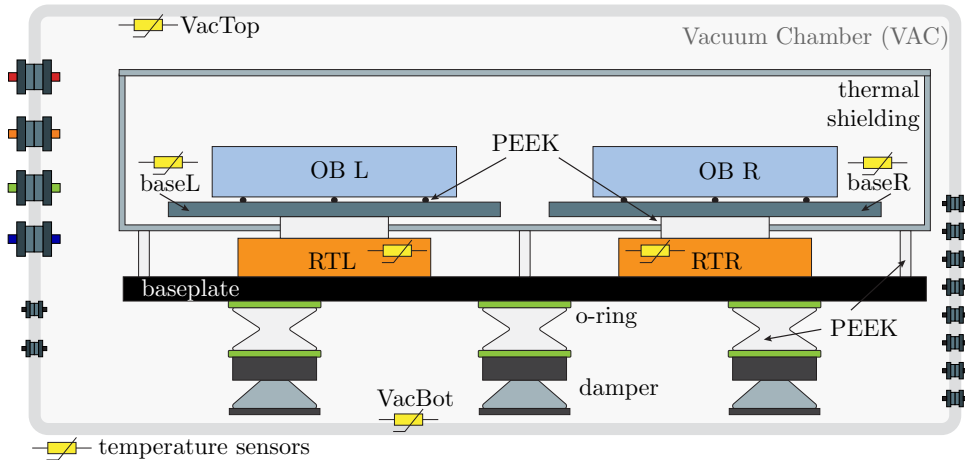


Fig. 4.4.: Sketch of the TBI vacuum chamber, the left rotation table (RTL) and right rotation table (RTR) and the main interferometer on the optical benches OB L and OB R. The locations of selected temperature sensors are also depicted here.

can be individually optimized by adjusting the operating point via potentiometers for getting a maximum bandwidth.

## 4.2 Vacuum set-up

The environment to test the TBI has to provide vacuum, a thermal stability of better than  $1 \cdot 10^{-4} \text{ K}/\sqrt{\text{Hz}}$  at 1 mHz and two co-rotating baseplates enabling a rotation of about  $\pm 1.5^\circ$  each. To achieve this we implemented two rotary tables, each one carrying one interferometer, on a common baseplate, with a size of  $(680 \times 680 \times 20) \text{ mm}^3$ , positioned inside a vacuum chamber, as illustrated by Figure 4.4. Around the interferometers, excluding the rotary tables, we placed a passive thermal shielding (TSH) covered by multilayer insulation (MLI) foil. The thermal shield and the common baseplate are thermally isolated from each other as well as from the vacuum chamber by adapters made of a low-outgassing thermal insulator material polyether ether ketone (PEEK). To reduce an inverted pendulum motion of the rotary table payload we also included vibration damping feet and vibration isolation of the vacuum pumps. This also helps to decouple the experiment from external vibrations originating from the laboratory environment and pumps whereas the PEEK provides the first stage of thermal isolation from temperature fluctuations of the laboratory. The vacuum chamber is furthermore covered with styrofoam on the outside to reduce temperature fluctuations from the laboratory. Together with the TSH, the two rotary stages are also fixed to the main



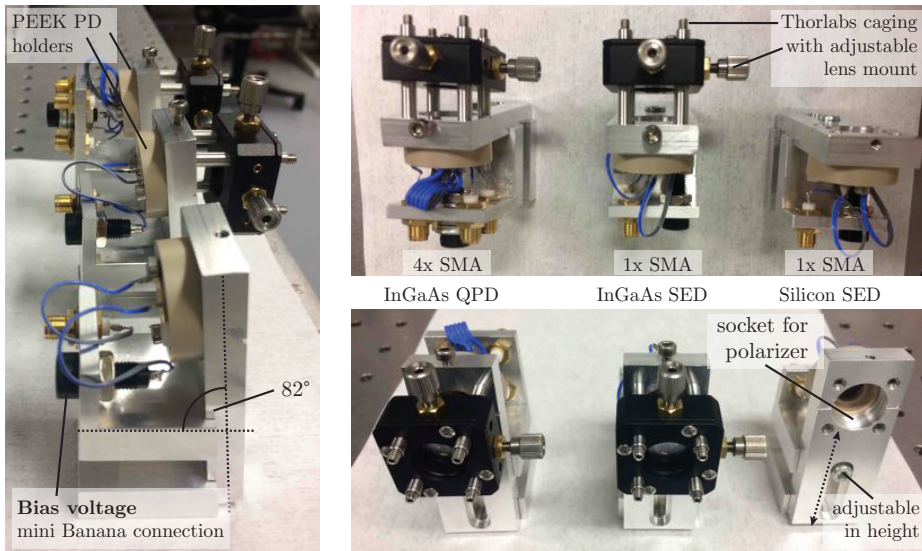


Fig. 4.5.: Photographs of the photodiode mounts for InGaAs QPD GAP1000Q, InGaAs SED LAPD-1-09-17-TO46 and silicon (Si) PC50. The aluminum front plate is angled by  $8^\circ$ , as well as the socket for the thin-film polarizers. The diode is isolated from the aluminum mount by an adapter made of PEEK. Focusing lenses for small diodes are installed in a XY translational mount from Thorlabs, SCP05, mounted by a 16 mm Caging System.

baseplate with their rotary shafts extending through the thermal shield, inside of which each of them is attached to a secondary aluminum baseplate. These rotating secondary baseplates, in turn, carry the actual optical benches, supported by three 4 mm diameter spheres of PEEK, along with the active devices, i.e. photodiodes and actuator mirrors. This saves space on the optical benches and avoids the dissipation of electronically produced waste heat and thermal fluctuations on the optical benches. To achieve temperature fluctuations as low as possible in the vacuum chamber, most electronic devices and circuits are placed outside.

#### 4.2.1 Photodiode mount

Early on we decided to use kHz heterodyne frequencies instead of MHz to allow a separation of photodiodes from transimpedance amplifiers (TIAs). The design of the photodiode mounts for the TBI experiment is based on the layout from an earlier experiment, but with a smaller base size since the TBI requires ten detectors per bench. They consist of an aluminum base on which a plate that holds the photodiode can be mounted. This plate is made of aluminum, angled by  $8^\circ$  and can be adjusted in height. Figure 4.5 shows some photographs of the assembly. Three PEEK photodiode holders with different socket size were built, allowing the use of

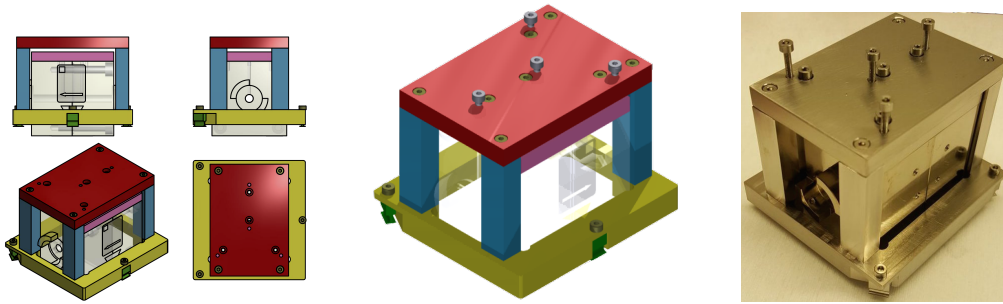


Fig. 4.6.: Thermally compensated mount for the Faraday rotator. Schematic drawing and 3D model are shown on the left, photograph of the assembly with a Faraday rotator is shown on the right.

photodiodes with different packaging. This ensures that the photodiode is isolated from the aluminum mount, and, thus, it is only connected to the bias voltage and signal pins. In general the InGaAs photodetectors LAPD-1-09-17-TO46 from Roithner Lasertechnik are used for the interferometric readout in the TBI. These SEDs have an active area of 1 mm diameter. For the FBBL the QPDs GAP1000Q from Opto-Electronic Components (OEC GmbH) are used, also having an active area of 1 mm diameter which is divided into four segments, separated from each other by a slit of about 20  $\mu\text{m}$ . Due to the small diode size we use focusing lenses with 25.4 mm focal length in front of them. They are mounted in a XY translational mount from Thorlabs, SCP05, which is compatible with the 16 mm Caging System by which they are mounted at the aluminum plate. The third photodiode which will be used for the laser power stabilizations is the Si SED PC50 from Pacific Silicon Sensor (now: First Sensor). This photodiode has a large active area of about 7.98 mm, thus there is no need for focusing lenses. In comparison to the InGaAs photodiodes the alignment of the PC50 is very easy, but the spectral response is only about 0.15 A/W for 1064 nm and the bandwidth is limited by a few kHz with low bias voltages, while we can monitor MHz signals with 0.7 A/W responsivity with InGaAs detectors, hence a change to MHz optical frequencies later on is relatively simple.

#### 4.2.2 Faraday mount

For the two Faraday rotators in the TBI, FI-1060-3SC LO from Qi Optik, a thermally compensated mount was designed by Oliver Gerberding and simulated by Richard Benett from the UK Astronomy. Here, we use only the rotator, the polarizing beam splitters are directly bonded onto the optical benches. The final version of the mount is shown in Figure 4.6. It consists of three flexure feet (green)

made of titanium which are screwed to the base frame, also made of titanium (shown in yellow). These flexure feet are later glued onto the optical bench. Any thermal gradients can be compensated by the flexure feet such that eventual displacements of the Faraday holder can be reduced. The four pillars, highlighted in blue, are made of monel 600, a nickel alloy, primarily composed of nickel and copper. The combination of the two different materials, monel 600 and titanium, makes the mount thermally compensated, taking into account that the Faraday itself is made from aluminum. On the top (red) another titanium plate is screwed, on which an intermediate plate is mounted (pink) underneath with four locking screws and four adjustment screws. All screws are also made of titanium and allow an alignment of tilts of the Faraday rotator.

### 4.2.3 Temperature sensors

To monitor temperature fluctuations we placed thermal sensors throughout the set-up. To reduce the thermal load within the vacuum chamber we minimized the amount of active electronics. Two different types of thermistors are used as temperature sensors inside the vacuum chamber. The resistance of Negative Temperature Coefficient (NTC) thermistors decreases towards higher temperatures while the resistance of Positive Temperature Coefficient (PTC) (here we use PT10000) thermistors increases. For small temperature changes the resistance response of the NTC is non-linear and accurate temperature noise measurements can be performed at room temperature with a lower white noise floor in comparison to the PTC thermistor. The PTC has a linear response and is therefore less sensitive in this temperature regime but has a higher absolute range. The dependency of resistance,  $R$ , on the temperature,  $T$ , for both thermistors is shown in Figure 4.7. The relations are given by

$$T(R)_{\text{PTC}}[\text{°C}] = \frac{-R_0 \cdot A + \sqrt{(R_0 \cdot A)^2 - 4.0 \cdot R_0 \cdot B \cdot (R_0 - R)}}{2.0 \cdot R_0 \cdot B} \quad (4.1)$$

$$T(R)_{\text{NTC}}[\text{°C}] = \frac{1.0}{A + B \cdot \log(R) + C \cdot \log(R) \cdot \log(R)} - T_0 \quad (4.2)$$

while the parameters for the PTC thermistor are  $R_0 = 10 \text{ k}\Omega$ ,  $A = 3.9083 \cdot 10^{-3}$  and  $B = -5.775 \cdot 10^{-7}$ . The NTC thermistor temperature calculation is based on the Steinhart-Hart equation and the parameters for this system are  $A = 0.7477 \cdot 10^{-3}$ ,  $B = 0.2169 \cdot 10^{-3}$ ,  $C = 1.029 \cdot 10^{-7}$  and  $T_0 = 273.15 \text{ K}$ , whereby the coefficients of the NTC are determined by measuring the thermistor at three different temperatures and fitting three Steinhart-Hart equations to the data by which the coefficients are determined [SH68].

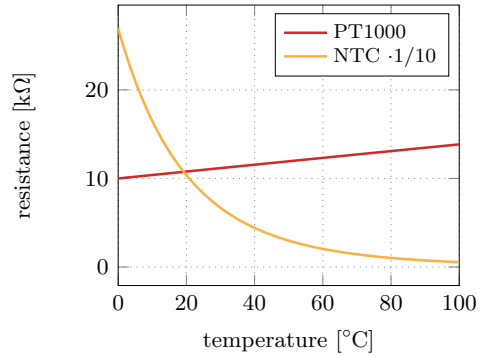
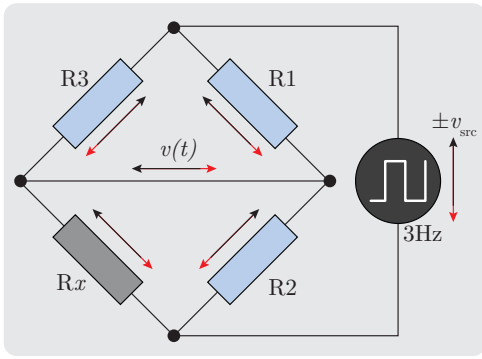


Fig. 4.7.: Circuit diagram of a Wheatstone bridge (left). The unknown electrical resistance  $R_x$  is going to be measured,  $R_1$ ,  $R_2$ ,  $R_3$  are known values. The temperature dependencies of the resistance of the PTC (PT10000) and NTC thermistor are shown on the right plot. The resistance value for the NTC is divided by 10.

An electrical circuit is used to measure the resistance of both types of temperature sensors which was initially designed by Gerhard Heinzl, based on a design of LTP, which uses a Wheatstone bridge circuit. Figure 4.7 shows a typical Wheatstone bridge, consisting of two legs, while the first leg contains two known resistor values,  $R_1$  and  $R_3$ , and the other leg includes the unknown component,  $R_x$  and the resistor  $R_2$ . By balancing those two legs the unknown electrical resistance can be measured very accurately. For each temperature sensor such an electrical circuit was built, with  $R_x$  being the resistance of the thermistor [Hof74]. As voltage source we supply a rectangular signal with a rate of 3 Hz. This allows measurements with different signs that are switching every 0.3 s. The common mode suppression of a Wheatstone Bridge by applying a bi-directional voltage is very high such that contact resistances and other noise sources cancel out, which makes the measurements even more precise and white noise levels on the order of  $1 \cdot 10^{-5} \text{ K}/\sqrt{\text{Hz}}$  can be measured. The resistor values of the Wheatstone bridge are matched to the according thermistor type. An electrical circuit board, designed at the AEI, provides input and output channels for eight thermistors and is connected via Universal Serial Bus (USB) to the personal computer (PC). This board is the heart of the thermometer, containing low-noise pre-amplifiers and high-resolution ADCs.

The combination of both thermistor types, integrated in a Wheatstone bridge circuit, provides temperature measurements with high accuracy over a large temperature range. A calibration of each thermistor and electrical circuit is recommended for measuring absolute temperatures. This calibration has not been done yet for the sensors used in the TBI experiment.

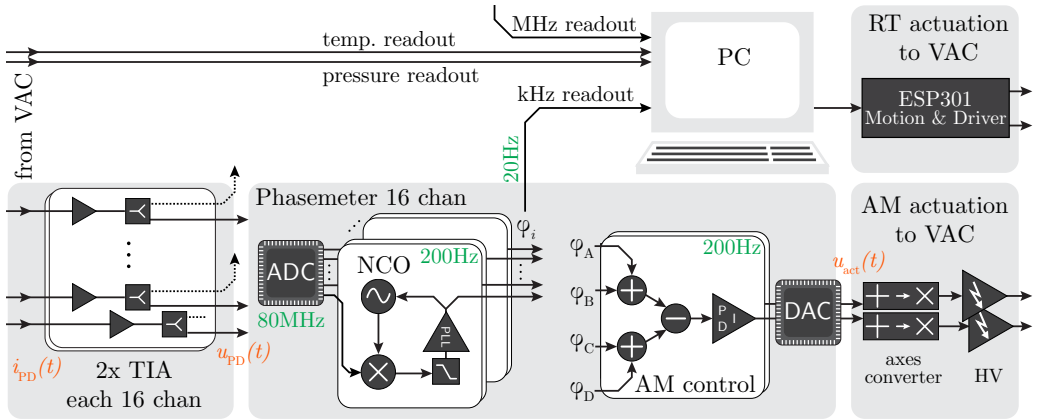


Fig. 4.8.: Phase readout and front- and back-end electronics for the TBI. Photodiode and other sensor signals (vacuum pressure and temperature) are coming from the left, actuation signals guided to the vacuum system exit on the right, like the rotary table (RT) control. In-between, the photoreceiver front-end (TIA) converts the photocurrent into a voltage that is digitized by the ADC and this digital signal is processed in the phasemeter via the PLL. The steering mirror control loop is implemented in the FPGA. A PC collects all the data and controls the readout programs for the phasemeter, temperature board, vacuum pressure and the controller ESP 301 driving the rotary stages. The amplitude detection is not shown in this picture.

### 4.3 Phasemeter and electronics

Two front-end electronic boxes, housing 16 TIA channels each, are placed next to the vacuum chamber to convert the photocurrents into voltage for each one of the 20 signals, as shown in Figure 4.8. The front-end boxes also provide the photodiode bias voltage of 5 V and monitor outputs that can be connected for diagnostic reasons to an oscilloscope.

The phase of the photodiode currents has to be extracted with a precision of better than  $2\pi \mu\text{rad}/\sqrt{\text{Hz}}$ . Thus, the actual TIA output is connected to a phasemeter via coaxial cables. The phasemeter is an FPGA-based device that is able to track the kHz photoreceiver voltage signals in 16 channels simultaneously with a sampling rate of 80 MHz. While the conventional LPF-style phasemeter uses a simple  $IQ$ -demodulation scheme that extracts the phase from kHz signals, we implemented a PLL in the TBI-readout phasemeter as it is used in MHz-tracking phasemeters [Ger+15]. The LPF-phasemeter is used for reading out interferometer signals with only small dynamic range. Due to the fixed frequency that is used for the  $IQ$ -demodulation, the bandwidth of this phasemeter is limited. For the TBI we require a phasemeter with somewhat higher bandwidths to also track the kHz signals with larger dynamics as it is the case for the free-beam backlink

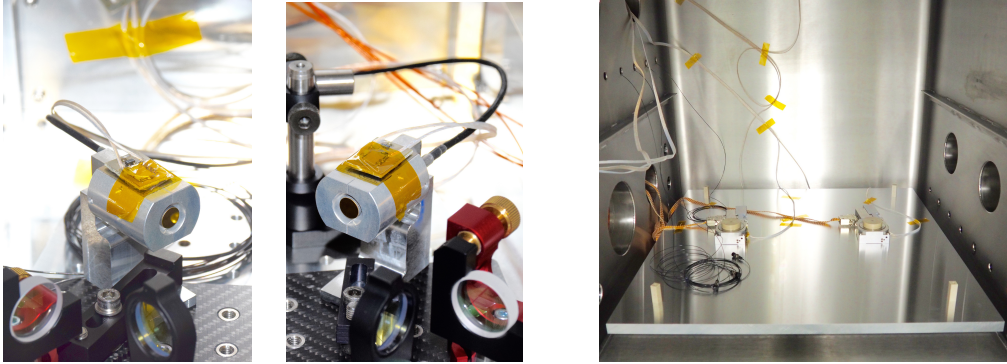


Fig. 4.9.: Photographs of the steering mirrors (left), AML and AMR, both S-334 from Physik Instrumente, integrated in the free-beam experiment and of the two rotary stages (right), URS50BPPV6 from Newport, mounted on the aluminum baseplate in the vacuum chamber. Both, actuator mirror and rotary stages, are equipped with temperature sensors, fixed with kapton tape.

connection. Due to the bench rotation and the compensating steering mirrors, fast, step-like changes in the phase and amplitude measurements are observed. The amplitude measured by the LPF-phasemeter would drop immediately for each rotation step since the resulting frequency runs outside the bandwidth, while a tracking-phasemeter will follow the phase or frequency changes by using an numerically controlled oscillator (NCO), integrated in the PLL. The phase difference between optical beat note and NCO directly provides the desired PLL error signal with 20 kHz rate after filtering, with which we are able to track the optical kHz signals up to a bandwidth of 1 kHz, which is sufficiently high for our applications. The signal is yet again down-sampled to a rate of 20 Hz before passing it on to a PC used for saving and analyzing the data [Isl+18].

#### 4.3.1 Free-beam control

We use the interferometer signals from the two QPDs to control the free-beam backlink steering mirrors. The two tip-tilt actuation mirrors, shown in Figure 4.9, correspond to the model S-334 by Physik Instrumente (PI). The DWS signal from each QPD provides highly sensitive measurements of optical tilts, with the corresponding calculation of the phase signal that is directly integrated in the FPGA. A sketch of the implementation of the control loop is shown in Figure 4.10. Due to the usage of a tracking-phasemeter, the implementation of the DWS calculation is rather easy since the desired phase information is already available in the FPGA. The calculation of the individual actuation signals depends on the coupling between the control loops, which can be optimized by lenses or



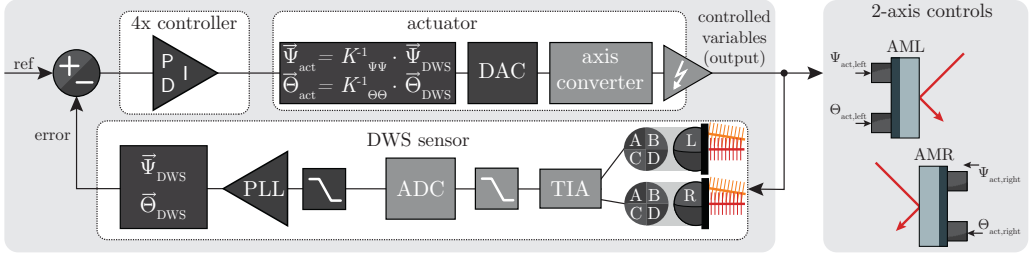


**Fig. 4.10.:** Control loop for the two-axes steering mirror control for AML and AMR. analog interfaces are highlighted dark gray, digital processing is highlighted light gray.

imaging systems. The relation between horizontal (yaw) DWS signals,  $\Psi_{DWS}$  and a horizontal mirror motion is given by the following equation,

$$\begin{pmatrix} \Psi_{DWS, \text{left}} \\ \Psi_{DWS, \text{right}} \end{pmatrix} = \begin{pmatrix} K1_{\Psi\Psi} & K2_{\Psi\Psi} \\ K3_{\Psi\Psi} & K4_{\Psi\Psi} \end{pmatrix} \cdot \begin{pmatrix} \Psi_{AML} \\ \Psi_{AMR} \end{pmatrix}, \quad (4.3)$$

as introduced in Section 3.6.3. Here,  $\Psi_{AML}$  and  $\Psi_{AMR}$  are the horizontal tilt for the left and right actuator mirror, AML, and AMR. The coupling between them is described by the matrix  $K_{\Psi\Psi}$ . An equivalent formula is given for the vertical (pitch) direction, which describes the vertical DWS signals,  $\Theta_{DWS, \text{left}}$  and  $\Theta_{DWS, \text{right}}$ , in relation to the vertical mirror motions,  $\Psi_{AML}$  and  $\Psi_{AMR}$ , via the coupling matrix  $K_{\Theta\Theta}$ . Any cross-coupling between the two tilt axes is described by the matrices  $K_{\Psi\Theta}$  and  $K_{\Theta\Psi}$ , the according relation is

$$\begin{pmatrix} \Psi_{DWS, \text{left}} \\ \Psi_{DWS, \text{right}} \end{pmatrix} = \begin{pmatrix} K1_{\Psi\Theta} & K2_{\Psi\Theta} \\ K3_{\Psi\Theta} & K4_{\Psi\Theta} \end{pmatrix} \cdot \begin{pmatrix} \Theta_{AML} \\ \Theta_{AMR} \end{pmatrix}. \quad (4.4)$$

Due to misalignments of the QPD and calibration errors of the steering mirror axes, a cross-coupling between horizontal and vertical motion and sensing is possible. The coupling coefficients in vertical and horizontal direction are simultaneously measured by applying a sinusoidal motion to the steering mirrors with a different frequency in each axis. By demodulating the QPD response with the corresponding frequency, the influence on the DWS signals is recovered for each mirror and each axis. This procedure allows a simultaneous measurement of all DoFs. After the coupling coefficients are measured for different rotations of the optical benches, the inverse of the matrices is determined and inserted in the phasemeter, which calculates in real time the individual actuation signals via

$$\Psi_{\text{act, left}} = \hat{K}1_{\Psi\Psi} \cdot \Psi_{DWS, \text{left}} + \hat{K}2_{\Psi\Psi} \cdot \Psi_{DWS, \text{right}}, \quad (4.5)$$

$$\Psi_{\text{act, right}} = \hat{K}3_{\Psi\Psi} \cdot \Psi_{DWS, \text{left}} + \hat{K}4_{\Psi\Psi} \cdot \Psi_{DWS, \text{right}}, \quad (4.6)$$

here shown for the horizontal direction. The appropriate actuation signals are fed to the steering mirrors via DACs, axes converters and HV amplifiers. The DAC provides the output voltages corresponding to the digital actuation signals. The tilt axes of the mirrors are rotated by  $45^\circ$  in comparison to the horizontal and vertical directions from the optical set-up. A linear operational amplifier circuit, with integrated offset adder, is used to adjust the axes independently. The corrected analog voltages are then sent to the PZT controller, E-616 from PI, that amplifies an input signal from  $-2$  to  $12$  V to a high voltage output from  $-30$  to  $130$  V. Due to the integration of the control loop in the FPGA, an appropriate unity-gain frequency of  $100$  Hz for the mirror control can be achieved [McN05; Die+09; Ger+15].

### 4.3.2 Rotary stage control

The control of the two rotary stages, URS50BPPV6 provided by Newport, shown in Figure 4.9, is done by the motion controller from Newport, ESP301. The controller can be controlled either locally or via a serial USB interface from the PC, as shown in Figure 4.8. It is a command-driven system and can be operated with a host terminal on the PC that transfers ASCII character commands to the respective communication protocol, which was realized by a Python script. With this script the actual position of the two stages can also be read out simultaneously with a rate of about  $0.47$  Hz. The driver estimates the position with an accuracy of  $0.001^\circ$ , limited by the controller output bit size. The desired sinusoidal motion of the two rotary stages was implemented by using a third, virtual axis around which the other two move along an arc, which is by design sinusoidal. A counter-rotating movement between the two axes could be achieved. A rotation magnitude of  $\pm 0.75^\circ$  and a period of  $13.6$  h was observed for a velocity of  $0.0001^\circ/\text{s}$  and an acceleration, and deceleration, of  $8^\circ/\text{s}^2$ , applied on the axes parameters.

## 4.4 Planned experiments

The TBI experiment is used to compare the non-reciprocity of the three backlinks relative to each other. The non-reciprocity is the phase difference of light beams propagating in opposite directions through a backlink connection compared to a reference measurement. The design of the TBI is advantageous in terms of common noise sources which cancel out due to the mirror symmetry of the two optical benches in certain signal combinations. Also the influence of the laser preparation set-up, like air density and temperature fluctuations driving the phase noise of laser beams propagating through air or in fibers, is assumed to be common mode for all lasers guided to the vacuum chamber due to the reciprocity measurements where we



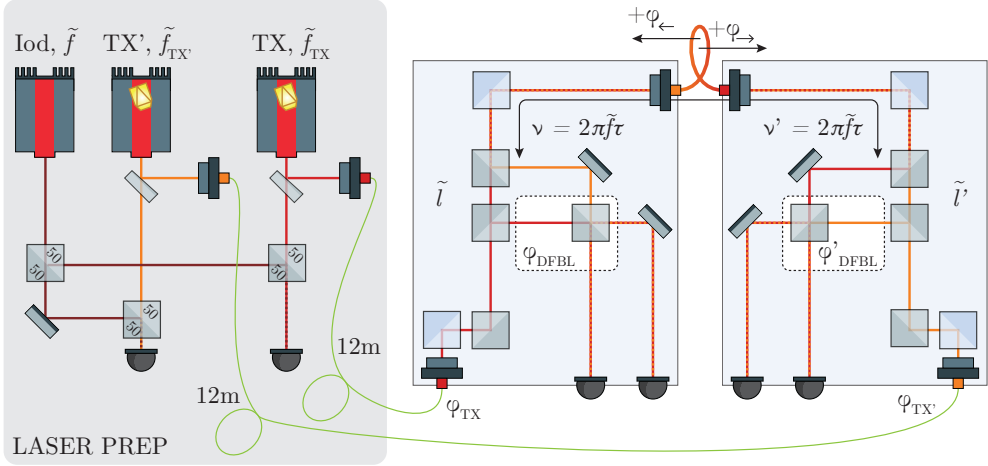


Fig. 4.11.: Description of phase noise illustrated for the example of the DFBL. The optical pathlength noise,  $\tilde{l}$ , is assumed to be negligible due to the high stability of quasi-monolithic set-ups.

should have common mode rejection. Only phase disturbances accumulated on the proper optical benches are considered. For a temperature stability of  $0.1 \text{ mK} / \sqrt{\text{Hz}}$  and a quasi-monolithic interferometer bonded on an optical bench with a CTE of  $1 \cdot 10^{-8} / \text{K}$ , we assume that the pathlength noise is below  $1 \text{ pm} / \sqrt{\text{Hz}}$  for 1 m arm lengths. Typical interferometer arm length mismatches are even shorter due to the compactness of optical set-ups, in addition we often reach thermal stabilities of  $10 \mu\text{K}$  for evacuated experiments, slowly increasing for frequencies below 10 mHz. The limiting noise sources are consequently assumed to be laser frequency noise (LFN) due to the unequal interferometric arms, and phase noise coming from the backlink connection.

For the contribution of LFN it is assumed in the following that the initial frequency fluctuations are on the same order of magnitude for all laser sources, thus  $\tilde{f}_1 = \dots = \tilde{f}_4 = \tilde{f}$ . The absolute propagation length of one bench is denoted by  $\tau$ , the index of this variable defines starting and ending point, e.g.  $\tau_{\text{TX} \rightarrow \text{DFBL}}$  for the beam propagation from the TX FIOS to the recombination beam splitter of the DFBL interferometer. Backlink phase noise denotes the reciprocal phase noise of the backlink path. The laser beam collects a phase,  $\varphi_{\rightarrow}$ , by traveling from the left to the right and bench, and  $\varphi_{\leftarrow}$  for the opposite direction. The discrepancy between them,  $\varphi_{\text{NR}} = \varphi_{\rightarrow} - \varphi_{\leftarrow}$ , is the measured non-reciprocity of a backlink connection.

#### 4.4.1 Non-reciprocal backlink phase noise

To extract the non-reciprocity of a backlink connection the interferometric phase is measured on both benches. We will distinguish between these two measurements by priming the variables of the right bench. Therefore,  $\varphi_{\text{BL}}$  is the interferometric phase measured on the left bench, and  $\varphi'_{\text{BL}}$  is measured on the right. The phase of the beam with the lower absolute frequency is subtracted from the one with the higher absolute frequency such that we achieve in each interferometer effective frequencies with only positive values, such as the phasemeter will provide, like  $\varphi_1 - \varphi_2 > 0$ . Thus, we define the following order,  $f_1 > f_2 > f_3 > f_4$ , for the frequencies of the lasers TX, TX', ALO and ALO'. For the DFBL we can write the photodiode signals for the left bench,  $\varphi_{\text{DFBL}}$ , and for the right bench,  $\varphi'_{\text{DFBL}}$ , according to Figure 4.11 as followed,

$$\begin{aligned}
 \varphi_{\text{DFBL}} &= \underbrace{[\varphi_{\text{TX}} + \nu(\tau_{\text{TX} \rightarrow \text{DFBL}})]}_{\varphi_1} - \underbrace{[\varphi_{\text{TX}'} + \nu(\tau_{\text{TX}' \rightarrow \text{DFBL}}) + \varphi_{\leftarrow}]}_{\varphi_2} \\
 &= [\varphi_{\text{TX}} - \varphi_{\text{TX}'}] - [\nu(\tau_{\text{TX}' \rightarrow \text{DFBL}}) - \nu(\tau_{\text{TX} \rightarrow \text{DFBL}})] - \varphi_{\leftarrow} \\
 &= [\varphi_{\text{TX}} - \varphi_{\text{TX}'}] - \tilde{\nu}(\Delta\tau_{\text{DFBL}}) - \varphi_{\leftarrow}, \tag{4.7}
 \end{aligned}$$

$$\begin{aligned}
 \varphi'_{\text{DFBL}} &= \underbrace{[\varphi_{\text{TX}} + \nu(\tau_{\text{TX} \rightarrow \text{DFBL}'}) + \varphi_{\rightarrow}]}_{\varphi_1} - \underbrace{[\varphi_{\text{TX}'} + \nu(\tau_{\text{TX}' \rightarrow \text{DFBL}'})]}_{\varphi_2} \\
 &= [\varphi_{\text{TX}} - \varphi_{\text{TX}'}] + [\nu(\tau_{\text{TX} \rightarrow \text{DFBL}'}) + \nu(\tau_{\text{TX}' \rightarrow \text{DFBL}'})] - \varphi_{\rightarrow} \\
 &= [\varphi_{\text{TX}} - \varphi_{\text{TX}'}] + \tilde{\nu}(\Delta\tau_{\text{DFBL}'}) + \varphi_{\rightarrow}, \tag{4.8}
 \end{aligned}$$

where  $\tilde{\nu}(\Delta\tau_{\text{DFBL}})$  and  $\tilde{\nu}(\Delta\tau_{\text{DFBL}'})$  describe the LFN that couples into the phase measurement due to the propagation delay of the two interfering beams,  $\Delta\tau_{\text{DFBL}} = |\tau_{\text{TX}' \rightarrow \text{DFBL}} - \tau_{\text{TX} \rightarrow \text{DFBL}}|$  and vice versa for the right bench. Due to the mirror-symmetry of the TBI the coupling is identical for both benches, thus  $\tilde{\nu}(\Delta\tau_{\text{DFBL}}) = \tilde{\nu}(\Delta\tau_{\text{DFBL}'})$ . The phase sum and phase difference between the left and right measurements are determined via

$$\begin{aligned}
 \varphi_{\text{DFBL}} - \varphi'_{\text{DFBL}} &= -2\tilde{\nu}(\Delta\tau_{\text{DFBL}}) - l_{\text{DFBL}} \\
 \varphi_{\text{DFBL}} + \varphi'_{\text{DFBL}} &= 2[\varphi_{\text{TX}} - \varphi_{\text{TX}'}] + \varphi_{\text{NR,DFBL}} =: \Phi_{\text{DFBL}}.
 \end{aligned}$$

Any LFN cancels out for the phase combination,  $\Phi_{\text{DFBL}}$ , containing the non-reciprocal phase,  $\varphi_{\text{NR,DFBL}} = \varphi_{\rightarrow} - \varphi_{\leftarrow}$ , if the two benches are fully mirror-symmetric without arm length mismatch differences. A reference measurement must be subtracted to achieve the backlink's non-reciprocity. The other phase

combination contains information about the backlink length,  $l_{\text{DFBL}}$ , and twice the LFN.

Equivalent phase signals, as given by Equations (4.7) and (4.8) for the DFBL, are valid for the FBBL. The phase combinations for the FBBL can therefore be written as,

$$\begin{aligned}\varphi_{\text{FBBL}} - \varphi'_{\text{FBBL}} &= -2\tilde{\nu}(\Delta\tau_{\text{FBBL}}) - l_{\text{FBBL}}, \\ \varphi_{\text{FBBL}} + \varphi'_{\text{FBBL}} &= 2[\varphi_{\text{TX}} - \varphi_{\text{TX}'}] + \varphi_{\text{NR,FBBL}} =: \Phi_{\text{FBBL}}.\end{aligned}$$

The FFSFBL however uses two additional laser frequencies which is why an additional reference interferometer is required and, therefore, the following four photodiode signals must be considered,

$$\begin{aligned}\varphi_{\text{FSFBL}} &= [\varphi_{\text{TX}} - \varphi_{\text{ALO}}] - \tilde{\nu}(\Delta\tau_{\text{FSFBL}}) - \varphi_{\leftarrow}, \\ \varphi'_{\text{FSFBL}} &= [\varphi_{\text{TX}'} - \varphi_{\text{ALO}}] - \tilde{\nu}(\Delta\tau_{\text{FSFBL}'}) - \varphi_{\rightarrow}, \\ \varphi_{\text{REF}} &= [\varphi_{\text{TX}} - \varphi_{\text{ALO}}] - \tilde{\nu}(\Delta\tau_{\text{REF}}), \\ \varphi'_{\text{REF}} &= [\varphi_{\text{TX}'} - \varphi_{\text{ALO}'}] - \tilde{\nu}(\Delta\tau_{\text{REF}'}).\end{aligned}$$

With the resulting differential and summed phases,

$$\begin{aligned}\varphi_{\text{FSFBL}} - \varphi'_{\text{FSFBL}} &= [\varphi_{\text{TX}} - \varphi_{\text{TX}'}] + [\varphi_{\text{ALO}} - \varphi_{\text{ALO}'}] + \varphi_{\text{NR,FSFBL}}, \\ &=: \delta\varphi_{\text{FSFBL}} \\ \varphi_{\text{FSFBL}} + \varphi'_{\text{FSFBL}} &= [\varphi_{\text{TX}} - \varphi_{\text{ALO}}] + [\varphi_{\text{TX}'} - \varphi_{\text{ALO}'}] - 2\tilde{\nu}(\Delta\tau_{\text{FSFBL}}) - l_{\text{FSFBL}}, \\ &=: \sigma\varphi_{\text{FSFBL}} \\ \varphi_{\text{REF}} - \varphi'_{\text{REF}} &= [\varphi_{\text{TX}} - \varphi_{\text{TX}'}] - [\varphi_{\text{ALO}} - \varphi_{\text{ALO}'}], \\ &=: \delta\varphi_{\text{REF}} \\ \varphi_{\text{REF}} + \varphi'_{\text{REF}} &= [\varphi_{\text{TX}} - \varphi_{\text{ALO}}] + [\varphi_{\text{TX}'} - \varphi_{\text{ALO}'}] - 2\tilde{\nu}(\Delta\tau_{\text{REF}}), \\ &=: \sigma\varphi_{\text{REF}}\end{aligned}$$

we can find combinations that deliver equivalent results compared the ones of the other backlink interferometers, only containing the non-reciprocity information and the remaining phase noise between the two TX lasers,

$$\begin{aligned}\sigma\varphi_{\text{FSFBL}} - \sigma\varphi_{\text{REF}} &= -2\tilde{\nu}(\tau_{\text{FSFBL}}) + 2\tilde{\nu}(\tau_{\text{REF}}) - l_{\text{FSFBL}}, \\ \delta\varphi_{\text{FSFBL}} + \delta\varphi_{\text{REF}} &= 2[\varphi_{\text{TX}} - \varphi_{\text{TX}'}] + \varphi_{\text{NR,FSFBL}} =: \Phi_{\text{FSFBL}}.\end{aligned}$$

By comparing the signals,  $\Phi_{\text{DFBL}}$ ,  $\Phi_{\text{FBBL}}$ ,  $\Phi_{\text{FSFBL}}$ , of the backlink candidates among each other the differential non-reciprocity between the implementations

is shown for each combination, while the remaining phase noise,  $2[\varphi_{\text{TX}} - \varphi_{\text{TX}'}]$ , cancels out,

$$\begin{aligned}\Phi_{\text{DFBL}} - \Phi_{\text{FBBL}} &= \varphi_{\text{NR,DFBL}} - \varphi_{\text{NR,FBBL}}, \\ \Phi_{\text{FBBL}} - \Phi_{\text{FSFBL}} &= \varphi_{\text{NR,FBBL}} - \varphi_{\text{NR,FSFBL}}, \\ \Phi_{\text{FSFBL}} - \Phi_{\text{DFBL}} &= \varphi_{\text{NR,FSFBL}} - \varphi_{\text{NR,DFBL}}.\end{aligned}$$

With this calculation it is possible to analyze the noise behavior of the individual backlinks.

#### 4.4.2 Non-reciprocity of the Faraday rotator

The TBI experiment can also be used for measuring the phase stability of the Faraday rotator at mHz frequencies. A sketch of the possible set-up is shown in Figure 4.12. Six additional components are required, two mirrors, M1 and M2, three beam splitters, BS1, BS2 and BS3 and one half-waveplate that are partly placed outside of the TBI optical bench. Mirror M1 is placed behind the polarizing beam splitter pbs6. The TX beam is backreflected and passes the Faraday again, in opposite direction, as illustrated on the right of Figure 4.12. It leaves the pbs1 now by the second output port. This beam is interfered with the ALO at beam splitter BS2, forming the interferometer MEAS. The REF interferometer, initially required for the FSFBL, provides a phase measurement where the Faraday is only passed once by the TX beam. Another reference measurement between TX and ALO without the Faraday, REF2, is performed by using the reflection output port of the two attenuation beam splitters, att1 and att2. The additional beam splitter BS3 is used for the recombination of those two beams. The following phase signals are therefore measured by the three interferometers,

$$\begin{aligned}\varphi_{\text{REF}} &= [\varphi_{\text{TX}} - \varphi_{\text{ALO}}] + \varphi_{\uparrow} - \tilde{\nu}(\Delta\tau_{\text{REF}}), \\ \varphi_{\text{REF2}} &= [\varphi_{\text{TX}} - \varphi_{\text{ALO}}] - \tilde{\nu}(\Delta\tau_{\text{REF2}}), \\ \varphi_{\text{MEAS}} &= [\varphi_{\text{TX}} - \varphi_{\text{ALO}}] + \varphi_{\uparrow} + \varphi_{\downarrow} - \tilde{\nu}(\Delta\tau_{\text{MEAS}}),\end{aligned}$$

where  $\varphi_{\uparrow}$  is the phase increment of the TX beam when traveling through the Faraday crystal on the way in, and  $\varphi_{\downarrow}$  is the phase increment when traveling on the way back. The contribution of LFN does not cancel out in the signal combination, as it does for the non-reciprocity calculation for the backlink connection. Thus, it couples in each interferometer according to their individual arm length mismatches. The REF interferometer is already constructed quasi-monolithically and has an arm length mismatch of 8.2 cm according to Table 3.2. Therefore it is proposed to

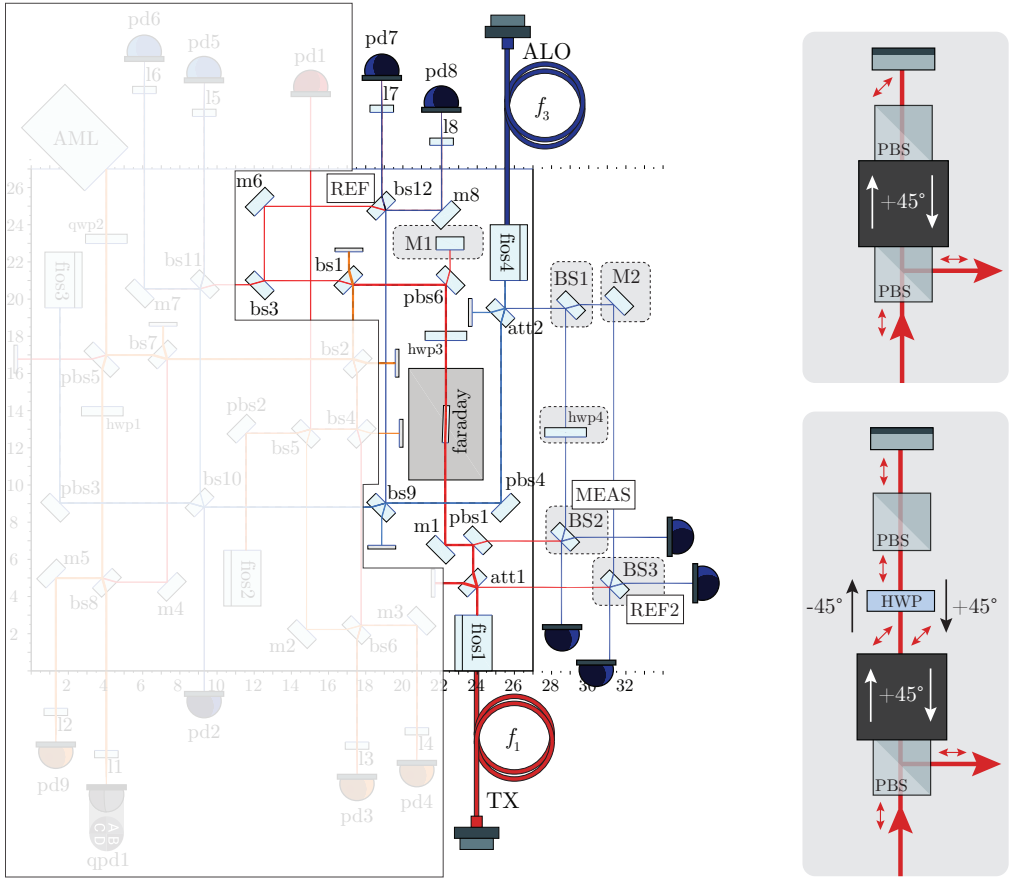


**Fig. 4.12.:** Experimental set-up for the measurement of the non-reciprocity of the Faraday isolator. The quasi-monolithic set-up of the TBI is equipped with two more mirrors, M1 and M2, and three additional beam splitters, BS1-BS3, here illustrated for the left bench (left). On the right, we show the polarization rotation caused by the Faraday crystal, with and without half-waveplate.

construct the additional two interferometers with the same arm length differences such that the LFN cancels out in the signal combinations,

$$\varphi_{\text{MEAS}} - \varphi_{\text{REF}} = \varphi_{\downarrow} - \tilde{\nu}(\Delta\tau_{\text{MEAS}}) + \tilde{\nu}(\Delta\tau_{\text{REF}}) = \varphi_{\downarrow}, \quad (4.9)$$

$$\varphi_{\text{REF}} - \varphi_{\text{REF2}} = \varphi_{\uparrow} - \tilde{\nu}(\Delta\tau_{\text{REF}}) + \tilde{\nu}(\Delta\tau_{\text{REF2}}) = \varphi_{\uparrow}. \quad (4.10)$$

The phase stability of the Faraday rotator is determined by these signal combinations, the non-reciprocal phase noise is provided by the difference of Equations (4.9) and (4.10). Even if LFN is not common mode and, thus, does not cancel out in the signal combinations, it does not limit the phase measurement according to

$$\delta f = \frac{2c_0\Delta x}{\Delta l\lambda_0} = \frac{2 \cdot 3 \cdot 10^8 \text{ m/s} \cdot 1 \text{ pm}/\sqrt{\text{Hz}}}{10 \text{ cm} \cdot 1064 \text{ nm}} = 5.6 \text{ kHz}/\sqrt{\text{Hz}}. \quad (4.11)$$

This calculation provides a number for the required laser frequency stability for interferometers having an arm length mismatch of 10 cm and a displacement sensitivity of 1 pm/ $\sqrt{\text{Hz}}$ . In the experiment, we expect a higher frequency stability of the laser sources since each one is stabilized to an iodine reference, having a frequency stability below 100 Hz/ $\sqrt{\text{Hz}}$ . The stability of the additional components will be critical for the achievable performance.

#### 4.4.3 Backscatter measurements of various fibers

The backlink fibers in the TBI are connected via fiber connectors to the FIOSs. Some unwanted additional reflections at these fiber connections could enlarge the backscattering from fibers, but this allows the use of a wider variety of backlink fibers. Different lengths and types of fibers can be connected to the TBI and their influence on the phase measurement can be investigated. Also interesting is the effect of radiation, which is analyzed in another experiment by Max Zwetz, at the time of writing this thesis. Different fibers, like various lengths, PM- and single-mode fibers and Zing<sup>TM</sup>-fibers [Fib], will be radiated with neutrons and gamma particles, the resulting fiber backscatter will then be measured. These fibers can later be connected to the TBI and the performance of a backlink with radiated fibers can be investigated. Especially Zing<sup>TM</sup> polarizing optical fibers have interesting properties which might be advantageous for high precision interferometry. According to the manufacturer, Fibercore Zing<sup>TM</sup> fibers guide only a single polarization through the fiber. The fiber acts as fiber-based polarizer and promises polarization extinction ratios of at least 30 dB/m over a wavelength window of  $\pm 50$  nm for different center wavelengths. This is achieved by using a bow-tie geometry PM fiber that can create extreme birefringence. Areas of boron-doped glass are integrated in the silica surrounding of the core along the slow

axis of the fiber. By inducing tension on the fiber the boron-doped material shrinks more than silica which causes birefringence. A higher index of refraction is therefore appearing parallel to the applied stress axis, and a lower index perpendicular to it [Fib].

#### 4.4.4 Dynamic range suppression of balanced detection

The prior fiber backlink experiment was able to reach the  $1 \text{ pm}/\sqrt{\text{Hz}}$ -goal by using balanced detection for suppressing the phase error caused by ghost beams. Two orders of magnitude must be subtracted by balanced detection in this experiment, while the fiber backscatter was assumed to be on the order of 20 ppm. Since it is assumed that this value might increase in LISA due to radiation effects in flight, it is necessary to investigate the maximum dynamic range of ghost beam suppression achievable with balanced detection. The TBI is an excellent test-bed for this purpose. It provides a large number of redundant sensors and the laser preparation set-up allows to tune the heterodyne frequencies in the interferometers. By matching the frequencies of the TX and ALO', and, vice versa, from the ALO and TX', the interferometers of the FSFBL are measuring a high ghost beam influence due to fiber backscatter at critical beat notes. An increased dynamic of the ghost beams is achieved if one installs a fiber length actuation by a ring PZT at which a small disturbance is applied. With these implementations the dynamic range of balanced detection can be tested.





# EXPERIMENTAL WORK AND RESULTS

” *Results of the free-beam backlink experiment  
and the current status of the TBI.*

The goal of the PRDSs discussed in this work is to achieve the target non-reciprocity of at most  $2\pi \mu\text{rad}/\sqrt{\text{Hz}}$  in the frequency band from 0.1 mHz to 1 Hz, equivalent to  $\approx 1 \text{ pm}/\sqrt{\text{Hz}}$  for a wavelength of 1064 nm. The noise characteristics of the two alternative backlink candidates, the FBBL and the FSFBL, will be compared in the TBI, with the prior, successfully tested direct fiber connection. A prior implementation of the FBBL has been conducted by commercially available adjustable components on two carbon fiber breadboards within the master thesis project of Lea Bischof [Bis18]. This free-beam experiment allows a full investigation of the experimental infrastructure of the TBI as described in the latter chapter, including the rotation of two interferometers relatively to each other in a fully equipped vacuum chamber. Additionally, the phasemeter, front- and back-end electronics, the free-beam feedback control loop and the temperature dissipation are also analyzed in this experiment.

Experimental results of the free-beam laser link between two optical set-ups that are co-rotating by  $\pm 1^\circ$  are presented in the first part of this chapter. The optical set-up of the free-beam pre-experiment is introduced first, together with the alignment procedure. Finally, the results of the phase performance are shown for the free-beam pre-experiment and the temperature dissipation in the vacuum chamber with and without bench rotation is discussed. This experiment demonstrates sufficient thermal stability during rotation of less than  $1 \cdot 10^{-4} \text{ K}/\sqrt{\text{Hz}}$  at 1 mHz and an operation of the free-beam steering mirror control over more than one week. The results shown here are also partly published in [Isl+18].

The two optical benches of the TBI are currently under construction. The status of the on-going construction work is given in the second part of this chapter.

## 5.1 Free-beam experiment

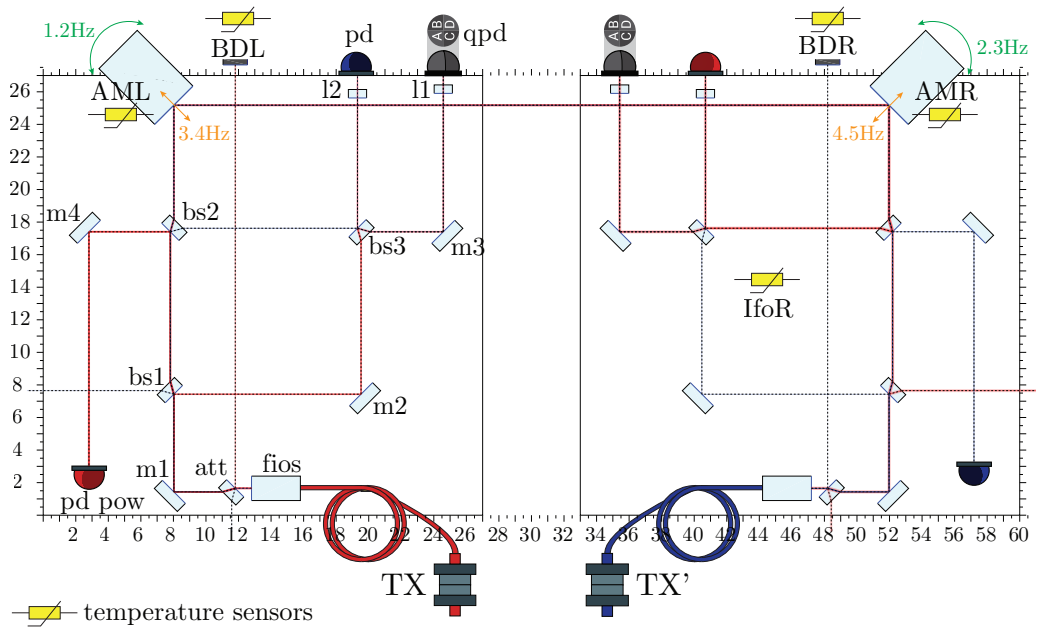
To test the thermal stability of our set-up during bench rotation, a preliminary interferometer was set up. We implemented a free-beam backlink prototype by which not only the experimental environment can be tested for the TBI, but also the FBBL control loops. It has been conducted with two optical benches realizing only this aspect of the TBI. The interferometer is also designed with IfoCAD and set up with off-the-shelf components and commercial fiber injectors placed on carbon breadboards, as shown in Figure 5.1. The dimensions of the set-up are the same as the ones planned for the TBI, using the same steering mirrors and similar beam parameters. In contrast to the TBI, we did not implement polarization encoding, but used a stronger beam attenuation, 99 % instead of 95 % reflectivity, at the input TX FIOS. By these means, we are able to fully pre-investigate and debug the measurement infrastructure of the TBI, on the one hand, and to test the rotary stages and the control loops required for the FBBL, on the other hand, using one single pre-experiment based on the same parameters.

### 5.1.1 Optical set-up

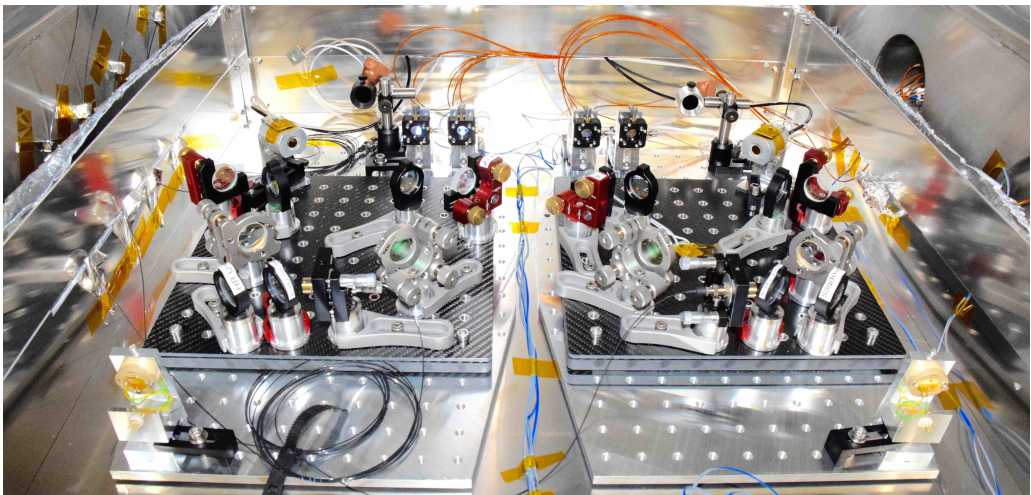
The free-beam experiment consists of two carbon fiber breadboard benches, each having a size of  $(270 \times 270)$  mm<sup>2</sup>. We use fiber collimators from Schäfter und Kirchhoff (SuK), producing a 1 mm diameter beam with a waist position at the local steering mirror position. The two TX beams are used for the free-beam experiment, each having an optical output power of 320 mW. 99 % of the light is split after the fiber output coupler and dumped into a snake-shape baffle that has a very low backreflection. The remaining 3.2 mW laser light power passes the attenuation stage. Half of the light is used for the local interferometry, the other half is again split, once for a power pick up and once for the light exchange between the two benches. Laser powers of 0.8 mW, for the reference beam, and 0.2 mW for the backlink beam are detected on each photodetector. Two QPDs, one per bench, are used as DWS sensors for the actuator mirror control loops. The other output ports of the recombination beam splitters are equipped with SEDs. We use the same photodiode assemblies as introduced in Section 4.2.1, but without thin film polarizers in front of them. The lens, mounted in the XY translational stage, allowed a precise beam alignment in the center of the QPD. The power monitor PDs were not used in the free-beam pre-experiment.

### 5.1.2 Alignment of the free-beam backlink

The alignment of the free-beam backlink of both, the pre-experiment and the TBI, must produce a collinear overlap of the in-bound and out-bound backlink beams



(a) 2D output of the free-beam pre-experiment generated with IfoCAD. fios: fiber injection optical subassembly, att: attenuation beam splitter ( $R = 99\%$ ), bs1-bs3: beam splitter ( $R = 50\%$ ), m1-m4: deflection mirrors, BDL/BDR: beam dumps left/right, AML/AMR: actuator mirror left/right.



(b) Photograph of the pre-experiment in the vacuum chamber surrounded by a thermal shielding.

Fig. 5.1.: Layout (a) and photograph (b) of the experimental set-up of the free-beam pre-experiment.

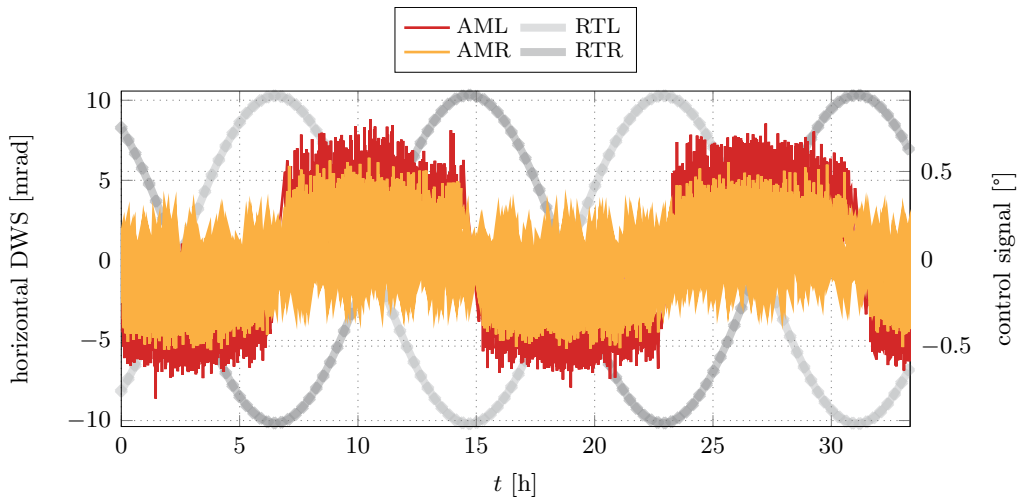
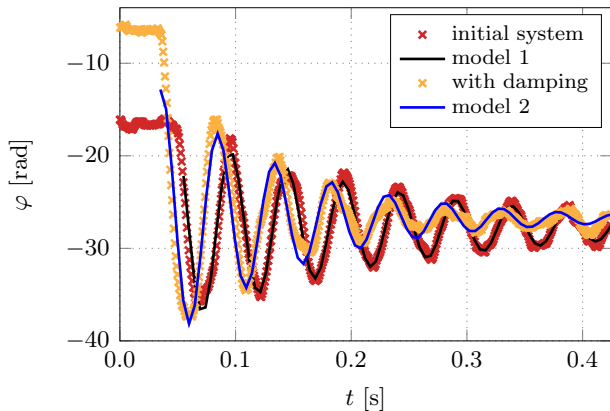


**Fig. 5.2.:** Time series of the rotary stage control signals of the free-beam pre-experiment operating in vacuum (right axis). The two rotary stages actuate on the interferometer benches with a period of  $T_L = 16.3795$  h and  $T_R = 16.3838$  h and an amplitude of  $0.9386^\circ$ . Also shown are the time series of the in-loop horizontal DWS signals of left actuator mirror (AML) and right actuator mirror (AMR) (left axis).

even while the benches are rotating relatively to each other. Otherwise, additional pathlength noise would couple into the phase measurement. In order to achieve this alignment separately on each bench, we temporarily block the FBBL connection with an adjustable PZT mirror that reflects the light back onto the local bench. The mirror is aligned in such a way that it couples the light back into the fiber coupler. With a fiber beam splitter, or rotator, the backreflection is optimized. By applying a sinusoidal small jitter motion on the PZT, the contrast in the FBBL interferometer can be observed and the interferometer on the one bench can be aligned. Finally, the temporary PZT mirror is removed and the two steering mirrors are aligned such that the contrast, that has previously been achieved purely with local beams, is recovered using the actual inter-bench beam combinations. This ensures the collinearity of the two opposing backlink beams while simultaneously achieving high interference contrast [Isl+18]. A similar procedure will also be used for the alignment of the FBBL in the TBI as described in Section 3.7.

### 5.1.3 Rotation of two benches relative to each other

First tests have shown that the two rotary stages can be rotated by  $0.75^\circ$  with a period of approximately 13.6 h. The motion of both stages is done simultaneously with a relative delay of less than 0.02 s. A time series measurement is depicted in Figure 5.2. Due to the use of stepper motors we observe phase jumps during rotation



	model 1	model 2
$\gamma$ [1/s]	5.22	8.57
$\omega_1$ [1/s]	129.35	128.38
$a$ [rad]	4.02e-18	-6.97e-30
$c$ [rad]	-27.69	-26.81
$b$ [rad]	-8.28	1.30
$f_1$ [Hz]	20.59	20.43
$\omega_0$ [1/s]	129.45	128.66
$f_0$ [Hz]	20.60	20.47

**Fig. 5.3.:** Measured optical phase during the motion of two co-rotating benches. The time series data for a single step of the two rotation tables is shown with and without eddy current damping. It shows an underdamped harmonic oscillator response for both cases with the damping factors  $\gamma$  and an oscillation at the ringing frequency  $\omega_1 = 2\pi f_1$ . The fitted model and parameters are shown in the table.

in the phase measurement tracked with the phasemeter, also shown in Figure 5.2 for the DWS signal. The minimum incremental stepper motion of  $0.0015^\circ = 26 \mu\text{rad}$  corresponds to an additional pathlength deviation of  $4.3 \mu\text{m}$  per step on each bench in the free-beam backlink path at the steering mirror position (163.45 mm measured from the rotary axis). The antisymmetric bench rotation produces a total accumulated pathlength for two simultaneous steps of  $8.6 \mu\text{m}$ , which corresponds to almost 9 cycles considering a wavelength of 1064 nm. This explains the observed cycle skips in the phase measurement. Furthermore, an underdamped oscillation with a frequency on the order of 20 Hz was observed, as shown in Figure 5.3, that is caused due to the set-up's resonance frequency being excited due to the stepper motion. An excitation of only the intermediate baseplates showed an oscillation frequency of 20 Hz, while the ground plate resonance frequency is at about 200 Hz [Bis18].

The integration of eddy current brakes can be used to damp the resonance frequency of the set-up. Copper plates are installed on top of the thermal shielding, below the intermediate baseplate. Two strong neodymium magnets are mounted in a stock on top of the intermediate plates. Each magnet has a holding force of about 18 kg. The distance between copper and magnet is on the order of 1 mm. The resulting damping is shown in Figure 5.3, also the models, including fitted

parameters, are shown in the table on the right. Both systems can be described by the model for an underdamped system, given by

$$f(t) = a \cdot e^{-\gamma \cdot t} \cos(\omega_1 \cdot t - b) + c \quad \text{with} \quad \omega_1 = \sqrt{\omega_0^2 - \gamma^2}, \quad (5.1)$$

where  $\gamma$  is the damping factor,  $\omega_1 = 2\pi f_1$  the ring-down frequency and  $\omega_0$  the natural frequency. For both systems the frequencies are very similar at about 20 Hz. The damping factor can be enhanced by 40 % with the implementation of eddy current damping from 5.22 1/s to 8.57 1/s.

The additional damping influences the rotation table control, leading to slight deviations from the desired motion with an amplitude of 0.9° (instead of 0.7°) and 16 h (instead of 13.6 h) period, equivalent to a frequency of about  $2 \cdot 10^{-5}$  Hz. By optimizing the control parameters for the driver the initial values for period and magnitude could be recovered [Isl+18; Bis18].

#### 5.1.4 DWS coupling coefficients

The actual actuator mirrors for the TBI are currently installed in the free-beam pre-experiment to test their behavior in a closed-loop operation mode. The coupling coefficients are measured by applying a sinusoidal motion to the steering mirrors with frequencies of 1.2 Hz, 2.3 Hz, 3.4 Hz and 4.5 Hz, as shown in Figure 5.1a. The coupling coefficients for the horizontal and vertical DWS control loops, calculated via Equation (4.3), are

$$K_{\Psi\Psi} = \begin{pmatrix} 9323 & 4689 \\ 5193 & 8794 \end{pmatrix} \frac{\text{rad}}{\text{rad}}; \quad K_{\Theta\Theta} = \begin{pmatrix} 6860 & 3561 \\ 3844 & 6476 \end{pmatrix} \frac{\text{rad}}{\text{rad}}. \quad (5.2)$$

And for the cross-coupling we measured residual coefficients of

$$K_{\Psi\Theta} = \begin{pmatrix} 445 & 168 \\ 92 & 33 \end{pmatrix} \frac{\text{rad}}{\text{rad}}; \quad K_{\Theta\Psi} = \begin{pmatrix} 132 & 24 \\ 104 & 107 \end{pmatrix} \frac{\text{rad}}{\text{rad}}. \quad (5.3)$$

We achieve a decoupling factor of about 1.7 in both mirror axes by using imaging lenses with a focal length of 25.4 mm in front of the photodiodes. These results are consistent with the optical simulations performed for the TBI, which yield to similar coupling coefficients of about 7600 rad/rad and 5200 rad/rad for the horizontal direction, and 3900 rad/rad and 2600 rad/rad for the vertical one (see Section 3.6.3). The according decoupling factors are therefore about 1.5, and the condition numbers  $\text{cond}(K_{\Psi\Psi}) = 5.7$  and  $\text{cond}(K_{\Theta\Theta}) = 5.2$ . For the measured matrices we achieve even smaller condition numbers of  $\text{cond}(K_{\Psi\Psi}) = 3.4$  and  $\text{cond}(K_{\Theta\Theta}) = 3.5$ , which can be explained by some misalignment of the free-beam link, leading to a further decoupling of the system, or the slightly different layout of

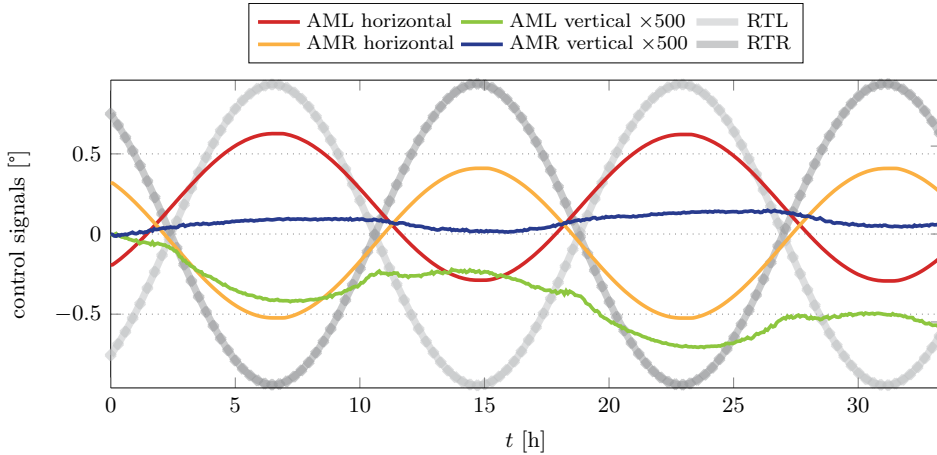


**Fig. 5.4.:** Time series of the steering mirror actuation signals. By monitoring the DWS signals on both benches, the actuation signals for the horizontal and vertical control loop of the steering mirrors are derived by calculating the mirror misalignments from zero. The actuation signals has been scaled to corresponding angle. The sinusoidal motion of the rotary stages is plotted as reference.

free-beam experiment and TBI. Furthermore, in the simulation we observe different coupling coefficients depending on the distance between lens and photodiode, which was not further optimized in this experimental set-up. This can also explain the deviation of experimental and simulated results as well as the deviation of the coupling coefficients between photodiodes. Ideally, the coupling coefficients should not change during rotation, as the simulations have indicated. The experimental measurements show a worst case deviation of 5% for  $0.75^\circ$  and  $-0.75^\circ$  bench rotation, which is slightly higher than the prediction of only 1.6% for a rotation of  $\pm 1.5^\circ$ . The beam parameters were not verified for this measurement, only rough collimation of commercial couplers are used, producing a beam waist of about  $800\ \mu\text{m}$ , which might explain this discrepancy.

### 5.1.5 Steering mirror control loop

After the coupling matrices are measured for the free-beam experiment, the inverse matrices are calculated and used for the calibration of the system. Linear combinations of the DWS signals provide the error signals for each mirror and axis according to the Equations (4.5) and (4.6). This is then fed into PID-controllers generating the actuation signals, as introduced in Section 4.3.1. A unity-gain frequency of 81 Hz for the horizontal direction and 105 Hz in the vertical, both exceeding a  $30^\circ$  phase margin, could be achieved. The difference between the unity-gain frequencies can be explained by the different gains between horizontal



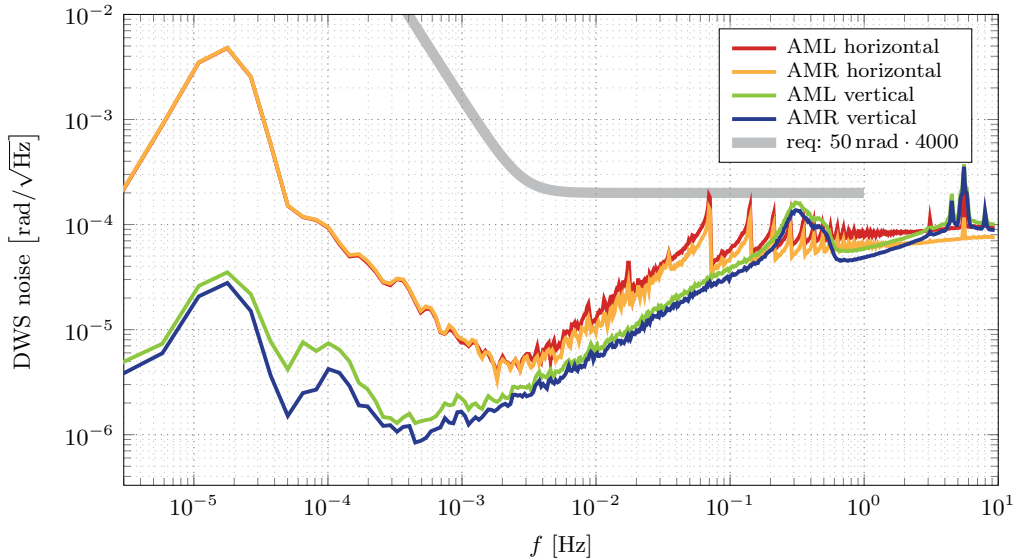


**Fig. 5.5.:** Linear spectral densities of the differential wavefront sensing signals corresponding to the left and right actuator mirror (AML and AMR) and both directions, horizontal (Figure 5.2) and vertical. The plotted requirement corresponds to 0.2 mrad DWS accuracy, with the assumption that the coupling coefficient from phase to DWS is at least 4000 rad/rad.

and vertical tilt, since the laser beam hits the surface under an AOI of  $45^\circ$  for the horizontal tilt, slightly changing during rotation, and under  $90^\circ$  for the vertical tilt, not changing during rotation. The gain difference between the two control loops is therefore about a factor of  $\sqrt{2}$ , which is derived by geometry. This is nearly the same factor as the one between the two unity-gain frequencies.

With the imaging lenses integrated into the free-beam pre-experiment a closed-loop operation during bench rotation could be achieved. For this, the two benches are co-rotated against each other. The interferometers were locked over the full period of 32 h while the benches were rotated by  $\pm 0.9^\circ$  relatively to each other. The actuation signals for both mirrors on both axes, horizontal and vertical, are shown in Figure 5.4, together with the sinusoidal motion of the rotary stages. The horizontal actuation signals follow the motion of the benches and compensate the beam tilt during this longterm measurement. Due to the initial offset the actuation is not fully symmetric. The vertical actuation signals are enhanced by a factor of 500 in this plot and show the remaining cross-coupling of horizontal bench rotation into DWS signal. This is caused by misalignment of the QPDs, a residual offset in the transformation of the mirror axes from  $45^\circ$  to  $90^\circ$  and by a wobble motion of the rotary stages.



The horizontal DWS signals for both benches are shown in Figure 5.2. The jumps caused by the stepper motors in the rotary stages are visible in the time series of the DWS signal, but also as spikes in the spectral densities shown in Figure 5.5. One should note that the non-stationary behavior of the spikes somewhat limits the meaningfulness of the spectral density in this case. To estimate whether the spikes will limit the performance of the free-beam connection, a DWS requirement has been derived. For this calculation we use the simulation results from Section 3.6.1 where a pathlength coupling of 20 pm/ $\mu$ rad is measured for a interferometer with misaligned recombination beam splitter (10  $\mu$ m displacement misalignment). For achieving a displacement noise of 1 pm/ $\sqrt{\text{Hz}}$ , any beam pointing fluctuations must be below 50 nrad/ $\sqrt{\text{Hz}}$ , resulting in a DWS noise requirement of 0.2 mrad/ $\sqrt{\text{Hz}}$  if one assumes a coupling coefficient on the order of 4000 rad/rad. The measured DWS noise is below this requirement and even the spikes do not limit the performance. Further post-corrections can also be applied in case of insufficient closed-loop suppression of the steering mirror control if the DWS sensing noise is below the requirement [Isl+18].

### 5.1.6 Long term phase measurements

We performed two identical measurements on each bench by monitoring both ports of the recombining beam splitters, bs2, by using the SED and the QPD. The QPD is also used to monitor the respective in-loop DWS signal. The SED measured therefore the out-of-loop phase noise and serves as a diagnostic reference measurement. This photodetector constellation provides five phase signals in total per bench. For the left bench we detect the SED phase signal,  $\varphi_{\text{SED}}$ , and the phase signals of the four segments of the QPD,  $\varphi_{\text{A}}$ ,  $\varphi_{\text{B}}$ ,  $\varphi_{\text{C}}$  and  $\varphi_{\text{D}}$ . The right bench detects the same signals, but we will prime those phase notation in the following,  $\varphi'_{\text{SED}}$  and  $\varphi'_{\text{QPD}}$ . The calculation of the total phase of a QPD is based on the equations given in Section 1.3.3. The investigation of noise sources in the current experimental set-up makes use of different combinations of these phase signals. The so-called  $\pi$ -measurement compares the two output ports of a single recombination beam splitter. The difference of the corresponding phase signals,

$$\varphi_{\pi} = \varphi_{\text{SED}} - \varphi_{\text{QPD}} \approx \pi, \quad (5.4)$$

theoretically reduces to a constant phase shift of  $\pi$ . All photodetectors and segments show a similar noise behavior that is given by the red curve in Figure 5.6. Also shown are the phase linear spectral density of the  $\pi$ -measurement on the left,  $\varphi_{\pi}$ , by the orange curve and on the right bench,  $\varphi'_{\pi}$ , by the green curve. Here, a typical stray light noise shoulder is observed in both spectra with different noise levels. Additional spurious beams on the left photodiode likely lead to a shoulder

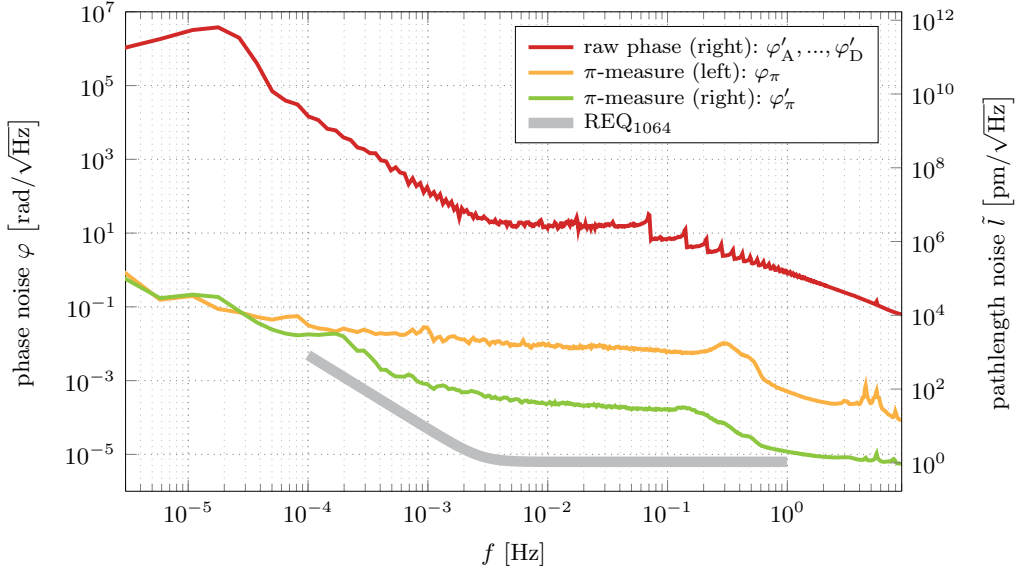


Fig. 5.6.: Optical phase noise measured in the free-beam pre-experiment including results of a  $\pi$ -measure. Shown are the raw phase measurement on the right bench of each QPD segment,  $\varphi'_A, \dots, \varphi'_D$ . The  $\pi$ -measurements,  $\varphi_\pi$  and  $\varphi'_\pi$ , are formed by combining the phase measurements of the two redundant photodetectors located at the two beam splitter output ports for each bench.

noise level of  $1 \cdot 10^{-2} \text{ rad}/\sqrt{\text{Hz}}$  while the photodiode on the right shows almost two orders of magnitude less noise in its phase measurement. A detailed analysis of the time series shows that the absolute phase of the spurious light beam increases to 15 mrad during each semi-period and becomes minimal at the reversal points. Without motion the phase of the spurious light is in the range of 3 mrad. The right photodiode monitors a spurious beam with a phase magnitude of 0.75 mrad.

For the investigation of the backlink connection, the signals of both benches are combined by calculating the phase sum of the two benches according to Section 4.4.1,

$$\Phi_{\text{SED}} = \varphi'_{\text{SED}} + \varphi_{\text{SED}} = \varphi_{\text{NR}} + 2\varphi_{\text{CPN}},$$

This combination contains the non-reciprocity,  $\varphi_{\text{NR}}$ , and a common phase noise (CPN) term,  $\varphi_{\text{CPN}}$ . A direct measurement of the non-reciprocity would require a reference signal to subtract the CPN term from  $\Phi_{\text{SED}}$ , which consist of the differential phase between the TX and the TX' beam,  $2[\varphi_{\text{TX}} - \varphi_{\text{TX}'}]$  (see Section 4.4.1), and some other pathlength noise due to the non-monolithic set-up. However, a

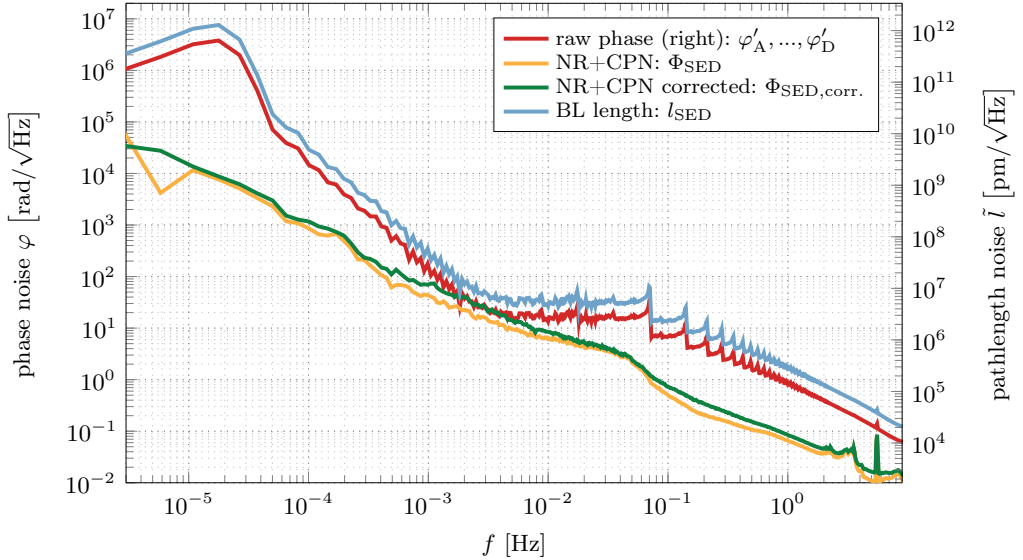


**Fig. 5.7.:** Non-reciprocal phase noise measured in the free-beam pre-experiment without reference subtraction. Shown are again the raw phase measurement of the right QPD. The phase sum between left and right measured signal,  $\Phi_{\text{SED}}$ , shows an upper limit for the non-reciprocity, since the common phase noise (CPN) term cannot be subtracted due to the missing reference measurement. The differential phase between left and right measurements provides an absolute length measurement of the backlink path,  $l_{\text{SED}}$ , including LFN.

reference measurement has not been implemented in our pre-experiment. The last combination is the difference of the left and right benches' phase signals

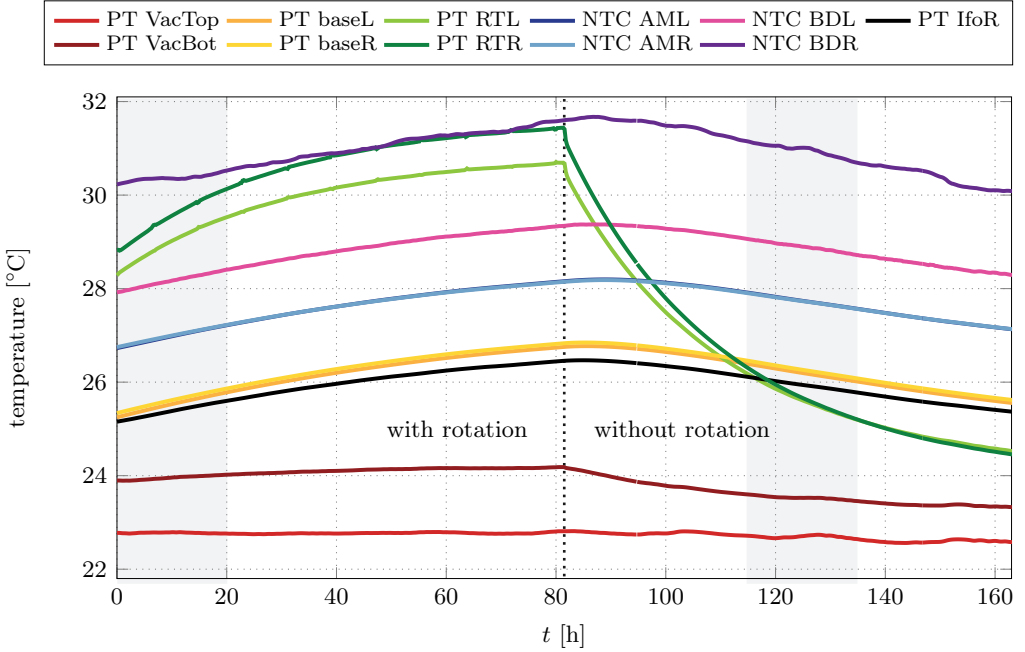
$$l_{\text{SED}} = \varphi'_{\text{SED}} - \varphi_{\text{SED}},$$

which directly corresponds to twice the length of the backlink path and includes LFN. Figure 5.7 shows the linear spectral densities of the measured phases along with their relevant combinations. The pathlength change,  $l_{\text{SED}}$ , due to the rotation is proportional to the motion itself, which was to be expected. This is demonstrated in the spectrum by the light blue curve, showing the same oscillation pattern as the spectrum of the horizontal DWS from Figure 5.5. The phase combination,  $\Phi_{\text{SED}}$ , exhibits a  $1/f$  decrease in the spectral density with  $65 \text{ mrad}/\sqrt{\text{Hz}}$  at  $1 \text{ Hz}$ , which is equivalent to  $16 \text{ nm}/\sqrt{\text{Hz}}$  at  $1 \text{ Hz}$ . However, the goal of the free-beam experiment has never been to reach the  $1 \text{ pm}/\sqrt{\text{Hz}}$  noise level, but rather to investigate and improve upon its operational reliability and temperature behavior as well as our electronics and laboratory infrastructure. The main reason for this significant deviation is the missing phase reference measurement. In the TBI,

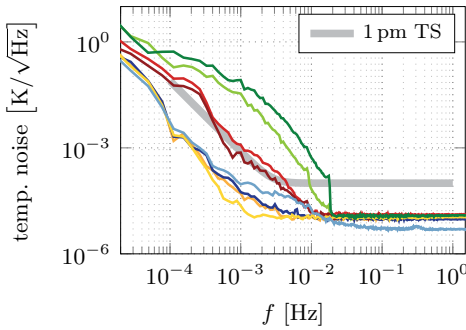
the other backlink interferometers will provide potential reference measurements, especially the direct fiber backlink since it has already undergone a full investigation. Therefore, the CPN term can be eliminated as shown in Section 4.4.1. Considering the fact that, unlike the TBI, the pre-experiment did not rely upon a quasi-monolithic set-up and includes no complex spurious beam suppression whatsoever, all contributing to the CPN term, these results are already on the right order of magnitude and constitute a good intermediate achievement. The excess noise is driven by phase noise from the laser preparation in air and two 12 m long fibers. In the TBI the direct fiber backlink will be used as local reference with  $1 \text{ pm}/\sqrt{\text{Hz}}$  non-reciprocity, enabling us to measure the phase noise behavior of the other phase references down to the same level. Furthermore, the TBI's performance will improve through ghost beam suppression, usage of a quasi-monolithic set-up, polarization cleaning, power stabilization and potentially fiber length stabilization. We are optimistic that we will be able to reach the requirement with the improvements mentioned before in the TBI itself, based on the detailed design presented earlier in Chapter 3.

### 5.1.7 Thermal measurement results

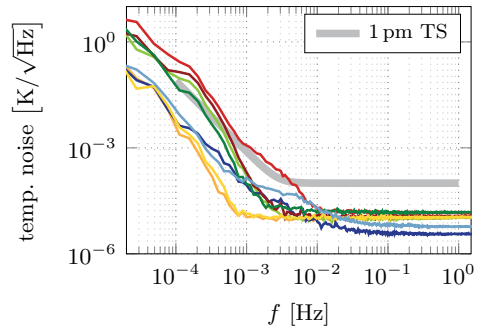
To verify the thermal stabilities we read out the temperature sensors at critical points throughout the experiment. We attached 16 temperature sensors of two different types, PTC and NTC, to the inside of the vacuum tank and to the most critical components. Figure 5.1a and Figure 4.4 show the positions of a selected few that are relevant for the analysis, while the measurement results are compiled in Figure 5.8. The temperature behavior in the evacuated vacuum chamber was monitored over several days, here 160 h are shown. During the first 80 h measurement the two benches were rotating against each other by  $0.9^\circ$ , while the following 80 h data was monitored without bench rotation. The time series plot shows the predicted temperature drop when the rotary table motion was turned off. In both cases the actuator mirrors are supplied with control voltages, but, for the second case, these turn out to be almost constant. The increase of the absolute temperatures during rotation, which can be observed in the first half of the time series, was to be expected. This effect is very significant for the rotary tables themselves, which reach a maximum temperature of  $31.4^\circ\text{C}$  in this measurement, corresponding to an increase of  $2.6^\circ\text{C}$  over 80 h. The highest temperature, namely  $31.6^\circ\text{C}$ , is measured at one of the beam dumps, while the most stable temperature could be observed at the ceiling plate inside the vacuum chamber. Once the motion of the tables is completed the temperatures start to decrease. Again, this is most significant for the sensors on the rotary tables. They detect a decrease of  $7^\circ\text{C}$  down to  $24.4^\circ\text{C}$ .



(a) Time series of the temperatures for an evacuated chamber with and without rotating tables.



(b) Temperature noise during rotation.



(c) Temperature noise without rotation.

**Fig. 5.8.:** Measured absolute temperature and noise inside the vacuum chamber with rotating free-beam experiment inside. PTC and NTC thermistors are used to monitor various locations in the vacuum chamber, as shown in Figures 5.1a and 4.4. The lower two plots show the linear spectral densities of the temperatures for the time intervals highlighted in the time series plot above for selected temperature sensors. The requirement for the thermal stability (TS) is derived from a  $1 \text{ pm}/\sqrt{\text{Hz}}$  displacement stability and is  $0.1 \text{ mK}/\sqrt{\text{Hz}} \cdot \text{NSF}(f)$ .

The linear spectral density graphs below the time series plot display the temperature noise for both cases. The highlighted areas in the time series mark the sections used for the calculation of the spectra. As reference, a requirement for the thermal stability (TS) is also plotted that is derived from a  $1 \text{ pm}/\sqrt{\text{Hz}}$  displacement noise. For this we assume that the interferometer has an absolute arm length mismatch of  $1 \text{ m}$  at maximum and the optical bench an CTE of  $1 \cdot 10^{-8} /\text{K}$  which provides a coupling coefficient from temperature fluctuations to displacement changes of  $1 \cdot 10^{-8} \text{ m}/\text{K}$ . For achieving the above mentioned displacement noise a TS of about  $0.1 \text{ mK}/\sqrt{\text{Hz}}$  must therefore be reached, here relaxed by the NSF towards lower frequencies. With rising absolute temperature, also the noise levels of the temperature of the rotary tables increase for frequencies up to  $2 \cdot 10^{-2} \text{ Hz}$ , while the noise levels stay mostly stable at about  $1 \cdot 10^{-5} \text{ K}/\sqrt{\text{Hz}}$  and is reached somewhere between  $2.2 \cdot 10^{-3} \text{ Hz}$  and  $1.8 \cdot 10^{-2} \text{ Hz}$ . The most relevant temperature behavior with regard to the TBI is the thermal stability of the two rotating intermediate baseplates (baseL and baseR in Figure 4.4), carrying the interferometric benches. For both cases, with and without rotation, the two relevant sensors (orange and yellow curves) attest to a sufficiently low temperature noise of  $1 \cdot 10^{-4} \text{ K}/\sqrt{\text{Hz}}$  at  $1 \text{ mHz}$  [Isl+18]. Since the rotation tables are the main source of temperature noise during operation an active temperature stabilization of them might be beneficial in the future.

### 5.1.8 Beam dumps characterization

Since the TBI showed a large amount of ghost beams in the optical simulations, small beam dumps have been designed and ordered which can be placed at critical points on the optical benches. They have an obelisk-shape and are made of the filter glass KG5 which has a high absorption for a wavelength of  $1064 \text{ nm}$ . Each side surface is angled by  $3^\circ$  such that eventual backreflections leave the interferometer plane. Furthermore, the used material ensures a very high absorption such that only about  $0.012\%$  of the light is transmitted for  $2 \text{ mm}$  propagation length, and only  $0.095\%$  is reflected by the AR-coated, polished surfaces. Experimental measurements verified these statements of the manufacturer. The transmission at the beam height in the TBI of  $15 \text{ mm}$  is even lower, since the obelisk has a thickness of  $2.5 \text{ mm}$ , relating measurements have shown that only  $0.0012\%$  is transmitted for this beam height [Bis18]. Differential temperature rises of  $0.9 \text{ K}$  and  $21 \text{ K}$  have been measured in an evacuated environment once for a beam with  $15 \text{ mW}$  optical power, and once for a  $300 \text{ mW}$  beam. Even though the obelisk is not damaged after radiating it with high power laser beams, the obelisk is still heated up to temperatures above  $40^\circ\text{C}$ , which makes this type of beam dumps not ideal for blocking high power beams directly on the optical bench, like those that

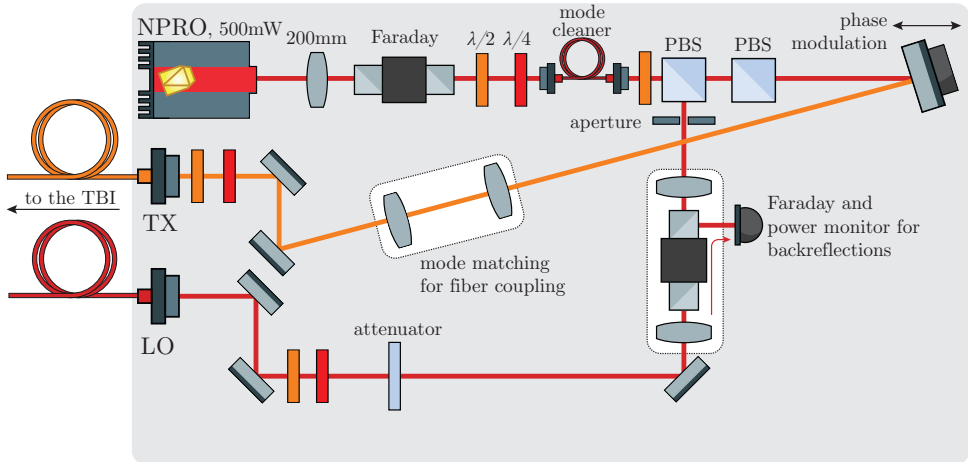


Fig. 5.9.: Optical set-up of the laser preparation in the cleanroom [Bis18]. A 500 mW NPRO laser is prepared by using waveplates and a Faraday isolator, a fiber is used as mode cleaner.

are generated by the attenuation beam splitters in the TBI. Thus, another type of beam dump in the shape of a snail made from metal will be used, from which the in-bound light cannot escape [Bis18]. Those were originally designed for the LISA optical bench.

## 5.2 Status of the Three-Backlink interferometer

During time of writing this thesis, the first optical bench of the TBI is constructed in the cleanroom by a team consisting of Oliver Gerberding, Daniel Penkert, Lea Bischof, Juliane von Wrangel and the author. A dedicated laser modulation bench is prepared for this purpose, providing two laser beams that are coupled into fibers and can be used for the construction of the TBI.

### 5.2.1 Laser modulation bench

Two beams with adjustable optical power levels are required to simulate the injected TX and LO beams. For contrast monitoring between those two a sinusoidal phase modulation is injected on one of these via a PZT mirror on the modulation bench. An NPRO laser is set up on the optical table in the cleanroom, having an output power of 500 mW. A combination of half-waveplate and PBS is used to split the beam into two arms and also to adjust the optical power ratio between these two paths. One arm is equipped with a PZT mirror for injecting the phase modulation on it. The laser beam is then coupled into a fiber and will mainly be used as TX

beam for the TBI. The second arm has an additional variable attenuator (gray filter) for further reducing the optical power if desired. A Faraday isolator is also integrated in this path by which eventual backreflected light coming from the TBI can be detected. The beam is coupled into a second fiber afterwards [Bis18].

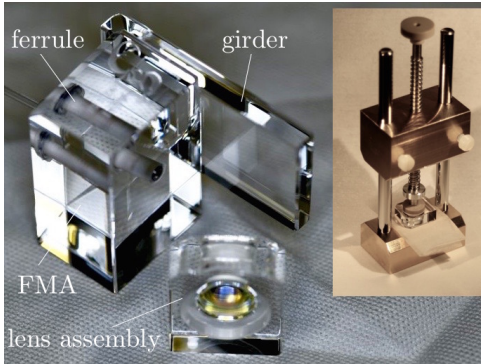
### 5.2.2 Monolithic fiber output couplers

An evolved version of the FIOSs that are currently used in the Hexagon experiment [Sch15; Sch18] is foreseen to be used in the TBI, developed by Daniel Penkert. The construction procedure of these components has been optimized whereby the accuracy of the beam height, polarization state and mode can be better matched to the desired values. As first step the ferrule of the fiber is inserted into the fiber mount assembly (FMA). Because of the extremely tight fit of ferrule into FMA a handle is required. The polarization is adjusted by the orientation of the ferrule's handle and monitored by a polarimeter. For the TBI we are aiming for a clean s-polarization. The ferrule is then glued with UV epoxy into the FMA, which is then glued to the longitudinal girder afterwards. Figure 5.10a shows all parts of the FIOS, while the lens is not yet glued to the assembly. The inlet in this figure shows the glueing process of the lens into its holder by applying a well-defined amount of pressure via a spring onto the lens outer area [Sch15; Pen16].

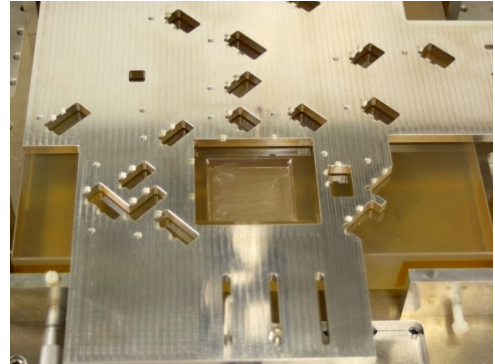
### 5.2.3 Monolithic set-up

For the FIOS we use a UV epoxy from Optocast (3553-LV-UTF) instead of hydroxide catalysis bonding. With this technique the optical components can be adjusted relative to each other with small layers of glue in-between until the desired alignment is achieved. By radiating the layer of glue with a UV wavelength of 365 nm (Norland Opticure LED 200), the glue will cure and the positioning is permanent. The final construction of the FIOS will be done directly on the optical bench. Figure 5.10b shows the template for the left bench of the TBI which is positioned below. The template is adjusted with respect to the hole for the Faraday rotator mount. This mount is then glued to the baseplate by using a two-component epoxy (Hysol EA9461) with 100  $\mu\text{m}$  ceramic balls for controlled layer width. During the curing process the mount is pushed in the three-point positioning spheres in the template with an elastic band that is spanned between the mount and a beam screwed into the template, as shown in Figure 5.10c. Figure 5.10d shows the front of the Faraday. Some optical components are already glued with the UV epoxy. As next step the first FIOS, providing the TX beam, must be integrated on the optical bench. The FIOS alignment tool is shown in Figure 5.10e and is roughly adjusted to the desired FIOS position. Figure 5.10f shows how the FIOS parts are held by the tool and how they can be moved against

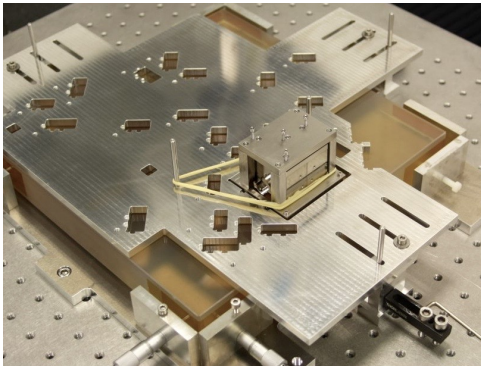




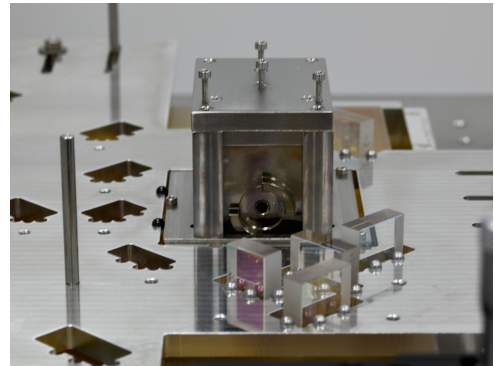
(a) Parts of the quasi-monolithic FIOS and the lens glueing tool.



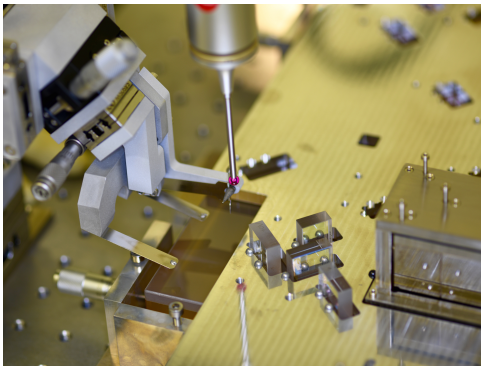
(b) Template is aligned with respect to the notch in the baseplate for the Faraday rotator.



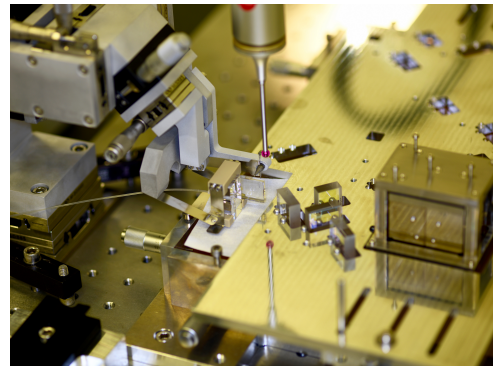
(c) Positioning of the Faraday rotator, the mount is glued with two-component epoxy.



(d) First batch of optical components is glued with Optocast UV glue.



(e) Positioning of the FIOS alignment tool next to the optical bench via CMM.



(f) Parts of the first FIOS during the construction process on the optical bench.

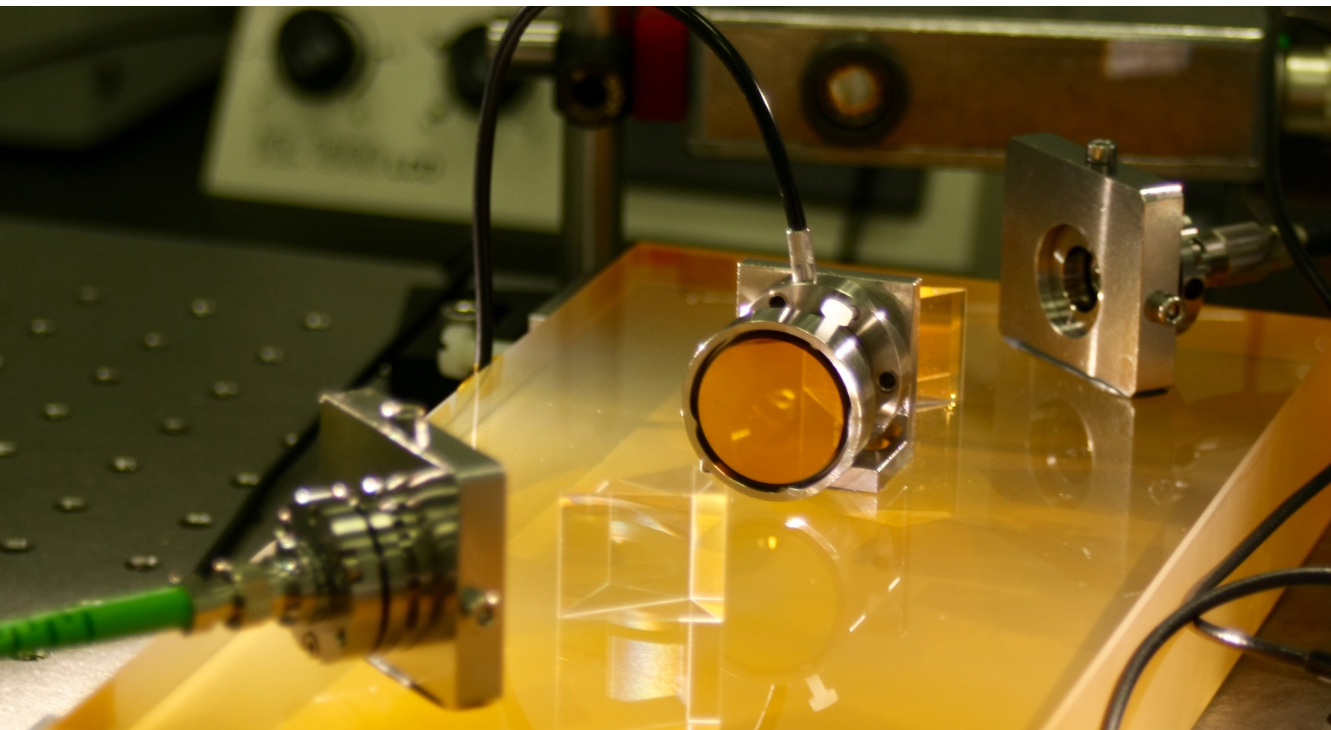
**Fig. 5.10.:** Shown are the different alignment stages of the construction process for the TBI in the cleanroom. A CMM ensures an accurate positioning of the template by which the uncritical components are bonded. The fiber injection optical subassembly (FIOS) is assembled directly on the optical bench and adjusted.

each other to adjust the beam height, propagation direction and waist position. The measurement of the beam propagation direction is critical for this step, since any vertical misalignment cannot be compensated afterwards. The current method of using the ruby ball of the CMM as lens and measuring the beam position with a QPD at two different positions is rather time consuming [Sch+14b] and under review to ensure the desired beam alignment accuracies for the free-beam link (Section 3.6.1) are achieved. An accelerated beam alignment might be achieved by a so-called calibrated QPD pair [Fit+13; Deh12], which is investigated in parallel as alternative approach. While the TBI construction is expected to require a fair amount of further effort, we are highly confident that the experiment will be able to achieve the desired performance in the end. This stems both from the detailed design laid out in this thesis and from the inclusions of a number of methods and techniques that were found to be critical for LISA interferometry experiments in the past [Deh12; Fle12; Die13; Ger14; Sch18; Arm+18].

# Part II

---

Deep frequency modulation interferometry:  
Advanced optics for space applications





# MULTI-CHANNEL INTERFEROMETRY

” *Fundamentals about test mass interferometry and alternative interferometer techniques that can be used to simplify optical set-ups in the future.*

High precision interferometry with a dynamic range over multiple interference fringes is the core metrology technique for the space-based low-frequency gravitational wave detector LISA [aC13]. This technology is also well suited as auxiliary readout system for ground-based detectors, for example for suspension point interferometry [Dah+12]. One very promising concept is to apply such a readout not only to a single test mass in one direction, but to all DoFs of multiple test masses in a gradiometer configuration. It is expected that the usage of optical interferometry will significantly increase the sensitivity of current accelerometers using electrostatic readout [Tou+99]. This would be of great benefit for future geodesy missions that aim to improve on the gravity sensing capabilities of missions, such as GRACE-FO [She+12] and GOCE [Dri+06]. The classic heterodyne interferometry used for the 2-test-mass-readout in LPF is too complex to be adapted for e.g. six test masses and a full optical readout of all 36 DoFs [Isl+16b]. Reduced optical complexity is therefore an attractive improvement considering satellite missions, especially those that aim to measure many DoFs of multiple test masses. Within the project A07 of the SFB geo-Q multi-channel interferometry optics are developed for future gradiometer applications. New interferometer schemes using different phase modulation techniques, like digital interferometry (DI) [Isl+14; Sut+12; Sha07; DV+09], deep phase modulation (DPM)[Hei+10; Sch+14c] and deep frequency modulation (DFM) [Ger15; Isl+16b], are currently investigated to simplify the optical part of future experiments in gravitational physics and for metrology experiments.

The basic concepts of test mass interferometry are introduced first in this chapter, together with the interferometric readout noise sensitivity that is required for future



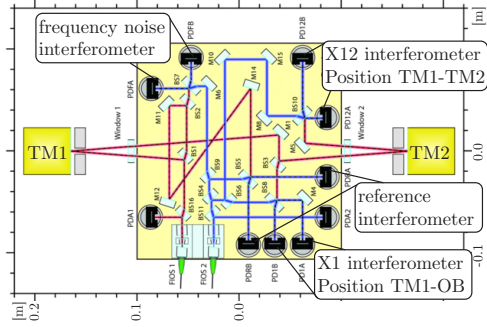
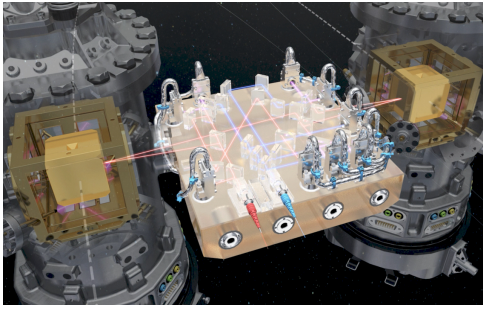
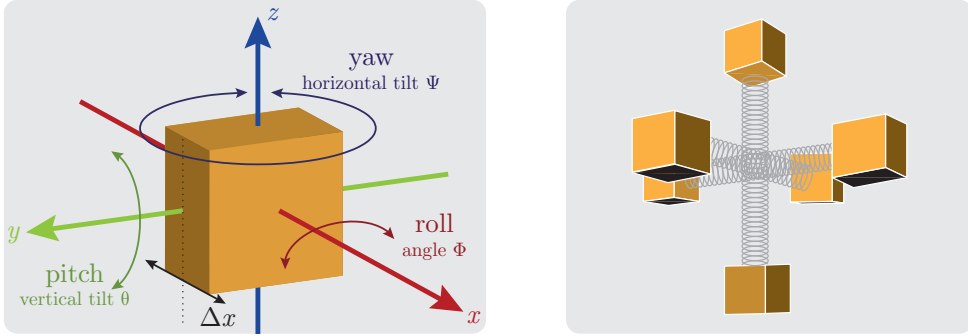


Fig. 6.1.: Optical bench of LISA Pathfinder. On the right, the interference points of the four interferometers are highlighted: the phase reference interferometer, the frequency noise interferometer, the X1 interferometer measuring the relative motion between OB and test mass, and the X12 interferometer sensing the relative displacement and angle between the two test masses. Image credit: [ESA18] and [Rob+13].

geodesy missions. After this the core interferometer technology in this thesis, deep frequency modulation (DFM), will be introduced in detail and its potential to be used as key technology for future miniaturized optical sensors, e.g. for multi-channel test mass interferometry, is highlighted. Alternative phase modulation interferometer techniques and their advantages, or disadvantages, are introduced afterwards. In the last section a comparison between the interferometer techniques is given and their individual, possible application fields are studied.

## 6.1 Test mass interferometry

Classic test mass interferometry, as applied in LPF, uses heterodyne interferometers to measure differential test mass motions. Figure 6.1 shows a model and the optical layout of the optical bench in LPF. The optical metrology subsystem of LPF, responsible for the readout of position and angles of the test mass, consists of four units. The laser unit provides a Nd:YAG NPRO laser with a wavelength of 1064 nm and an optical output power of about 40 mW. The laser modulator unit splits the laser light into two beams. Each one passes an AOM which shifts the laser frequency of each by 80 MHz and 80.001 MHz, respectively. The next unit is the optical bench interferometer onto which the prepared beams are injected. The phasemeter unit is used for converting the photocurrents into digital signals and for extracting the phase information via a heterodyne demodulation scheme. The optical bench interferometer of LPF is the unit of interest for the work presented in this part of the thesis. It contains four heterodyne interferometers in total, each providing an optical signal with 1 kHz beat note that is measured



**Fig. 6.2.:** Definition of displacement and yaw, pitch and roll angle of a test mass and a six-test mass gradiometer in cross-shape constellation.

by QPDs. The reference interferometer provides a phase reference, similar to the reference interferometer in LISA. It delivers the error signal used for the pathlength stabilization between the two laser beams. The frequency noise interferometer has an arm length difference of about 384 mm which enhances its sensitivity to LFN such that this interferometer is used as frequency reference. The relative motion between the first test mass and optical bench is measured by the so-called X1 interferometer. It measures three DoFs, the displacement along the  $x$ -axis and the pitch and yaw angles,  $\Theta$  and  $\Psi$ . Figure 6.2 shows the definition of these motions. The X1 interferometer is not sensitive to other displacement directions or the roll angle. The main interferometer, measuring the relative motion of displacement and angle between the two test masses, is the X12 interferometer. The LPF mission aim was to achieve an accuracy of  $6.3 \text{ pm}/\sqrt{\text{Hz}}$  and  $20 \text{ nrad}/\sqrt{\text{Hz}}$  in the frequency range of 1 mHz to 30 mHz for the measurement of relative test mass motion and tilt, a requirement that has been derived from the desired test mass acceleration sensitivity. This could be achieved and even exceeded as the experimental results of the mission have shown [Arm+18].

With a dedicated AC readout, heterodyne interferometry allows us to measure very large phase signals with dynamics greater than  $2\pi$ , while the usage of quasi-monolithic set-ups shows that low displacement sensitivities on the order of a few  $\text{pm}/\sqrt{\text{Hz}}$  are measurable on ground [Deh12; Deh+12] or even better in space [Arm+16]. However, classic heterodyne interferometry requires complex optical set-ups for generating two coherent beams with a constant frequency offset between them. Typically, AOMs and radio frequency (RF) power amplification are used for the associated frequency generation of each beam. This scheme of using a second laser beam requires always an additional reference interferometer, measuring the phase noise between the two beams. This noise is driven by the injection

fibers, the AOMs or other non-common mode devices. Considering multi-channel test mass readout with six or more test masses, forming three gradiometers in a cross-shape constellation as depicted in Figure 6.2, the complexity per bench would massively increase by simply adopting the heterodyne scheme of LPF. Upscaling the LPF two-test mass readout scheme would make the optical unit for future gradiometers very complicated, complex and heavy. To overcome these fundamental limitations of heterodyne interferometry, other methods, using sinusoidal phase shifting interferometry, have been investigated. [SO86; Sas+87; GD08; Gro09; Fal+09; Kis+15]. These alternative techniques promise more compact optical set-ups, while achieving interferometer sensitivities that are similar to the one achieved with LPF and LISA technology. The gained simplicity of the optical part leads to more complexity in other units, prominently the phasemeter unit, where the desired phase information must be recovered from the complex photocurrent spectrum.

For future geodesy missions we aim to have a gradiometer noise of  $n_g = 1 \cdot 10^{-4} \text{ E}/\sqrt{\text{Hz}}$ , equivalent to  $1 \cdot 10^{-13} \text{ s}^{-2}/\sqrt{\text{Hz}}$ . From this the interferometric readout noise sensitivity,  $n_i(f)$ , can be determined by

$$n_i(f) = \frac{L}{6\sqrt{2}} \cdot \frac{n_g}{(2\pi f)^2 + \omega_s^2} =: \text{SG}(f) \quad (6.1)$$

with a gradiometer lever arm of  $L = 1 \text{ m}$  and an electrical stiffness of  $\omega_s^2 = 8.27 \cdot 10^{-4} \text{ s}^{-2}$ . The desired displacement requirement is derived directly from Equation (6.1) and is defined in the frequency range between 0.5 mHz and 10 mHz as

$$\text{SG1}(f) = \frac{1 \text{ m}}{6\sqrt{2}} \cdot \frac{1 \cdot 10^{-13} / \sqrt{\text{Hz}}}{[2\pi f / (1 \text{ Hz})]^2 + 0.827 \, 413 \, 638 \cdot 10^{-3} \text{ s}^{-2}}. \quad (6.2)$$

In absolute values the displacement requirement is about  $14 \text{ pm}/\sqrt{\text{Hz}}$  at 0.1 mHz and  $2.5 \text{ pm}/\sqrt{\text{Hz}}$  at 10 mHz, which shows the similarity between the LISA mission and future geodesy concepts. A more strict requirement defined for frequencies between 0.5 mHz and 20 Hz, is given by

$$\text{SG2}(f) = \frac{1 \text{ m}}{6\sqrt{2}} \cdot \frac{1 \cdot 10^{-13} / \sqrt{\text{Hz}}}{[2\pi f / (1 \text{ Hz})]^2 + 0.827 \, 413 \, 638 \cdot 10^{-3} \text{ s}^{-2}} \cdot \frac{1}{1 + [f / (6 \text{ mHz})]^3}, \quad (6.3)$$

which leads to a similar interferometer readout noise at low frequencies but shows a higher constraint at 10 mHz with  $0.4 \text{ pm}/\sqrt{\text{Hz}}$  [Dou+17b; Dou+17a; Dou+17c].

Most of the interferometers using phase shift keying methods are typically designed for measurements on very short time scales. Our goal is to measure continuously in real time over long timescales with a high sensitivity at low frequencies.



## 6.2 Deep frequency modulation interferometry

DFMI is a recently proposed interferometer scheme to simplify optical set-ups [Ger15]. It is a type of frequency modulated continuous wave (FMCW) technique [Zhe05] that uses strong laser frequency modulations in unequal arm length interferometers in combination with a phase readout based on fitting the complex amplitudes of the modulation harmonics [Sch+14c], or Kalman filter methods [Vor17]. DFMI is originated from sinusoidal phase shifting interferometry which uses a Bessel function method and anticipates a sinusoidal phase modulation at a fixed frequency,  $f_{\text{mod}}$ , in one interferometer arm. The so-called " $J_1\dots J_4$ " method, as used in prior experiments by [SS89; Jin+91; SC93], requires effective modulation depths on the order of  $m \approx 1$  to 5 rad. The interferometric spectrum of the associated photocurrents has components at multiple higher harmonics of the modulation frequency. With complex amplitudes these can be composed in terms of Bessel functions,  $J_n(m)$ . A phase difference,  $\varphi$ , due to interferometric pathlength changes, re-allocates the complex amplitudes of the higher components. By using analytic formulae to solve for the unknown parameters  $m$ ,  $\varphi$ , modulation phase  $\Psi$  and amplitude  $A$ , the phase information can be extracted from the harmonic amplitudes. The complex amplitudes can be detected by a spectrum analyzer or by applying some kind of Fourier transform to the digitized data. By using this " $J_1\dots J_4$ " method one was able to achieve accuracies on the order of 10 to 100 mrad/ $\sqrt{\text{Hz}}$  which makes this approach not suitable for applications requiring 1 pm/ $\sqrt{\text{Hz}}$  noise levels. For DFMI we generalize this approach as it has already been investigated for DPM interferometry by [Hei+10] and [Sch+14c]. We are using a higher modulation depth,  $m$ , of about 6 to 9 and use all higher harmonics up to 10. This enhances the number of observations, makes the system more complex and prevents a simple analytic solution. A numerical solution is therefore used, based on a least-squares fit algorithm. This is a standard approach to approximate the solution of overdetermined systems. This method allows consistency checks and the signal-to-noise ratio can be improved. In comparison to heterodyne interferometry, the data processing for re-covering the phase information from the photocurrent pattern is more complex for DFMI and DPM interferometry. It is however a preferable solution since classic heterodyne detection requires often additional optics or electronics. While DPM requires a phase modulator in one interferometer arm of each interferometer [Hei+10], DFM requires only unequal arm length interferometers without additional components. All interferometers can be operated with a single, dedicated laser source, which is deeply tunable in its frequency [Ger15]. This makes DFMI more attractive for multi-channel interferometry and, therefore, a suitable candidate for future test mass readout in satellite geodesy missions.

### 6.2.1 Theory

For DFMI we combine an unequal arm length interferometer and a frequency modulated laser source as illustrated in Figure 6.3. A strong sinusoidal frequency modulation of

$$f_{\text{DFM}}(t) = \Delta f \cdot \cos(2\pi f_{\text{mod}}t + \psi) \quad (6.4)$$

is applied on the laser, where  $\Delta f$  is the strength of the frequency modulation,  $f_{\text{mod}}$  is the modulation rate and  $\psi$  the modulation phase. Due to the interferometric arm length mismatch any LFN will couple into the optical phase measurement, alike the applied frequency modulation. In general this coupling of laser frequency variations is supposed to be eliminated or reduced, while DFMI makes use of this effect as it will be shown in the following mathematical description. The resulting electric field equation of a laser beam gets an additional phase term that is calculated via the integral of the frequency modulation,  $\phi(t) = 2\pi \int_0^t f_{\text{DFM}}(t')dt'$ , which leads to the following expression for, e.g., the measurement beam

$$E_m = \frac{1}{2}E_{\text{in}} \sin \left[ \omega_0 t + \varphi + 2\pi \Delta f \int_0^t \cos(2\pi f_{\text{mod}}t' + \psi) dt' \right] \quad (6.5)$$

$$= \frac{1}{2}E_{\text{in}} \sin \left[ \omega_0 t + \varphi + \frac{\Delta f}{f_{\text{mod}}} \sin(2\pi f_{\text{mod}}t + \psi) \right]. \quad (6.6)$$

Due to the required propagation delay of measurement and reference beam, the electric field of the reference arm is written with an additional term,  $\tau$ , that describes a certain time delay between the two electric fields entering the detector

$$E_r = \frac{1}{2}E_{\text{in}} \sin \left[ \omega_0(t - \tau) + \frac{\Delta f}{f_{\text{mod}}} \sin(2\pi f_{\text{mod}}(t - \tau) + \psi) \right]. \quad (6.7)$$

The optical output power on the detector is written by using these two frequency modulated electric fields and further simplified by the usage of trigonometric identities, neglecting terms of  $2\omega_0$  and using the approximation of  $f_{\text{mod}}\tau \ll 1$

$$\begin{aligned} P_{\text{out}} &\propto (E_m + E_r)^2 \\ &= \frac{1}{2}E_{\text{in}}^2 (1 + \cos[\varphi + m_{\text{DFM}} \cos(2\pi f_{\text{mod}}t + \psi)]), \end{aligned} \quad (6.8)$$

with the resulting, effective modulation depth of

$$m_{\text{DFM}} = 2\pi \Delta f \tau. \quad (6.9)$$

A detailed calculation can be found in Appendix B.1. A feature of DFMI is the dependency of the modulation depth and the arm length mismatch on the effective

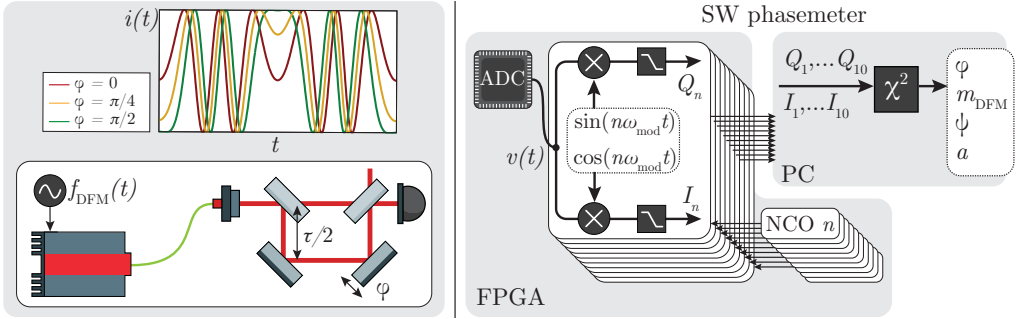


**Fig. 6.3.:** DFM interferometry uses a deeply frequency modulated laser source and an unequal arm length interferometer. The effective modulation depth depends on the strength of the laser modulation and on the arm length mismatch. A trade-off between these two values allow for modulation depths that are in the same order of magnitude as for DPM.

phase modulation  $m_{DFM}$  as shown by Equation (6.9). By tuning  $\Delta f$  of the laser modulation one can read out any interferometer with any arm length mismatch. However, for building very compact optical heads, like they might be used for test mass interferometers, a modulation strength on the order of several GHz needs to be applied on the laser to achieve cm-scale dimensions. Assuming a rapidly tunable laser source with a modulation frequency of 1 kHz and modulation depth of 9 GHz, a time delay of 160 ps needs to be achieved between the measurement and reference beam, in order to achieve compact optical set-ups with an arm length difference of only 4.8 cm in vacuum.

The photocurrent output, converted into a voltage, provides the output signal  $v(t)$  of a phase-modulated self-homodyning interferometer

$$v(t) = A [1 + \kappa \cos(\varphi + m_{DFM} \cos(\omega_{mod}t + \psi))]. \quad (6.10)$$

Here,  $A$  is the signal amplitude, that combines constant factors such as optical power and the photodiode efficiency,  $\kappa$  is the contrast and  $\omega_{mod} = 2\pi f_{mod}$  the angular modulation frequency. An example of a DFM photocurrent pattern is shown in Figure 6.3 and shows, equivalent to the one of DPM [Hei+10], an output that is periodic with  $f_{mod}$  and a waveform shape which depends on the interferometer phase  $\varphi$ . Except for an additional laser frequency noise term accumulated due to the unequal arm lengths in DFM interferometers the interferometric linearity of DFM is identical to the one of DPM which makes the DPM fit algorithm also applicable for DFMI [Ger15; Isl+16b]. This readout technology was successfully demonstrated for effective modulation depths on the order of  $m \approx 9$  by [Hei+10].

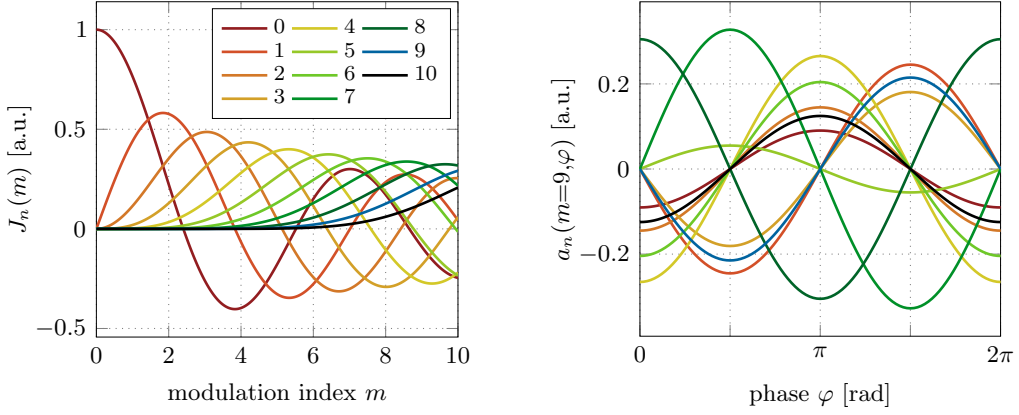


**Fig. 6.4.:** Bessel functions and their amplitudes for the first  $n = 10$  harmonics. The Bessel functions (left) show a larger contribution of higher harmonics for an increasing modulation index,  $m$ . The dependency of their harmonic amplitudes,  $a_n(m, \varphi)$ , with respect to the phase,  $\varphi$ , is plotted on the right for a modulation depth of  $m = 9$ .

For this purpose Equation (6.10) is expanded into its higher components by using a Bessel function approach

$$v(t) = A [1 + \kappa J_0(m) \cos(\varphi)] + \sum_{n=1}^{N=\infty} a_n(m, \varphi) \cos(n[\omega_{\text{mod}}t + \psi]) \quad (6.11)$$

$$= v_{\text{DC}}(\varphi) + v_{\text{AC}}(n, m, \varphi, \omega_{\text{mod}}, \psi) \quad (6.12)$$

with the effective modulation depth  $m = m_{\text{DFM}}$  and

$$a_n(m, \varphi) = C J_n(m) \cos(\varphi + n\frac{\pi}{2}), \quad (6.13)$$

$$v_{\text{DC}}(\varphi) = A [1 + \kappa J_0(m) \cos(\varphi)]. \quad (6.14)$$

Here,  $J_n(m)$  are the Bessel functions and  $a_n(m, \varphi)$  the according harmonic amplitudes, both shown in Figure 6.4, and  $C = 2\kappa A$  is a common constant factor. Depending on the actual modulation index,  $m$ , the contribution of relevant Bessel functions increases, as the left plot of Figure 6.4 shows. For utilizing a modulation depth of about  $m = 9$  at least higher harmonics up to  $n = 10$  must be considered. The right plot in Figure 6.4 shows the dependence of the Bessel amplitudes,  $a_n(m, \varphi)$ , for a modulation index of  $m = 9$ , with respect to the interferometric phase  $\varphi$ . The readout technique of DFM/DPM is based on these harmonic amplitudes, since they can directly be measured by applying a numerical Fast Fourier Transform (FFT) to the photocurrent data and they provide knowledge about the unknowns  $\varphi$ ,  $m$ ,  $\psi$  and  $C$  according to Equation (6.14). Typically, modulation

depths on the order of  $m \geq 6$  are used in DFM/DPM experiments such that the system is overdetermined if one uses  $N = 10$  harmonics for solving the four parameters. The DC value  $v_{\text{DC}}(\varphi)$ , corresponding to  $a_0(m, \varphi)$ , is not used by the fit algorithm. Due to environmental disturbances, such as stray light from external sources or electronic noise, the noise level is typically increased for the DC measurement. Therefore this measurement is only used for alignment purposes and to monitor the contrast of the interferometer.

### 6.2.2 Signal processing

The photocurrent,  $i(t)$ , measured by the photodetector, passes a TIA and is converted into a voltage signal,  $v(t)$ . After an appropriate analog filter which reduces aliasing effects, the signal is digitized with a sampling rate of  $f_s > 2 \cdot 10 \cdot f_{\text{mod}}$ . The digitized data is downsampled by the readout system such that it is split into smaller segments of length  $N_{\text{buffer}}$ . Each segment is now processed by a Discrete Fourier Transform (DFT) which demodulates with sine and cosine tones at the relevant harmonics of the modulation frequency. The  $IQ$ -demodulation determines the measured complex amplitudes of the  $n$ -th harmonic, in terms of quadrature,  $Q_n$ , and in-phase  $I_n$  [Abr74; Hei+10],

$$Q_n(m, \varphi) = \cos(n\omega_{\text{mod}}t) \cdot v_{\text{AC}} \approx \frac{1}{2} C J_n(m) \cos\left(\varphi + n\frac{\pi}{2}\right) \cos(n\psi), \quad (6.15)$$

$$I_n(m, \varphi) = \sin(n\omega_{\text{mod}}t) \cdot v_{\text{AC}} \approx -\frac{1}{2} C J_n(m) \cos\left(\varphi + n\frac{\pi}{2}\right) \sin(n\psi). \quad (6.16)$$

Further detailed mathematics steps, showing the applied approximations for achieving Equations (6.15) and (6.16), are demonstrated in Appendix B.2. In total, a set of  $2N$  equations is provided after the  $IQ$  processing which can be split into two uncorrelated system of equations

$$n\psi = \arctan\left(\frac{Q_n(m, \varphi)}{I_n(m, \varphi)}\right), \quad (6.17)$$

$$\alpha_n(m, \varphi) = \sqrt{Q_n(m, \varphi)^2 + I_n(m, \varphi)^2}, \quad (6.18)$$

where  $\alpha_n(m, \varphi)$  are the measured complex amplitudes. A non-linear fit algorithm is used to find a batch of parameters,  $\varphi$ ,  $m$ ,  $\psi$  and  $C$ , providing an analytic computation for  $a_n(m, \varphi)$ , which matches the measured value  $\alpha_n(m, \varphi)$  best. A Levenberg-Marquardt fit algorithm is used which solves the set of equations iteratively and minimizes the sum of squares (SSQ) according to the least-square expression

$$\chi^2(\varphi, m, \psi, C) = \sum_{n=1}^N (a_n(m, \varphi) - \alpha_n(m, \varphi))^2, \quad (6.19)$$

where  $a_n(m, \varphi)$  is the analytic solution and  $\alpha_n(m, \varphi)$  is obtained by the demodulation of the measured signal [Mar63]. In general, the fitted parameters for different segments of length  $N_{\text{buffer}}$  do not vary and a fast convergence of the non-linear fit algorithm can be expected. However, large disturbances or errors in the initialization of the start values used for the fit cause processing delays. In this case a more robust fit is used, only for finding valid initial values, which is based on a Nelder-Mead Simplex algorithm [NM65]. In dependency on the modulation depth and the amount of bins,  $N$ , used in the DFM signal processing, the performance of the system varies. A numerical analysis of  $\chi^2(\varphi, m, \psi, C)$  has shown that one achieves best values of  $m$  for the fit algorithm if one considers  $N \geq 8$  harmonics for a modulation depth of  $m = 6$  and  $N \geq 10$  harmonics for a modulation depth of  $m = 9$ , suggesting a best resolution for the interferometric phase  $\varphi$  [Hei+10].

Potential improvements can be achieved by replacing the fit algorithm by other signal processing techniques. A Kalman filter or loops for locking the modulation depth  $m$ , similar to a PLL phasemeter, might increase the speed of real time processing [Vor17]. Kissinger and his group have shown that range-resolved interferometry is possible even with DFMI, similar to the multiplexing capabilities of for example DI [Sha07]. For this a novel signal processing technique is used which suppresses unwanted DFM signals in the demodulation process by using a smooth window shape function as filter. Based on their propagation delay through an unequal arm length DFM interferometer the individual signals can be distinguished from each other with cm resolution. The sensitivities that could be achieved with this scheme are on the order of  $1 \cdot 10^{-4} \text{ rad} / \sqrt{\text{Hz}}$  above 10 Hz [Kis+15].

An excitation of higher harmonics of the modulation tone in the laser frequency modulation can be caused by non-linearities in the frequency actuation [Ger15; Kis+15]. To analyze this, a set of fits, which are operating in the time domain, can be used. For an analysis in the time domain high bandwidth time data is required. With the full sampling rate of our data acquisition system of about 250 kHz we can include higher modulation harmonics not taken into account by the frequency domain fit that is used for the phase extraction. The following model can be used for this purpose if one assumes a frequency modulation of the laser excited at a single frequency,

$$h_1(t) = E + E \cdot \kappa \cdot \cos(\varphi + m \cos[\omega_{\text{mod}}t + \psi]), \quad (6.20)$$

which is based on Equation (6.10). The amplitude,  $A$ , is split into an optical amplitude  $E$  and the contrast  $\kappa$  in front of the interference term. Under the assumption that the laser is not perfectly modulated at a single frequency but also

excited at higher harmonics (here we consider up to 10), Equation (6.20) expands to

$$h_{10}(t) = E + E \cdot \kappa \cdot \cos \left( \varphi + \sum_{i=1}^{10} m_i \cos[i \cdot \omega_{\text{mod}} t + \psi_i] \right). \quad (6.21)$$

The residuals that are showing up by subtracting the model from the data gives an estimate of the linearity of the applied frequency modulation and DFM interferometry. For getting real time and long term phase data over several hours or days this analysis scheme cannot be applied. Due to the huge file sizes resulting from the 250 kHz sampling a large amount of processing power and time would be required in further processing steps. A more efficient way for long term measurements is the usage of the frequency domain analysis, thus the *IQ*-demodulation and the non-linear fit.

### 6.2.3 Optical head design

To perform a multi-DoF and multi-channel readout of various test masses certain requirements must be fulfilled. The sensor must show a certain displacement sensitivity, equivalent to an interferometer readout noise of about  $1 \text{ pm} / \sqrt{\text{Hz}}$ , and small set-ups are preferable such that the optics are easily scalable to multiple channels. These types of very compact optical interferometric structures we will call optical heads (OHs). Each OH is used to measure one lateral displacement,  $\Delta l$  and two angles, yaw  $\Psi$  and pitch  $\Theta$ , of one test mass surface. The usage of QPDs enables DWS which can be utilized to measure optical angles very accurately if the wavefronts of the interfering beams are not disturbed [Sch17]. Otherwise, if QPDs are not applicable, at least three (often better four) independent interferometric measurements are required to measure optical pathlength changes at different points from the test mass surface. Regarding future satellite missions, the test masses are placed inside a closed housing, surrounded by electrodes. The borders will reflect potential stray light beams back into the interferometer where they interact with the nominal interference signals and disturb the phase performance.

Since DFM implies the usage of interferometers with unequal arms, mainly two constellations are thinkable, namely a Michelson-OH or a Mach-Zehnder-OH. With both interferometer architectures different optical layouts can be designed and optimized. In the following some of them are introduced and their individual advantages and disadvantages are highlighted.

Figure 6.5 shows a selection of possible test mass interferometers using the MI layout as a baseline. The usage of an on-axis MI, as shown in Figure 6.5a, is the easiest way to implement an OH. A fiber output coupler brings the frequency modulated light onto the optical bench where it is split by a beam splitter. A part of the light is sent to the test mass where it is reflected, the other part of the

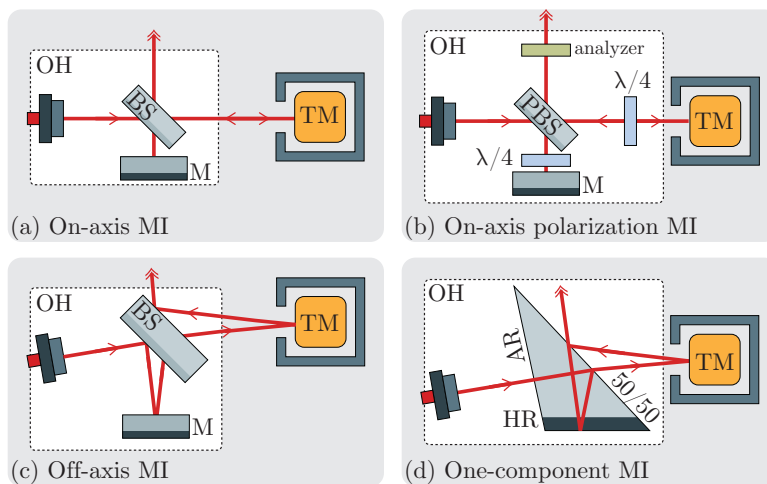
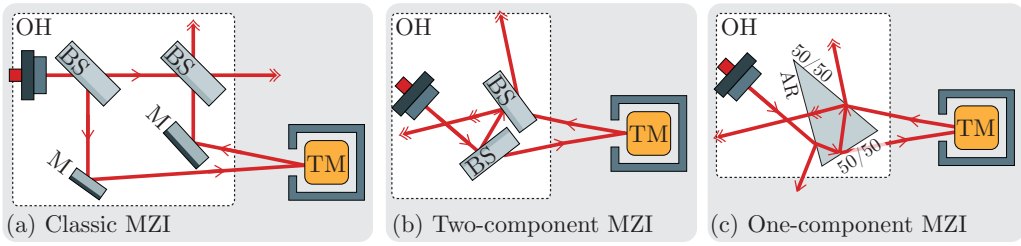


Fig. 6.5.: Possible MI constellations for a test mass readout using DFM technology with interferometers having unequal arm lengths. The designs differ by their applicability, optical compactness and ghost beam contamination.

light travels a shorter pathlength towards a stable reference mirror. Both light beams interfere with each other at the same beam splitter. The interference leaves both output ports which is why half of the light travels back to the fiber output coupler. Due to backscatter of the fiber coupler interface and Rayleigh scattering generated inside the fiber itself, the OH-interferometry will be contaminated by ghost beams that travel collinear with respect to the nominally injected beam. A MI with integrated polarizing optical components is able to prevent laser beams in traveling back to the fiber output coupler. But this polarization encoding technique, illustrated in Figure 6.5b, requires two polarizing components, together with two quarter-waveplates, one in each interferometer arm, which makes this optical design more complex. A further, more compact alternative of MIs, is a so-called off-axis design that is shown in Figure 6.5c. Both the measurement beam to the test mass and the reference beam to the mirror, are reflected under an angle which is unequal to  $0^\circ$ . Optical simulations have shown that the ghost beam propagation directions could be angled in such a way that all critical beams are leaving the interferometer axis and would not disturb the phase measurement. High contrast can be achieved by aligning the stable reference mirror. A further reduction of the amount of optical components can be achieved by combining the beam splitter and the reference mirror to a single component with different coatings, as shown in Figure 6.5d. But optical simulations have shown that this approach did not lead to a properly aligned interferometer using a commercially available rectangular prism for example. Angled beams, propagating along two





**Fig. 6.6.:** Possible MZI constellations for a test mass readout using DFM technology with interferometers having unequal arm lengths. The designs differ by their optical compactness, especially the amount of optical components used.

arms with different lengths, cannot be aligned with a single surface that is used for both, the beam splitting and recombination action. A customized component with dedicated dimensions and angles needs to be designed, simulated and optimized in IfoCAD. The additional DoFs must be included in the minimizer function which was used to align the interferometer.

Using a MZI architecture, as shown in Figure 6.6a, requires more optical components at first appearance since it uses separate beam splitters for the beam separation and recombination action. Furthermore, two deflection mirrors are used to guide the laser beams through the measurement and reference arm. By using an evolved geometry of beam propagation the deflection mirrors can be eliminated. Figure 6.6b shows that a MZI can also be constructed by only utilizing two beam splitters. The distance between the beam splitters is limited by the beam angle under which the measurement beam is reflected by the test mass. Thus, the vertical size of the beam splitters defines the AOIs for the test mass reflection, similar to the two-component scheme of a MI. A further reduced MZI architecture is shown Figure 6.6c. It consists of a single component in a shape of a prism. Two of the three surfaces have a coating with 50% reflectivity, which replace the two beam splitters in the design mentioned before. The third surface is not required for the MZI functionality, but an AR-coating for beams coming from inside of the optical medium is useful to prevent ghost beams. A high transmission is also advantageous for beams coming from the fiber output coupler such that most of the light is used for the interferometry. Only a fraction is being reflected which serves as a potential power monitor.

Optical simulations of the prism have shown that this one-component interferometer is a promising candidate towards compact OHs for test mass experiments. In contrast to the one-component MI the prism-interferometer has the advantage that a second, diagnostic, interferometric output port is available, as usual for MZIs. By comparing both output ports an optical  $\pi$ -combination can be deter-

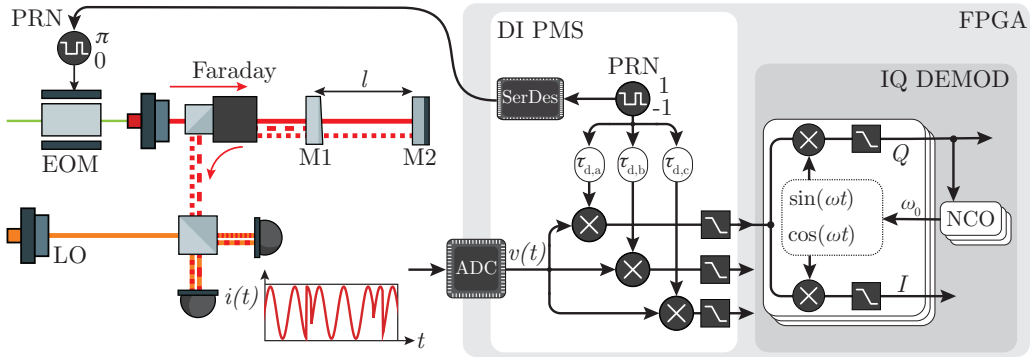


Fig. 6.7.: A digital interferometer imprints a pseudo-random noise (PRN) phase modulation on the measurement beam via a fast, thus often fiber-coupled, electro-optical modulator (EOM) before the beam hits the targets. The digitally enhanced heterodyne interferometry (DEHeI) technique has a frequency shifted laser beam as LO. For recovering the signal a dedicated digital demodulation algorithm multiplies the data with an exact, but delayed, copy of the PRN code. If the delay is matched to the optical travel time a typical heterodyne signal is recovered and the IQ-demodulation scheme can be used to extract the phase information.

mined in post-processing, that gives insight into potential noise sources that couple differently in both ports.

### 6.3 Alternative interferometer techniques

Different, alternative interferometer techniques are also available and have been investigated previously, but are not chosen to be used for test mass interferometry experiments in this thesis. In the following, a selection of relevant techniques is described and their advantages and disadvantages will be discussed on the basis of conceptual example implementations.

#### 6.3.1 Digitally enhanced interferometry

In terms of multiplexing capabilities DI is the most promising candidate for achieving very compact optical systems probing various devices under test with a single interferometric arm. A sketch of this principle is shown in Figure 6.7 where the displacement of two mirrors, M1 and M2, is probed with a single beam simultaneously. Two types of DI exist in general, the so called digitally enhanced heterodyne interferometry (DEHeI) and digitally enhanced homodyne interferometry (DEHoI). Both techniques combine the classic interferometer concepts, either heterodyne or homodyne interferometry, with a PRN high speed phase modulation.

DEHeI uses the binary phase shift keying (BPSK) technique, which introduces a phase shift by either zero or  $\pi$  on the optical signal that is used as measurement beam for the test mass readout. The phase shift effectively imprints an amplitude modulation,  $c(t - \tau)$ , of either  $+1$  or  $-1$  on the beam. The electric field of the measurement beam on the photodetector therefore depends on the light travel time  $\tau$  and can be expressed via

$$E_m = \frac{1}{2} E_{in} \sin[\omega_0 t + \varphi] c(t - \tau). \quad (6.22)$$

Considering multiple targets get hit by the beam, their signals accordingly differ by the various positions of the targets, changing the light travel time

$$E_m = E_1 \sin[\omega_0 t + \varphi_1] c(t - \tau_1) + E_2 \sin[\omega_0 t + \varphi_2] c(t - \tau_2) + \dots \quad (6.23)$$

A non-modulated laser beam with a slightly different frequency is used as local oscillator, or reference beam, according to the one used in heterodyne interferometry. This beam is interfered with the measurement beam on a high-speed GHz-photoreceiver which is used to monitor the optical power. The resulting photocurrent,  $i(t)$ , is converted into an output voltage,  $v(t)$ . By neglecting terms of the orders of  $2\omega_0$ ,  $2\omega_r$  and  $\omega_0 + \omega_r$  the photodetector voltage output signal can be written as

$$\begin{aligned} v(t) = & \frac{1}{2} (E_1^2 + E_2^2 + E_{in}^2/4) + \\ & E_1 E_{in} \cos[(\omega_0 - \omega_r)t + \varphi_1] c(t - \tau_1) + \\ & E_2 E_{in} \cos[(\omega_0 - \omega_r)t + \varphi_2] c(t - \tau_2), \end{aligned} \quad (6.24)$$

with  $c(t - \tau_i)c(t - \tau_i) = 1$  whereas  $c(t - \tau_i)c(t - \tau_j)$  remains a random code that approaches the background noise floor and can be made small. After a high speed digitization and filtering of the voltage output the interferometric phase must be recovered from the PRN-encoded signal. For this purpose, the detector output is multiplied by a delayed version,  $c(t - \tau)$ , of the same code that was initially imprinted optically. For isolating the individual signals from the targets  $\tau$  needs to match the exact light travel time delay of the beam to the desired target. For example, to isolate the signal from target M1, the photodetector output is

multiplied by a version of the PRN code that is delayed by  $\tau_1$ ,  $v_{M1} = v_{\text{out}} \times c(t - \tau_1)$ . The according AC part can then be expressed by

$$v_{M1,AC} = \frac{1}{2}E_1E_{\text{in}} \cos[(\omega_0 - \omega_r)t + \varphi_1] + \frac{1}{2}E_2E_{\text{in}} \cos[(\omega_0 - \omega_r)t + \varphi_2]c(t - \tau_2)c(t - \tau_1). \quad (6.25)$$

The digital demodulation reverses the initial optical phase modulation and recovers a typical heterodyne signal that contains the desired phase information of one particular target. Other signals, whose demodulation delays differ more than one code chip from its optical delay, remain randomly pseudo-modulated. In the noise spectra these signals appear as broadband background that can be suppressed by dedicated phasemeter filters. The technique also allows to improve the phase noise performance by subtracting two target signals from each other after both are digitally demodulated. Common mode noise sources that spoil the optical phase before the first target is hit can be eliminated with this technique.

For DEHeI it has been shown that signals reflected from various objects with cm-distance and entering the same photodetector can be distinguished from each other due to their different travel time by using PRN phase modulation speeds in the order of 1 GHz. The optical complexity for multi-channel systems decreases rapidly but GHz electronics are required for the modulation and demodulation, the detection and the signal digitization. High speed DEHeI achieved a phase performance of  $3 \text{ pm}/\sqrt{\text{Hz}}$  at 10 Hz using an active clock jitter correction [Sha07; Isl13; Isl+14] and might be still limited by the bandwidth of the electronics or spurious signals whose optical delays are within one code chip of the digital delay used for the recovered signal.

The DEHoI scheme allows for further simplification by removing the second laser frequency, as it is the case for the classic interferometer schemes. Instead of BPSK it uses the quadrature phase shift keying (QPSK) scheme to inject two perpendicular PRN phase modulations onto the light. The achieved displacement measurement noise floor is  $3 \text{ pm}/\sqrt{\text{Hz}}$  at 4 Hz [Sut+12; DV+09].

Because of the multiplexing capability both, DEHeI and DEHoI, are promising candidates for multichannel interferometry with easily duplicatable optical heads. Furthermore, DI is by design insensitive to stray light which makes it very attractive for multi-channel test mass readouts with small dimensions in a closed test mass chamber with electrodes. But the current limitations of the electronic and digital bandwidth must be solved first before DI can be used for high-precision interferometry at low frequencies.

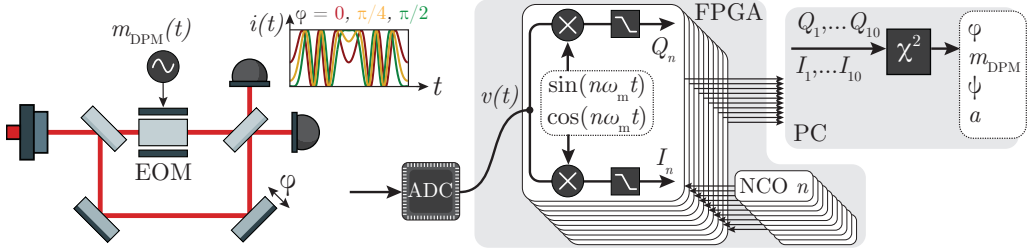


**Fig. 6.8.:** For DPM a very deep sinusoidal phase modulation over multiple fringes is applied on the phase of one of the beams. This results in an AC signal on the photodetector oscillating with the DPM frequency and higher harmonics of this frequency. The amount of higher harmonics in the interferogram depends on the strength of the modulation. The readout algorithm typically works by using the first ten harmonics, demodulating them to get the complex amplitudes, and fed them into a Levenberg-Marquardt fit (or Kalman filter) to estimate the phase information among others.

### 6.3.2 Deep phase modulation interferometry

DPM interferometry is an interferometry technique that combines a sinusoidal phase modulation with homodyne interferometry. Such interferometer systems are also known as self-homodyning, also like DFMI, since a single laser beam can be used as shown in Figure 6.8. A laser beam is split into two arms whereby a deep phase modulation ( $m_{\text{DPM}} \gg 2\pi$ ), realized by an EOM, is applied in one arm (here the reference arm). The electric field of the reference arm is therefore given by

$$E_r = \frac{1}{2} E_{\text{in}} \sin[\omega_0 t + \varphi + m_{\text{DPM}} \cos(\omega_{\text{mod}} t + \psi)] \quad (6.26)$$

where  $m_{\text{DPM}}$  is the modulation depth,  $\omega_{\text{mod}}$  is the modulation frequency and  $\psi$  is the modulation phase. The reference electric field is given by the equation of a classic, non-modulated local oscillator field, oscillating at the same frequency,  $\omega_0$ . By neglecting higher order frequency terms the voltage output power of the photodetector can be written as

$$v_{\text{out}} = A [1 + \kappa \cos(\varphi + m_{\text{DPM}} \cos(\omega_{\text{mod}} t + \psi))]. \quad (6.27)$$

The interferometric output has a pattern that is periodic with  $f_{\text{mod}}$  that depends on the interferometric phase difference between measurement and reference beam,  $\varphi = \varphi_m - \varphi_r$  [Hei+10; Sch+14c]. For extracting the phase information a non-linear fit algorithm is used which has been introduced in Section 6.2.2 for DFMI. A phase performance of  $1 \text{ pm}/\sqrt{\text{Hz}}$  at 0.1 mHz could be achieved. This is currently limited by white digitization noise. Since DPM uses a phase modulation in the kHz frequency range similar photoreceivers as used in LISA Pathfinder or other

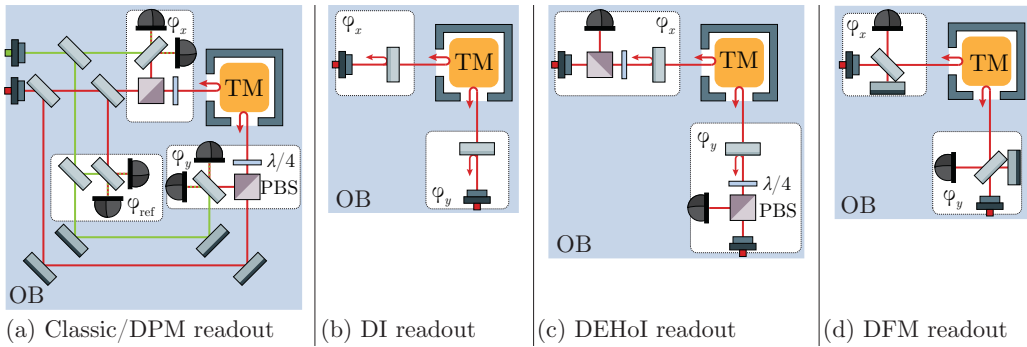


**Fig. 6.9.:** Shown are the optical set-ups for the readout of two longitudinal (and four angular) degrees of freedom of one test mass: Non-multiplexing classic interferometry and also DPM is shown in (a), a possible set-up that can be realized by both DI techniques is shown in (b) and two set-ups using the self-homodyning scheme that can be implemented by using DEHoI or DFM interferometry are shown in (c) and (d). Image credit: Based on [Ger14].

heterodyne interferometers can be used. DPM would typically applied externally and possibly require a local reference interferometer.

## 6.4 Comparison and applications of interferometer techniques

The content of this section is based on the publication [Isl+16a] where different interferometry techniques are compared with each other to find the best trade-off candidate for multi-DoF test mass readout. Beside this application, alternative interferometer techniques also provide high potential for other usages, like laser preparation set-ups or stray light experiments, which will shortly be introduced.

### 6.4.1 Test mass interferometry

The complexity of the optical set-ups can be simplified by using alternative interferometer techniques like DI or DFM. Figure 6.9 shows the optical designs for different techniques in comparison to the classic heterodyne readout scheme, here shown for test mass readouts. Using the alternative DI set-up, shown in Figure 6.9b, the reflections of the test mass and the reference mirrors are interfered with an oscillator beam behind the injection fiber. In this case, multiple signals can be collected by only one photodetector, but DWS cannot be used since the wavefront is destroyed by the fiber coupling. Angular fluctuations could be measured, however, by combining multiple longitudinal DoF measurements. The advantage of DEHoI and DFM schemes, illustrated in Figure 6.9c and 6.9d, are their self-homodyning capabilities such that no additional laser beams are required which eliminates the

**Tab. 6.1.:** Comparison of the new interferometer techniques DPM, DI and DFM with the classic heterodyne interferometer. Here,  $n$  denotes the number of test masses within a satellite. <sup>1</sup>based on experimental results, <sup>2</sup>the difference of one optical signal split after photodetector, <sup>3</sup>the difference of one optical signal split before photodetector, \*assuming set-ups shown in Figure 6.9 [Isl+16a].

technique	local ref. ifo	electronic bandwidth modulation	readout	DWS capability*	demonstrated sensitivity [pm/ $\sqrt{\text{Hz}}$ ]
classic	$\geq n$	—	k/MHz	yes	1.4 at 3 mHz <sup>1</sup> [Hei+04]
DPM	$\geq n$	kHz	kHz	yes	1.0 at 0.1 mHz <sup>1,2</sup> [Sch+14c]
DI	0	GHz	GHz	no	3.0 at 10 Hz <sup>1</sup> [Isl+14]
DEHoI	0	GHz	homod.	yes	1.0 at 20 Hz <sup>1</sup> [Sut+12]
DFM	0	kHz	kHz	yes	1.0 at 0.1 Hz <sup>1</sup> [this thesis]

reference interferometers in these designs. The laser beam is interfered with a delayed version of itself on the OH and the signal can be monitored on a QPD to perform DWS. However, QPDs are currently not available in such small sizes that DEHoI signals with several GHz rates could be detected. Also the data acquisition at GHz frequencies rate is challenging, which is why DFM turned to be out more applicable since it provides an interferometric pattern oscillating at kHz rates.

Table 6.1 shows a short comparison of the interferometer techniques and their demonstrated sensitivities. In terms of optical complexity and excluding GHz electronics and photodiodes the DFM technique turned out to be the most promising candidate for a multi-DoF readout of multiple test masses, even though it does not provide the stray light insensitivity of DI. Other potential optical techniques for test mass readout, not included here, are for example fiber micro-cavity based sensors [Smi+09] and optical lever/shadow sensing [Car+12].

#### 6.4.2 Laser preparation

Phase modulation interferometer techniques also simplify the set-ups for the laser preparation that implicates offset-shifted laser beams as shown in Figure 6.10. In LISA Pathfinder this problem was solved by using two AOMs which shift each of the two laser beams by several MHz plus a small kHz offset relatively to each other. In LISA a second laser source will be used that is offset-phase-locked to the master laser with an offset frequency of a few MHz. While the LISA Pathfinder laser preparation achieves beat notes on the order of a few kHz, LISA interferometers will be operated at MHz beat notes. With phase modulation techniques one is able to produce a signal with a high dynamic range oscillating in the kHz frequency range, similar to the signals achieved with the heterodyne interferometers in LPF. Two AOMs (as used for LPF) or two lasers (LISA-style), can be replaced by one EOM and the DPM technique or completely removed by using the DFM

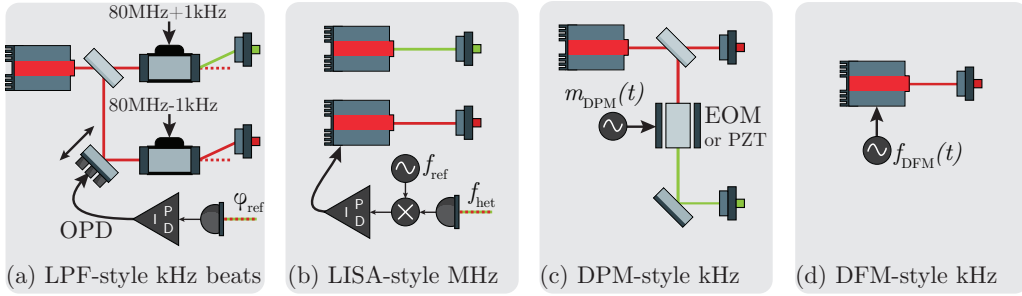


Fig. 6.10.: Laser light preparation for various interferometer types. (a) shows the LPF-style modulation for kHz beat notes. The LISA-style laser preparation is used to prepare MHz beat notes and is shown in (b). Inlets (c) and (d) show the application of DFM or DPM to simplify kHz frequency readouts.

technique. This enables a kHz readout without the need for an optical pathlength difference (OPD) stabilization. However, it remains to be investigated which other stabilization schemes are required for DPM and DFM. Both, DPM and DFM simplify the classic LISA Pathfinder scheme by eliminating the need for an OPD stabilization by substituting the AOMs with an EOM, required for DPM, or a deeply tunable laser source as required for DFM. With either of these two schemes the laser preparation is only needed once while separate OPD stabilizations and, thus, reference interferometers are needed for each pair of fibers feeding light to each optical bench [Isl+16a].

### 6.4.3 Stray light suppression in a Michelson interferometer

An experiment for investigating the achievable dynamic range of stray light suppression in a MI by using PRN phase modulated light as laser input has been set up at the AEI together with Oliver Gerberding, Melanie Meinders and Sina Köhlenbeck. Figure 6.11 shows the experimental set-up. The MI is designed in such a way that the PRN modulated light accumulates nearly the same pathlength in both interferometer arms. A homodyne detection lock stabilizes the length of both arms relative to each other. Due to the same pathlength the coherence between measurement and reference beam is recovered by an optical demodulation at the recombining beam splitter. The initially imprinted PRN phase modulation can be optically reverted for beams having the same propagation delay. One end mirror in the MI only reflects a part of the light, about 80%. The remaining light passes the optical component and propagates to a mirror, M2, whose position is actuated sinusoidally with a frequency  $f_{SL}$  and an amplitude  $m_{SL}$ . This reflection simulates a stray light beam that enters the actual MI where it disturbs the phase performance of the homodyne detection if no PRN code is applied initially on



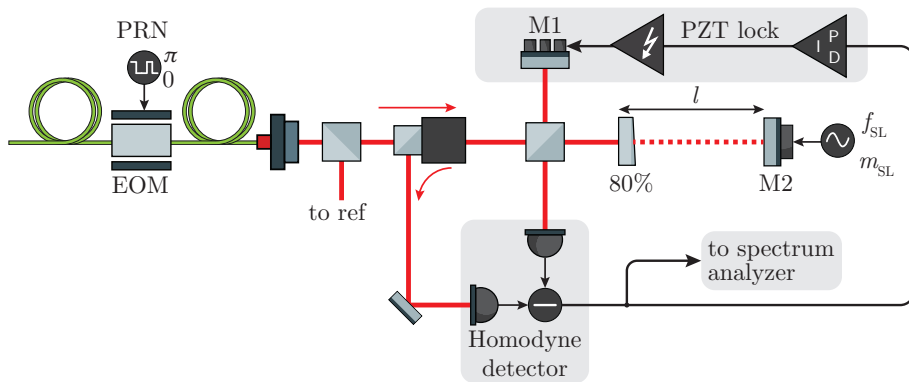


**Fig. 6.11.:** Set-up for a stray light suppression experiment by using a MI with homodyne detection. The balanced homodyne detection of a MI without PRN encoding is disturbed by the stray light beam coming from mirror M2, which is modulated with a frequency  $f_{SL}$  and a strength  $m_{SL}$ .

the laser phase. Operating the homodyne detection with PRN-encoded light the coherence is destroyed for beams that have a longer propagation time than the chip rate of the PRN code and the suppression of stray light beams by using DI technology can be measured.

#### 6.4.4 Identification of stray light sources

By using a digital interferometer all laser beams entering the same photodetector can be recovered if the matched delay is found. By scanning the demodulation delay over the photodiode current potential stray light beams can therefore be identified. The spatial resolution of this technique is limited by the speed of the PRN modulation. Stray light beams within one code chip cannot be distinguished from each other. Assuming that a phase modulation of 1 GHz can be achieved, this would allow us to identify stray light sources within 10 cm spatial resolution. For ghost beams coming from reflections by secondary surfaces a finer resolution is required. For an optical component with a thickness of 7 mm, the optical delay is 14 mm due to the reflection, an optical PRN phase modulation with a frequency of  $f_{PRN} = c_0/14 \text{ mm} = 21 \text{ GHz}$  needs to be generated.

#### 6.4.5 Simultaneous measurements of multiplexed optical signals

Similar to the investigation of stray light sources, digital interferometry can also be used in industry, e.g. for the characterization process of coated components. A stack of components, positioned in one line with a certain distance can be analyzed with only one laser beam in one direction to get information about the coating due

to the backreflected amplitude of a single beam. With DI, the individual component reflections are distinguishable if the spatial distance between two surfaces to be analyzed is within a few cm. To allow smaller distances between two reflecting surfaces without further increasing the phase modulation speed, one could very precisely place the surface at the edge of the PRN phase modulation. The reflection of the secondary surface is not within the same code chip and does not influence the measurement. It is assumed however that the chip edges are sharp and do not smear out over the component dimensions.

Kissinger et. al have shown that DFM, in combination with a demodulation scheme that uses a smooth gaussian window shape functions, is already able to resolve beams from each other due to their propagation delay within cm-level ranges. The surfaces of various objects placed within a single measurement beam path can be measured simultaneously and measurements of the reflectivity, vibration and resonance frequency can be performed for each [Kis+15]. Kissinger has also shown that this kind of multiplexed optical signal processing is useful for fiber segment interferometry, where weak backreflectors are placed at equidistant positions over the whole fiber length. By subtracting pairs of signals of neighbored fiber sensors a long-gauge interferometric length measurement is possible, which provides information about the bending and temperature of the fiber [Kis+13].

#### 6.4.6 Absolute distance measurements

Absolute distance measurements with laser interferometry is interesting for future geodesy missions. The distance between the test masses within one satellite needs to be known with some accuracy for the gradiometer calibration. While the microscopic distance is measurable with an interferometer by detecting phase changes between to laser wavelengths on nm-scales, macroscopic length measurements need other wavelengths or techniques, or a reference. Since the signal pattern of DFMI directly depends on the macroscopic arm length mismatch, this technique enables to directly track absolute distance changes by measuring the change of the effective modulation depth  $m_{\text{DFM}}$  if the strength of the frequency modulation applied on the laser is kept constant. A calibration via an unequal arm length interferometer with a well-known arm length mismatch is required and the precision of the absolute distance measurement would depend on the accuracy of this calibration and the stability of the frequency modulation.

” *Results of optical simulations for the reference MZI and the Test Mass in the Middle experiment, including an estimation of TTL coupling.*

The usage of DFM implies the construction of unequal arm length interferometers. For the test mass readout in future satellite missions the sensitivity of the optical phase measurement must show displacement sensitivities on the order of  $1 \text{ pm} / \sqrt{\text{Hz}}$ . To achieve this requirement, stray light and ghost beam mitigation strategies are essential for the interferometer design, a knowledge that has been gained by experiments for LISA performed on ground, e.g. the TBI introduced in the first part of this thesis. For this purpose several unequal arm length interferometers have been simulated in IfoCAD, optimized and analyzed. From the simulations, a template for the component positions can be extracted that will later be used in the cleanroom for the construction of quasi-monolithic interferometers.

The first section of this chapter shows the design of a classic unequal arm MZI that is later used as frequency reference for DFM experiments. If quasi-monolithically bonded for a high mechanical and thermal stability, such an interferometer may form the basis for stabilizing the average frequency noise of the deeply modulated laser source. An IfoCAD simulation is required for the exact positioning of the optical components, an estimation of potential ghost beams and, if necessary, their mitigation. The longitudinal pathlength signal and TTL coupling influence is estimated for differently wedged optical components and for beam pointing fluctuations caused by the fiber output coupler.

The second part of this chapter shows the results of optical simulations for a one-component MZI in the shape of a prism. The required component parameters are defined by using IfoCAD. Furthermore, the optical design of the so-called TMITM experiment is demonstrated. It uses two prisms for reading out the motion of a test mass mirror from two sides. The TTL coupling for an angular test mass motion of about  $\pm 200 \mu\text{rad}$  is analyzed and optimized.

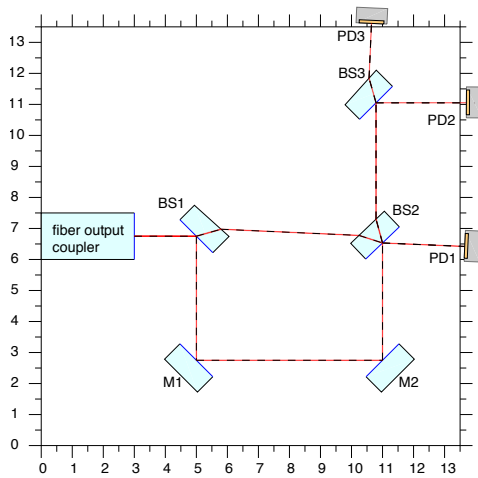
## 7.1 Mach-Zehnder reference interferometer

A MZI has been designed for its application as frequency reference for future DFM experiments. The MZI has an arm length mismatch of about 70 mm allowing LFN to be detected. The dimensions of the interferometer are designed such that it fits onto a 135 mm  $\times$  135 mm baseplate that has a thickness of 36 mm and a very low CTE of  $1 \cdot 10^{-8}/\text{K}$ , ensuring the thermal stability of this interferometer. As fiber output coupler a commercially available output collimator from SuK will be used, mounted in an adjustable three-axis stage from Owis, since quasi-monolithic FIOSs were not available at the time of construction.

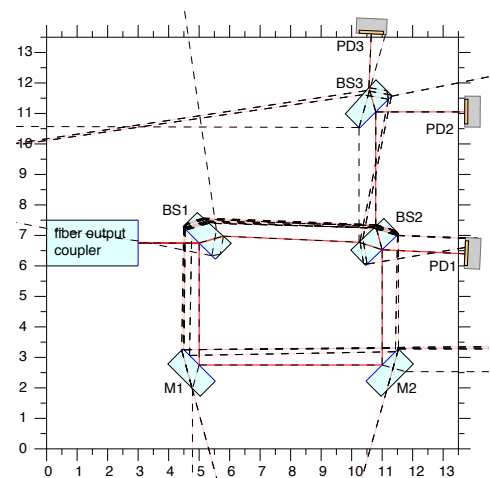
### 7.1.1 Optical design

Figure 7.1a shows the final 2D drawing of the reference Mach-Zehnder interferometer produced by IfoCAD. It has an arm length mismatch of 69.7871 mm, consists of two high-reflective (HR) mirrors, M1 and M2, and two beam splitters, BS1 and BS2. BS1 is a wedged component and serves as splitting beam splitter. BS2 is a non-wedged component and is the recombination beam splitter in the interferometer. The photodiode PD1 monitors the interference signal of one of its output ports. Another wedged component, the beam splitter BS3, splits the other output port of BS2 and, thus, delivers two identical optical signals with the same phase and amplitude behavior. Two photodiodes, PD2 and PD3, are used to monitor the signals that are phase shifted by a factor of  $\pi$  compared to the interference signal detected by photodiode PD1. This allows certain photodiode signal combinations, like optical zero- and  $\pi$ -measurements, which can be used for diagnostic analyses of common mode noise sources.

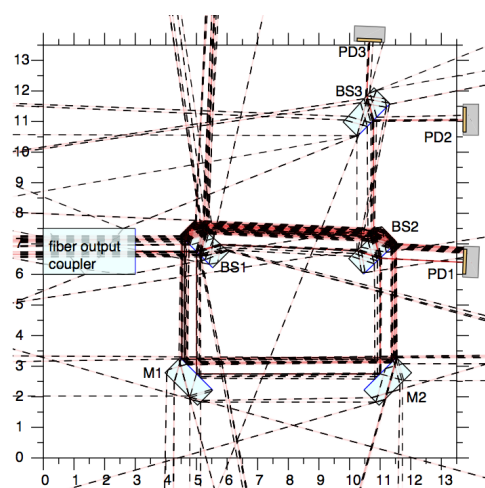
The components available at the institute for optical contact bonding have a size of 15 mm, a height of 20 mm and a thickness of 7 mm. The two wedged beam splitters have a wedge angle of  $3^\circ$ . All components are made for the application of hydroxide catalysis bonding and have therefore a perpendicularity of less than  $2''$  between the relevant vertical and horizontal surfaces. The beam splitters have a splitting ratio of 50 %, the mirrors have an HR coating of 99.9 %. The AR-coatings for both component types are typically assumed to be on the order of 0.1 %. These parameters are used for the IfoCAD simulation, only the vertical alignment of the components was assumed to be perfect for simplicity. The laser beam parameters used in the simulation are 1 mW of laser output power, a beam diameter of 2 mm and beam waist position of 100 mm behind the output coupler position.



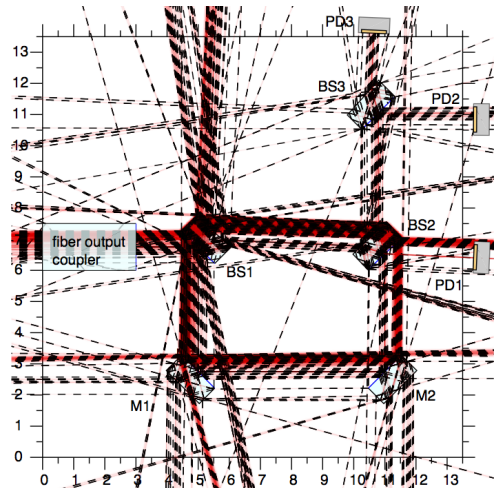
(a) Relative laser power levels below  $1 \cdot 10^{-3}$ .



(b) Relative laser power levels below  $1 \cdot 10^{-6}$ .



(c) Relative laser power levels below  $1 \cdot 10^{-9}$ .



(d) Relative laser power levels below  $1 \cdot 10^{-12}$ .

Fig. 7.1.: 2D drawing of the reference MZI, generated by IfoCAD. The arm length mismatch is 69.7871 mm. The beam splitters BS1 and BS3 have a wedge angle of  $3^\circ$ . The beam has a waist size diameter of 2 mm and a waist position of 100 mm after the fiber output coupler.

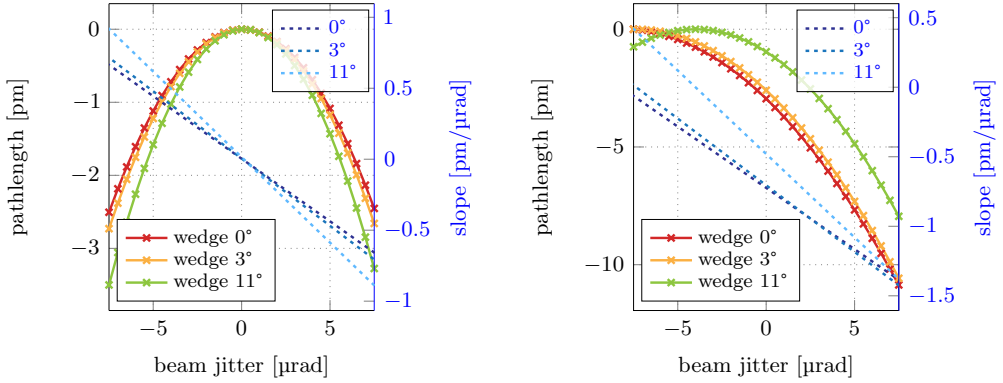
### 7.1.2 Ghost beams

Since the AR- and HR-coatings are not perfect, ghost beams will be generated by reflections at secondary surfaces and so forth. Different drawings of the reference Mach-Zehnder interferometer produced by IfoCAD are shown in Figure 7.1. From Figure 7.1a to Figure 7.1d the minimum laser power of visible beams in the graphical IfoCAD output was reduced. With this analysis, all ghost beams having powers down to a billionth of the incoming beam are visible in Figure 7.1d. The secondary surfaces of wedged components deflect the ghost beams of high laser power away from the main interferometer axes and prevent them from impinging on the photodiodes. By re-positioning the photodiodes (not shown in these drawings), the number of ghost beams entering the sensors can be minimized. The simulation has been repeated for various static misalignments that shift the component positions up to  $10\ \mu\text{m}$ , and tilt the components up to  $10\ \mu\text{rad}$ . This allows us to estimate the ghost beam influence for a static interferometer misalignment. The final interferometer design of the reference MZI is assumed to be ghost-beam-free down to power levels of  $1 \cdot 10^{-12}\ \text{mW}$ , based on the latest simulation results. However, for certain lens and photodiode positions, some spurious beams might still enter the detector and could produce a phase error according to the analytic description of ghost beam influences given in the first part of this thesis (see Section 2.3.2). Due to the redundant diagnostic output ports implemented in the monolithic interferometer design, one could apply balanced detection to reduce the error caused by ghost beams.

### 7.1.3 Tilt-to-length coupling by wedged components

Potential beam jitter, due to the adjustable fiber output coupler, is analyzed for horizontal tilts to estimate the TTL coupling effects in the reference MZI. Earlier experiments have shown that quasi-monolithic interferometers might be limited by adjustable fiber output couplers. Mechanical devices are sensitive to temperature fluctuations that effectively tilt the coupler and, thus, change the propagation direction of the laser beam. This so-called beam jitter, also known as beam pointing fluctuations, was assumed to be the limiting noise source in the original Hexagon experiment [Deh+12]. The Hexagon is an interferometer that has wedged components for ghost beam mitigation. One has considered that beams with pointing fluctuations, that are propagating through wedged components, might be the reason for the pathlength variations observed on the photodiodes.

To estimate the influence of beam pointing fluctuations in the reference MZI, a beam jitter on the order of  $\pm 7.5\ \mu\text{rad}$  was induced in the simulation and the longitudinal optical pathlength signal is observed on photodiode PD1, an SED with 10 mm diameter, without focusing lens. The simulation results are shown



(a) Pathlength signal on PD1 for perfectly aligned interferometers. Each interferometer has differently wedged beam splitters (BS1).

(b) Pathlength signal on PD1 for misaligned interferometers with  $1 \mu\text{rad}$  tilt applied to the recombination beam splitter BS2.

**Fig. 7.2.:** IfoCAD simulations of the longitudinal pathlength signal are shown in dependency on beam pointing fluctuations. The simulations are done for different wedge angles applied to BS1.

in Figure 7.2a for a perfectly aligned interferometer. All data sets correspond to quadratic fit functions with different slopes. For larger wedge angles of beam splitter BS1, the quadratic slope gets slightly steeper. The derivative of these quadratic functions shows a linear trend, the TTL coupling coefficient, whose slope is shown in Figure 7.3 for various wedge angles of BS1 between  $0^\circ$  and  $11^\circ$ . For a perfectly aligned interferometer, a TTL coupling factor of about  $0.1 \text{ pm}/\mu\text{rad}$  is achieved for wedge angles below  $4^\circ$ . To compare the simulations with experimental results from [Deh+12], a static interferometric misalignment caused by the positioning accuracy during the construction process is assumed. For this purpose, a lateral component displacement of up to  $10 \mu\text{m}$  and an angular displacement between  $1 \mu\text{rad}$  and  $10 \mu\text{rad}$  is induced. An example of the longitudinal pathlength signal on photodiode PD1 is shown in Figure 7.2b for angular misalignment applied of  $1 \mu\text{rad}$  applied on the recombination beam splitter BS2. Quadratic functions fit the data again for different wedge angles. But the functions are now shifted along the x-axis compared to the results shown in Figure 7.2a. The slope for each wedge is again on the order of  $0.1 \text{ pm}/\mu\text{rad}$ , but the ordinate-intercept is shifted such that the absolute slope value is larger in comparison to the aligned interferometer which is why a higher TTL coupling can be expected in experiments.

However, even though the simulation results show that the slope of TTL-coupling changes slightly for different wedges, the effect of wedged components is smaller than assumed by [Deh+12]. The measured beam pointing fluctuations from adjustable fiber output couplers measured by [Deh+12] show a DWS

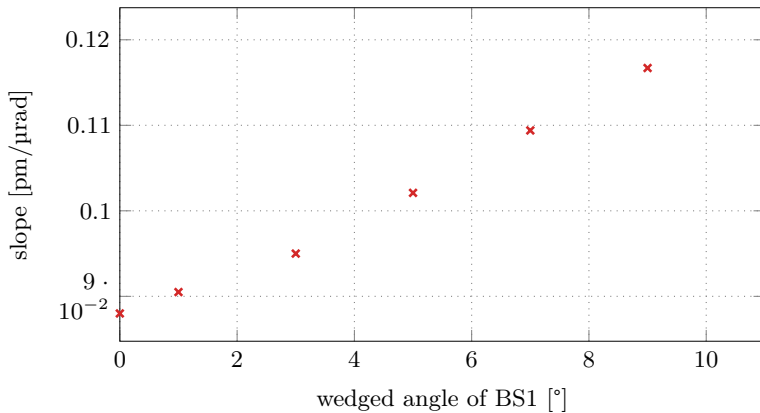


Fig. 7.3.: Linear TTL coupling coefficient for different wedge angles in a perfectly aligned interferometer. A beam jitter of  $\pm 7.5 \mu\text{rad}$  is induced in the simulation.

signal of  $8 \cdot 10^{-4} \text{ rad} / \sqrt{\text{Hz}}$  at 1 mHz. The DWS coupling factor is on the order of 4000 rad/rad which transfers the DWS signal into an optical phase of about  $0.2 \mu\text{rad} / \sqrt{\text{Hz}}$ , equivalent to  $1.2 \text{ pm} / \sqrt{\text{Hz}}$ . For a misaligned reference MZI, the TTL-coupling is on the order of  $1 \text{ pm} / \mu\text{rad}$ , which results in an optical pathlength fluctuation of about  $0.2 \text{ pm} / \sqrt{\text{Hz}}$  on the photodiode.

However, the estimation made by [Deh+12] includes the measured beam pointing fluctuations without the knowledge of the actual temperature fluctuations during this measurement. Since temperature fluctuations are assumed to be the dominating source driving this beam jitter, actual measurements performed with the reference MZI in another thermal environment might differ. The experimental results of the MZI are given in Section 9.2.1 later in this thesis. Here, the measured frequency stability shown in Figure 9.9 is below the requirement of  $4.5 \text{ kHz} / \sqrt{\text{Hz}}$ . Only at 1 mHz a peak is shown in this spectrum, exceeding the  $1 \text{ pm} / \sqrt{\text{Hz}}$ -level by a factor of about six. Since the temperature behavior of the experimental environment, given as spectral density in Figure 9.10, shows a similar peak at about the same frequency this excess phase noise might be driven by thermal fluctuations.

#### 7.1.4 Performance for a static interferometer misalignment

Focusing lenses in front of the photodiodes are included in the optical design of the reference MZI. This is required for the following simulations, utilizing QPDs as sensors with a size of only 1 mm diameter, to analyze the behavior of DWS and DPS signals for different interferometer misalignments in horizontal direction. Plano-convex focusing lenses with a focal length of 25.4 mm are placed in a distance of 21 mm in front of PD1, PD2 and PD3. This results in a beam spot size diameter of about 0.34 mm on the photodiodes.



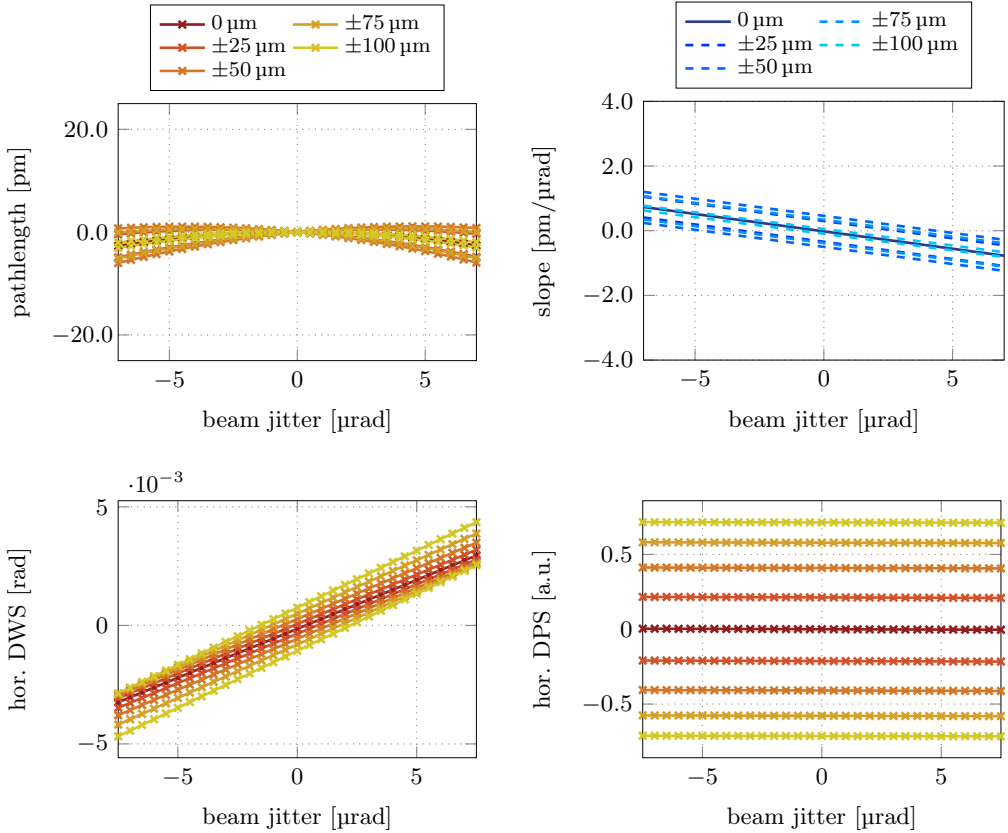


Fig. 7.4.: Simulated horizontal signals on PD1 shown for different lateral lens displacements  $\Delta_{L1}$  in 25  $\mu\text{m}$  steps.

The results of the longitudinal pathlength, plotted in Figure 7.4 for PD1, show a TTL coupling of 0.1 pm/ $\mu\text{rad}$  if the lens is perfectly aligned with respect to the beams,  $\Delta_{L1} = 0 \mu\text{m}$ . We can conclude that the focusing lens does not change the pathlength signals for aligned interferometers by comparing this with the results from the previous section. To estimate the required alignment accuracy of the lenses, which are later manually adjustable in the experiment, the pathlength, DWS and DPS signals are plotted in Figure 7.4 for various lateral lens displacements. The lens L1 is shifted by  $\pm 100 \mu\text{m}$  perpendicularly to the beam propagation in both directions. The changes in the longitudinal pathlength signal are identical for both directions, but with a different sign. The quadratic behavior between beam pointing fluctuations and pathlength signal remains, but the parabola is shifted along both axes in positive or negative direction, depending on the sign of the lateral lens displacement. This leads to a shift in the slope function, which is determined

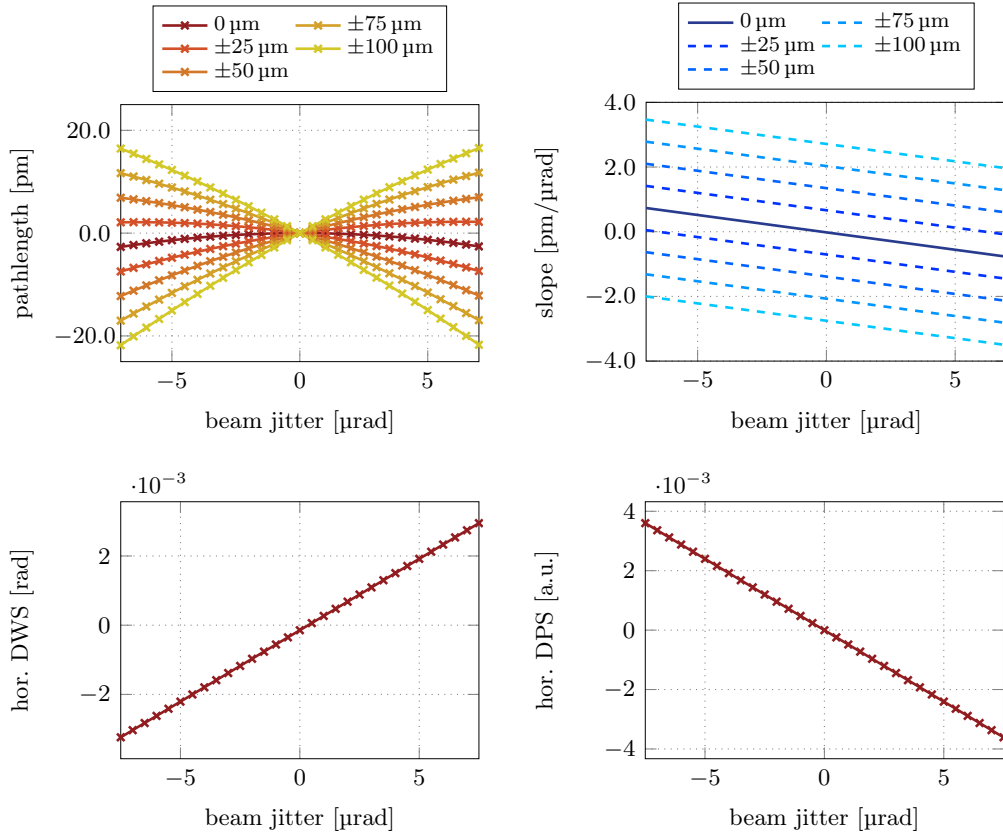
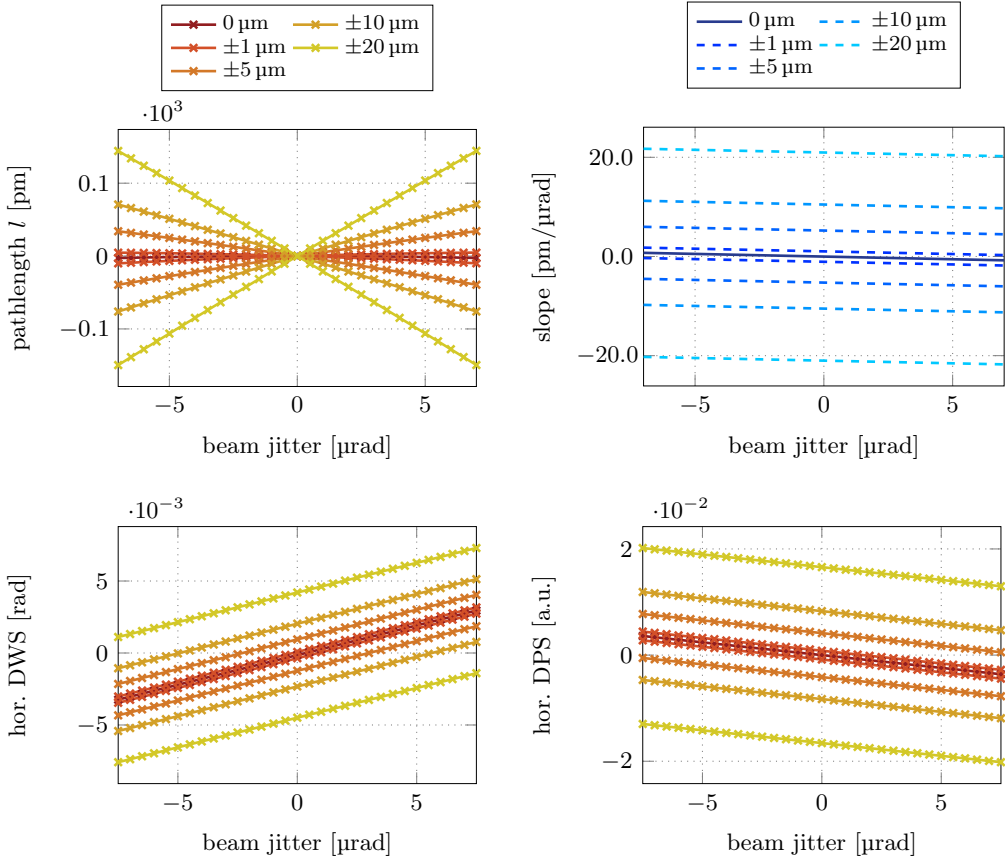


Fig. 7.5.: Simulated horizontal signals on PD1 shown for different lateral lens displacements  $\Delta_{L1}$  in 25  $\mu\text{m}$  steps. PD1 is re-aligned with respect to the reference beam after each lens displacement.

by the derivative of the parabola and shows the TTL coupling factor, increasing linearly with the lens misalignment. To achieve a negligible TTL coupling factor of about 1 pm/ $\mu\text{rad}$ , the alignment accuracy must be better than 100  $\mu\text{m}$  for  $\pm 5 \mu\text{rad}$  beam jitter. The DWS and DPS signals also show a non-vanishing influence of beam pointing fluctuations in dependency on the lens misalignment. A beam walk on the photodiode is expected according to the DPS signals if the photodiode is not re-aligned after the lateral lens shift. Figure 7.5 shows the same simulation results, but for a re-aligned photodiode after misalignment of the lens. The DWS and DPS signals are identical for each lens misalignment, but the TTL coupling increases. A re-alignment of the photodiode leads to more stringent constraints for the alignment accuracy of the lens of about 25  $\mu\text{m}$  to achieve again a TTL coupling factor of about 1 pm/ $\mu\text{rad}$ . The heterodyne efficiency of more than 99.62 % is



**Fig. 7.6.:** Simulated horizontal signals on PD1 shown for different displacements,  $\Delta_{BS8} = [\pm 1, \pm 5, \pm 10, \pm 20] \mu\text{m}$ , applied on the recombining beam splitter BS2. L1 and PD1 are re-aligned after the induced displacement.

not shown in the plots, but was identical for all simulations and did not change significantly over the applied beam jitter.

A displacement of up to  $\pm 20 \mu\text{m}$  was also applied on the position of the recombining beam splitter BS2. This simulates a misalignment of the interferometer during the construction process. The lenses and photodiodes are assumed to be perfectly aligned with respect to the reference beam after misalignment. The results are shown in Figure 7.6. The pathlength signal again shows the expected quadratic relation to beam pointing fluctuations, but its slope increases quickly for certain beam splitter misalignments. This leads to high constraints for the positioning accuracy of the recombining beam splitter to be below  $5 \mu\text{m}$  to achieve a tolerable TTL coupling factor of about  $5 \text{ pm}/\mu\text{rad}$ . Due to the interferometric misalignment a beam walk is observable on the photodiodes even though lens and detector are

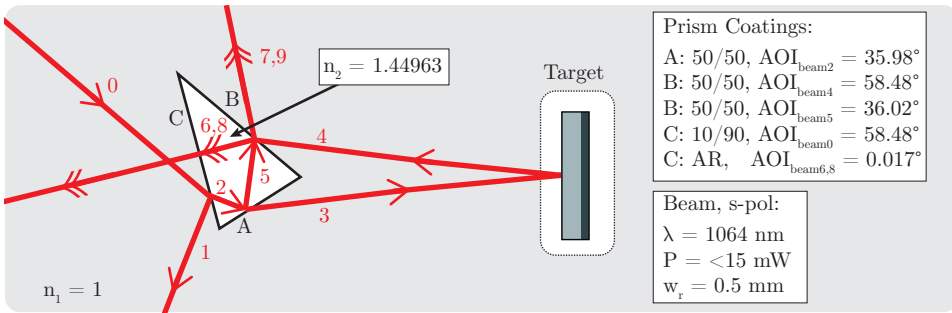


Fig. 7.7.: Sketch showing the prism dimensions and the beam geometry of an isosceles prism with a vertex angle of  $36^\circ$  angle and legs of 25 mm length.

re-aligned properly after the misalignment. The strict alignment accuracy for the interferometric components of about  $5 \mu\text{m}$  is not easily achievable, since template construction has an accuracy of 10 to  $50 \mu\text{m}$ , according to tools available in the mechanical workshop. The alignment of critical components, like recombining beam splitters, is done manually with pointing fingers and micrometer screws while monitoring the contrast. Even though the component can be shifted very accurately by micrometer steps, the sensing of contrast during the alignment is not sufficient. The change of heterodyne efficiency in dependency on the misalignment is only about  $0.5 \%/ \text{nm}$ .

## 7.2 Test Mass in the Middle experiment

A first prototype of a one-component interferometer has been designed and analyzed in IfoCAD. A so-called Test Mass in the Middle (TMitM) has also been designed and will be used to experimentally validate the functionality of these one-component prism-interferometers. The TMitM is also a first prototype experiment for future investigations towards test mass OHs. It contains a single, gold-coated mirror in the middle of a baseplate, which can be actuated. Two prism-interferometers are aligned with respect to the front and back surfaces of the test mass mirror. With this experimental set-up the overall achievable performance of DFM technology can be tested by detecting correlated test mass motions from two opposite directions.

### 7.2.1 Prism-interferometry

By utilizing single-component interferometry, the optical complexity is reduced in comparison to classic interferometric set-ups, as shown for the reference MZI, but the beam geometry of the component and the optical properties must be determined in advance. We will focus on the design of prism-interferometers, which

are the most promising one-component interferometer candidates as described in Section 6.2.3. Here, we use a prism with an isosceles triangle as ground surface and optically coated side surfaces which are perpendicular to the ground surface. Two of the side surfaces are used for the beam splitting and the beam recombination, the third surface is, in general, not needed for prism-interferometry. To achieve the best possible interferometer quality, thus maximum contrast, the beam splitter surfaces are coated with a power reflectivity of 50 %. A prism with these specific coatings is not commercially available, thus the optical component is designed in IfoCAD. Since IfoCAD does not support a class for creating arbitrary components, the new component class *Arbitrary\_Prism::Arbitrary\_Prism()* is written for this purpose and locally integrated into the C++ version of IfoCAD.

Various shapes of uncoated prisms are commercially available, like right angle prisms, dispersion prisms, equilateral prisms, penta prisms and more. A typical material used for these components is fused silica, having a refractive index of  $n = 1.44963$  and a CTE of about  $5.5 \cdot 10^{-7}/\text{K}$ . This material is used for bonding components and shows excellent properties for their application in high precision interferometry. Most of the commercially available prism shapes were tested in IfoCAD simulations. By the implementation of a minimizer algorithm the beam propagation and alignment of the interferometer is tested automatically. Figure 7.7 shows the beam propagation by using an isosceles prism. It has a vertex angle of  $36^\circ$  and base angles measuring  $72^\circ$ . The legs have a length of 25 mm. The resulting base is determined to be at 15.45 mm and the height is 20 mm. To ensure that the beams are not vertically misaligned by the prism the perpendicularity of side surfaces to ground surface is required to be at least  $2''$ , an estimation based on bonding components that were used so far in quasi-monolithic set-ups. By using this type of prism, the beam propagation through the set-up shows excellent properties particularly with regard to future test mass set-ups. The incoming beam is split at the front surface, C, whereby only a fraction is reflected while most of the light is transmitted into the optical medium. Surface A splits the transmitted beam. Half of the light, the so called reference beam, propagates inside the prism to surface B. The other part of the light leaves the optical medium and travels towards an external target, the motion of which is to be measured. This so-called measurement, or test mass, beam is reflected by the target and interferes at surface B with the reference beam. The propagation delay, which is required for DFMI, is ensured since the target is typically placed in a distance of a few cm, thus the measurement beam must propagate a longer distance than the reference beam which is internally reflected. Two redundant optical measurements are provided by each output port of the recombination surface. While one of the signals is directly leaving the prism, the other interference signal passes the optical medium again and propagates through surface C before it can be detected by a photodiode. For this

**Tab. 7.1.:** Spot size radii of the interfering beams for both output ports of the recombination surface. Beams 7 and 9 interfere to a signal that is directly reflected by the prism. The indirect interference signals of the beams 6 and 8 propagate through the prism.

beams	radii of reference beam		radii of measurement beam		contrast
	horiz. [mm]	vert. [mm]	horiz. [mm]	vert. [mm]	
6, 8	0.824	0.555	0.863	0.584	>0.99
ellipticity	0.67		0.67		
7, 9	0.551	0.553	0.581	0.582	>0.99
ellipticity	0.996		0.998		

reason, surface C is equipped with an AR coating that prevents the transmitted interference signal from being backreflected into the interferometer. Apart from this backreflection the prism-interferometer is assumed to be ghost-beam-free.

Due to the particular beam geometry of the prism-interferometer, the AOIs of the beams inside the prism are similar to the critical angle,  $\Theta_c$ , for light propagating from fused silica ( $n = 1.45$ ) into vacuum ( $n = 1$ ) that can be calculated by Snell's law via

$$\Theta_c = \arcsin\left(\frac{1.00}{1.45}\right) = 0.76 \text{ rad} = 43.6^\circ. \quad (7.1)$$

If a propagated electromagnetic wave impinges on an optical surface at an AOI that is larger than a specific critical angle the light cannot pass through the boundary if the refractive index is lower on the other side. This phenomenon is known as total internal reflection. The so-called critical angle is the AOI above which total internal reflection occurs. An AOI below this critical angle of  $43.6^\circ$  must be ensured for all beams propagating inside the optical medium. Other effects like evanescent waves and frustrated total internal reflection are not considered. This analysis is only based on Snell's law which is not affected by coatings that might be applied to the prism surfaces. However, Figure 7.7 shows the beam rays simulated with IfoCAD for a typical prism. The AOIs for all surfaces, A, B and C, and for all beams, number 0 - 9, are determined by the simulation and the critical beams traveling inside the medium, number 2, 5, 6 and 8, will not generate total internal reflections.

To achieve maximal contrast in the interferometer the laser powers of reference (number 5 in Figure 7.7) and measurement beam (3/4 in Figure 7.7) should be matched such that they are equal. Due to the sophisticated geometry, the AOIs are either  $36^\circ$  or  $58.8^\circ$ , depending on the beam. This makes the coating process, ensuring 50% reflectivity for two different AOIs, very challenging. The company Laseroptik in Garbsen was able to coat these surfaces with  $\pm 2\%$  precision. A

further issue in achieving high contrast is the profile of the two beams entering the photodiodes. Future experiments, in which the prisms will be used, require a beam waist size radius of about 0.5 mm with a waist position of 100 mm. The AOIs of the beams are not  $45^\circ$ , which is a typical AOI of beams in conventional interferometers. Table 7.1 shows the spot radii of measurement and reference beam on the photodiode in a distance of 120 mm, measured from the interference point at the recombination surface. The pathlength difference between these two is about 83 mm. Regarding the indirect output port of the recombination surface, the interfered signal propagates through the optical medium and both beam profiles have an ellipticity of 0.67. The other, direct output port is more balanced and almost perfect Gaussian beams are monitored on the photodiodes. The heterodyne efficiency is for both interference signals above 99 %, even for the interference signal generated by the two elliptic beams, since they are equally distorted. Due to the identical AOIs of beam 0 and 4, under which these enter the optical medium, the refraction into a medium with a higher refractive index is the same. The beam profile distortion is therefore identical for both beams. The beam profile distortion is reverted when the beam leaves the optical medium at an angle, as it is the case for the direct output port. In contrast, the beam profile distortion is not reverted for the beams 6 and 8 when leaving the prism through surface C, since the AOI on this surface is very small, nearly  $0^\circ$ . However, the interferometry is not limited by effects like small AOIs, beam ellipticity or laser powers. The ellipticity of the indirect interference signal might however have an influence on the DWS signals in future test mass readout experiments. An imaging system might be required to compensate the ellipticity of the beams and to correct the DWS signal.

Within the geo-Q project of the SFB, 15 coated prisms are ordered from Laseroptik Garbsen with the optical properties mentioned above. A detailed plot of the optical coating quality can be seen in Appendix C. These prisms are used in the TMitM DFM experiment which will be described in the following.

## 7.2.2 Optical design

In the TMitM experiment, the motion of a test mass mirror will be read out from two sides by prism-interferometers which are placed point-symmetrically. The test mass, prisms and fiber output couplers will be fixed to a glass ceramic baseplate with the same thermal properties as the one used for the reference MZI. The baseplate has a size of  $135 \text{ mm} \times 135 \text{ mm} \times 36 \text{ mm}$ .

Figure 7.8 shows the final version of the optical TMitM design. Only two prisms are used for the interferometry and no further optical components are required. The light from two fiber output couplers is sent to the prisms where 4 % of the light is reflected at surface C and can be used for detecting laser power fluctuations. The

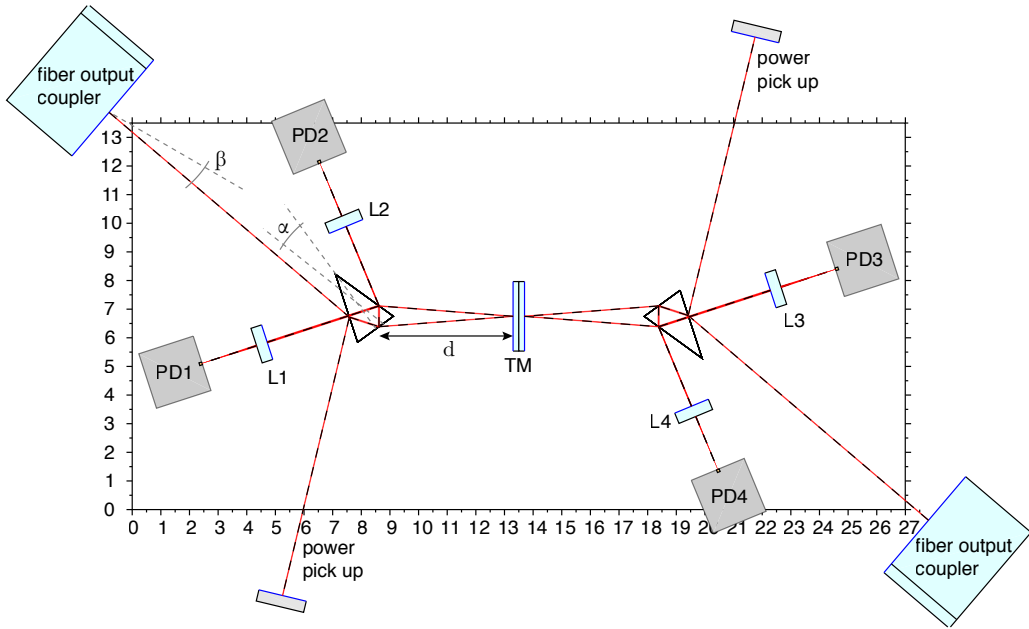
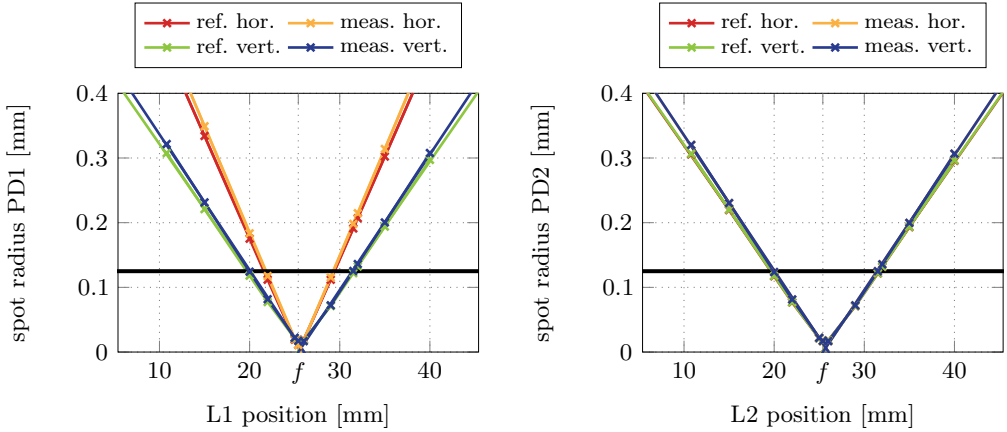


Fig. 7.8.: 2D sketch of the TMitM generated with IfoCAD. Both prism-interferometers have an arm length difference of about 83.3 mm. The test mass in the middle is an actuation mirror which is gold-coated from both sides. The displacement and tilt is monitored via prism-interferometry from both sides, providing two redundant measurements. The beam parameters of this simulation are 0.5 mm waist size radius and 100 mm waist position. The lenses are plano-convex and have a focal length of 25.4 mm.

major part of the light is sent into the prism where it is reflected at the second prism surface, A, that generates a reference and measurement beam. The reference beam travels inside the prism to the third surface, B. The measurement beam is used to scan the test mass motion via reflection under an angle of  $4.1^\circ$ . Reference and test mass beam are interfered at the third surface, B, and provide two redundant signals, one directly reflected by the prism, the other one indirectly by passing through the prism again. To align the interferometer the prism orientation,  $\alpha$ , is adjusted by using the minimizer function in IfoCAD. The accumulated optical pathlength from both beams differ by  $d \approx 83.3\text{ mm}$  which can be tuned by a few cm if desired. The orientation of the fiber output coupler,  $\beta$ , can then be used for compensating the induced tilt misalignment. The test mass is a Zerodur mirror that is gold-coated from both sides. The surfaces have a parallelism to each other of below  $2''$ . This mirror is mounted in a three-axis actuation mount to simulate particular test mass motions. Two commercially available adjustable fiber output couplers made of titanium from SuK are used to produce a collimated beam with 0.5 mm waist size radius. The photodiodes implemented in this simulation are QPDs





(a) Spot size radii monitored on PD1 for different lens positions of L1.

(b) Spot size radii monitored on PD2 for different lens positions of L2.

**Fig. 7.9.:** Spot size radii for the TMitM in dependency on the lens position (focal length:  $f = 25.4$  mm). The lens position is measured relatively to the position of the photodiode. The black curve shows the goal of 0.125 mm spot size radius.

with parameters that are based on the GAP1000Q, an InGaAs QPD provided by OEC GmbH, having an active area of 1 mm diameter. Plano-convex lenses with 25.4 mm focal length are required in front of each photodiode to decrease the spot size radii of the beams on the QPDs down to around 0.125 mm, a quarter of the size of the active area. Figure 7.9 shows spot size radii for the TMitM experiment in dependency on the lens position, relatively measured to the photodiode position. The spot size goal is achieved for a distance of 20 mm or 31 mm between lens and photodiode. The following simulations are realized by using the 20 mm distance.

### 7.2.3 Ghost beams

The second interferometer output port, passing through the prism, propagates through the surface C, see Figure 7.10a, before it is monitored by a photodetector. It has a small AOI of 1.3 mrad measured relative to surface C, which ensures a high transmission due to the AR coating of better than  $r_{AR,0^\circ} = 0.1\%$  for  $0^\circ$  AOI (as measured by Laseroptik and shown in Figure C.1). However, a fraction of the interference is reflected back (see Figure 7.10b) and propagates almost in parallel to the nominal beams through the prism and along the test mass path, but in opposite direction. A possible backscatter to the fiber output coupler can be neglected due to the beam angle of 1.3 mrad relative to the injected beam. But it is once again reflected by surface C under an angle other than  $0^\circ$ . The residual reflection for this AR coated surface for  $55.5^\circ$  is about  $r_{AR,55^\circ} = 2\%$ . Therefore, it is reflected

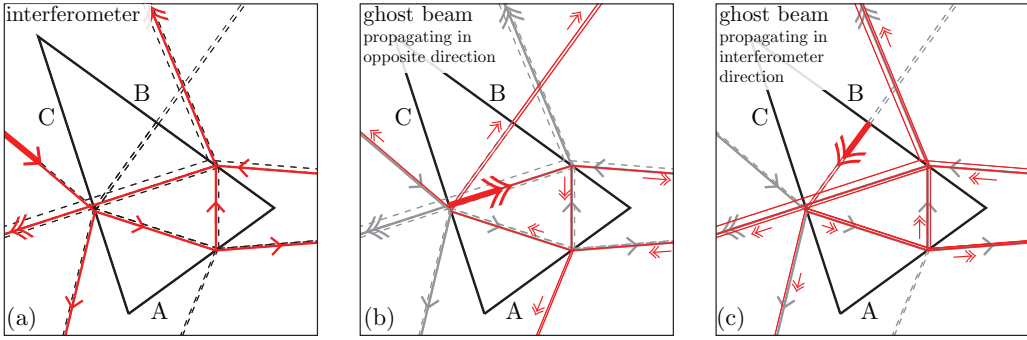


Fig. 7.10.: 2D ray propagation simulated with IfoCAD of the ghost beam through the prism. Highlighted in red are the actual interferometer rays, shown in (a). The occurrence of the ghost beam at the AR-coated surface C and propagation in opposite direction through the prism is shown in (b). The subsequent backreflection of this ghost beam at surface B (50/50) which then enters the interferometer and travels in a critical direction is shown (c).

by surface B almost under  $0^\circ$  (see Figure 7.10c). Since the small AOIs cancel out after two reflections, this secondary reflection of the ghost beam travels partly in parallel to the actual interferometry beam with a lateral shift of about 1 mm, but partly overlapping it as well. In total, four additional spurious interferences enter each interferometer output port, all having an estimated power of

$$\begin{aligned} P/P_0 &= r_{AR,0^\circ} \cdot 0.5 \cdot 0.5 \cdot r_{AR,55^\circ} \cdot r_{B,0^\circ} \cdot r_{AR,55^\circ} \cdot 0.5 \cdot 0.5 \\ &= 0.001 \cdot 0.5^4 \cdot 0.02^2 \cdot 0.25 = 6.25 \cdot 10^{-9}. \end{aligned}$$

Here it is assumed that surface B reflects only  $r_{B,0^\circ} = 25\%$  for an AOI of  $0^\circ$  and the power value is scaled relative to the main signal power of one output port. The amplitude ratio between interference signal and ghost beam signal, determined by the square root, is about  $80 \cdot 10^{-6}$ , which is proportional to an estimated phase error of  $80 \mu\text{rad}$ . All ghost beams are caused initially by the interference of the second prism output port, consequently they have the same interferometric phase information. The accumulated pathlength varies between the ghost beam signals because some of them travel inside the prism, while other travel once again along the test mass path. The compactness and stability of the prism-interferometer will likely reduce the ghost beam dynamics to negligible levels, while the lateral beam shift reduces the mode overlap on the photodiode. The actually achievable performance will validate the linearity and the dynamic range of prism-interferometry, given in Chapter 9.

In the following the motion of the test mass is investigated by optical simulations. We will analyze the lateral displacement along the  $x$ -axis to estimate the dynamic

range of prism-interferometry. TTL coupling is a well-known problem in test mass interferometers. A horizontal and vertical tilt will be induced to the test mass, simulating yaw and pitch motions. In dependency on the tilt axis, either the horizontal, or the vertical, DWS and DPS signals are plotted.

#### 7.2.4 Test mass displacement

The displacement to interferometric phase coupling of a test mass does not only depend on the measured phase, but also on the interferometer geometry. A test mass which reflects the measurement beam under an angle of  $0^\circ$  generates an optical pathlength change on the PD that is twice the actual test mass motion. The laser beam accumulates the displacement twice, the first time when it propagates towards the test mass and a second time on its way back after reflection. To compute the actual displacement the measured optical phase data is divided by a factor of two. The test mass mirror in the TMitM experiment reflects the laser beam under an angle of  $4.1^\circ$ , which can be seen in the 2D dimensional interferometer drawing in Figure 7.8. For this case the scaling factor changes and can be determined by geometry via  $2/\cos(4.1^\circ) = 2.0051$ . Moreover, optical simulations of the TMitM can be used to determine the expected interferometric behavior for certain test mass displacements. Figure 7.11 shows the simulation results for a test mass displacement of  $\pm 3$  mm along the x-axis. The scaling factor obtained by the IfoCAD simulation is given by the slopes of the upper plots in Figure 7.11, which for both photodiodes amounts to 1.99 mm/mm. This value differs from the geometrical result of 2.0051 which can possibly be explained by the effect of the focusing lenses which are placed in front of the photodiodes. For the experimental displacement results of the TMitM, shown in Section 9.3, we will scale the phase data of one interferometer by a factor of two, for simplicity's sake. For the comparison of the two prism-interferometers against each other one should keep in mind that the corresponding phase data contains four times the actual test mass displacement since the factor of two is measured on both test mass sides by each interferometer. In this case the combined phase data is scaled by a factor of four.

The horizontal DWS signals simulated for both photodiodes are also shown in Figure 7.11. While the signal on photodiode PD2 shows a linear trend over almost the full displacement range of  $\pm 2$  mm, the signal on photodiode PD1 follows a sinusoidal trend which is only linear in a range of about  $\pm 0.5$  mm. The elliptic beam shapes monitored only by PD1 are most likely the reason for these irregularities that influence the DWS signals on a QPD.

A test mass displacement along the x-axis causes a small parallel offset of the reflected beam, while the propagation direction of the beam does not change

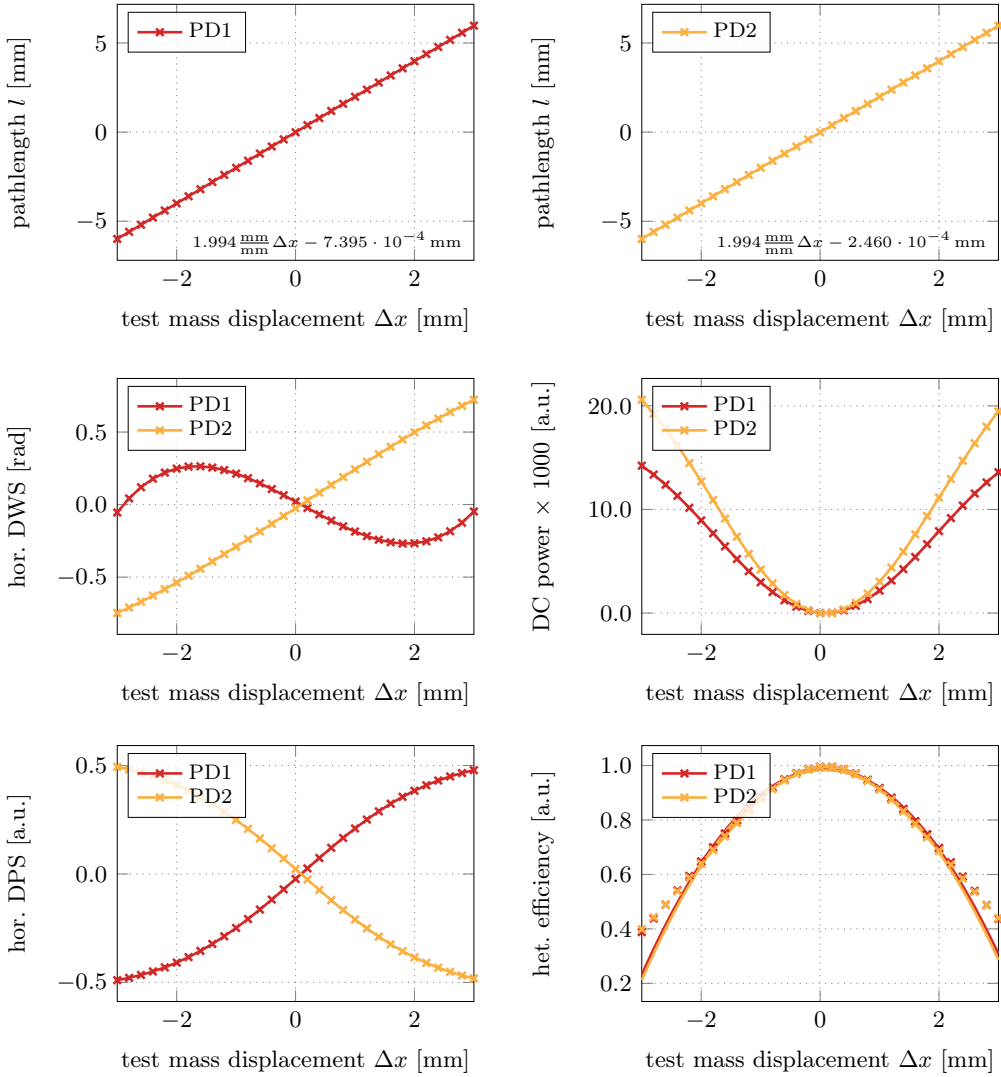


Fig. 7.11.: Performance of the prism-interferometer for  $\pm 3$  mm test mass displacement. with focusing lenses, L1 and L2, both having a focal length of  $f = 25.4$  mm, placed in 20 mm distance to the photodiodes PD1 and PD2, respectively.

(under the assumption that the test mass is not tilted). For a certain displacement the test mass beam does not interfere with the reference beam anymore. This effect will limit the dynamic range of the interferometric pathlength measurement. Figure 7.11 shows also the simulation results of the heterodyne efficiency if the test mass is shifted by  $\pm 3$  mm. A quadratic fit is applied to the data between  $\pm 2$  mm, the range where the interferometer response is still nearly linear. The results of the fit function show a heterodyne efficiency of more than 20 % over the full 6 mm range for both PDs. The actual, simulated data points do not even drop below 40 %. From these results we can conclude that the prism-interferometers can be used to measure over a range of about 6 mm, while the actual pathlength signal measured by the PDs corresponds to 12 mm.

### 7.2.5 Test mass tilt couplings

Cross coupling of angular jitter into the longitudinal pathlength signal is a significant noise source in LISA Pathfinder [Wan10]. Similar effects are to be expected from the test mass mirror in the TMitM experiment. For this reason optical simulations are used to investigate the coupling of test mass tilts into optical signals, such as the DWS, DPS and heterodyne efficiency, shown in Figure 7.12 and the longitudinal pathlength signal. The signals on both photodiodes, PD1 and PD2, from one side of the TMitM are simulated. Due to the mirror-symmetry of the set-up similar signals are expected for photodiodes PD3 and PD4. Based on the work of [Sch17] and [Wan10] a reduction of tilt couplings can be achieved by using lenses and imaging systems, whereby the alignment accuracy becomes important. For the following simulations the TMitM layout as shown in Figure 7.8 is used, with PDs of 1 mm diameter and lenses in a distance of 20 mm in front of them with 25.4 mm focal length. The test mass mirror is tilted by  $\pm 250$   $\mu$ rad once in yaw, and once in pitch direction. Its center of mass is used as pivot point, which is why an additional geometrical pathlength is induced for each tilt. The resulting pathlength signals are calibrated with respect to the pathlength value measured for the initial mirror rotation of 0  $\mu$ rad. In general, an absolute pathlength of about 83.3 mm is subtracted from each pathlength signal for the calibration.

Figure 7.13 shows the simulation results of the optical pathlength on the left side of this Figure, and the according slopes, the TTL coupling, on the right. The horizontal TTL coupling is about 10 pm/ $\mu$ rad for both photodiodes over the full tilt range of  $\pm 250$   $\mu$ rad. Indeed, the pathlength slope of PD2 shows a flat dependency for  $\pm 100$   $\mu$ rad test mass tilt whereby the TTL coupling coefficient is significantly reduced for this regime of mirror tilt in comparison to the signal on PD1. In order to investigate the influence of an induced, static misalignment the prism is shifted along the  $x$ -direction by  $\Delta_{\text{Prism}} = 1$  to 10  $\mu$ m. The TTL coupling

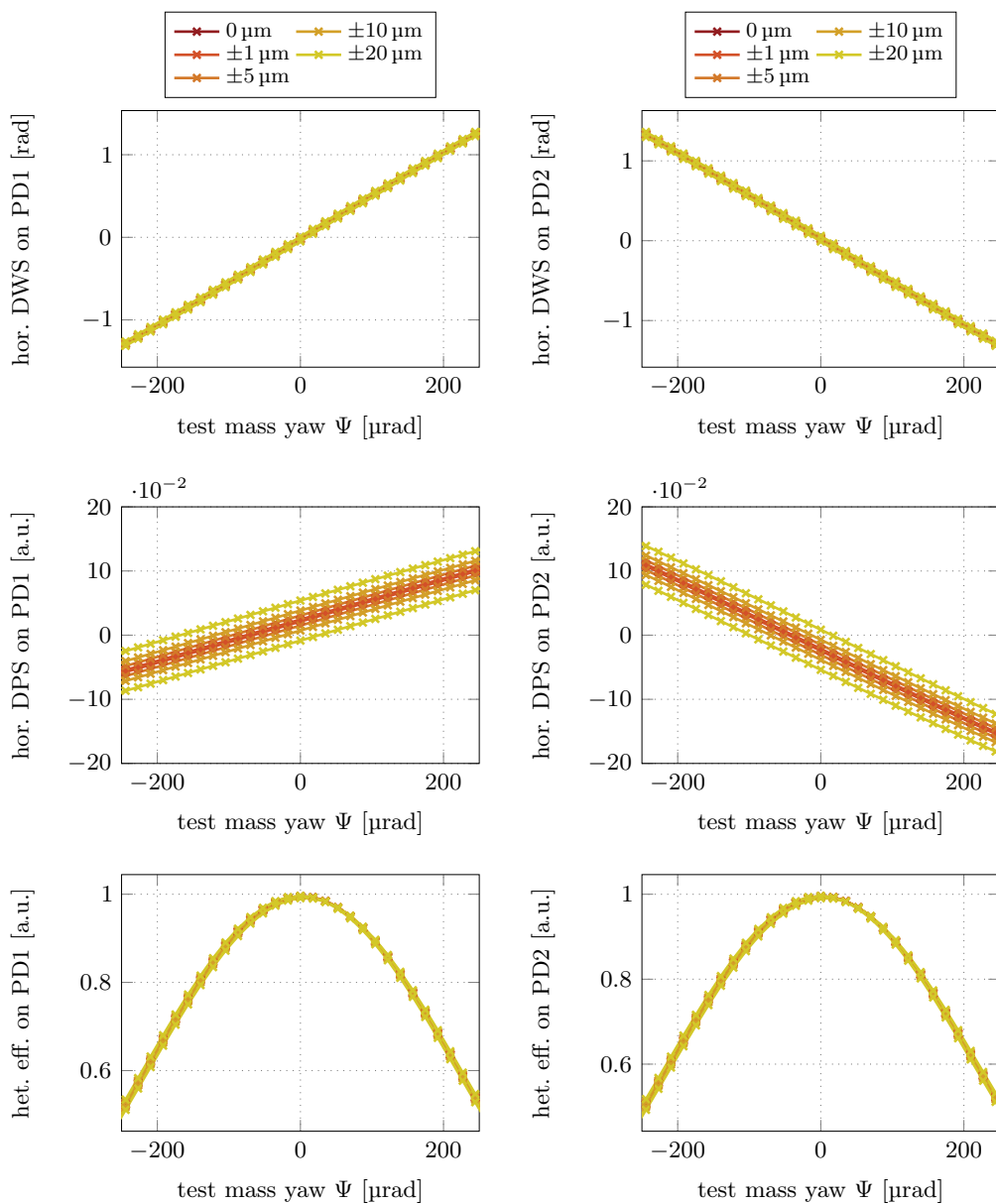
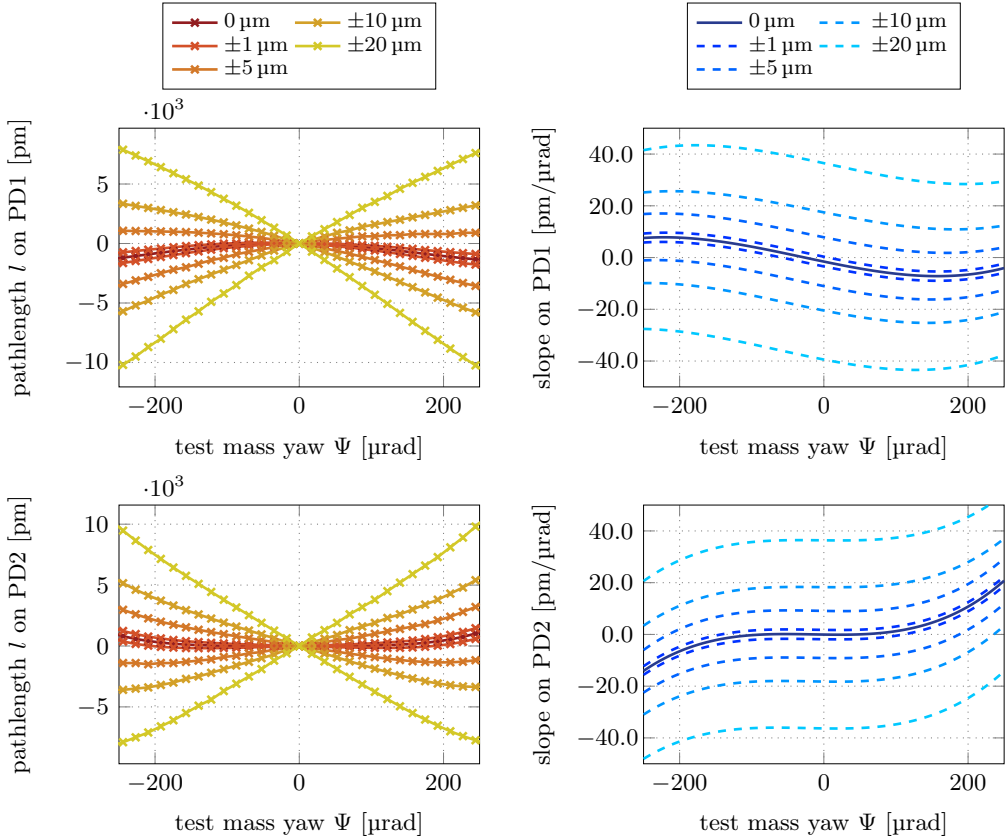


Fig. 7.12.: Performance of the prism-interferometer for  $\pm 250 \mu\text{rad}$  test mass tilt, with focusing lenses, L1 and L2, both having a focal length of  $f = 25.4 \text{ mm}$ , placed in  $20 \text{ mm}$  distance to the photodiodes PD1 and PD2, respectively. Shown are the signals for different misalignments  $\Delta_{\text{Prism}}$  of  $[\pm 1, \pm 5, \pm 10, \pm 20] \mu\text{m}$ .



**Fig. 7.13.:** Horizontal pathlength in dependency on a test mass tilt in the TMitM for different misalignments  $\Delta_{\text{Prism}}$  of  $[\pm 1, \pm 5, \pm 10, \pm 20] \mu\text{m}$ .

is enhanced for larger misalignments. The slope is shifted along the ordinate in positive or negative direction, depending on the sign of the prism shift. For  $5 \mu\text{m}$  misalignment the slope no longer shows a zero-crossing and the coupling coefficient is increased to about  $10 \text{ pm}/\mu\text{rad}$  for the initial test mass rotation of  $0 \mu\text{rad}$ .

To counteract the increased TTL coupling due to misalignment the lens position can be re-adjusted. The minimizer function in IfoCAD is used to find the optimal lens position such that the TTL coupling has a zero-crossing for  $0 \mu\text{rad}$  test mass tilt and the beam spot sizes are still in an adequate regime of about  $0.05$  to  $0.2 \text{ mm}$ . The coupling coefficients are calculated for  $\Psi = \pm 5 \mu\text{rad}$  test mass tilt around

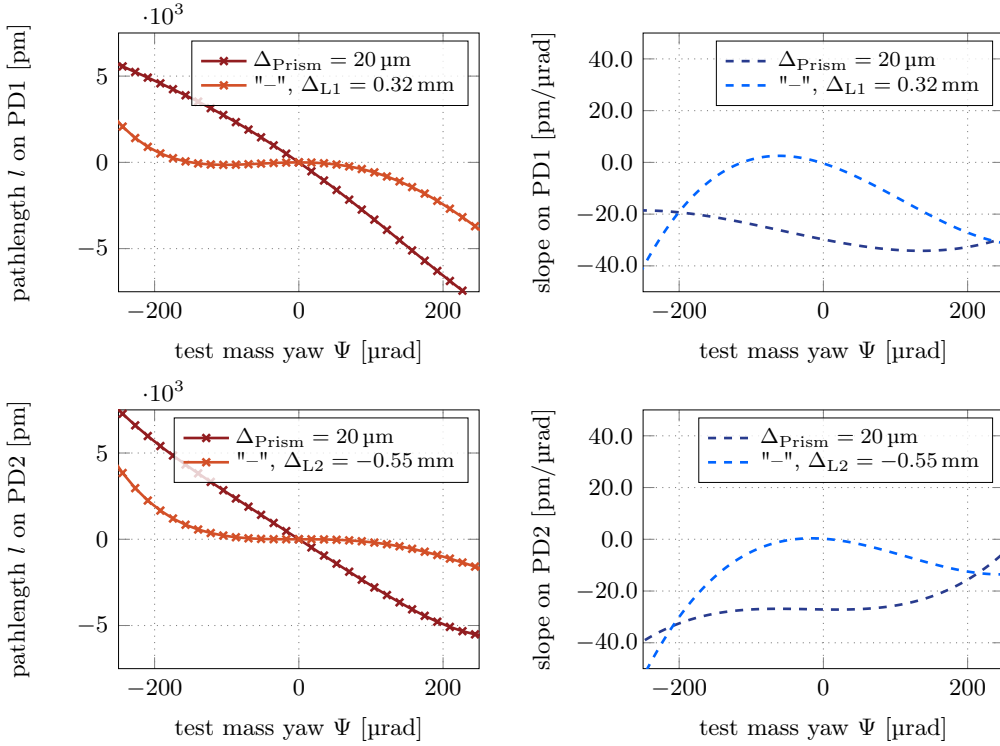


Fig. 7.14.: Horizontal pathlength of the misaligned prism-interferometer with lenses compensating for the test-mass-induced TTL coupling. The lenses are shifted perpendicularly to the beam propagation direction by  $\Delta_{L1}$  and  $\Delta_{L2}$ . The distance from test mass to L1 is 199.5 mm and to L2 is 117.7 mm. Photodiode PD1 is placed 21.7 mm behind L1, PD2 is placed 19.6 mm behind L2.

zero. The minimizer function requires a cost function value meant to be optimized, which is here defined as

$$y[0] = \left[ \left( \frac{\Delta l(10 \mu\text{rad})}{10 \mu\text{rad}} \right)^2 + 1 \right] \cdot g(c = 1 \cdot 10^7, \min = 0.05, \max = 0.2, w_r) \quad (7.2)$$

Here,  $\Delta l(\Psi)$  is the longitudinal pathlength difference,  $l(-5 \mu\text{rad}) - l(5 \mu\text{rad})$ , for the specific yaw angle,  $\Psi$ , and  $g(c, \min, \max, x)$  is the double-sided penalty function. Parameter  $c$  sets the gradient, or slope, of the penalty function. The larger the value for the  $c$ , the stronger is the slope,  $\min$  and  $\max$  sets the lower and upper limit for the penalty function and  $x$  contains data that is used for the penalty function's calculation, here we use the horizontal spot size radius  $w_r$  of the reference beam on PD1 and PD2, respectively. The parameters that are allowed to be tuned during the optimization are the lens positions of L1 and L2, and the distance



between test mass and photodiodes, or lenses respectively. The lenses are shifted once along the beam propagation direction back and forth with respect to the photodiode, or perpendicularly to the beam axis. The penalty function of the spot size radius limits the actual range for the lens displacement along the beam propagation direction. The maximum allowed perpendicular shift for the lenses,  $\Delta_{L1}$  and  $\Delta_{L2}$ , is limited by border values that are passed to the minimizer which are in this case  $\pm 3$  mm. Figure 7.14 shows the simulation results for a misaligned prism-interferometer by  $\Delta_{\text{Prism}} = 20 \mu\text{m}$ , once with perfectly aligned lenses and once according to the results of the minimizer. For both detectors we achieve a reduced TTL coupling effect by optimizing the lens and photodiode positions, but the parameters vary for both detectors. For the indirect interferometer output, detected by PD1, the simulation found an optimal distance between test mass and lens of 199.5 mm, while PD1 is placed in a distance of 21.7 mm with respect to L1, and L1 is shifted by 0.32 mm perpendicularly to the beam propagation direction. The optimal parameters for the direct interferometer output, detected by PD2, are accordingly 117.7 mm for the distance between test mass and L2, and 19.6 mm for the distance between PD2 and L2, while  $\Delta_{L2}$  is  $-0.55$  mm. The TTL coupling coefficient is no longer linear, or symmetrical, for small test mass angles around  $0 \mu\text{rad}$ , but the absolute coupling can be minimized within the range of  $\pm 5 \mu\text{rad}$  test mass tilt. Furthermore, within  $\pm 50 \mu\text{rad}$  the TTL coupling shows adequate coefficients of less than  $10 \text{ pm}/\mu\text{rad}$ , for PD2 even below  $5 \text{ pm}/\mu\text{rad}$ .

For completeness we also show the signals for a vertical tilt of the test mass,  $\Theta$ , in Figure 7.15. Both detectors show a quadratic-like longitudinal pathlength for  $\pm 250 \mu\text{rad}$  vertical test mass tilt. The resulting slope, indicating the TTL coupling, is small around the initial mirror position and shows a linear dependency for small pitch angles between  $\pm 100 \mu\text{rad}$ . Not shown are results of simulations with induced, static interferometer misalignment. For this case, we expect an enhanced vertical TTL coupling that is on the same order of magnitude as observed for the horizontal coupling. However, we assume that this effect can also be compensated for by a re-positioning of the lenses, this time in the  $z$ -direction. Both tilt angles generate DWS coupling coefficients of  $5000 \text{ rad}/\text{rad}$ .

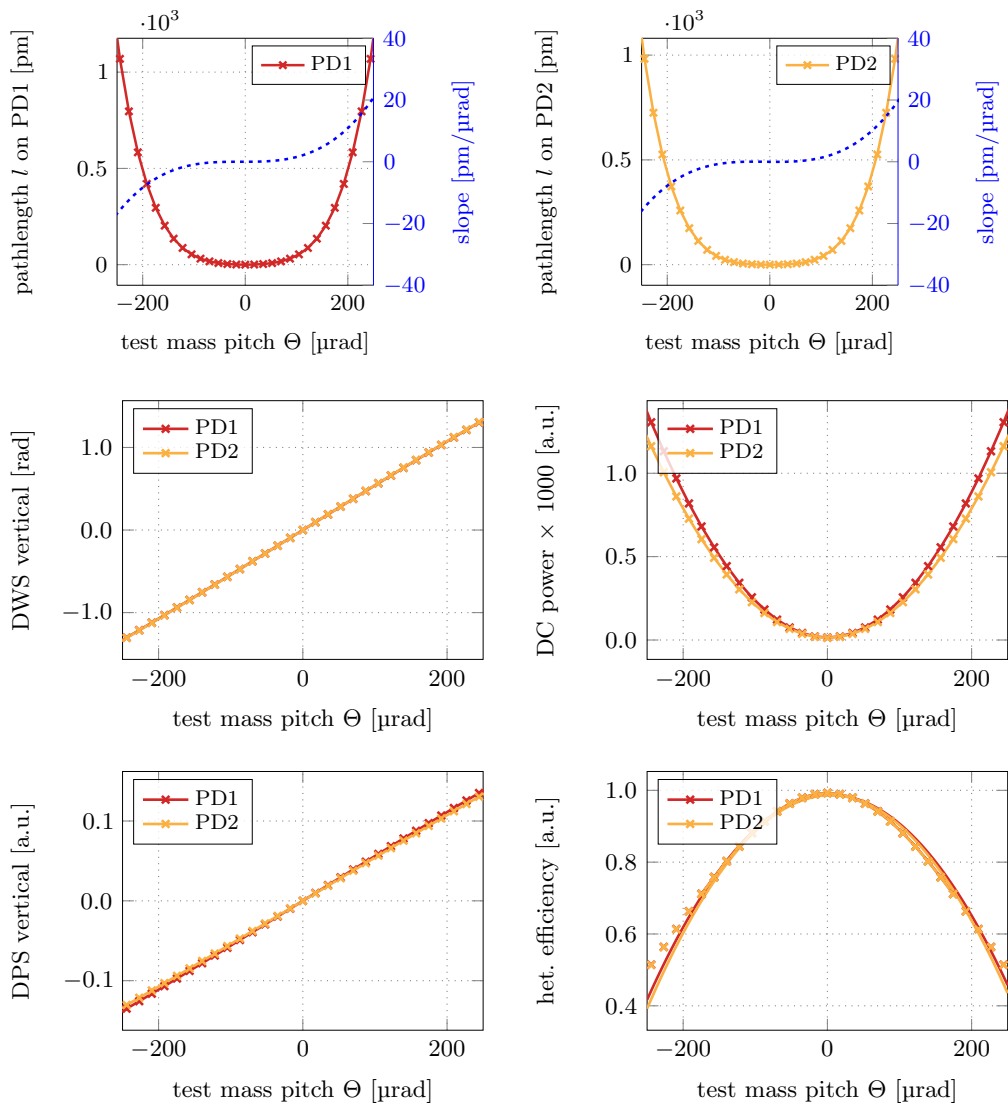


Fig. 7.15.: Vertical performance of the focusing lenses, L1 and L2, both having a focal length of  $f = 25.4\text{mm}$ , placed in 20mm distance to the photodiodes PD1 and PD2, respectively. The combination of focusing lens and photodiode are perfectly aligned with respect to the reference beam.

# EXPERIMENT PREPARATION

” *Description of the typical experimental infrastructure required for DFMI and the construction of quasi-monolithic interferometers.*

The first-proof-of-principle experiment of an interferometric set-up using DFM technology was demonstrated within the SFB geo-Q in Hannover in collaboration with the National Institute of Standards and Technology (NIST), Maryland, US. An exchange with NIST was convenient since the dedicated laser source, able to modulate the laser frequency by roughly 10 GHz with a rate of about 1 kHz, was available at this institution and the required optical set-ups can easily be built by using simple, commercially available, off-the-shelf components. After some initial measurements were taken at NIST, evolved investigations of DFM were continued at the AEI. The core components for DFM, like the dedicated laser source, were adapted from the experience gained at NIST, such that the main experimental infrastructure was kept the same apart from small parameter changes that will be highlighted in this chapter.

## 8.1 Frequency tunable laser sources

The usage of DFM interferometry promises very compact, small, and simple optical set-ups. To achieve interferometric set-ups on cm-scale, the frequency modulation applied on the laser beam must reach magnitudes in the order of a few GHz. This makes the search for usable laser sources very challenging. Pure diode lasers are deeply tunable but have very low output powers. Two laser candidates were found that are commercially available. The first one is an external cavity diode laser (ECDL), provided by Newport, because it has the desired frequency modulation parameters. A second candidate is the so-called SlowLight Laser from Orbits Lightwave which promises higher laser output powers with similar frequency

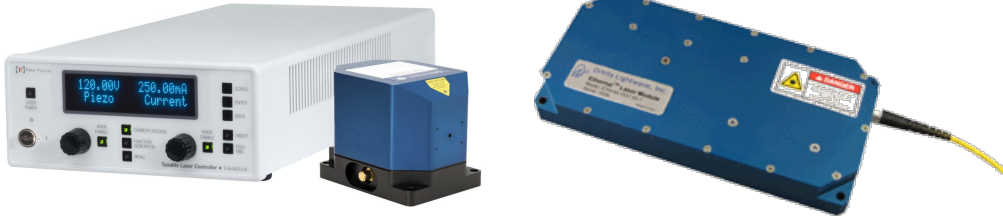


Fig. 8.1.: Picture of the rapidly tunable external cavity diode laser (ECDL) TLB 6821 from Newport and the corresponding low noise driver, TLB 6800-LN from Newport [New14] shown on the left. A picture of the Eternal™ SlowLight laser from Orbits Lightwave is shown on the right.

modulation opportunities. Both candidates were purchased within the SFB geo-Q and are available at the AEI for DFM experiments, photographs of them are shown in Figure 8.1.

### 8.1.1 Rapidly tunable external cavity diode laser

Promising candidates are so-called tunable ECDLs whose laser diode (LD) is the gain medium, meaning that the diode itself is inside the cavity. This is achieved by using a highly reflective coating for the LD's end mirror and an AR coating for the LD's output. An illustration is shown in Figure 8.2a. The laser diode is bonded to a temperature sensor and a thermoelectric cooling block. This ensures a diode temperature which is highly stable and actively controlled. A lens after the diode collimates the beam before it is diffracted at a grating. This high quality diffraction grating is precisely aligned and its position is fixed with respect to the diode. This class of lasers ensures a continuous, mode-hop-free tuning and can produce strong frequency modulations. They can be tuned over multiple wavelengths in excess of several GHz deviation at kHz-frequencies or higher which is achieved by a Littman-Metcalf configuration. The light of the LD is sent to a diffraction grating as shown in Figure 8.2b. While in the Littrow configuration the mode is selected via rotating the grating itself, the Littman-Metcalf configuration consists of an additional mirror in the cavity that will be rotated and scans the laser beam over the grating surface, which ensures a larger wavelength selectivity and a smaller line width. This allows movements on  $\mu\text{m}$ -levels, corresponding to wavelength changes in the sub- $\text{\AA}$ -levels [Haw+01; Wan+12a].

A rapidly tunable ECDL candidate is provided by Newport, the TLB 6700 Velocity. A fiber-coupled version of this laser was available at NIST with a wavelength selectivity from  $\lambda = 1520$  to  $1570$  nm and an output power of 20 mW. Initial measurements were performed at NIST to investigate the modulation depths

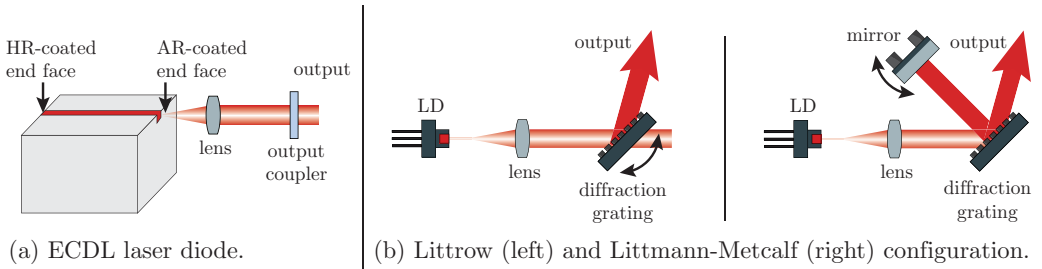


**Fig. 8.2.:** Architecture of an ECDL (a): A laser diode is placed into an external cavity. AR coatings prevent the diode from self lasing [New17a]. The Littrow and Littmann-Metcalf configurations are shown in inlet b. The laser diode (LD) light is sent to a diffraction grating. By tuning either the grating or an external mirror, certain wavelengths can be selected [New17a].

which can effectively be achieved with ECDLs. Figure 8.3 shows the results of the measured modulation index for a MI having an arm length of 5 cm, therefore a pathlength difference of about 10 cm is assumed. A frequency modulation is applied to the laser driver via a function generator. The modulation strength, equivalent to  $\Delta f$ , and the modulation frequency,  $f_{\text{mod}}$ , are scanned from 0.5 to 3 V<sub>pp</sub>, and 0.5 to 1.5 kHz respectively. As expected, higher modulation depths can be achieved by increasing the modulation strength  $\Delta f$ . A modulation strength of 2 V<sub>pp</sub> shows a modulation index of  $m_{\text{DFM}} \approx 9$ , which is sufficient for the DFM data processing via fit algorithm. By applying modulation rates above 1 kHz, the achievable modulation index is limited by the system’s bandwidth and slew rate. However, this class of rapidly frequency tunable lasers shows an appropriate frequency tunability and they can be used in DFM experiments.

For the DFM experiments done at the AEI, a similar variant of this laser class, the TLB 6821 Vortex Plus from Newport with a center wavelength of 1064.5 nm, was ordered. The difference between the TLB 6700 used at NIST and the TLB 6821 is the amount and mechanism of tunability. Table 8.1 summarizes the different parameters of the two laser systems as they are given in the data sheets. While the TLB 6700 can be modulated over a large wavelength range, the TLB 6821 can only be modulated by 20 GHz with modulation rates at 1 kHz, but this is still sufficient for our applications. It is assumed that the TLB 6821 has instead a higher frequency stability and is more linear due to the reduced number of mechanical movable components inside the cavity. One fiber-coupled and one free-beam variant of the TLB 6821 have been ordered and analyzed. Due to the non-ideal fiber-coupling efficiency, the output powers of the two laser systems vary. Whilst the free-beam variant produces an output power of more than 70 mW, the fiber-coupled laser showed less than 30 mW. However, preliminary experimental

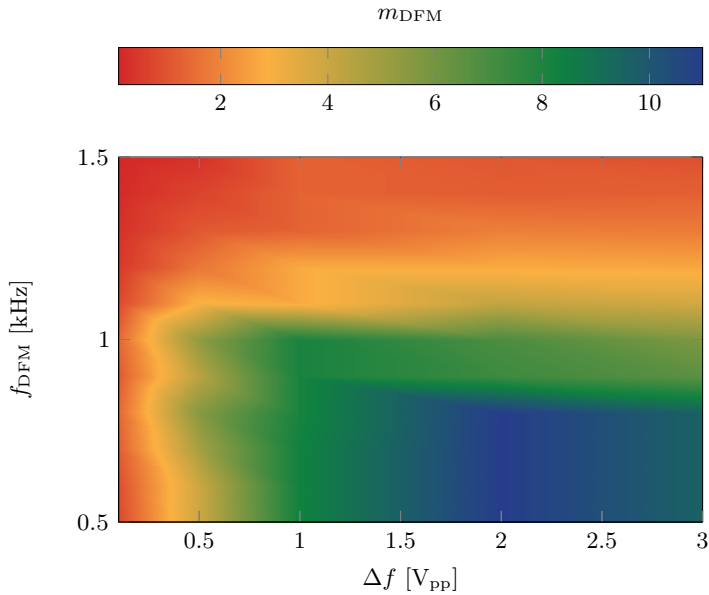


Fig. 8.3.: Modulation depth characterization of the TLB 6700 for 10 cm arm length mismatch in a MI.

tests of the free-beam variant show that ECDLs produce a laser beam containing higher order modes. To achieve a single-mode beam also for the free-beam TLB 6821, the light is coupled into a fiber that acts as mode cleaner and produces a Gaussian  $TEM_{00}$  mode. A good coupling efficiency is achieved by using an imaging system that decreases the spot size such that most of the elliptic beam profile can be coupled into the fiber. A steering mirror in front of the fiber coupling can be used to change the coupling efficiency and, thus, actuating on the laser power at the fiber output. With this, an amplitude stabilization can be set up by sensing the laser power fluctuations at the end of the fiber with a photodiode. A circular beam profile is detected after the fiber coupling and an output power of more than 35 mW could be achieved, about 15 % more laser power than provided by the commercially fiber-coupled TLB 6821 [New17b; New17c].

Both TLB 6821 are driven by the same low noise driver, namely the TLB 6800-LN from Newport, which has different input and output connectors for modulating the laser frequency via a piezo-electric crystal and the laser output power via the diode current with a bandwidth of 1 MHz. The driver has an internal built-in high voltage amplifier supplying 0 to 120 V, that amplifies the external frequency modulation signal connected by a factor between 0 and 10. By using the piezo-electric system, the wavelength of the LD can be tuned with sub-angstrom precision. The built-in analog current driver is a low-noise DC current supply. The maximum current

**Tab. 8.1.:** Overview of two of the ECDL systems provided by Newport and the Eternal SlowLight laser from Orbits Lightwave. The TLB 6700 [New17b] was used for the experiments at NIST. Two TLB 6821 [New17c] were ordered for the experiments at the AEI, one free-beam and one fiber-coupled variant. The SlowLight [Lig17] laser has not been used for DFM experiments so far.

Parameter	TLB 6700	TLB 6821	SlowLight
wavelength	1520 to 1570 nm	1064.5 nm	1064.52 nm
tuning range	50 nm	40 GHz	20 GHz
freq. mod. BW (20 GHz)	2 kHz	1.5 kHz	>10 kHz
current mod. BW	1 to 100 GHz	1 to 100 GHz	>100 kHz
long-term freq. stab.	2 pm (>12 hours)	2 pm (>12 hours)	<30 Hz / $\sqrt{\text{Hz}}$ at 100 Hz
output power	70 mW	70(30) mW	80(40) mW
linewidth	<200 kHz (50 ms)	<200 kHz (50 ms)	<1 kHz (1 ms)

that can be applied to the diode is 200 mA. For an external current modulation connected to the BNC adapter, the laser diode current needs to be set well below the allowed maximum current. Any current value exceeding this limit, will produce an error in the driver and the laser will be turned off immediately. Via the driver, the diode current can be modulated up to 1 MHz with a maximum amplitude of 20 mA using the BNC connector on the rear panel of the controller, and up to 100 MHz using the SMA connector on the laser head. The available output signals are an internal function generator of the driver and a trigger generator. Furthermore, the driver can be controlled via USB or RS-232 and a computer on which the dedicated USB drivers are installed [New14].

Sweeping the laser frequency of the TLB 6800 with a voltage of  $-2.25$  to  $2.25$  V applied on the BNC connector changes the laser frequency from  $-30$  to  $30$  GHz, depending on the specific laser model and on the rate of the modulation. A full 20 GHz modulation is only available at rates up to 1.5 kHz, as shown in Table 8.1. Figure 8.3 shows the measured modulation depth, extracted via fit in the time domain, for different modulation strengths and modulation frequencies. Due to the low-pass behavior of the laser and laser driver, the effective modulation depth also decreases with the modulation rate, and not only with the modulation strength as it was expected. The frequency modulation signal is provided by a two-channel Tektronix arbitrary function generator which can also be controlled via USB and a computer. A fixed sinusoidal modulation is typically applied on the driver with a modulation frequency of 800 Hz and a peak-to-peak amplitude of the order of 800 mV. With a PZT gain of 8, set in the laser driver, effective modulation depths of the order of  $m_{\text{DFM}} \approx 6$  can be achieved in interferometers with arm length mismatches of the order of 10 to 15 cm.

### 8.1.2 Eternal™ SlowLight Laser from Orbits Lightwave

The SlowLight laser from Orbits Lightwave is described by the manufacturer as an evolved development based on the technology of Orbits Lightwaves' Eternal™ laser. The original Eternal™ laser uses a so-called Virtual Ring Laser Oscillator, a new cavity architecture that is fiber-based throughout and ensures small, compact optical set-ups. With the Virtual Ring laser technology the intra-cavity light speed is slowed down. The decreased speed of light extends the laser cavity lifetime, thus also the optical pathlength, and reduces the amplitude, frequency and RIN noise levels. Since some laser noise parameters depend on the square of the cavity length, the noise dynamics can be suppressed by orders of magnitude with this technique. A dedicated HV driver is required for the operation of this laser to tune its frequency. The driver is not part of the delivery and must therefore be designed and built by the customer, which is why this laser type has not been used for the DFM experiments shown in this thesis.

## 8.2 Front-end electronics

The interferometric output consists of a pattern that is periodic with  $f_{\text{mod}}$ , according to Equation (6.10). The usage of at least ten higher harmonics of  $f_{\text{mod}}$  requires photodetectors with a flat transfer function over the according frequency range from about 0.1 to 20 kHz and an anti-aliasing filter with a steep cut-off frequency at around 100 kHz.

### 8.2.1 Photoreceiver

Therefore, we use small InGaAs photodiodes having a size of 1 mm in diameter and a responsivity of about 0.7 A/W. Due to the small active area we achieve high bandwidth, but lenses are required to achieve an adequate beam spot size on the photodiode. The photodiodes are mounted in aluminum housings that are angled to prevent direct backreflections. The according photoreceiver front-end is separated from the actual experimental set-up. The photocurrents of all photodiodes are guided to a TIA front-end box, containing 16 channels in total. This device is based on the circuit layout of the LISA optical bench photoreceiver box (built by Germán Fernández Barranco) and was modified by Oliver Gerberding. The box provides 16 readout channels, the bias voltages (5 V), trans-impedance amplifiers with additional offset voltages (for the phasemeter or the data acquisition (DAQ) card input) and additional oscilloscope outputs.



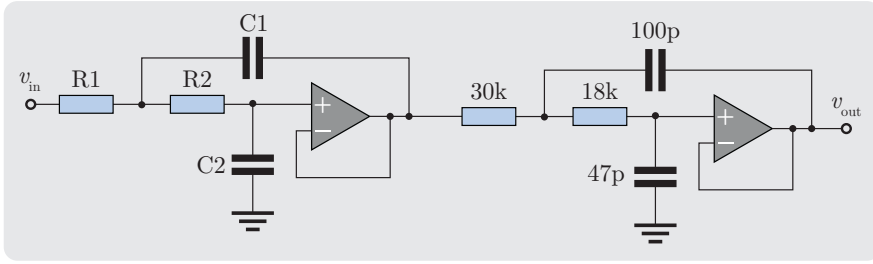


Fig. 8.4.: Schematic of a two-stage second order Sallen-Key low-pass filter. The values for resistors and capacitors are the same for both.

### 8.2.2 Low-pass filter

To reduce aliasing effects the output voltages of the TIA must be filtered above a cut-off frequency of about 100 kHz. Since DFMI generates optical signals containing frequencies in the range from 0.5 to 10 kHz, depending on the injected modulation frequency, the design of a low-pass filter with 100 kHz cut-off frequency and sufficient suppression for frequencies above is challenging. A low-pass filter featuring a Sallen-Key topology is one possibility to achieve an adequate filter behavior. A two-stage second order Sallen-Key low-pass filter, shown in Figure 8.4, is implemented using analog electronics for eight channels. It shows a relatively flat magnitude and phase response at frequencies up to 10 kHz and a hard cut-off at

$$\omega_0 = \frac{1}{\sqrt{R_1 R_2 C_1 C_2}} = 99.9 \text{ kHz} \quad (8.1)$$

for resistor values of  $R_1 = 30 \text{ k}\Omega$ ,  $R_2 = 18 \text{ k}\Omega$  and capacitance of  $C_1 = 100 \text{ pF}$ ,  $C_2 = 47 \text{ pF}$ . The according frequency response of a one-stage Sallen-Key filter is given by

$$H(s) = \frac{\omega_0^2}{s^2 + s\omega_0/Q + \omega_0^2} \quad \text{with} \quad Q = \frac{\sqrt{R_1 R_2 C_1 C_2}}{C_2(R_1 + R_2)} \quad (8.2)$$

with the Laplace operator  $s = i2\pi f$ . The knowledge about the complex values of the transfer function,  $H(s)$ , can be used to correct the DFM complex amplitudes during the data processing in the software phasemeter.

## 8.3 Data acquisition

In general, two approaches for the digitization of the data can be used. The first one is the straightforward approach, using a commercial DAQ card for the digitization and a software program, here written in C, to demodulate the digitized data via single-bin Fourier transform (SBFT) in real time at the desired frequencies

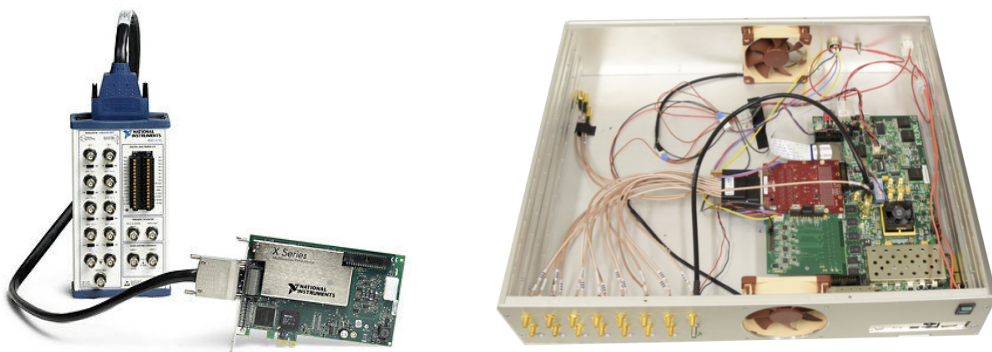
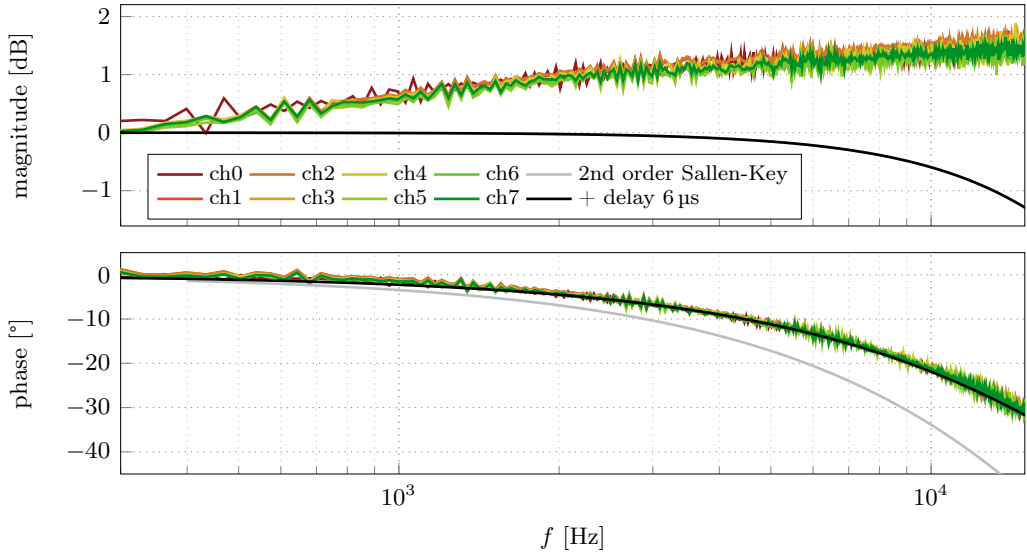


Fig. 8.5.: Picture of the DAQ card (left) from NI with eight channels simultaneously sampling with 250 kS/s with 16 bit, and a picture of the phasemeter, an FPGA-based Xilinx evaluation board, that was developed in parallel to this work but not yet integrated in the experimental infrastructure [Vor17].

and for applying the non-linear fit algorithm. The second variant is a dedicated hardware phasemeter with a System-on-a-Chip (SoC) (including microprocessor and FPGA/programmable logic) on board. Photographs of both systems are shown in Figure 8.5. The advantage of a FPGA-based phasemeter is the very high sampling rate of multiple MHz and the fast  $IQ$ -demodulation on the FPGA board. With an integrated micro-processor, on which the fit algorithm can be run, and a DAC card connected to the FPGA, very fast feedback control loops can be integrated, directly using the fitted parameters like the measurement phase or modulation depth. The investigation of a dedicated FPGA-based phasemeter is not part of this work but was done within the master thesis of Christoph Vorndamme, supervised by Thomas Schwarze [Sch18; Vor17]. A prototype phasemeter used for DPM was initially set up by Thomas Schwarze in his master thesis, supervised by Oliver Gerberding, and it was almost able to meet the phase measurement requirement for LISA [Sch+14c]. However, the results shown in this thesis are processed with the DAQ card PCI-6143 S from National Instruments (NI) in combination with a software phasemeter implemented in C running on a computer with a Linux-based operating system.

To perform the first tests at NIST, a simple DAQ card was used allowing a simultaneous sampling of eight channels with a maximum rate of 250 kHz. The  $IQ$ -demodulation was implemented in the LabView software that was reading out the digitized data from the DAQ card. At NIST, the data rate was reduced down to 100 Hz during the demodulation process and the integration runs over 10 samples for calculating the complex amplitude, thus, the fit algorithm operated



**Fig. 8.6.:** Measured transfer functions of the DAQ system, including ECDL, photodiodes, TIA, low-pass filter, DAQ card and PC data time series processing. Also shown is the simulated model for the 2nd order Sallen-Key low-pass filter, once only  $H^2(s)$  based on Equation (8.2), once with an additional delay,  $\tau = 6 \mu\text{s}$ , leading to  $H^2(s)/e^{-s\cdot\tau}$ .

only with a rate of 10 Hz. The fit algorithm was initially written as a C program by Gerhard Heinzl which could be embedded in the LabView environment. This readout rate is sufficiently high for the phase spectra up to 5 Hz, and low enough such that the time-consuming fit algorithm keeps operating. In the last step, the fit algorithm estimates the four signal parameters [Hei+10]. The data is processed live on a personal computer. A similar readout system was also chosen to be used for the experiments conducted at the AEI. The DAQ card PCI-6143 from NI is used to digitize the data of eight channels simultaneously, again with a sampling rate of 250 kHz. The digitized data is demodulated in a software phasemeter, written in C, on the computer, that decimates the data down to a rate of 100 Hz. The complex amplitudes are again fitted with the fit algorithm and saved in files with a rate of 100 Hz or 20 Hz.

For measuring the interferometric pattern in the time domain, we use the same DAQ card, but a readout script, written in C, that takes the data with the full sampling rate of 250 kHz. The time series signals are saved into data files which can be analyzed in post-processing with MATLAB, for example for fitting a time series model to the data that matches the expected interferometric pattern.

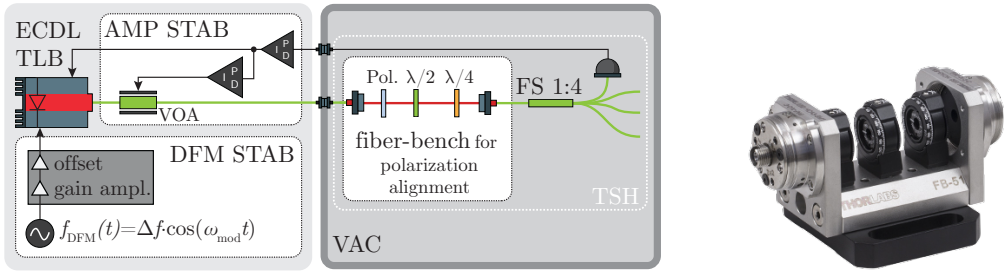


Fig. 8.7.: Optical set-up of the DFM laser preparation (left). The optical part is all fiber-based, with PM-fibers, besides a fiber-to-fiber-bench (right, Image credit: Thorlabs) for compensating amplitude and polarization fluctuations. The design of the analog variable gain amplifier and offset circuit is shown in Figure 8.8.

### 8.3.1 Measured transfer function

To characterize the flatness of the full processing system's frequency response, the transfer functions for each channel are measured. A frequency sweep is applied to the current modulation input of the ECDL. Frequency modulations are not applied to the laser. One interferometer arm is blocked in each optical set-up such that only amplitude modulations are detected. Different photodiode signals are connected to the TIA box, low-pass filter and the DAQ card. As reference, the according reference sweep is connected to the first (ch0) and second channel (ch1), such that the response off all eight channels can be measured. The resulting transfer functions are shown in Figure 8.6, together with the expected transfer function model of a two-stage second order Sallen-Key filter. The measured magnitude is normalized with respect to its initial value at around 680 Hz and a constant offset of  $5^\circ$  was subtracted from the measured phase. All channels show a similar behavior in the relevant frequency regime between 300 Hz and 15 kHz. The transfer function of the Sallen-Key low-pass filter dominates the measured transfer functions of the readout system. Regarding the phase behavior, the match between model and data can be enhanced by adding a delay of  $6 \mu\text{s}$  to the low-pass filter model. The increase of the transfer function's magnitude cannot be explained by this model. It is assumed that the low-pass behavior of the ECDL current modulator on which the frequency sweep was applied, leads to this magnitude rise, but a dedicated model describing this effect could not be found. The actual frequency response of the channels might therefore differ for actual DFM measurements and follow the Sallen-Key low-pass behavior, which is flat within 0.5 dB up to 10 kHz.

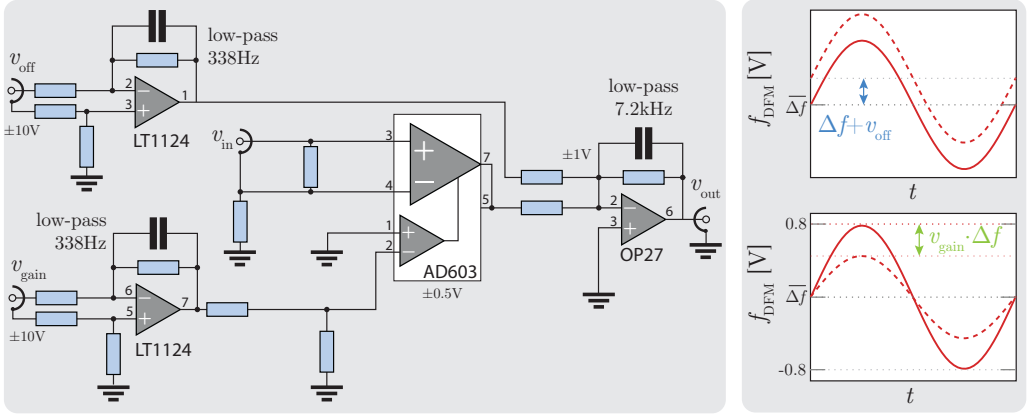


Fig. 8.8.: Schematic of a variable gain amplifier and offset circuit. The variable gain amplifier changes the amplitude of an incoming sinusoidal voltage, as illustrated in the plot on the bottom. The mean value of the RF voltage signal can be adjusted by adding an offset voltage, as shown in the plot on the top.

## 8.4 Laser preparation

One advantage of DFMI is a single laser preparation, separated from the actual experiments, that can be used simultaneously in multiple interferometers. Due to the strong frequency modulation applied on the ECDL we expect a non-negligible coupling into amplitude fluctuations. These must be suppressed by analog electronics over the full modulation bandwidth from 0.1 to 20 kHz. Besides the limited line width of the laser source, the strong frequency modulation lead to additional LFN which is accumulated over the arm length difference in DFM interferometers. The average laser frequency however can be stabilized. An adequate suppression is required within the measurement bandwidth between 0.1 mHz and 1 Hz. A stabilization for the effective modulation depth,  $m = 2\pi\Delta f\tau$ , is also conducted.

The main components of the all-fiber-based DFM laser preparation are shown in Figure 8.7. While the experiment at NIST used non-PM fiber components, we implemented at the AEI fiber-benches (fiber-to-fiber U-bench from Thorlabs) inside the vacuum chamber (VAC) to match the polarization for the fiber coupling. The fiber-coupled ECDL source is placed on an optical table and connected to the laser driver. An Arbitrary Function Generator (AFG) (from Tektronix) generates a sinusoidal output voltage which is applied to the frequency modulation input of the laser driver. We use typically a modulation strength of 950 mV<sub>pp</sub> and a frequency of  $f_{\text{mod}} = 800$  Hz. The fiber is connected to a fiber-based variable optical attenuator (VOA) which is used to compensate slow laser amplitude fluctuations. The laser light is guided via feedthroughs into the VAC. A second adjustable fiber-bench serves as passive amplitude stabilization stage inside the chamber. On the

fiber-bench, the laser is coupled from one coupler to another one. The polarization is matched in-between with a thin-film polarizer, half-waveplate and quarter-waveplate. The quarter-waveplate compensates circular-polarization components that might be caused by other optical components like the lenses from the fiber collimators [Sch18]. This re-coupling of the beam in a fiber inside the vacuum chamber shall reduce amplitude fluctuations that are caused by polarization changes in the fiber feedthrough due to refractive index fluctuations. A PM single-mode fiber beam splitter (1:4) is connected to the collimator and guides the light to the TMitM, reference MZI and the laser power sensor.

Analog actuation signals for the laser frequency stabilization are provided by a DAC card (USB-3104 from measurement computing (MC)) that is connected via USB to the PC. The DAC has eight analog voltage outputs, all with 16 bit resolution. It provides outputs voltages in the range between  $-10$  to  $10$  V with a throughput of  $100$  Hz, depending on the number of channels. These control voltages can either be directly connected to the inputs of the AFG, or, as implemented here, to an additional analog circuit. It changes the amplitude and offset of an incoming sinusoidal signal by these control voltages. Figure 8.8 shows the equivalent analog circuit design, where a low-noise variable gain amplifier, AD603, is used for changing the modulation depth applied on the laser. An adder circuit shifts the mean value of the frequency modulation by an offset voltage.

#### 8.4.1 Amplitude stabilization

By applying a strong frequency modulation on the ECDL, a residual amplitude modulation is observed, not only at the modulation frequency but also at higher harmonics. Figure 8.9 shows on the left the time series of the relative intensity when the laser's frequency is modulated with a rate of  $f_{\text{mod}} = 800$  Hz and a depth of  $850$  mV<sub>pp</sub>. This measurement was performed by using the reference MZI while one interferometer arm is blocked. The amplitude pattern depends on the strength of the frequency modulation and on the modulation rate, but it varies also with time, temperature and polarization. The shape of this amplitude fluctuation is similar to the actual interferometric DFM signal. This may indicate that additional amplitude modulations are caused by spurious beams that interfere with the nominal beam with a propagation delay and, thus, show a typical DFM pattern. An active amplitude stabilization is implemented that reduces the coupling of DFM into amplitude fluctuations. At NIST, a commercially available PID controller and a fiber-coupled electro-optical amplitude modulator (EOAM) were used. A fiber-coupled photodiode served as sensor. At the AEI, two analog servos were constructed. The first servo was designed to control fast amplitude fluctuations which is achieved by modulating the laser diode current via the TLB 6800-LN laser

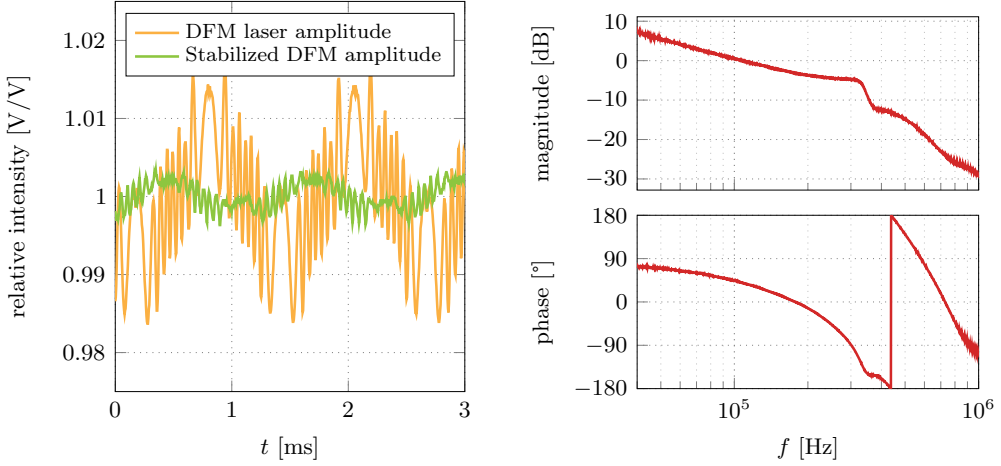


**Fig. 8.9.:** Time series of the residual relative intensity of the lasers amplitude by applying a DFM on the laser's frequency (left) and open-loop transfer function of the DFM amplitude stabilization (right).

driver. For compensating long-term amplitude drifts a fiber-coupled attenuator was used. A photodiode inside the tank is used as sensor for the control loop. The light is collimated with a fiber output coupler. A focusing lens with 25.4 mm focal length produces a beam with 3 mm diameter on the InGaAs photodiode sensor. While at NIST proper transfer functions were not measured, Figure 8.9 shows on the right the AEI results for the fast amplitude stabilization, reaching a unity-gain frequency of 108.1 kHz and a phase margin of 39.36°. Figure 8.10 shows the out-of-loop relative intensity noise spectra measured in the MZI and in both prism-interferometers in the TMITM while one interferometer arm is blocked in each one. A relative intensity noise suppression of one order of magnitude can be achieved at the first harmonic of the modulation frequency in all interferometers, reaching a noise level of about  $1 \cdot 10^{-4} / \sqrt{\text{Hz}}$  with amplitude stabilization. Each measurement data is analyzed for a time interval of 1 s. Also shown in Figure 8.10 is the intensity noise for ten higher harmonics. These are the amplitudes that are relevant for the fit algorithm to recover the phase information of the interferometric pattern. The relative intensity is distributed differently at the higher harmonics in each interferometer. This discrepancy between the individual interferometers indicates that spurious beams influence the amplitude measurements in addition to the residual coupling of the laser's frequency modulation. It is assumed that the spurious beams are mainly caused by focusing lenses that are placed in front of each photodiode. The lenses are adjusted to 0° AOI which produce eventually ghost beams propagating collinear to the actual beam. The two lens surfaces act as



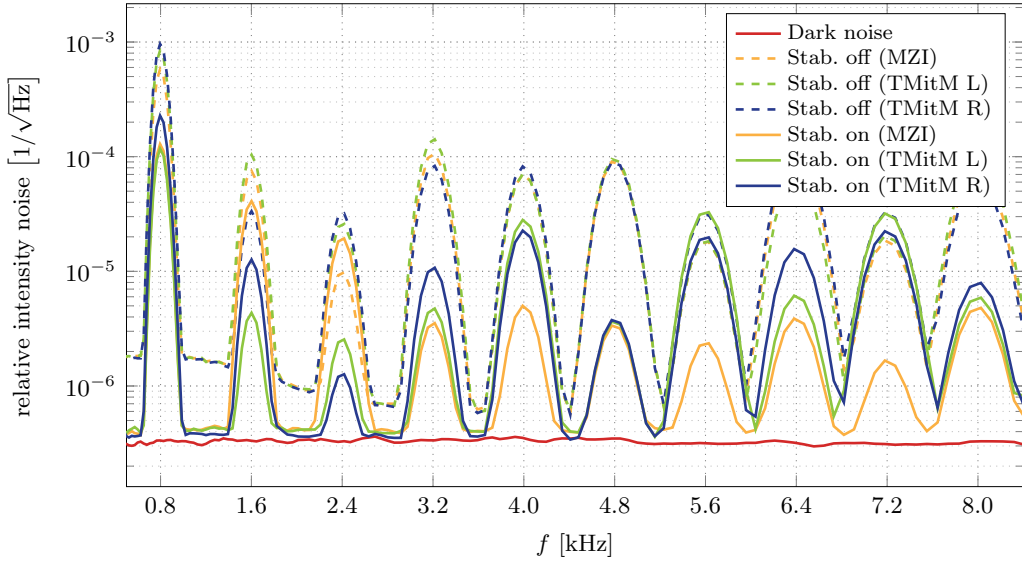


Fig. 8.10.: Relative intensity noise spectra of the DFM laser with amplitude stabilization measured on different photodiodes for a time interval of 1 s: one measurement in the MZI and one from each side of the TMitM, left (L) and right (R). The dark noise of one photodiode, and measurements without amplitude control, are shown as references.

cavity end mirrors and generate a reflection that could directly hit the photodiode or travel back to the fiber collimator which produces again a ghost beam entering the interferometer. The lens alignment and the power sensing photodiode differ for each interferometer, which might explain the discrepancy between the higher harmonic contributions for the individual photodiode measurements.

The stabilization scheme can be improved by using an adequate sensor that ensures that no ghost beam influence is imprinted on the sensor signal. A photodiode with larger active area, like Silicon photodiodes, can be used to monitor beams having larger beam sizes such that focusing lenses are not required. This would eliminate ghost beams caused by the lenses, but the constraints for the photoreceiver front-end box increase. The bandwidth of several kHz must still be achieved, which is not trivial using large area photodiodes. The use of a one-to-four fiber splitter, made from polarizing fibers, might also help to reduce the out-of-loop amplitude noise in the future, reducing unwanted polarization fluctuations between the four fiber splitter output ports.

#### 8.4.2 Frequency stabilization

Since DFM requires unequal arm length interferometers, laser frequency noise will couple into the phase measurement. For the stabilization of the averaged laser's



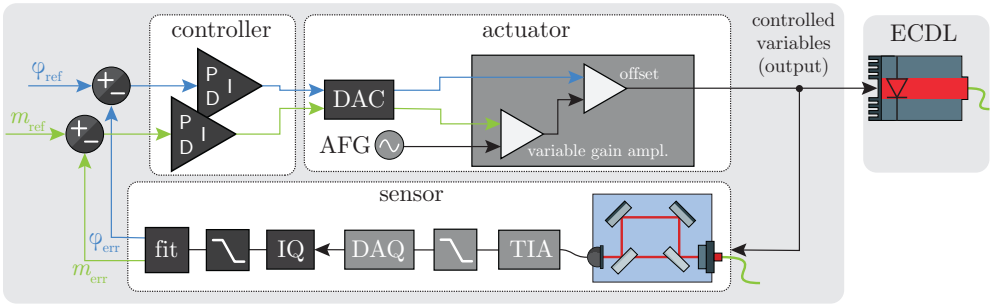


Fig. 8.11.: Sketch of the control loop for the DFM frequency and modulation index stabilization. The reference MZI serves as sensor. The frequency modulation applied on the ECDL,  $f_{\text{DFM}}$ , is controlled by a variable gain amplifier.

frequency and compensating long-term drifts, we use a photodiode signal from the reference MZI. This interferometer is sensitive for LFN over the arm length mismatch of about 70 mm. One output port of the MZI serves as sensor signal from which the phase noise information is extracted digitally via the fit algorithm. A feedback control loop is implemented in software in the C program that is used for the data acquisition and processing, as depicted in Figure 8.11. The set point for the loop is the initial phase measurement value  $\varphi_{\text{ref}}$  acquired just before loop initialization. The value of  $\varphi_{\text{ref}}$  is arbitrary, but keeping it constant locks the averaged laser frequency to the arm length difference of the interferometer. An analog voltage is sent via the DAC card to the input of the amplifier and offset circuit, controlling the mean value of the modulation signal.

Figure 8.12 shows the measured open-loop and closed-loop transfer functions for different gains of the digital PID-controller. With a high proportional gain of  $-16.0$ , and an integral gain of  $-8.0$ , we achieve a unity gain frequency of about 9.55 Hz with  $81.64^\circ$  phase margin. The corresponding closed-loop transfer function shows an overshoot between 20 Hz and 30 Hz. The unity gain frequency for a control loop with a proportional gain reduced by a factor of 32 is 5.6 Hz with a phase margin of  $65.17^\circ$ . The frequency stabilization loop is limited by the readout rate of the phase measurement. The data acquisition samples with 250 kHz. The data is averaged with 100 Hz, an adequate data rate for the fit algorithm. Since the unity gain frequencies are close to the Nyquist frequency, the transfer function measurements show some irregularities at frequencies above 50 Hz and their measured trend might be disturbed. The usage of an FPGA-based phasemeter would simplify the feedback control system since it provides the opportunity to integrate a DAC on the evaluation board. And more importantly, the unity gain frequency could be increased beyond the current DAC throughput of 100 Hz, which limits the currently achievable bandwidth. Furthermore, the transfer function of the fit itself

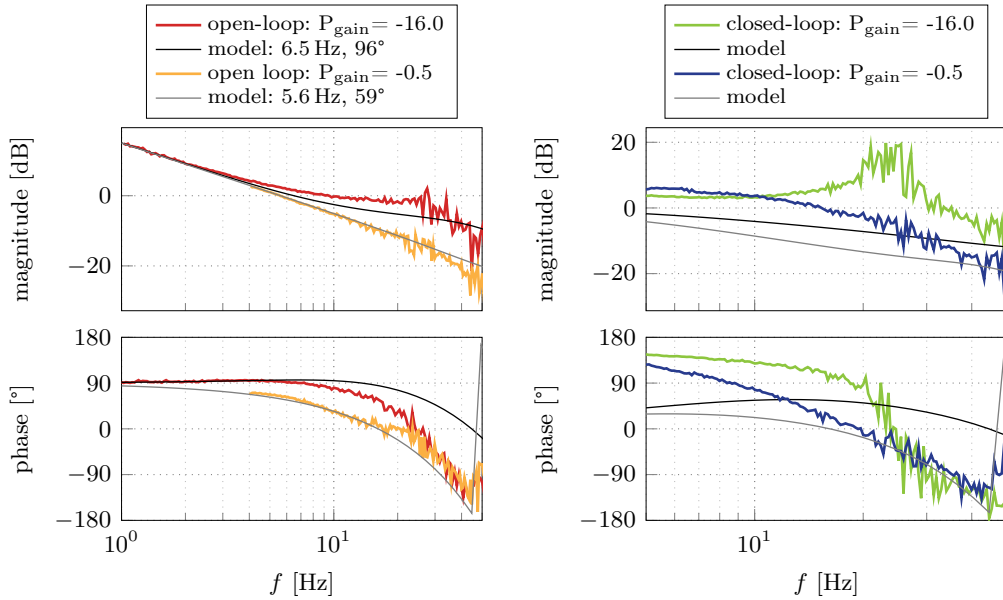


Fig. 8.12.: Open-loop (left) and closed-loop (right) transfer function of the DFM frequency stabilization for different proportional, and integral gains in the C-program.

has not been determined or measured so far, but it might be the reason for some non-linearities in the transfer functions which would also explain the discrepancy between the model of the PID-controller with filter and the measured transfer function data.

### 8.4.3 Modulation index stabilization

The control for the modulation depth uses the same feedback architecture as utilized for the frequency stabilization and is also depicted in Figure 8.11. The MZI photodiode is used as sensor. The fitted parameter for the modulation depth is compared to a reference value, here 7.5, and the resulting error signal is used in a further digital PID-controller. The DAC interface provides a voltage signal, used as input signal in the gain-amplifier circuit, which changes the DFM strength  $\Delta f$ . Results are presented in Chapter 9.

## 8.5 Test mass control

The test mass in the TMitM can be actuated by a three-axis PZT mount, S-311.10 from PI. By applying high voltages from 0 to 100 V, the mirror can be tilted by 600  $\mu\text{rad}$ . A maximum mirror displacement of 6  $\mu\text{m}$  can be achieved by actuating

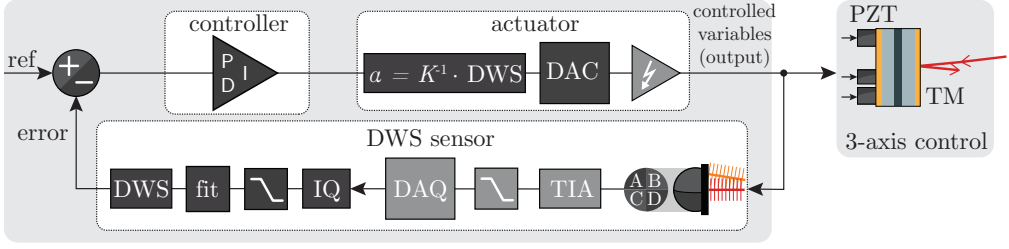


Fig. 8.13.: Control loop diagram of the three-axis test mass stabilization. A QPD installed at one output port of the right prism-interferometer is used as sensor. The DWS signals provide error signals for the digital control loop. The digital actuation signals are sent to the PZT controller which generates HV control voltages for each axes.

on all three axes. A high power PZT controller system, the E-505 Amplifier Module from PI, provides output voltages in the range from  $-30$  to  $130$  V. The HV output voltages can be adjusted by connecting analog input signals, by using the potentiometers or remotely by using a PC.

The feedback control loop, as implemented in this experiment, is shown in Figure 8.13. A QPD is used as sensor to monitor the DWS signal of the right prism-interferometer. It is placed at the direct output port of the prism, thus at the position of PD4, which detects non-elliptic beams. Optical simulations in Chapter 7 have shown that a test mass displacement, and yaw and pitch tilts, generate a zero-crossing DWS signal. The DWS coupling coefficients are about  $250 \text{ rad}/\mu\text{m}$  for displacement changes, and about  $5000 \text{ rad}/\text{rad}$  for pitch and yaw tilts. By determining the DWS signal in the experiment, we are therefore able to control the test mass position and tilt very accurately due to the high gain of the DWS signals. The displacement could also be controlled by monitoring the combined pathlength signal of the QPD. The output voltages of each QPD segment are monitored by the data acquisition system. The phases are firstly extracted by the fit algorithm and then subtracted from each other to achieve the horizontal and vertical DWS signals according to Section 1.3.4. A PID-controller, implemented in software, is used to determine the control signals, from which the actuation signals for all mirror axes can be formed. The relation between mirror motion and optical signals can be described by a coupling matrix,  $K$ , according to

$$\begin{pmatrix} \Psi_{\text{DWS}} \\ \Theta_{\text{DWS}} \\ \varphi_{\text{PL}} \end{pmatrix} = \underbrace{\begin{pmatrix} K1 & K2 & K3 \\ K4 & K5 & K6 \\ K7 & K8 & K9 \end{pmatrix}}_K \cdot \begin{pmatrix} \alpha_x \\ \alpha_y \\ \alpha_z \end{pmatrix}. \quad (8.3)$$

where  $\Psi_{\text{DWS}}$  is the measured horizontal DWS signal,  $\Theta_{\text{DWS}}$  the measured vertical DWS signal and  $\varphi_{\text{PL}}$  the longitudinal pathlength signal. The vector  $\vec{\alpha} = (\alpha_x, \alpha_y, \alpha_z)$

describes the three-axes actuation signal that is applied on the test mass mirror. To implement a control loop, the coupling coefficients must be experimentally measured and the matrix must be inverted such that we can solve the Equation (8.3) for the vector  $\vec{\alpha}$ . By applying sinusoidal signals with different frequencies to each PZT axis, the coupling coefficients between the axes and the DWS and pathlength signals can be measured individually for each DoF by demodulating the signals at the according frequencies. The actuation signals are calculated within the software phasemeter for the PZT via

$$\alpha_x = M1 \cdot \Psi_{\text{DWS}} + M2 \cdot \Theta_{\text{DWS}} + M3 \cdot \varphi_{\text{PL}}, \quad (8.4)$$

$$\alpha_y = M4 \cdot \Psi_{\text{DWS}} + M5 \cdot \Theta_{\text{DWS}} + M6 \cdot \varphi_{\text{PL}}, \quad (8.5)$$

$$\alpha_z = M7 \cdot \Psi_{\text{DWS}} + M8 \cdot \Theta_{\text{DWS}} + M9 \cdot \varphi_{\text{PL}}, \quad (8.6)$$

where  $Mi$  are the coefficients of  $M$ , the inverted matrix of  $K$ . The so-generated digital control signals are sent to the PZT amplifier module which converts these into HV control voltages.

## 8.6 Interferometer construction

From the IfoCAD simulations shown in Chapter 7 we can extract the actual positions of each optical component and the fiber output coupler. In general, non-critical components can be placed with a template, made of brass or aluminum, which has pockets with a three-point mounting, consisting of three stainless steel 4 mm-diameter bearing balls, for each component. The positions for the bearing balls are typically extracted from the simulations and imported into a computer-aided design (CAD) software like Autodesk Inventor to construct a template and for designing mechanical components that are required to adjust the baseplate and holding the template. Both, a complete model of the interferometer set-up and the template are shown in Figure 8.14 for the MZI. The templates are made of brass and have a thickness of 5 mm. The boxes for the baseplates and the holders for the template are made of aluminum. The holders for the fiber output coupler are made of invar because of its very low thermal expansion coefficient. Both interferometer baseplates are made of Clearceram CCX-HS, a glass ceramic with a CTE of  $(0.0 \pm 0.1) \cdot 10^{-7}/\text{K}$  at ambient temperature.

### 8.6.1 Reference Mach-Zehnder interferometer

The reference MZI was constructed with a single template, having a size of 230 mm  $\times$  165 mm. The pockets have a size of 23.3 mm  $\times$  15.3 mm, such that the template can be shifted away from the component surface without damaging it. This

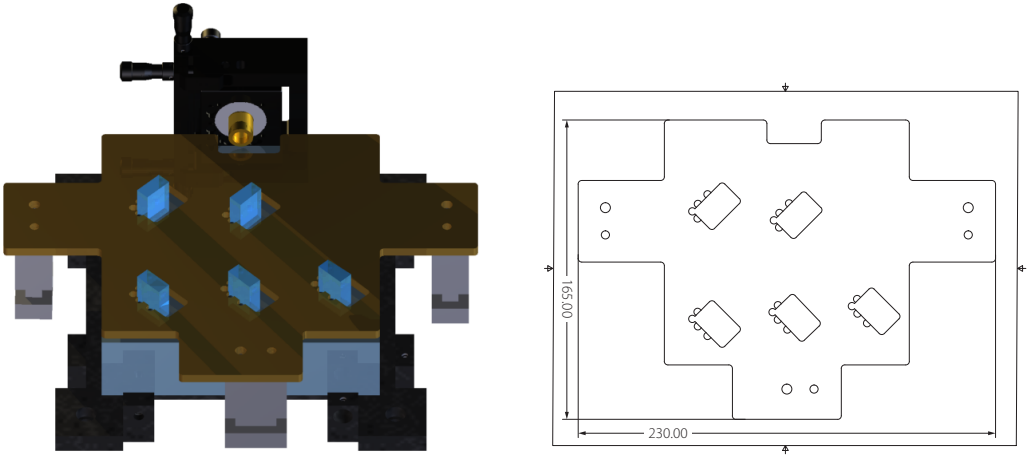


Fig. 8.14.: The full interferometer designed in Autodesk is shown, including a box (dark grey), the baseplate and the interferometer components (blue), the template (brass) and the template holder (grey). The schematic for the template as it was manufactured in-house by the mechanical workshop is shown on the right.

ensures that the template can be removed after bonding without touching the optical coatings. Each pocket contains three holes in which bearing balls with an accurate diameter of 4 mm are placed. These precision spheres provide a three-point mounting in the pockets in which the according optical component can be pushed. Three aluminum posts are designed to hold the template in its position, about 3 mm above the optical bench, such that the laser beam propagates above the template. In the posts we implemented some rods for helping the user to move the template in upwards direction without touching optical surfaces. The light is brought onto the bench (135 mm  $\times$  135 mm  $\times$  36 mm) using a commercial fiber collimator from SuK creating a collimated beam with 1 mm waist radius mounted in an adjustable tip-tilt, x-y mount from Owis, a x-y-fine adjustment stage (FV 65-XY-40x40x-MS) and a transmitting mount (TRANS 40-D25-MS). This is mounted on an adapter made of invar that is glued with a two-component epoxy to the side of the baseplate, as shown in Figure 8.15a. The components are coated fused silica parts with a thickness of 7 nm. The component alignment is done using a coordinate measurement machine and a combination of template-assisted positioning for uncritical components, as demonstrated in Figure 8.15c, and an adjustable pointing finger assembly for the recombination beam splitter, shown in Figure 8.15d. For the alignments of the input beam relative to the template, shown in Figure 8.15b, we use an in-house-developed beam measurement technique [Sch+14b]. The bonding of the components is done using a UV-cured optical adhesive Optocast (3553-LV-UTF) that is applied using only minimal amounts (1 to 2  $\mu\text{l}/\text{cm}^2$ ) of glue to achieve thin,

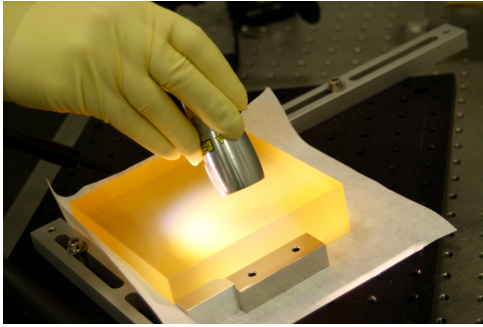
planar bonding layers. Similar techniques have been implemented previously, for example, based on a two-component epoxy [Sch+09]. The final recombination beam splitter alignment is done with a continuous contrast monitoring by applying a deep frequency modulation, enabling straightforward optimization with the adhesive already applied to the component before UV curing. Figure 8.15 shows photographs ordered chronologically for the different assembly stages. In the end, an optical contrast of more than 95 % could be achieved, that remained constant during the UV-curing, which takes less than 2 min. No degradation of contrast is observed after four months of storage and operations, indicating also a decent long-term stability of the UV bond [Ger+16]. Strong temperature fluctuations however could destroy the glue layer due to the different CTE of optical bench (glass ceramic) and fused silica components. The induced stress would break the adhesive bond. On ground we do not expect temperature fluctuations as the ones during flight, which is why this technique can be used for laboratory experiments only. The usage of adhesive bonding for space missions should be avoided, especially to bond optical components made of different materials.

### 8.6.2 Test Mass in the Middle experiment

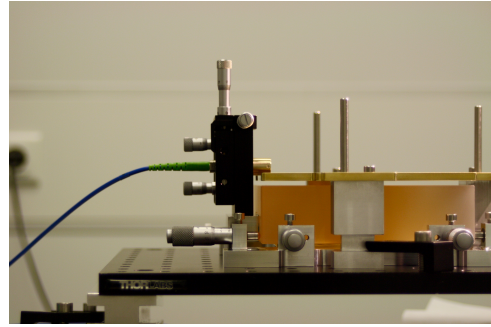
For the TMitM, two templates are required for the positioning of the fiber output couplers. Because of the particular geometry of prism-interferometry, a single template cannot be removed from the optical bench (270 mm × 135 mm × 36 mm) after bonding. For this reason, two different templates were designed that can be shifted in opposite directions, away from the components, such that they can be removed after bonding. The three-point bearing balls in the template pockets and the holding posts are identical to the ones used for the reference MZI. The constraint surface for the alignment of the templates is one surface of the gold-coated test mass mirror in the middle. Figure 8.16a shows the alignment of the test mass mount on the baseplate with pointing fingers. The absolute position is not crucial since the templates are placed relative to the mirror surface and not to the baseplate. The L-shaped mirror mount is made of invar and contains holes for alignment and locking screws, with which the actuation mount can be pre-aligned. As mirror mount we use the three-axis PZT mount S-311.10 from PI. A Zerodur mirror, gold-coated from both sides, is screwed into an adapter, made of invar, which is then fixed to the PZT stage of the mount. This test mass assembly is screwed into its mount, as demonstrated in Figure 8.16b. The perpendicularity between mirror surface and baseplate is measured with the CMM, and is adjusted by using the alignment screws to better than 0.001°. Since the template is carefully pressed with the three-point mounting towards this surface, shown in Figure 8.16c, any tilt of the mirror would cause a lateral shift of the

template. With this alignment the fiber output coupler mount, made of invar, is glued onto the baseplate. The prism is positioned in its pocket and three-pointing fingers are aligned to this position. After removing the template, the pointing fingers are used to position of the prism while the contrast is monitored. To achieve best contrast, the propagation direction of the injected beam is adjusted by the alignment of the fiber collimator from SuK, made of titanium. The contrast is optimized by aligning the beam direction and the prism rotation. This process is shown in Figure 8.16d. After achieving more than 90 % contrast on one side, the prism is glued and the procedure is repeated for the second side.

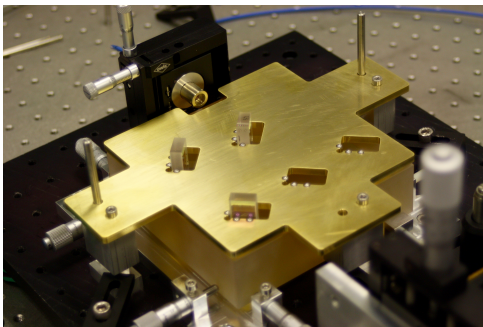




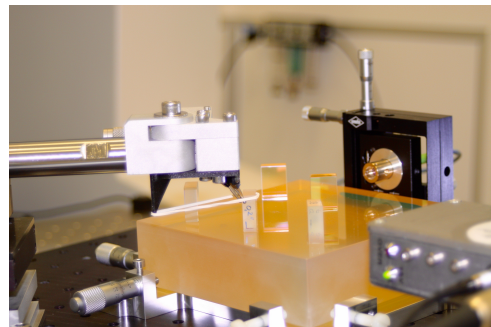
(a) Invar-based adapter plate for the fiber output coupler glued to the baseplate.



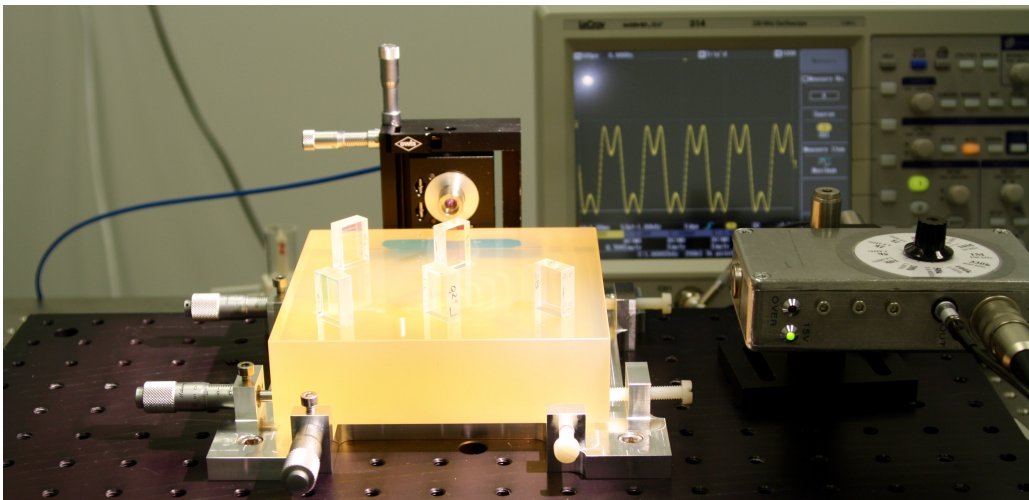
(b) Template is aligned with respect to the laser beam collimated by the fiber output coupler.



(c) Uncritical components positioned with a template and glued with Optocast UV glue.



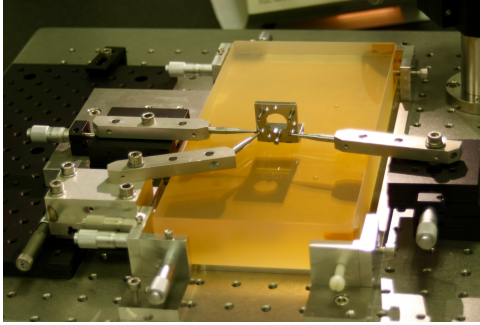
(d) Recombining beam splitter aligned with pointing fingers while monitoring contrast.



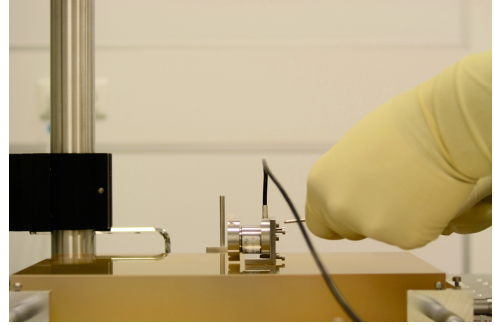
(e) Reference MZI after construction in the cleanroom, achieving a contrast of more than 95%.

**Fig. 8.15.:** Construction of the reference MZI in the cleanroom. The alignment of the recombination beam splitter is done with a pointing finger assembly while monitoring the interferometric contrast using a strong laser frequency modulation.

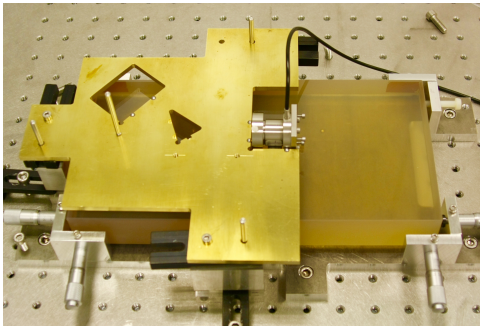




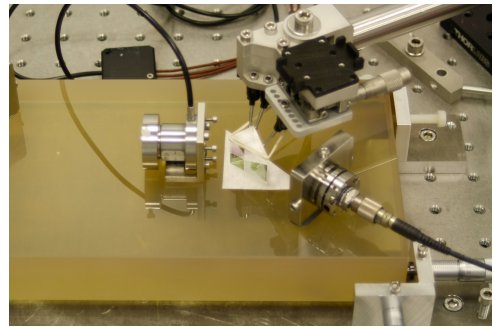
(a) Test mass mount glued to baseplate.



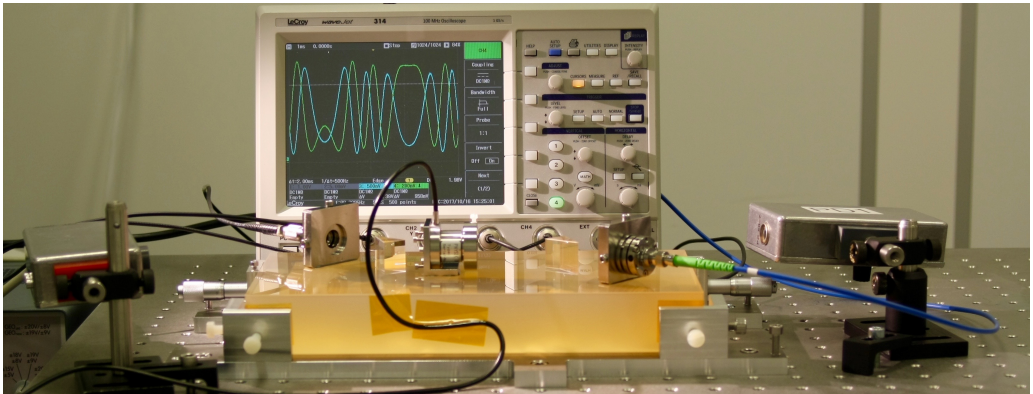
(b) Tilt alignment of the actuator mirror.



(c) Template adjustment for the left prism.



(d) Prism alignment by using pointing fingers.



(e) Final construction stage of the TMitM experiment. The contrast is about 90% for both sides.

**Fig. 8.16.:** Construction of the TMitM experiment in the cleanroom. Two templates are required for the positioning of the fiber output couplers, with the actuator mirror surface serving as reference constraint for each one. The prisms are aligned afterwards for each side separately.



## RESULTS

” *Experimental validation and phase performance of DFMI applied in the TMITM, a test-bed for measuring test mass motions.*

The results of the DFM interferometry experiments are shown in this chapter. Together with the measured phase spectral densities the LISA requirement is plotted for an equivalent displacement noise of  $1 \text{ pm}/\sqrt{\text{Hz}}$  and the interferometer readout requirement, SG1 and SG2, required for the test mass readout in satellite gravimetry missions.

The results from the experiments performed at NIST are presented in the first section and are based on the publication [Isl+16b]. Here, first proof-of-principle experiments were implemented, investigating different modulation parameters of DFM in unequal arm length interferometers in both, the time and frequency domain, for a center wavelength of 1550 nm. The applicability of the DPM fit algorithm was validated by these experiments and integrated into the data acquisition system at NIST. First phase performances of two breadboard interferometers are shown, reaching noise levels on the order of  $5 \text{ pm}/\sqrt{\text{Hz}}$  from 0.1 to 1 Hz in a  $\pi$ -measurement. The linearity of the frequency modulation is analyzed by means of different time series fits.

The continuation of DFM experiments at the AEI is based on the experiences gained at NIST. A quasi-monolithic unequal arm MZI is built to serve as frequency reference for future DFM set-ups. The overall frequency stability of the MZI is demonstrated in the second section of this chapter, which is based on the publication [Ger+16], successfully validating its functionality as suitable frequency reference for DFM interferometry, but also for LISA. Frequency noise levels on the order of  $8.17 \text{ kHz}/\sqrt{\text{Hz}}$  at 2 mHz are achieved, which is equivalent to  $1 \text{ pm}/\sqrt{\text{Hz}}$  displacement noise. The residual frequency noise can be explained by temperature fluctuations of the environment.

The phase performance of DFMI is investigated in the TMITM, consisting of two single-component prism-interferometers. Each one monitors displacement

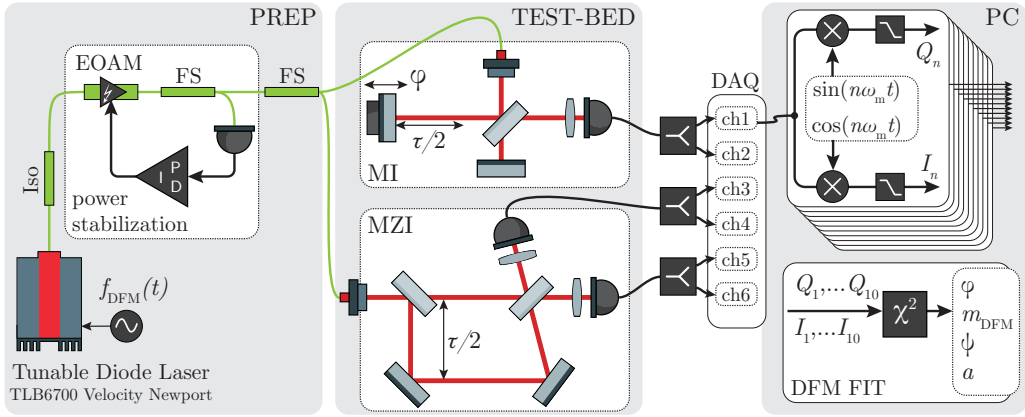
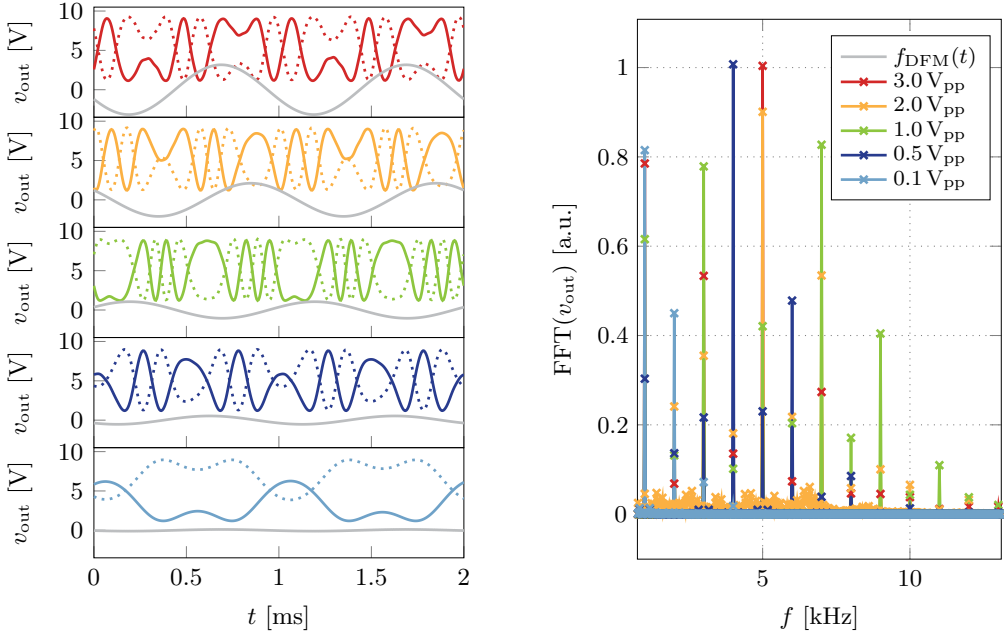


Fig. 9.1.: Sketch of the experimental DFM set-up as it has been investigated at NIST. The laser preparation shown in PREP is a fiber-based set-up with amplitude stabilization. The test-bed consists of a MI and a MZI which are free beam set-ups, not being operated in vacuum but in a closed chamber to reduce air density and temperature fluctuations. The third part, DAQ and PC, shows the data post-processing system using an  $IQ$ -demodulation scheme and the fit algorithm, both implemented in software on a PC to extract the phase, amplitude and modulation information. Here the demodulation process is only shown for a single channel.

changes of a steering mirror, or test mass, from one side. An equivalent laser source with a center wavelength of 1064.5 nm is used. It is shown that the average laser frequency can be stabilized with DFMI and the reference MZI down to noise levels of  $6 \text{ kHz}/\sqrt{\text{Hz}}$  at about 50 mHz. Furthermore, DWS was performed in real time by DFMI. The final performance of the experimental set-up is presented together some noise hunting procedures and a discussion of the limiting effects.

## 9.1 First proof-of-principle measurement

The set-up, as it has been used at NIST for first experimental DFM investigations, is shown in Figure 9.1. The laser preparation is all fiber-based and consists of a single laser source providing the deeply frequency modulated light for all interferometric set-ups. An EOAM is used for stabilizing the laser amplitude, which fluctuates due to the frequency modulation and due to the inherent noise of the diode laser itself. Via a fiber splitter (FS) the laser is fed into two interferometers operated in air. The ECDL TLB 6700 Velocity from Newport is used as laser source that provides a laser beam with a wavelength of 1550 nm and a maximum laser power of 20 mW.



**Fig. 9.2:** DFM photodiode signals measured on both output ports of the MZI and the according FFT for different modulation strengths of  $3.0 V_{pp}$  down to  $0.1 V_{pp}$ . The modulation frequency for all measurements is  $f_{mod} = 1 \text{ kHz}$ . The FFT shows how the contribution of higher harmonics of the modulation frequency increases for higher modulation strengths.

### 9.1.1 Experiment description

The two interferometers that are used as DFM test-beds are constructed on an aluminum breadboard, the first one is an unequal arm length MI, the second one is based on the MZI layout. While the MZI enables us to detect two complementary optical measurements of one interference signal by monitoring both output ports of the recombining beam splitter, the MI is used for sinusoidal signal injection at one of its end mirrors. The purpose of this is to test the functionality of the fit algorithm under dynamic disturbances and to simulate phase signals appearing in one of the interferometer arms which should be recovered by the algorithm. Both interferometers have optical pathlength differences of  $94 \text{ mm}$  and  $137.5 \text{ mm}$  for the MI and the MZI, respectively. Applying a frequency modulation amplitude of  $\Delta f \approx 3.1 \text{ GHz}$  therefore results in different effective modulation depths of  $m \approx 6.16$  for the MI and of  $m \approx 9.01$  for the MZI. The interferometers and the laser preparation are operated in air and without any temperature stabilization other than standard laboratory air conditioning.

### 9.1.2 Optical signals

Different modulations, each with 1 kHz modulation rate but various modulation strengths, of  $3.0 V_{pp}$ ,  $2.0 V_{pp}$ ,  $1.0 V_{pp}$ ,  $0.5 V_{pp}$  and  $0.1 V_{pp}$ , were generated by a function generator and applied to the laser driver modulating the laser frequency by several 1 GHz, depending on the actual strength. Figure 9.2 shows the interferometer pattern monitored on a photodiode, which is similar to the typical DPM signal, as it was expected for DFM interferometry. This result shows the close resemblance of DPM and DFM interferometry, as expected and theoretically described in [Ger15]. For larger modulation strengths the interferometric pattern changes and an increase of the effective modulation depth can be observed in the time series. The FFT of each time series is shown in Figure 9.2. It shows that the complex amplitudes at the modulation rate of 1 kHz and its higher harmonics up to ten contribute the most. Again, by increasing the modulation strength the effective modulation depth changes, here observed by the redistribution of the complex amplitude values for the individual harmonics. The results show that the DPM fit algorithm is also applicable to DFM data, measured in unequal arm length interferometers.

### 9.1.3 Time domain analysis of frequency modulation linearity

An effect that can spoil the overall readout performance of DFM is the excitation of higher harmonics of the modulation tone in the laser frequency modulation [Ger15; Kis+15]. This can for example be caused by non-linearities in the frequency actuation, realized here by changing the laser cavity length with a PZT crystal. To analyze this in our set-up we utilize another set of fits, which are operating in the time domain. The fits are implemented in MATLAB and each one uses a 10 ms long time-series of our photodiode output of the MZI (here with a slightly different effective modulation depth), sampled at 250 kHz. With the full sampling rate we can include higher modulation harmonics not taken into account by the frequency domain fit used for the phase extraction.

According to Section 6.2.2 the two following models are used, assuming that the sinusoidal frequency modulation of the laser is perfect

$$h_1(t) = E + E \cdot \kappa \cdot \cos(\varphi + m \cos[2\pi \cdot 1 \text{ kHz} \cdot t + \psi_{\text{mod}}]), \quad (9.1)$$

and under the assumption that the laser was not perfectly modulated at a single frequency but also excited at higher harmonics,

$$h_{10}(t) = E + E \cdot \kappa \cdot \cos\left(\varphi + \sum_{i=1}^{10} m_i \cos[i \cdot 2\pi \cdot 1 \text{ kHz} \cdot t + \psi_{\text{mod},i}]\right). \quad (9.2)$$

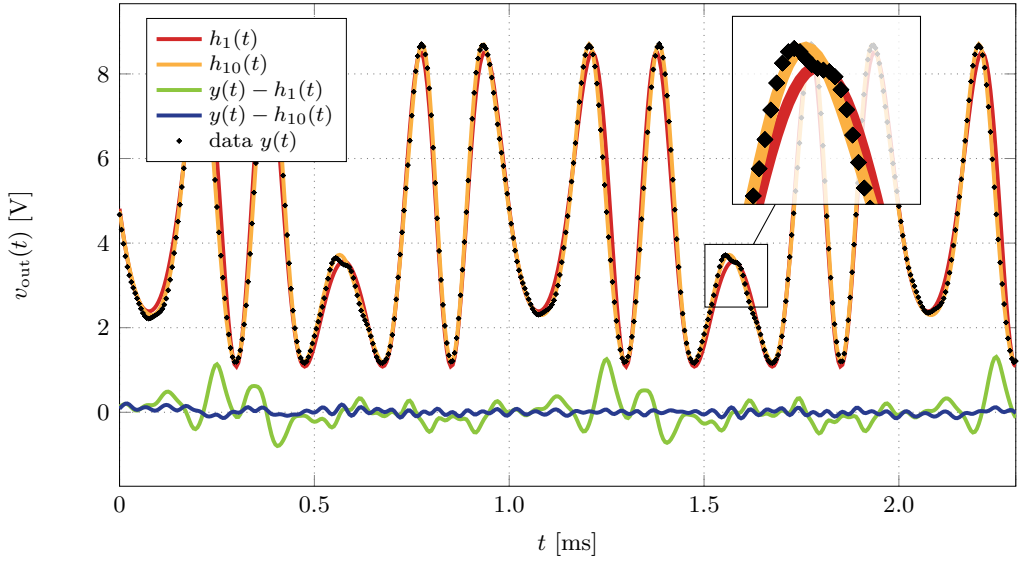


**Fig. 9.3.:** A typical DFM signal in the time domain of a data series measured for  $f_{\text{mod}} = 1 \text{ kHz}$  (black dots) and a modulation depth of  $m = 6.47$ . The model  $h_1(t)$  has a sum of squared errors (SSE)  $227.1 \text{ V}^2$ . The model  $h_{10}(t)$ , includes frequency modulations at harmonics of  $1 \text{ kHz}$  due to the very deep frequency modulation and has an error of  $\text{SSE}=8.8 \text{ V}^2$ . The remaining two curves show the difference of the measured data and the two fit functions.

The result of  $h_1(t)$  is shown (red line), together with the measurement data (black dots), in Figure 9.3. It matches the data with a sum of squared errors (SSE) of  $227.1 \text{ V}^2$ . The extrapolated function  $h_{10}(t)$  (orange curve) matches the measured data set better, especially at the turning and reversal points. The improvement is clarified by plotting the residuals of the fit functions to the measured data (green and blue line). The SSE of our fit could be improved by a factor of 25 when using  $h_{10}(t)$  as model. Regarding the fit output parameters, the values for amplitude  $E$  and contrast  $\kappa$  differed by 3%-4% for the different fit functions, but the effective amplitude, given by the product of these values, was identical. The modulation depth for the first harmonics was determined to be  $m_1 = 6.47$  for both cases. The first three higher harmonics make up the major contribution to the undesired additional frequency modulation with an effective modulation depth of  $m_2 = 0.09$ ,  $m_3 = 0.08$  and  $m_4 = 0.12$ . The maximal contribution of the higher harmonics is about 4.5% which, if not addressed, will limit the displacement performance in future implementations [Ger15].



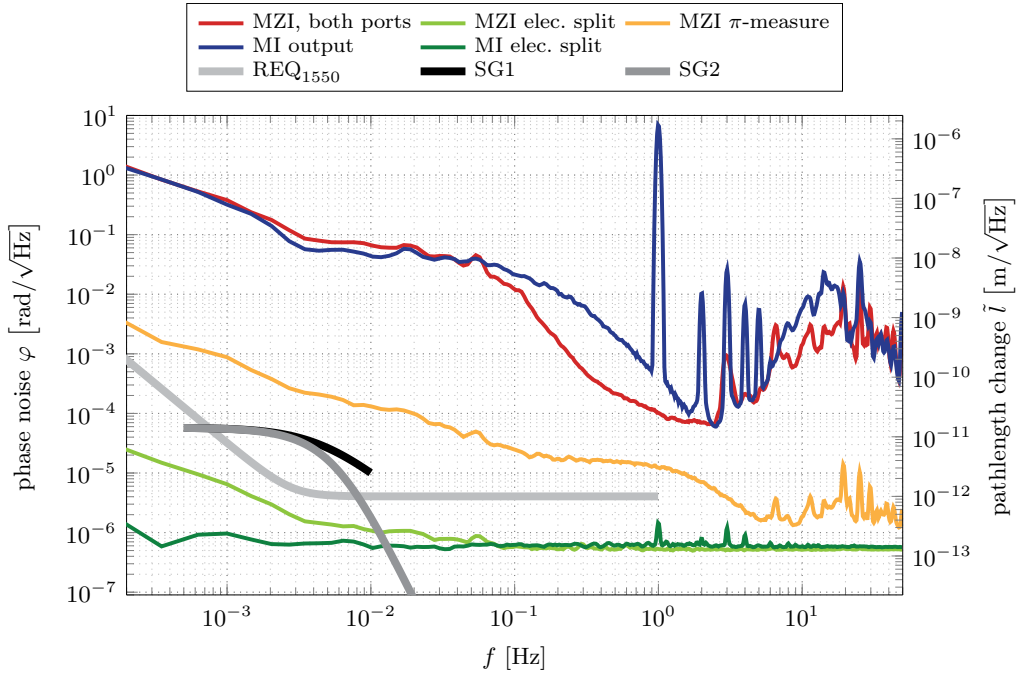


**Fig. 9.4.:** Spectral densities of the phase determined from the DPM fit algorithm with the modulation parameters  $f_{\text{mod}} = 800$  Hz,  $m \approx 6.16$  for the MI and  $m \approx 9.01$  for the MZI. The red line shows the phases from both interferometric outputs of the MZI. The dark blue curve shows the phase measurements from the MI. The residuals between two measurements which are electronically split are given by the green lines for the MZI and MI. The residuals of the  $\pi$ -combination are shown in the orange curve.

#### 9.1.4 Phase performance of DFM

The phase noise of the two unequal arm length interferometers, MI and MZI, is shown in Figure 9.4. The data is taken with a sampling rate of 250 kHz and a modulation strength of about 3.1 GHz. The  $IQ$ -data is sampled with 100 Hz and the resulting complex amplitudes are saved into data files. The fit algorithm is applied in post-processing to extract the phase information of the interferometers. In addition, a length modulation of one MI interferometer arm is applied by actuating on the PZT mirror with 1 Hz and an amplitude of about 1 rad, equivalent to 250 nm. The red curve shows both redundant photodetector output signals from the MZI, the dark blue curve shows the single MI output. The PZT-induced length modulation is clearly visible in the phase noise data from the MI, together with some multiple higher harmonics up to 5 Hz. These are either artifacts from the PZT motion itself, or they are induced by some non-linearities of the readout and fit algorithm.



Both interferometer outputs show the expected influence of acoustic couplings, dominating above 2 Hz and the phase noise rises towards lower frequencies below 2 Hz. Certain phase combinations are used to analyze the presence of other limiting noise sources. The zero combinations for both interferometers, where the signal is electronically split and subtracted from each other, show a white noise floor of  $0.15 \text{ pm} / \sqrt{\text{Hz}}$  for both interferometers. This might be caused by additive noise in our signal acquisition, most likely due to ADC digitization noise that is usually present at these levels [Ger+15]. The two green curves in Figure 9.4 represent the according phase noise results. Optical noise sources, like shot noise and amplitude noise, are common mode for electronically split signals and, hence, do not contribute to this combination. The MI electronic split combination contains a small residual of the 1 Hz mirror modulation and its harmonics. This coupling might be induced by small differences in the detection bandwidth of the DAQ system, leading to non-linearities. The behavior can also be seen in the time series for the MI and the MZI data. Figure 9.5 shows the according time series data on the left. Both channels detect almost the same signal, but the difference shows a residual correlation between them that is not only white noise. A periodic-like pattern, correlated to the main signal, is observed. By shifting the two time series against each other the pattern changes slightly, but the overall effect cannot be eliminated. The remaining correlation might be explained by the data acquisition where third harmonic distortion (THD) or temperature fluctuations cause variances between the single channels in the DAQ card. However, a large dynamic range of about six orders of magnitude is observed for the 1 Hz-signal injection. The noise in the MZI combination increases slightly to lower frequencies which cannot be observed in the MI combination. The MZI has a larger effective modulation depth and the photodetector output will be spread more to higher harmonics. These are, in general, more sensitive to temperature induced phase variations in the analog components and we assume that this behavior causes the noise increase in the MZI electronic zero combination to lower frequencies [Ger+15]. However, both zero combinations showed an improvement of about one order of magnitude in comparison to similar zero measurements demonstrated earlier in DPM experiments [Sch+14c]. Also shown in Figure 9.4 is the so-called  $\pi$ -measurement where the optical signals of the two redundant ports of a recombination beam splitter are compared with each other. This combination is sensitive to amplitude fluctuations and will be described in the following section.

### 9.1.5 Residual amplitude fluctuations

The right plot in Figure 9.5 shows the time series data monitored by the two output ports of the MZI. The interferometric information of these two optical signals is

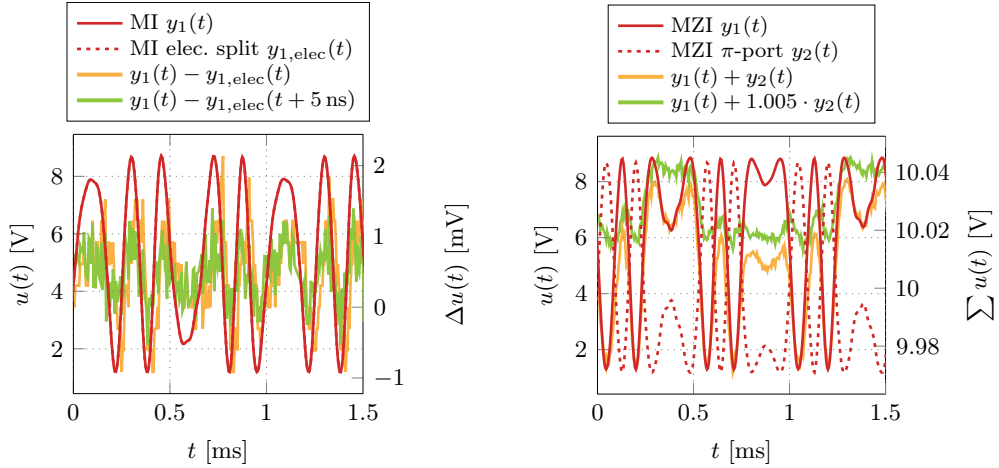


**Fig. 9.5.:** Time series DFM signals of the MZI and MI, showing residual amplitude and timing errors. On the left, the data of two MI channels, monitoring an electrical null (split), measurement are plotted, On the right plot the data of two MZI photodetector signals, performing an optical  $\pi$ -measurement. The residuals of  $\Delta u(t)$  (left) and  $\sum u(t)$  (right) are shown once for the raw data, once by including a correction term that shifts the time data by 5 ns (left), or scales the amplitude by 0.5% (right).

identical except for the phase shift of  $\pi$ . The  $\pi$ -combination is not sensitive to either displacement noise, LFN or non-sinusoidal frequency modulations because both beams contain the same interference. However, this phase shift causes amplitude fluctuations to couple differently in both outputs, making the  $\pi$ -combination sensitive to amplitude noise at the modulation harmonics, as well as shot noise, additive noise in the DAQ and, again, finite detection bandwidth. The sum of these signals is plotted as well. It shows periodic residuals whose pattern is highly correlated with the actual interferometer signals. The amplitude of one of the signals is corrected by a factor of 1.005, which somewhat reduces the amount of higher harmonics in the residuals, but does not eliminate the periodic residuals completely.

The  $\pi$ -combination for the MZI phase noise is plotted as orange line in Figure 9.4. The white noise floor of this combination is not clearly visible but it is probably on the same order of magnitude as for the electronic split measurements. Above 3 Hz this combination achieves a performance better than  $4 \mu\text{rad}/\sqrt{\text{Hz}}$ , equivalent to  $1 \text{ pm}/\sqrt{\text{Hz}}$ , except for some peaks that are also visible in the direct MZI phase. Here, a dynamic range of about three orders of magnitude is achieved. This is most likely caused by unwanted amplitude modulations that couple non-linearly in the measured phase. The finite detection bandwidth could also couple into this measurement, but a separate measurement of the flatness of the photoreceivers

transfer functions showed a high bandwidth of more than 1 MHz and even a correction of the data showed no improvement. Around 1 Hz the  $\pi$ -combination shows a characteristic noise shoulder, which is often caused by small vector coupling [Fle12; Ger+15], leading to a noise floor of  $20 \mu\text{rad} / \sqrt{\text{Hz}}$  between 100 mHz and 1 Hz. This small vector coupling is consistent with the noise shoulder, the non-linearities at higher frequencies and even the noise increase below 100 mHz which, again shows a dynamic range of about three orders of magnitude between the  $\pi$ -combination and the individual MZI phase measurements. This leads to a performance of  $1 \text{ mrad} / \sqrt{\text{Hz}}$ , equivalent to  $250 \text{ pm} / \sqrt{\text{Hz}}$  at 1 mHz.

Non-linearities in the optical part can also couple into this measurement, such as the transfer function of the individual photodiodes, their front-end electronics, or amplitude fluctuations of the laser beam. Also polarization fluctuations couple differently into the two output ports of an interferometer. The strong frequency modulation is expected to generate some residual amplitude modulations of the laser power at the critical frequencies. To some degree the amplitude modulations are suppressed by the power stabilization, but the effective residual amplitude modulation at the input of the interferometers has not been measured. Measurements without the power stabilization did not change the phase performance of the  $\pi$ -combination. Consequentially, laser induced amplitude modulations might not be the limiting factor, however we cannot fully exclude them either. A more probable explanation is poor polarization control since neither PM fibers, nor polarization components in the interferometers are used. Amplitude fluctuations can be generated due to polarization dependent optical properties of the components, or the presence of ghost beams in our set-up due to internal reflections in the beam splitters caused by non-ideal anti-reflecting coatings [Deh+12]. All these spurious signals form competitive interferometers with various absolute modulation depths that contribute differently to the measured complex amplitudes. Spurious optical signals that create small vector noise with a dynamic range of about three orders of magnitude will have power levels of about six orders of magnitude less than the beams of interest, as illustrated in Section 2.3.2. Such contaminations are easily introduced, but these effects can be suppressed in future implementations by using polarizers to reduce unwanted polarization components and by a detailed stray light analysis and optimization involving component placement and potentially wedged components to separate ghost beams and the actual interference.

### 9.1.6 Laser frequency noise correction

The residual noise of the raw phase signals at low frequencies might be caused by thermally driven length fluctuations of the interferometers, since they are built in air, or they are limited by LFN. Without having a suitable phase reference

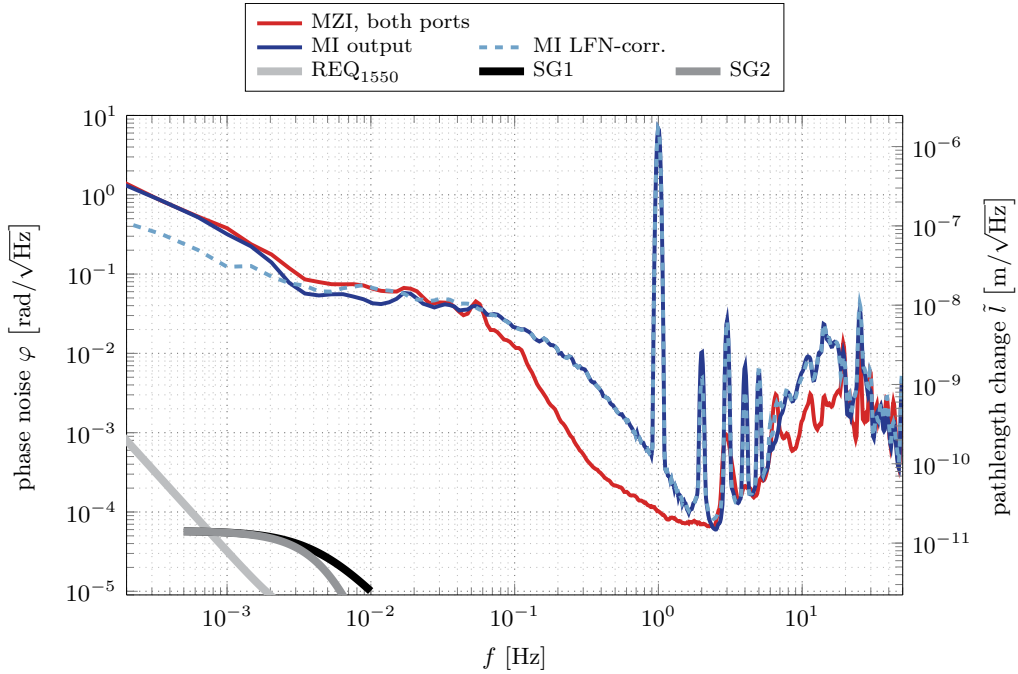


**Fig. 9.6.:** Spectral densities with LFN correction measured with  $f_{\text{mod}} = 800$  Hz,  $m \approx 6.16$  for the MI and  $m \approx 9.01$  for the MZI. The red and blue lines show again the initial measurements, the light blue dashed curve shows the LFN-corrected MI phase data by scaling the measurement from the MZI by the ratio of the modulation depths,  $6.16/9.01 = 0.68$ , and then subtracting it from the MI data.

measurement these two effects cannot be distinguished from each other. One of the fundamental concepts of DFM is the usage of a stable reference interferometer to either stabilize the laser frequency noise (see Section 9.3.2) or to provide a reference measurement which can then be subtracted from the data in post-processing. In the experiment shown here we can also consider the MZI as the reference interferometer and the MI as the readout interferometer, within the limits of our thermal and acoustic stabilities. Under this assumption the MI phase measurement can be corrected by using the ratio of the two respective modulation depths, which corresponds to the optical pathlength delays and takes into account the different coupling of LFN. The result is shown as light blue, dashed line in Figure 9.6. A noise reduction can only be observed at very low frequencies, but it already improves the readout of the MI by about a factor of two at 1 mHz and below. The residual low-frequency noise is therefore very likely dominated by thermal fluctuations and air density changes and not by LFN. To achieve  $1 \text{ pm}/\sqrt{\text{Hz}}$ -level sensitivities below 1 Hz, the interferometers have to be operated in vacuum and

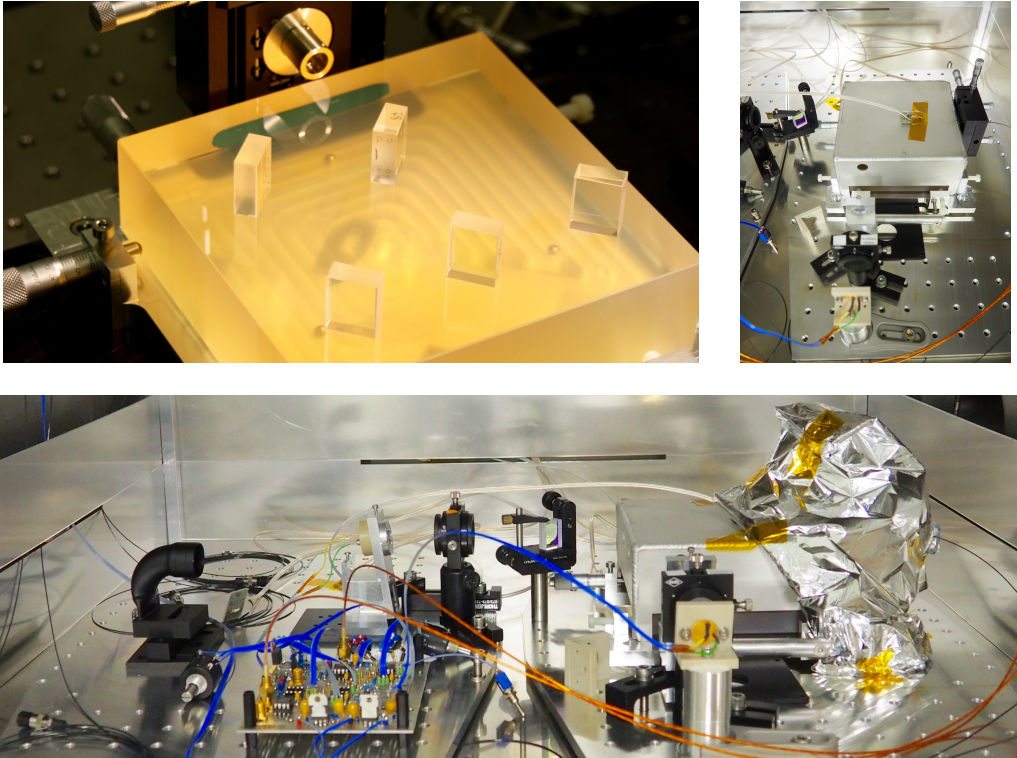


Fig. 9.7.: Photographs from the quasi-monolithic MZI constructed by using UV glue (top) and from the experimental set-up in the vacuum chamber (bottom). The adjustable fiber output coupler is separately covered by MLI foil to reduce thermal fluctuations from the electronics used for the balanced DC readout.

constructed from materials with low coefficients of thermal expansion, as shown in the following sections.

## 9.2 Frequency stabilization via balanced readout

With the quasi-monolithic MZI, shown in Figure 9.7, frequency stability measurements were performed to test the long term stability of glued interferometers, before the interferometer is used as reference for future DFM experiments which are shown in Section 9.3. The description of the results is based on [Ger+16], where more details of the experimental results are demonstrated.

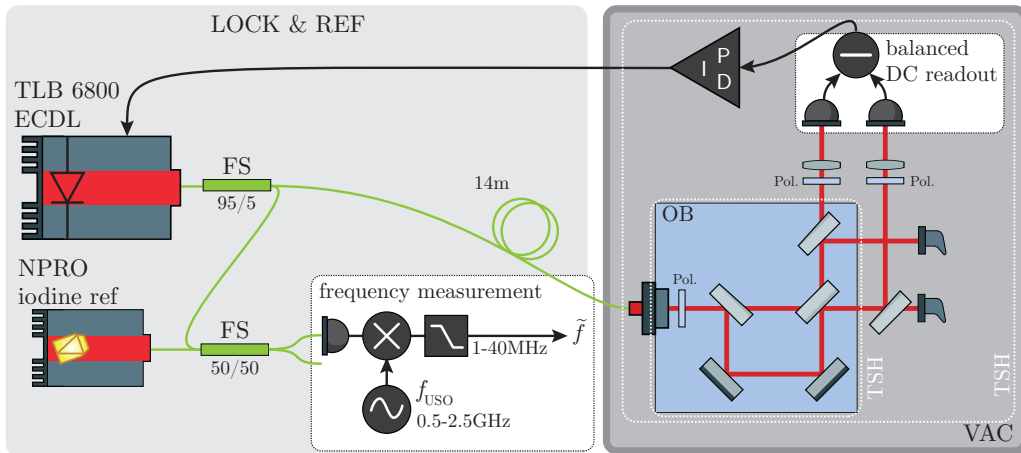
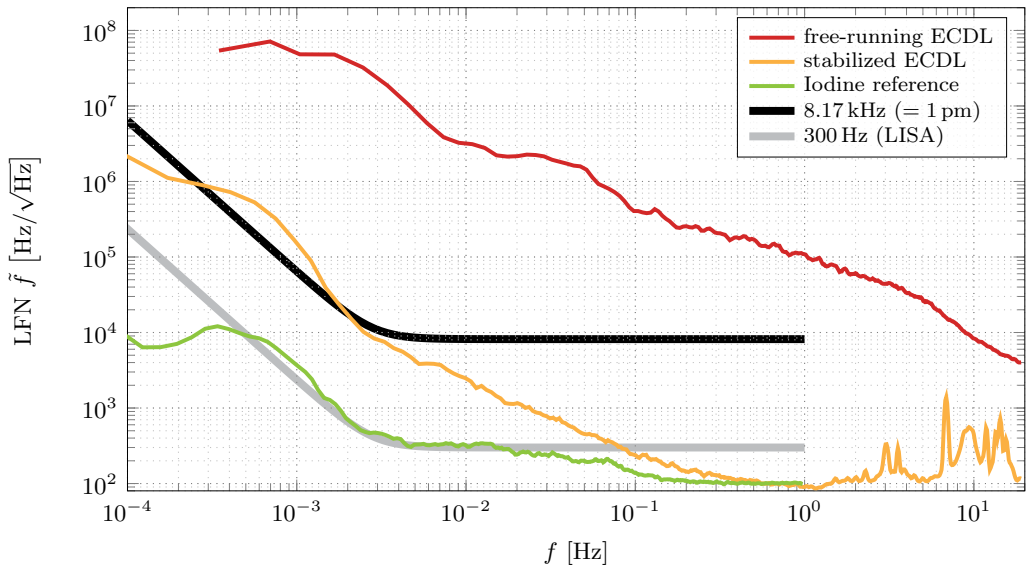


Fig. 9.8.: Sketch of the frequency-stabilization experiment. The optical set-up outside the vacuum chamber (VAC) consists of single-mode, PM fiber components. The interferometer and the analog electronics are placed inside a thermal shielding (TSH) mounted in the vacuum chamber via thermally isolating feet. An additional thermal shield is placed around the baseplate of the interferometer and extended to cover the fiber coupler with multilayer insulation foil. A dedicated analog PID-controller is used to provide feedback to the ECDL.

### 9.2.1 Experiment description

The reference MZI is placed in a vacuum chamber that is thermally isolated and equipped with a large thermal shield, as shown in Figure 9.7. The vacuum level during the experiment is on the order of  $5 \cdot 10^{-6}$  mbar. For the interferometer itself an additional thermal shielding is used and the fiber injector was covered with MLI foil to further reduce the thermal influence. Especially the electronics used for the balanced DC readout scheme, also placed inside chamber, are a significant heat source. The cable connection between photodiode and front-end electronics should be kept as short as possible and a thermally stable environment is also required. A sketch of the experimental set-up is shown in Figure 9.8. A balanced operation is achieved by using a second, externally placed, beam splitter in the east output of the reference interferometer. By the reflected beam's AOI the laser power is tuned to be equal on both photodiodes. A low-noise, low-drift operational amplifier in combination with ultra-stable photodiode bias voltages is implemented to perform a direct current subtraction followed by a high-gain TIA. The so-generated sinusoidal output signal contains regular zero crossings at the mid-fringe operation point which can be used for locking. An analog PID-controller feeds the actuation voltage to the ECDL (TLB-6821) which is placed outside the vacuum chamber and connected via a 14-m-long fiber feedthrough to





**Fig. 9.9.:** Frequencies spectral densities of the beat note between the iodine-stabilized NPRO laser and the ECDL without DFM, once free running and once stabilized to the MZI. Shown are also the frequency noise level of  $8.17 \text{ kHz}/\sqrt{\text{Hz}}$  and the LISA pre-stabilization requirement of  $300 \text{ Hz}/\sqrt{\text{Hz}}$ . The frequency noise measured between two iodine-stabilized lasers is plotted as reference.

the interferometer. Around 5% of the stabilized light is interfered with light from an iodine-stabilized NPRO laser [Coh13], using its frequency stability of about  $100 \text{ Hz}/\sqrt{\text{Hz}}$  as reference. The according beat frequency between those two lasers is first mixed down to a frequency between 1 MHz and 40 MHz with an ultra-stable oscillator (USO) and then tracked by a digital PLL implemented in a LISA-like phasemeter. Based on the results of the optical simulations in Section 7.1 the arm length difference of the MZI is  $\Delta l = 7 \text{ cm}$ , which provides a frequency stability requirement of

$$\tilde{f} = \frac{\tilde{x} \cdot c_0}{\Delta l \cdot \lambda_0} = 4.084 \text{ kHz}/\sqrt{\text{Hz}} \quad (9.3)$$

for achieving a displacement noise of  $\tilde{x} = 1 \text{ pm}/\sqrt{\text{Hz}}$  by using the laser wavelength  $\lambda_0 = 1064.5 \text{ nm}$  and the speed of light  $c_0$ . Taking into account reflection set-ups, an additional factor of about two is gained by geometry (see Section 7.2.4), leading to a frequency noise requirement of about  $8.17 \text{ kHz}/\sqrt{\text{Hz}}$ .

### 9.2.2 Measured frequency stability

Figure 9.9 shows the frequency noise stability of the MZI. Additionally, the free-running frequency stability of the ECDL is shown as reference, together with the

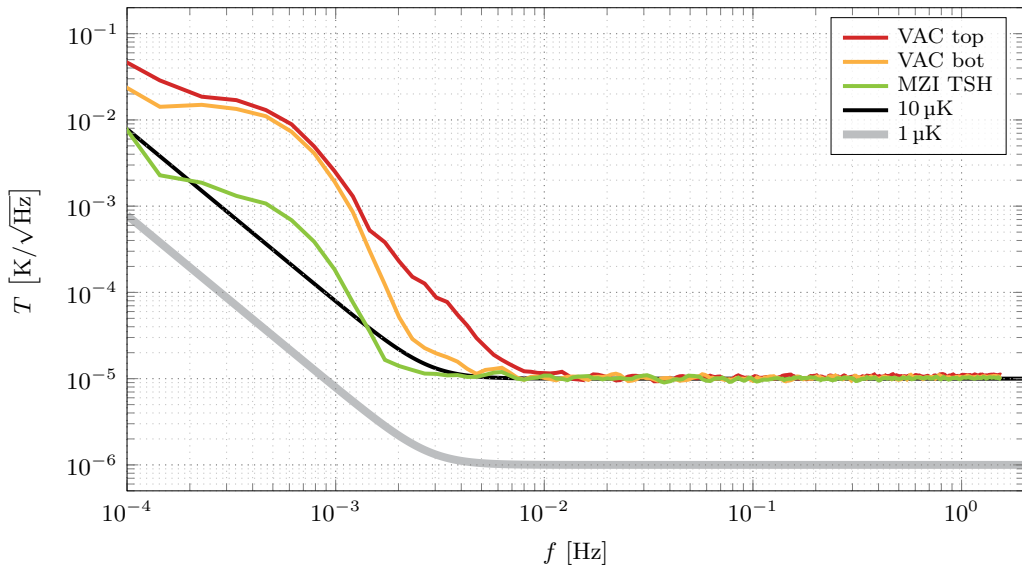


Fig. 9.10.: Measured temperature spectral densities of the temperature sensors placed inside the VAC and the thermal shielding. Shown is also the temperature stability goal for the optical bench in LISA, 1  $\mu\text{K}$  white noise level relaxed to lower frequencies.

frequency spectrum measured between two iodine lasers. The frequency readout noise floor (not shown) is measured separately using only electronic signals and is on the order of  $1 \text{ Hz}/\sqrt{\text{Hz}}$ , slightly increasing towards lower frequencies. At 1 Hz the frequency stability measurement is actually limited by the iodine reference. The  $8.17 \text{ kHz}/\sqrt{\text{Hz}}$  sensitivity is achieved at all frequencies above 2 mHz, slowly rising towards lower frequencies. Some couplings due to vibrations and acoustics are visible at frequencies above 1 Hz, either introduced by the interferometer sensing or by excess fluctuations induced in the ECDL that are not sufficiently suppressed by the loop gain. The unity gain frequency of the stabilization is in the order of 1 kHz and mainly limited by the bandwidth of the frequency actuation PZT amplifier.

For analyzing any thermal couplings into the frequency stability temperature sensors are placed on the optical bench of the reference MZI and on the top and bottom of the vacuum chamber. The temperature stabilities are measured, and the corresponding linear spectral densities, computed after subtracting a linear drift, are shown in Figure 9.10. A correlation between temperature fluctuations and frequency stability is clearly visible comparing these two plots. The excess noise observed at around 0.3 mHz is identified as outside excitation of our thermal environment. A time series analysis of both, temperature and frequency stability, shows also a correlation with a coupling factor of about  $0.5 \text{ MHz}/1 \text{ mK}$ . Based on the IfoCAD simulations shown in Section 7.1.4, a beam tilt of  $\pm 5 \mu\text{rad}$  generates a



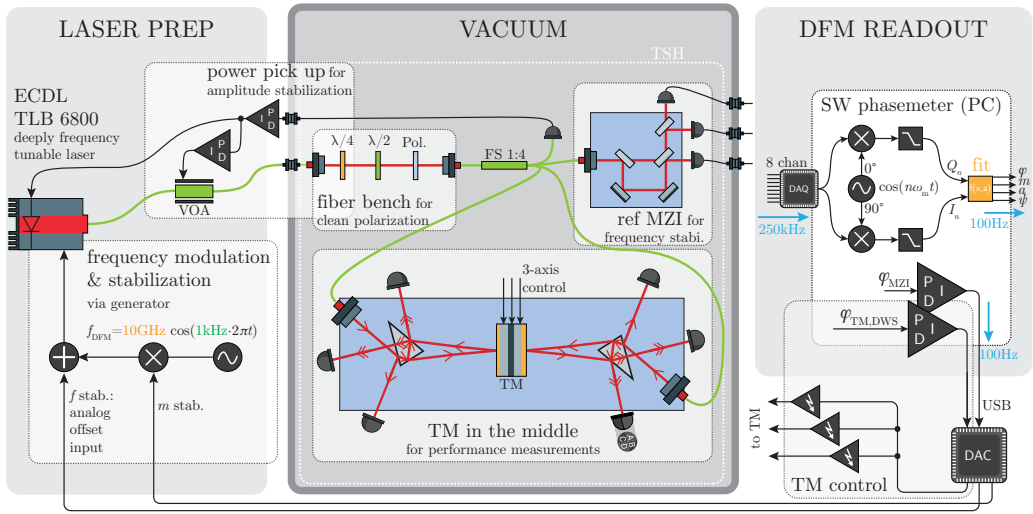


Fig. 9.11.: Sketch of the TMitM experiment altogether including the laser preparation (PREP), the monolithic set-ups of the MZI and the prism experiment in the vacuum chamber. A variable optical attenuator (VOA) and the LD pump current is used to actuate on the laser power. A fiber-bench is used for polarization cleaning. The prominent DFM data processing via software (SW) phasometer and Levenberg-Marquardt-based fit algorithm is shown on the right.

TTL coupling of about  $10 \text{ pm}/\mu\text{rad}$ , assuming a static interferometric misalignment of  $10 \mu\text{m}$ . Due to the usage of a commercial, adjustable fiber output coupler it is assumed that temperature fluctuations will generate beam pointing fluctuations by this device, as measured by Dehne et al. [Deh+12; Deh12]. These couple into the longitudinal phase measurement via the simulated TTL coupling coefficient. However, the LISA frequency pre-stabilization requirement down to  $100 \text{ mHz}$  could be achieved. More stable, quasi-monolithic FIOSs ([Kil+16], Section 5.2.2) could be used for improving this performance down to  $1 \text{ mHz}$  in the future.

### 9.3 Test Mass in the Middle experiment

The TMitM is used for the determination of test mass motions by comparing the interferometric measurements from both sides of an actuation mirror with each other. With this, the overall achievable performance of DFMI can be tested for its dynamic range by modulating the test mass. Noise sources can be analyzed by comparing redundant measurements with each other.

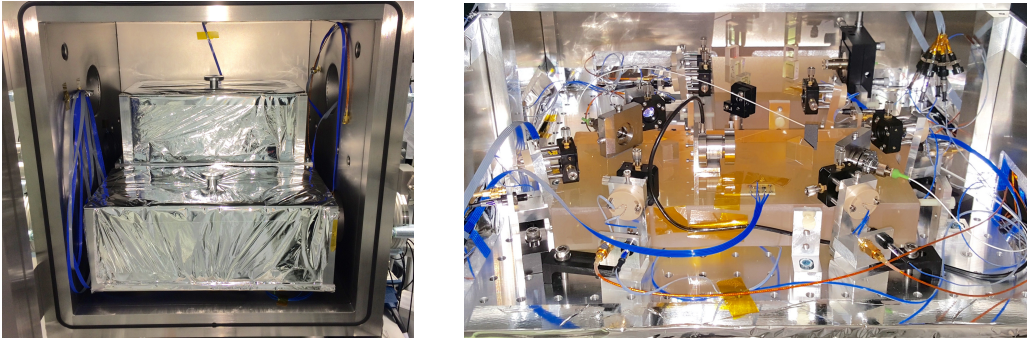
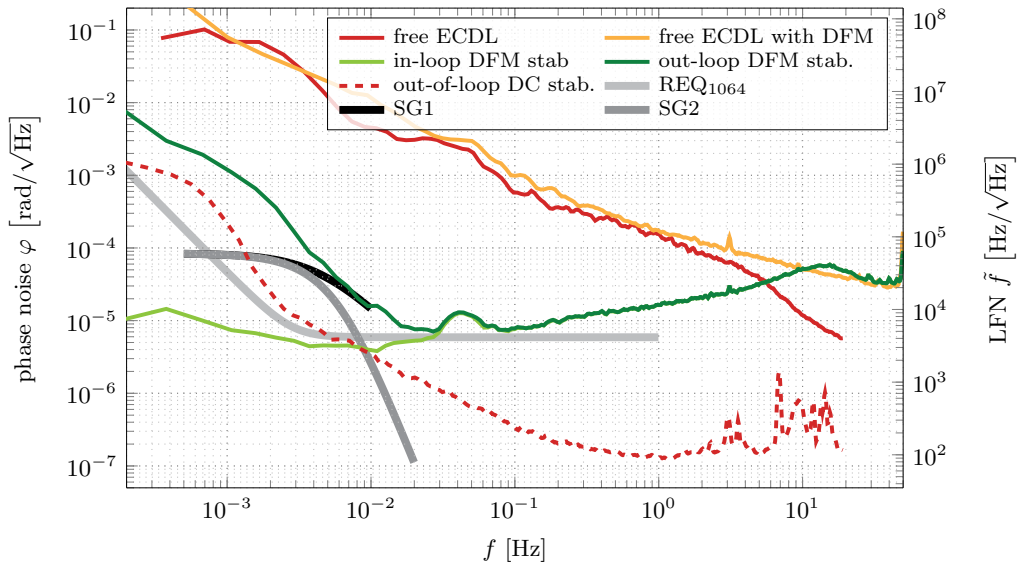


Fig. 9.12.: Photographs of the TMitM experimental set-up inside the vacuum chamber. A two-level thermal shield is made of aluminum, covered with MLI foil. The quasi-monolithic optical set-ups are placed on the lower level, surrounded by photodiodes. On the upper level a fiber splitter guides the light towards the interferometers, and to the laser power monitor, that consists of a fiber-bench with output coupler, lens and photodiode.

### 9.3.1 Experiment description

The complete test-bed of the TMitM experiment, shown in Figure 9.11, contains three interferometers, one reference MZI and two prism-interferometers. They are all operated with laser beams provided by a single laser source (TLB 6821). The AFG modulates the laser frequency by about 5 GHz, corresponding to a voltage output of  $950 \text{ mV}_{\text{pp}}$ , with a modulation rate of 800 Hz. The light is guided via a fiber feedthrough to the vacuum chamber. The amplitude, average frequency and modulation strength of the ECDL are stabilized, as shown in Sections 8.4.1, 8.4.2 and 8.4.3.

All optical components are placed inside a thermal shielding (TSH). As shown in Figure 9.12, the TSH consist of two levels. The aluminum breadboard on the bottom has a size of  $440 \text{ mm} \times 440 \text{ mm}$  and carries the two monolithic experiments. The upper level of the set-up has an aluminum breadboard as baseplate with the dimensions  $440 \text{ mm} \times 220 \text{ mm}$ . The fiber-bench, fiber splitter and the power monitor are installed on this upper level. Various temperature sensors (PTCs, see Section 4.2.3) are placed on the ceramic optical benches, the aluminum breadboards, the TSH and on the inside of the vacuum chamber. Three SEDs are aligned to the output ports of the MZI, two SEDs monitor the test mass motion from the left side and one SED and one QPD are installed on the right side of the TMitM. Together with the power sensor, 11 photodiode currents, including the four segments of the QPD, are guided via cable feedthroughs to the TIA. It is placed outside the chamber to reduce the heat dissipation in vacuum. The photodiode voltages are monitored by the DAQ-based processing system, where the modulation and interferometer parameters are extracted via fit algorithm and analyzed by means



**Fig. 9.13.:** Frequency spectral densities showing the achievable laser frequency noise suppressions that can be reached by utilizing DFMI. For comparison, the prior frequency stability results achieved with a balanced DC readout without DFM are plotted in red, once when the ECDL was free-running and once stabilized to the MZI. The in-loop and out-of-loop phase measurements of the DFM-frequency feedback control loop are both measured by the MZI (green).

of MATLAB. Due to the limited number of DAQ channels, only data from eight photodiode signals can be measured simultaneously.

### 9.3.2 Frequency stabilization

The MZI can be used as feasible frequency reference for the stabilization of the DFM laser as it has been demonstrated by the results shown in the previous section. As comparison, the results from the balanced DC readout lock are again plotted in Figure 9.13, once for the free running ECDL (red line) and once stabilized to the MZI (dashed red line). The integration of DFMI influences the achievable frequency stability, while the absolute phase noise of the free-running ECDL is similar for frequencies below 1 Hz regardless of whether a deep frequency modulation is applied or not (red and orange line). Above 1 Hz, the deviation between those increases and reaches about one order of magnitude differential phase noise at 20 Hz. The DFMI phase noise levels are also plotted in Figure 9.13, scaled to equivalent frequency noise for their respective arm length differences. Only the averaged laser frequency can be stabilized due to the underlying strong frequency modulation in DFMI. Additionally, the fit algorithm is integrated in the

control loop to recover the phase information. The light green curve shows the in-loop signal of the MZI, the dark green curve the out-of-loop signal from another MZI photodiode. The out-of-loop measurements in the TMITM show a similar phase noise behavior (not shown here). An overshoot above 10 Hz is visible in both, the in-loop and out-of-loop measurement. The out-of-loop DC stabilization (see Section 8.4.2) shows a low white noise floor of about  $100 \text{ Hz}/\sqrt{\text{Hz}}$ , while the overshoot in the DFM frequency lock brings the LFN to levels that are close to  $100 \text{ kHz}/\sqrt{\text{Hz}}$ . A possible explanation is the limited bandwidth of the DFM control at 100 Hz. The sampling rate of the fit algorithm limits the phase response of the open-loop gain. This leads to a noise increase near the unity-gain frequency. Also the complex data processing, especially the fit algorithm itself, might generate some additional non-linearities that can lead to an increased white noise floor. Below 5 Hz the LFN decreases and a dynamic range of two orders of magnitude is measured at 30 mHz. At this frequency, the phase noise of  $5 \text{ } \mu\text{rad}/\sqrt{\text{Hz}}$  corresponds to a residual LFN of about  $5 \text{ kHz}/\sqrt{\text{Hz}}$ , very close to the requirement to achieve  $1 \text{ pm}/\sqrt{\text{Hz}}$ -level displacement noise. Below 30 mHz the in-loop phase noise shows a further increased dynamic range of four orders of magnitude at 0.6 mHz. The equivalent out-of-loop measurement shows a higher phase noise at lower frequencies and is about one order of magnitude above the out-of-loop phase noise of the balanced DC stabilization.

The results indicate that even by applying strong laser frequency modulations the averaged laser frequency can be stabilized to adequate noise levels on the order of  $4.5 \text{ kHz}/\sqrt{\text{Hz}}$ . Frequency stabilities of this order of magnitude are required for future satellite gradiometry missions. A LFN suppression with a dynamic range of two orders of magnitude could be achieved from 0.6 mHz to 100 mHz. The current limitations are caused by the limited processing power and bandwidth of the readout system and again by temperature fluctuations. Replacing the DAQ card and the PC by a dedicated phasemeter, the control loop can be operated with higher bandwidth and the overshoot can be reduced in the future. By the implementation of the same, lower LFN-levels are also expected at higher frequencies up to 1 Hz.

### 9.3.3 Readout noise limitations

In order to analyze the residual noise sources in the electronic and the optical parts of the experiment, various phase combinations are calculated. Figure 9.14 shows an electronic split measurement of the TMITM, an optical split measurement of the MZI and  $\pi$ -measurements of all three interferometers. All data is measured simultaneously with laser frequency and amplitude stabilization applied. This measurement was done before the installation of the QPD on the right side of the test mass. The background noise floor above 100 mHz deviates by a factor of

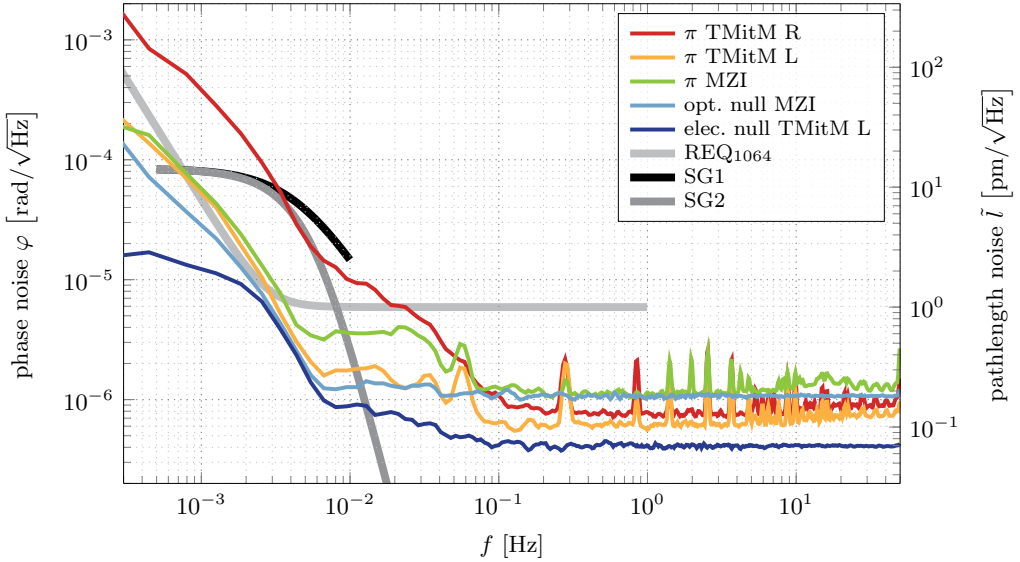


**Fig. 9.14.:** Electronic and optical phase noise combinations of different interferometer signals. The measurements are taken simultaneously with applied laser frequency and amplitude stabilization. For the electrical null measurement the signal was split directly before the DAQ card and then fed into two separate channels. All other measurements use the individual photodiode signals and separate TIA and filter channels.

five between the individual signal combinations. The electrical null measurement demonstrates a noise level of  $0.4 \mu\text{rad}/\sqrt{\text{Hz}}$ , theoretically achievable with the set-up. An increase of the white noise floor can either be explained by smaller optical amplitudes, which enlarges the digitization noise, or by residual optical amplitude fluctuations that are not suppressed by the amplitude stabilization. This effect would couple differently into the two redundant photodiode signals used for the  $\pi$ -measurement. However, all combinations meet almost the requirements, except for the interferometric measurement on the right test mass side (TMitM R, red curve). Apart from some temperature variations, polarization fluctuations or ghost beams might drive the phase noise at low frequencies which could limit the interferometer performance. The TTL coupling also varies between the redundant photodiodes due to photodiode and lens misalignments (see Section 7.2.5). This would also limit the dynamic range of the  $\pi$ -combinations.

### 9.3.4 Modulation depth stabilization

In order to characterize the feedback control loop of the laser modulation depth stabilization (see Section 8.4.3), the spectral densities of the fitted parameter  $m$  are shown in Figure 9.15. The absolute modulation depth value,  $m$ , is stabilized

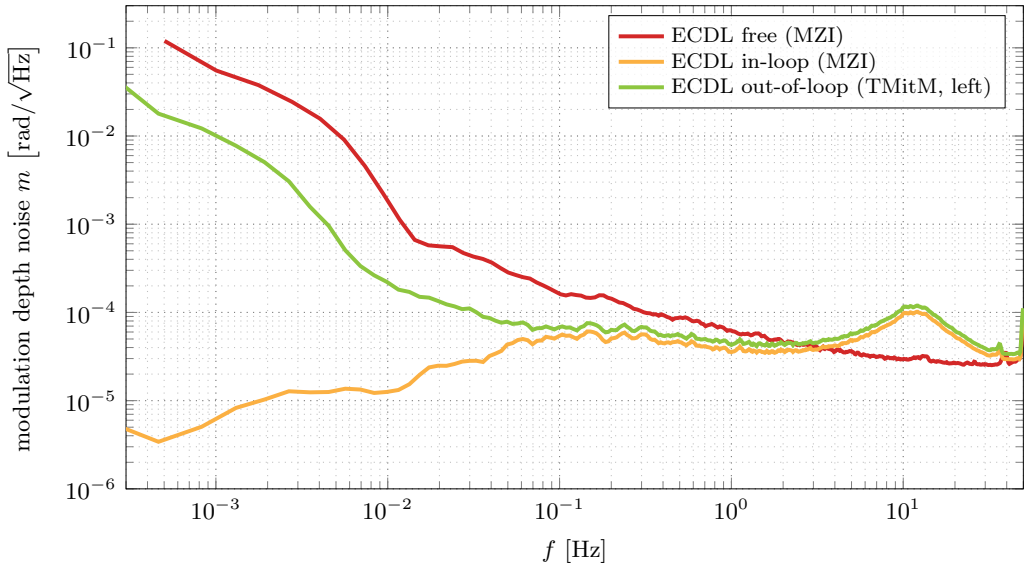


**Fig. 9.15.:** Spectral densities of the modulation depth are shown while the absolute modulation index is stabilized to 7.5 in the reference MZI. An out-of-loop measurement is shown by one of the TMitM photodiodes. As comparison the modulation depth noise without stabilization is given by the red line.

to  $m = 7.5$  in the MZI. By using the simulated arm length mismatch of 69.78 mm, the equivalent modulation strength applied on the laser is therefore stabilized to  $\Delta f = 5.132$  GHz. The prism-interferometers detect an absolute value of about  $m = 8.9$  (left) and  $m = 9.2$  (right), slightly increased due to the arm length mismatches. The in-loop modulation depth noise (orange line) shows a dynamic range of about four orders of magnitude at 1 mHz, compared to the free-running laser modulation strength. The out-of-loop measurement in the TMitM is only suppressed by a factor of five at this frequency, indicating that some other noise is dominating the modulation index fluctuations in these interferometers. Due to the lack of a test mass stabilization in this measurement, the modulation depth variations might be caused by actual length changes, maybe driven by temperature drifts, or other additional non-linearities in the TMitM. However, this control scheme stabilizes the operation point of the interferometer and the fit algorithm, reducing the dynamic range of the modulation index and making the readout process more linear. The achievable modulation depth stability in the out-of-loop measurements of about  $1 \cdot 10^{-2}$  rad/ $\sqrt{\text{Hz}}$  at 1 mHz and  $1 \cdot 10^{-4}$  rad/ $\sqrt{\text{Hz}}$  above 30 mHz correspond to an absolute pathlength noise level of  $93 \mu\text{m} / \sqrt{\text{Hz}}$  and  $930 \text{ nm} / \sqrt{\text{Hz}}$ , respectively. This gives an estimated accuracy for future absolute pathlength measurements with DFMI.



**Tab. 9.1.:** The AOIs in the prism for different environments (vacuum with a refractive index of  $n = 1.0$ , air with  $n = 1.00028$ ) are calculated. The initial AOI for the injecting beam is identical for both environments,  $\alpha$  is the angle of the first refracted beam into the prism,  $\beta$  is the angle at the first 50/50 surface,  $\gamma$  is the AOI from the beam traveling inside the prism to the recombining 50/50 surface. The angle  $\delta$  is the test mass AOI and  $x$  denotes the orientation of test mass with respect to the prism. This cancels out in the comparison.

$n$	init	$\alpha[^\circ]$	$\beta[^\circ] = 72^\circ - \alpha$	$\gamma[^\circ]$	$\delta[^\circ] = -90^\circ + x + \gamma$
1.00000	58.48	36.0188891	35.9811109	58.395355	$-31.604645 + x$
1.00028	58.48	36.0305538	35.9694462	58.3432232	$-31.656777 + x$

### 9.3.5 Effect of refractive index changes

During evacuation of the experiment to vacuum, pressures below  $1 \cdot 10^{-4}$  mbar are achieved. The refractive index of air changes from  $n = 1.00028$  to the one of vacuum of about  $n = 1.0$ . This causes changes in the angles of refraction due to Snell's law. For the TMITM, the expected angle difference between air and vacuum environment is determined for the two interfering beams. One beam propagates inside the prism, the reference beam, and the other one, the measurement beam, is reflected by the test mass. The different AOIs are shown in Table 9.1 for both indices of refraction. The reference beam is tilted by about 0.2 mrad during evacuation, the measurement beam by 0.91 mrad. This leads to a total optical phase angle of 1.11 mrad between those beams that is only caused by refractive index changes during evacuation. Due to the point-symmetry of the TMITM, the same behavior is observed on both sides identically. The simulated coupling coefficient of 5000 rad/rad predicts a DWS shift during evacuation of about 5 rad. We observe however a total shift of only about 3 rad on the QPD. This discrepancy might be caused by the effective beam parameters of the fiber output couplers used in the TMITM, which have not been measured. A lower DWS coupling coefficient of about 3000 rad/rad might hence be more realistic, but would have to be verified separately. The DWS shift limited initially the control range of the test mass stabilization in vacuum since the TMITM was aligned in air. The actuation range of the HV amplifier is limited by  $\pm 100$  V and together with the relatively high mass of the gold-coated test mass mirror and its mount, the resulting lever arm is limiting the possible absolute actuation range for the test mass angle (which is 0.6 mrad at most for 100 V). The misalignment of 3 rad DWS angle in vacuum is prevented by an offset-calibration of the horizontal test mass angle in air. With this we are able to achieve a zero-crossing DWS signal after evacuation.

This effect is also critical for other interferometers, especially those that are using wedged components. Due to the refractive index changes, and in dependency

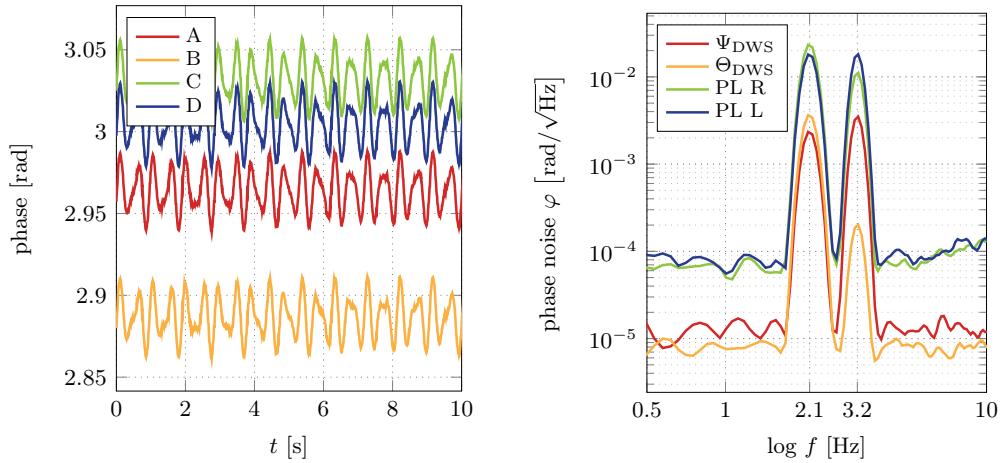


**Fig. 9.16.:** Measuring coupling coefficients of the test mass control loop. Shown are the time series for each QPD segment (left plot), and the spectra of horizontal and vertical DWS signals,  $\Psi_{\text{DWS}}$  and  $\Theta_{\text{DWS}}$ , respectively, as well as the PL signals sensed from both test mass sides (right plot). The PZT mirror axes were modulated at 1 Hz, 2.1 Hz and 3.2 Hz with a strength of 1 V.

on the initial AOI, the operation point of the interferometer will change during evacuation. But also non-wedged components produce a small lateral shift of the beam propagation. Even though these effects are often tiny and not always measurable by monitoring the interferometric contrast, they might influence the interferometer behavior significantly. Especially highly sensitive optical signals, like the longitudinal pathlength, the TTL coupling and DWS, might be influenced by this effect. Future implementations have to take this into account.

### 9.3.6 Test mass stabilization and increased tilt-to-length coupling

In order to achieve a closed-loop operation, coupling coefficients needs to be measured (see Section 8.5). By injecting sinusoidal signals on the PZT mirror axes (here 1 Hz, 2.1 Hz and 3.2 Hz) the resulting coupling into the DWS signals can be determined. Figure 9.16 shows the time response of each QPD segment in the left plot, and the phase spectrum of the according horizontal and vertical DWS signal in the right plot. The first PZT axis (modulated at 1 Hz) couples only barely into the DWS signals. The second axis couples in both directions almost to the same



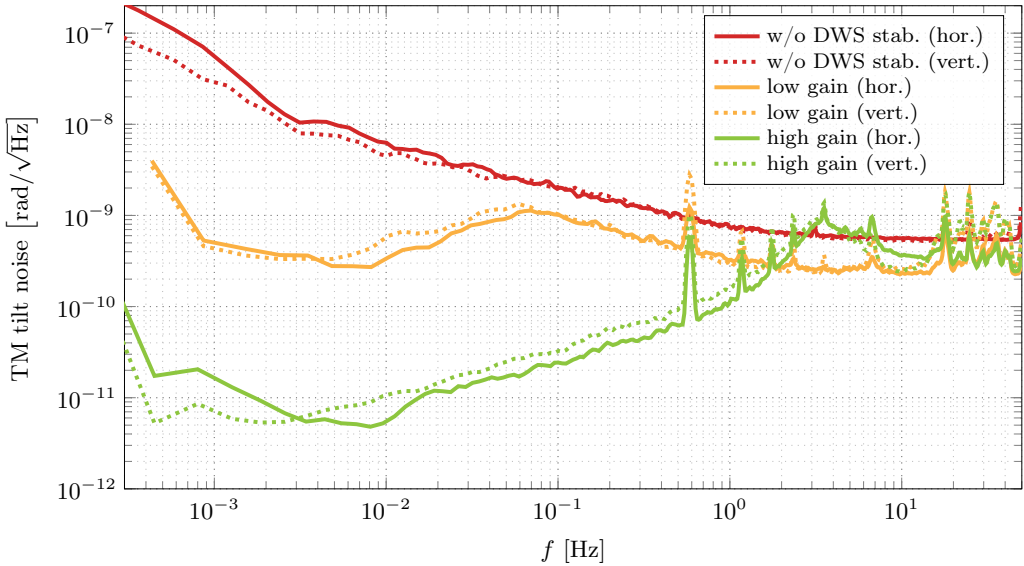


**Fig. 9.17.:** Test mass tilt noise with feedback control using different integral gains in the software PID-controller. The optical phase extracted from the fit algorithm is scaled by a factor of 5000 rad/rad to achieve the corresponding test mass tilt noise from the DWS signals. Shown are the signals of the in-loop photodiode.

degree, while the third one influences the horizontal direction more. As introduced in Section 8.5 the coupling matrix is calculated. The inversion of this matrix,

$$M = \begin{pmatrix} 940 & 310 & 120 \\ -0.7 & -0.4 & -0.14 \\ 0.59 & 0.52 & 0.04 \end{pmatrix} \frac{1}{\text{rad}}, \quad (9.4)$$

provides the individual gains for each PZT axis according to Equations (8.4), (8.5) and (8.6). Since the first PZT axis does not couple significantly into the DWS signals, the coupling matrix entries are overcompensated. Since the PZT mount is designed for a load of about 2 to 3 g (equivalent to the mass of a single optical component), the additional mirror holder made of titanium significantly enhances the load and limits currently the tilt range in pitch direction due to its weight. In the following, the first PZT is not included in the DWS control loop. Also the pathlength of the test mass is not stabilized, since an unexpected high coupling of test mass tilt into optical pathlength is observed. The TTL coupling simulated in Section 7.2.5 is about 40 pm/ $\mu$ rad for 20  $\mu$ m prism misalignment, assumed to be identical for both tilts, pitch and yaw. The measurement shown in Figure 9.16 shows a much higher TTL coupling of about 6 nm/ $\mu$ rad measured on both sides from the test mass. The third PZT contributes the most to these pathlength signals.

The TTL coupling coefficient is  $46.7 \text{ nm}/\mu\text{rad}$  and  $76.2 \text{ nm}/\mu\text{rad}$  measured on the right and left side, respectively. An increased TTL coupling might be explained by interferometric misalignments. As shown by the simulation results in Section 7.2.5, a misalignment increases the TTL coupling significantly. Also unknown in our experiments is the absolute test mass orientation. This changes the interferometer operation point and makes the TTL coupling larger and non-linear. Also a reduced DWS coupling coefficient could explain the observed deviations. For the measured TTL coupling coefficient we assumed a DWS coupling of  $5000 \text{ rad}/\text{rad}$ , as indicated by the simulation results. The actual DWS coupling in the experiment might deviate due to slightly different beam parameters or other noise sources, but a reduction of three orders of magnitude is unlikely. As shown in the previous section the coupling coefficient determined from the DWS shift during evacuation is on the order of  $3000 \text{ rad}/\text{rad}$ . The discrepancy of these orders of magnitude between experimental results and simulations must be caused by some additional, unknown TTL coupling effects, which have not been considered in the simulations.

Figure 9.17 shows the horizontal and vertical DWS in-loop signals measured for different control parameters, and scaled by a factor of  $5000 \text{ rad}/\text{rad}$ . This value corresponds to the simulated coupling coefficient in Section 7.2.5 and converts the measured DWS signals into actual test mass tilt noise. Due to the lack of a second QPD in the experiment and enough DAQ channels, an out-of-loop DWS measurement could not be performed. The free-running tilt noise shows a white noise floor of about  $0.3 \text{ nrad}/\sqrt{\text{Hz}}$  above  $1 \text{ Hz}$ . The DWS noise increases towards smaller frequencies and reaches a level of about  $30 \text{ nrad}/\sqrt{\text{Hz}}$  at  $10 \text{ mHz}$ . By controlling the test mass angle, the in-loop DWS noise can be reduced significantly over the full frequency range. The integral gain of the PID-controller was optimized by enlarging the gain such that the system is properly operating without oscillation. A dynamic range of more than three orders of magnitude is achieved at  $1 \text{ mHz}$  for both tilt angles, pitch and yaw.

The according test mass pathlength noise is shown in Figure 9.18. The division factor of four results once from the reflection set-up, that provides a factor of about two in each prism-interferometer, and another factor of two by comparing the measurements from the left and right test mass side with each other. Their difference is plotted here and referred to as test mass phase noise. By applying the DWS stabilization, the test mass phase noise could be reduced by a factor of five at frequencies up to  $1 \text{ Hz}$ . Above this frequency the phase noise is limited by control loop overshoot and some acoustic couplings. However, these measurements were only taken over a few minutes to ensure that the thermal environment did not change significantly in-between. Additional experimental results have shown that the phase drift rising towards lower frequencies depends also on temperature fluctuations. These can further influence the dynamic range of the DWS control

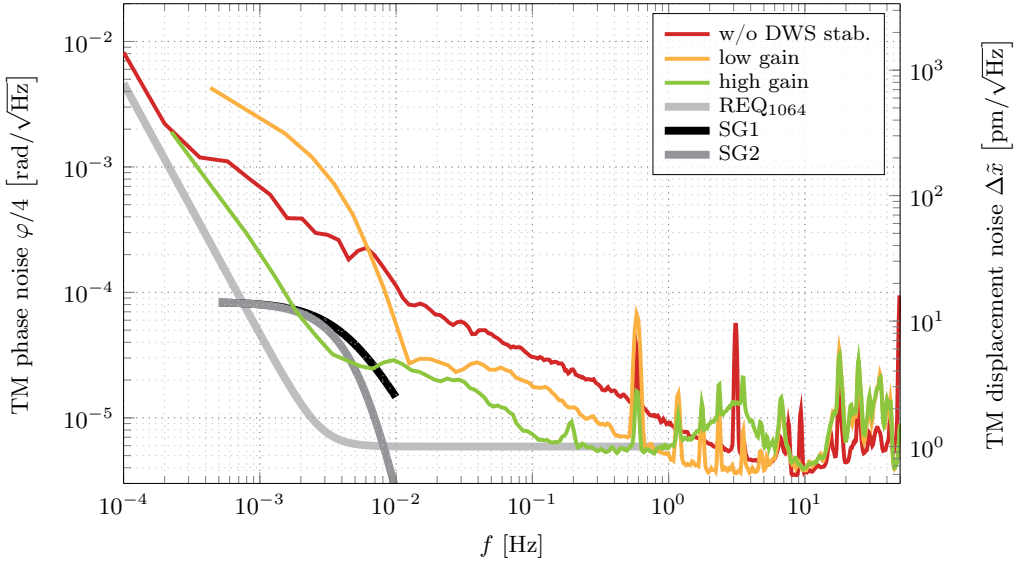


**Fig. 9.18.:** Test mass displacement noise with feedback control using different integral gains. The measured phase is scaled by a factor of four due to the reflection set-up and the redundant measurement from both sides.

loop. One should note that LFN is suppressed in these combinations by the frequency stabilization and the subtraction of the left and right interferometer signals.

### 9.3.7 Test mass readout performance

As mentioned in the previous section the test mass displacement can be recovered from the measured phase noise by utilizing scaling factors by which the according phase measurements are divided.

Figure 9.19 shows some of the best individual displacement performances measured from both test mass sides, therefore only divided by a factor two. During this measurement all stabilization schemes (laser amplitude, frequency and modulation depth, and test mass control) are applied. The  $\pi$ -measurement of the left prism-interferometer is only plotted as reference and not divided by the scaling factor. Some residual temperature fluctuations, limiting the low-frequency noise of the  $\pi$ -measurement, dominate also the test mass readout noise at both sides. The right prism-interferometer shows a lower phase noise level that can be explained by the DWS stabilization which controls the test mass tilt via a QPD in the same interferometer. Residual temperature drifts, driving the test mass mirror and the fiber output couplers dynamics, are imprinted on the actuation signal of the DWS control loop and might be the reason for the increased phase noise measured in

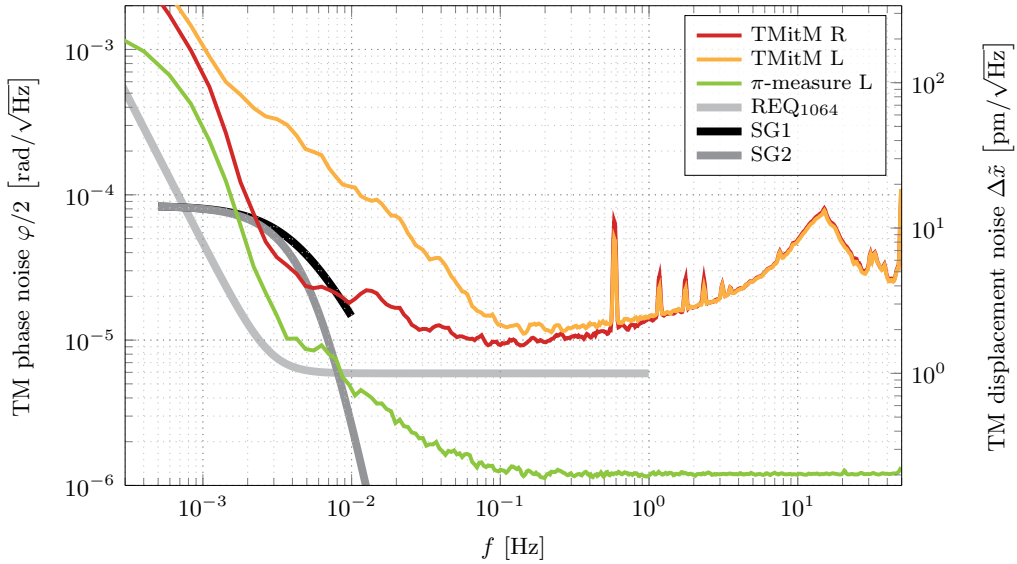


**Fig. 9.19.:** Test mass displacement noise measured on one side of the TMitM experiment. All stabilization schemes are applied (amplitude, frequency, modulation depth and test mass tilt). The phase measured on each side, TMitM R and TMitM L, is divided by a factor of two in order to achieve the actual test mass displacement. The  $\pi$ -measurement of the left interferometer is plotted as reference, without division by two.

the other interferometer on the left. An analysis of the time series data has shown that the test mass phase of the signal combination from both sides has a linear drift of about  $32 \mu\text{rad/s}$ , slightly flattened with respect to the temperature drift of  $3.6 \mu\text{K/s}$ , shown in Figure 9.20. A more sensitive test mass readout is expected for a better thermalized system, especially the combination of the left and right interferometer signals should provide a higher performance.

The current experimental set-up shows already a remarkable low test mass displacement noise of  $1 \text{ pm}/\sqrt{\text{Hz}}$  from 0.1 to 1 Hz by comparing the interferometric measurements from both test mass sides with each other (see Figure 9.18). The singular test mass displacement measurements, shown in Figure 9.19, demonstrate that LISA-like noise levels can be achieved by using DFMI. A displacement noise of below  $2 \text{ pm}/\sqrt{\text{Hz}}$  is achieved at 100 mHz for the right prism-interferometer. Within the frequency band relevant for future satellite gradiometers, we achieve an interferometer readout noise of  $3.5 \text{ pm}/\sqrt{\text{Hz}}$  at 10 mHz and  $10 \text{ pm}/\sqrt{\text{Hz}}$  at 2.5 mHz. These low phase noise measurements could only be achieved by an intense polarization cleaning and other optimizations. Polarization-maintaining fibers are used to feed the light into the vacuum chamber. A second fiber-bench placed outside the tank is used to optimize the coupling into these feedthroughs. The polarization adjustment is verified with a polarimeter for both fiber-benches,

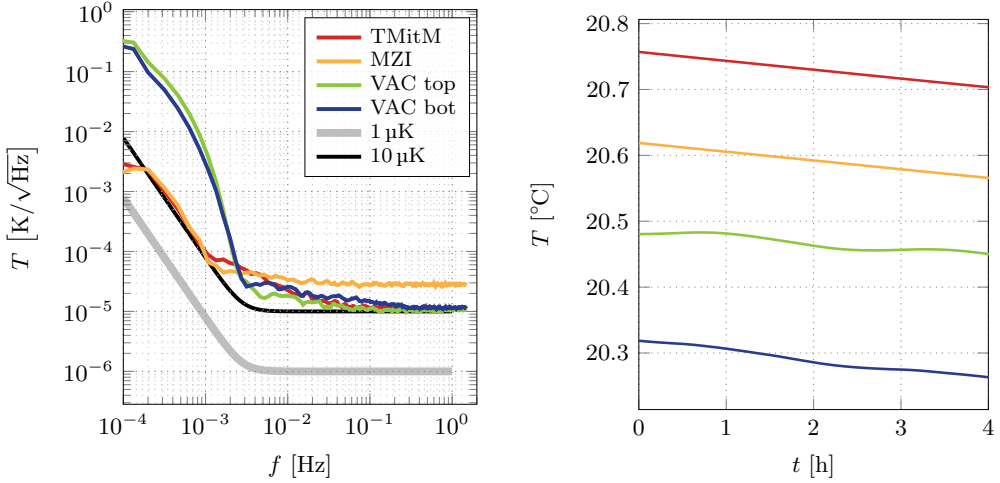


**Fig. 9.20.:** Temperature drift and spectral noise measured during the performance measurement shown in Figure 9.19. The legend shown on the left is valid for both plots in this Figure. The LISA requirement of  $1 \mu\text{K}/\sqrt{\text{Hz}}$  is plotted as reference. The time series on the right plot matches a linear trend of  $13 \text{ mK/h}$ . The measurements on the top and bottom of the VAC show also a residual oscillation resulting from the laboratory air conditioning. The temperatures measured on the interferometer baseplates of the TMitM and the MZI show no visible oscillations in the time series, but all measurements exceed the temperature noise floor of  $10 \mu\text{K}/\sqrt{\text{Hz}}$ . A linear drift was subtracted from the data to calculate the noise spectrum.

in- and outside of the chamber. The usage of polarizers in front of the photodiodes is also essential. A correction of the complex amplitudes to compensate the low-pass behavior of the analog front-end (see Sections 8.2.2 and 8.3.1), has shown no significant influence on the phase performance so far. Non-linearities, as already observed in the results from NIST (see Section 9.1.3), are still present in these experiments as shown in Figure 9.21. A linearization of the deep frequency modulation will further improve the interferometric readout sensitivity. In order to implement this, a new phasemeter is required that provides a larger amount of readout channels and higher processing capabilities.

Experiences from earlier experiments have shown that noise hunting at  $1 \text{ pm}/\sqrt{\text{Hz}}$ -levels often takes several years. More noise hunting (than the passed five months) is expected to lead to further significant improvements.

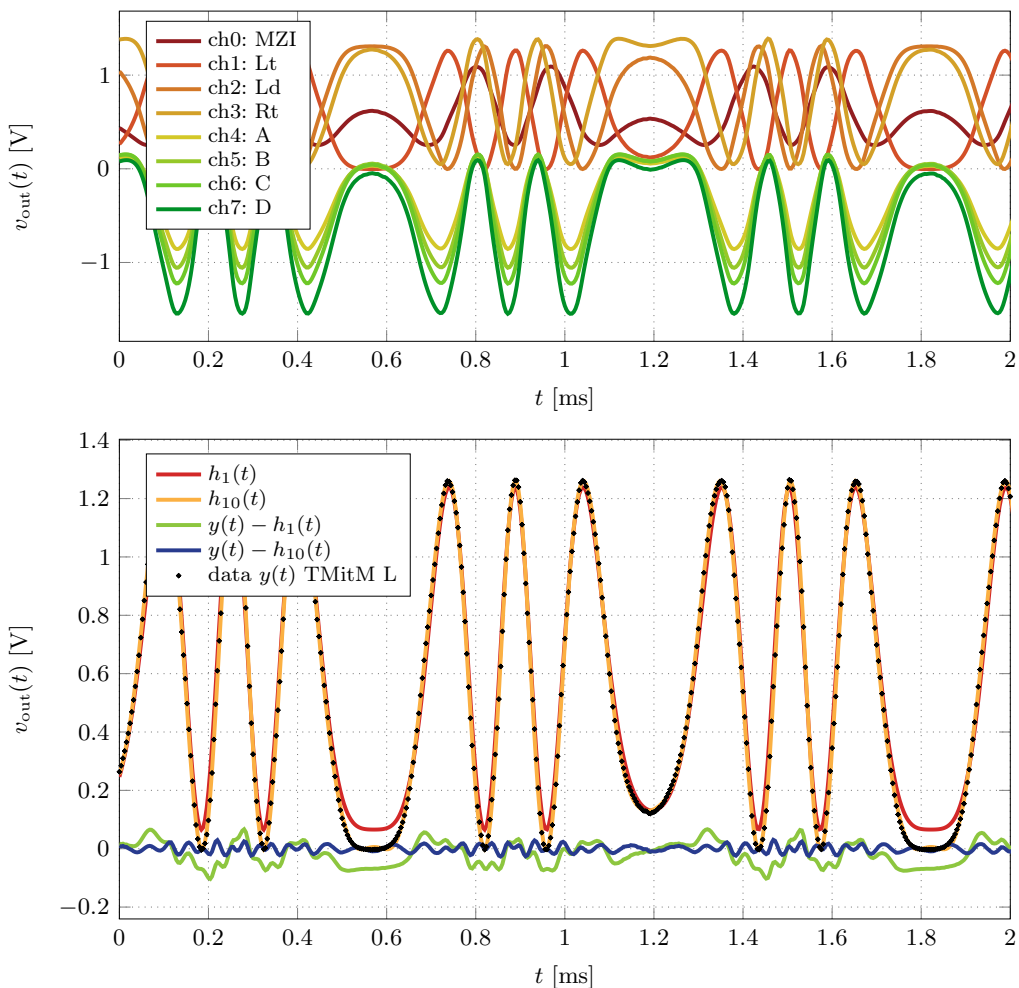


Fig. 9.21.: Time series data of the TMitM and MZI. The upper plot shows all readout channels of the DAQ system. The QPD signals on the segments A, B, C and D are enhanced by additional amplifying electronics, also introducing a sign change. The plot below shows two fitted models matching the data of channel 1 (TMitM left). The model  $h_1(t)$  has an SSE of  $4.8 \text{ V}^2$ . The model  $h_{10}(t)$  includes frequency modulations at harmonics of 800 Hz and has an SSE of  $0.3 \text{ V}^2$ . The residuals of model and fit are also plotted. The higher harmonics contribute less than 1.5% to the overall modulation depth.

This thesis describes advances in precision laser interferometer at low frequencies for future space missions like LISA and satellite geodesy missions. In the first part a comprehensive analysis, design and experiments for the optical PRDS (backlink) of LISA have been presented, laying the ground work for solving one of the most critical challenges of the LISA interferometry. In the second part a new interferometer technique has been developed, achieving LISA-like measurement performance levels with much simpler optical set-ups, making such readout highly scalable and more readily available for future satellite geodesy missions and further experiments and applications.

### 10.1 Three-Backlink interferometer

In connection with the results from the prior fiber backlink experiment, a backlink study was conducted to investigate alternatives for LISA. A few selected schemes are demonstrated in the publication [Isl+17]. The goal is to find an optical set-up by which an interferometric readout noise of  $1 \text{ pm}/\sqrt{\text{Hz}}$  is achieved in the LISA bandwidth. The prior fiber backlink experiment required a number of active stabilization and post-correction methods to achieve this. To understand the current limitations, a ghost beam catalogue has been developed and an analytic model describing the expected phase disturbances was derived. The idea of the investigation of the non-reciprocal phase noise of three backlinks against each other in a single test-bed was initially introduced by Fleddermann [Fle12]. More relevant environmental conditions for LISA are additionally achieved by constructing the so-called Three-Backlink interferometer (TBI) on two separate optical benches that are rotatable against each other by  $1.5^\circ$ . A direct fiber backlink (DFBL), an evolved version of the prior fiber backlink, a frequency separated fiber backlink (FSFBL) and a free-beam backlink (FBBL) are integrated in the TBI. The two optical benches are mirror-symmetrical to each other and their design has been developed by using the optical simulation tool IfoCAD. The final 3D Autodesk Inventor model of the TBI experiment is shown Figure 10.1. The relevant optical signals were predicted by

these simulations and optimized to achieve an optimal interferometer design which is not limited by shot noise, ghost beam phase errors or TTL coupling. For the FBBL connection the expected coupling coefficients between steering mirror motion and DWS signals were simulated and validated by experimental results that were measured with a prototype of a free-beam link between two interferometers. This pre-experiment has been constructed by means of adjustable optical components and fiber output couplers and without an additional reference measurement against which it could be compared. Thus, the  $1 \text{ pm}/\sqrt{\text{Hz}}$  requirement could not be achieved with this interferometer, but the environmental infrastructure for the TBI could be tested and prepared in detail, as published in [Isl+18]. The vacuum chamber was equipped with a multi-stage thermal isolation system and various layers of passive thermal shielding which provided a sufficient thermal stability of  $1 \text{ mK}/\sqrt{\text{Hz}}$  at  $1 \text{ mHz}$  at the location of the interferometer benches, even during operation of the rotating benches. The laser preparation was set up externally to the vacuum chamber and consists of four NPRO lasers that are locked to an iodine reference laser and are then guided to the experiment via fibers. For the phase readout, two phasemeters were installed, one for locking the MHz laser frequencies to each other and the other one to monitor the kHz beat notes in the experiment. The rotary stages can simultaneously be rotated against each other by  $\pm 1^\circ$  over a period of about 16 h. The control loops for the steering mirrors in the FBBL pre-experiment could be operated over several weeks without disturbances and significant thermal dissipation in an evacuated environment. The measured DWS noise is below the requirement of  $0.2 \text{ mrad}/\sqrt{\text{Hz}}$  which has been estimated by means of simulation results. The construction of the quasi-monolithic TBI is ongoing, the first batch of optical components is already bonded on the left optical bench via template-assisted positioning. A dedicated laser preparation was installed in the cleanroom for achieving two beams, each one with adjustable power levels. The fiber injection optical subassembly (FIOS) design has been taken over from the one that is used in the Hexagon [Sch15], and was re-worked and optimized by Daniel Penkert [Pen16]. With this design we expect very high coupling efficiencies for the fiber-to-fiber backlink coupling and a high beam quality. The construction of the same is currently ongoing.

The TBI construction required highly accurate beam measurements, currently done with a method described in [Sch+14b]. In the future, a new calibrated quadrant photodiode pair will be constructed [Fit+13] to further simplify and accelerate the construction. In the end, the TBI will contain ten photodiodes, two of them QPDs, which requires a phase readout system with more than 16 channels as it is currently integrated. A phasemeter is under development in the LISA group at the AEI that integrates up to 64 channels, using a single FPGA, and including TIAs for converting the photocurrent into voltages also within



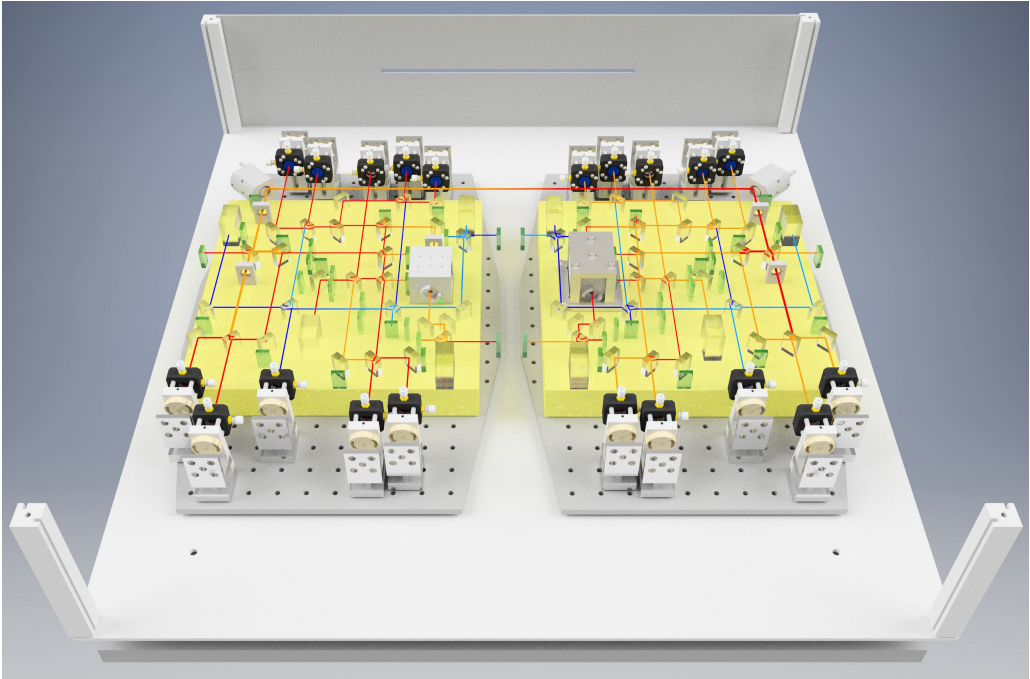


**Fig. 10.1.:** Final 3D model of the TBI experiment. The model of optical benches and components was generated by IfoCAD. The mechanical devices, such as the photodiode assemblies, steering mirror mounts, waveplate holders and Faraday rotators with mounts were integrated afterwards by using the step files provided by the manufacturers.

the phasemeter. This will further simplify the experimental infrastructure and increase the opportunities of redundant measurements. With the TBI we will be able to compare the three backlink candidates relative to each other and to test various types of backlink fibers, like classic single-mode PM fibers, radiated and non-radiated, or some other fiber types like Fibercore Zing™ fibers [Fib] or Hollow core fibers [Tho]. The detailed stray light and noise analysis and the inclusion of various lessons learned from previous LISA breadboarding experiments make the TBI one of the most complex interferometers ever constructed in the context of LISA and will ensure that performance levels below  $1 \text{ pm}/\sqrt{\text{Hz}}$  can be achieved.

The implementation of two rotary stages in a vacuum chamber provides an excellent experimental test facility for LISA, to be used in the future for testing an engineering model of the backlink and other prototypes of the LISA optical bench. The infrastructure allows us to freely tune the absolute laser frequencies over large ranges. This allows for even more realistic experiments regarding the LISA architecture in the future by choosing MHz-heterodyne frequencies and including active photoreceivers. The alternative backlinks that will be investigated in the TBI

have the potential to be less susceptible to fiber backscatter, promising lower noise levels and/or hardware requirements better-suited for the overall LISA mission. The usage of balanced detection puts additional constraints on the redundancy and readout channel numbers, but it is unavoidable if a direct fiber link is chosen. The alternative schemes are designed such that this correction should not be required, or to a much lower degree. However, a direct, experimental comparison of all three schemes is still necessary to validate the predicted noise assumptions. These results, together with other LISA breadboarding experiments, shall, in the end, allow us to choose the best overall solution for LISA [Isl+18].

## 10.2 Deep frequency modulation interferometry

Since the conceptualization of the idea of using deep frequency modulation interferometry (DFMI) for test mass readout by Gerberding [Ger15], several experiments have been conducted. We started with a first proof-or-principle experiment in cooperation with NIST where important knowledge about the experimental components was gained. The publication [Isl+16b] shows the outcome of these investigations, reaching  $250 \text{ pm}/\sqrt{\text{Hz}}$  at  $1 \text{ mHz}$  while the actual motion of a moving mirror could be tracked. The continuation of DFM experiments at the AEI implied the organization of a complete new laser infrastructure and preparation with deeply tunable laser sources and PM fibers, a new vacuum chamber with dedicated thermal isolation and a data processing system, all optimized for achieving the best performance. Two quasi-monolithic optical set-ups, an unequal arm length Mach-Zehnder interferometer and a Test Mass in the Middle (TMitM) experiment, were designed and optimized in IfoCAD, together with the development of a one-component prism-shaped interferometer. Both interferometers were constructed in the cleanroom by using adhesive bonding. The Mach-Zehnder interferometer was used in an initial experiment as frequency reference where an ECDL laser was locked to it via balanced DC readout at mid-fringe, while the achieved frequency stability was compared to an iodine reference laser. The publication [Ger+16] shows the results of the achieved frequency noise levels of  $100 \text{ Hz}/\sqrt{\text{Hz}}$  at  $1 \text{ Hz}$ , demonstrating that a simple unequal arm length interferometer can be used as LISA pre-stabilization system and that adhesive bonded interferometers can reach  $1 \text{ pm}/\sqrt{\text{Hz}}$  displacement stabilities. The core properties and limitations of DFMI were analyzed with the TMitM experiment. Here, we used the Mach-Zehnder interferometer as frequency reference by which we were able to stabilize the mean frequency noise of the DFM laser down to  $5 \text{ kHz}/\sqrt{\text{Hz}}$  at  $5 \text{ mHz}$  with approximately  $10 \text{ Hz}$  control bandwidth, showing that an adequate frequency stabilization can also be conducted for DFMI. A further stabilization scheme that was also tested for the first time in this thesis is the control of the effective modulation depth,

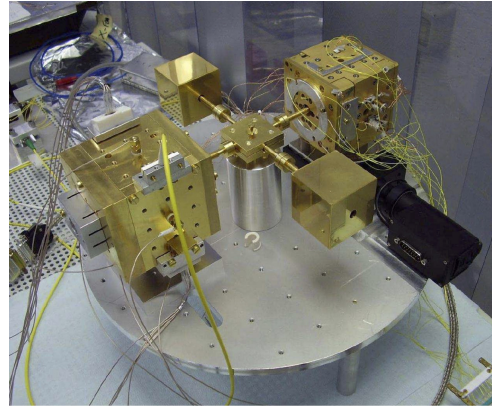
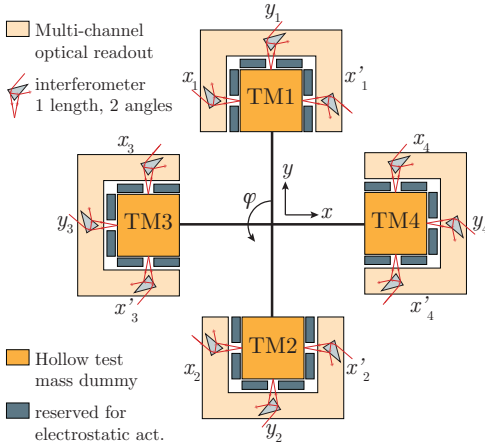


**Fig. 10.2.:** Sketch and photograph of a torsion balance payload for testing gravitational reference sensors. On the left a possible test set-up is illustrated that uses one-component interferometers with DFMI in the torsion balance (picture based on geo-Q proposal). A photograph of a torsion balance payload at the University of Trento is shown on the right that is used to develop the LPF Gravitational Reference Sensor. Picture courtesy from the University of Trento.

also by using the Mach-Zehnder interferometer as reference. In a last step, the test mass actuation mirror in the TMitM was stabilized with DFM technology in combination with DWS by using a quadrant photodiode at one side of the test mass. The interferometer readout noise for a test mass motion was measured to be  $3.5 \text{ pm}/\sqrt{\text{Hz}}$  at 10 mHz. By combining the two redundant measurements of both test mass sides, one is able to track the test mass displacement with a performance of  $1.0 \text{ pm}/\sqrt{\text{Hz}}$  between 0.1 Hz and 1 Hz. Future optimizations and noise hunting are likely to further improve the noise performance of the TMitM experiment.

One critical limitation of the current experiment is the bandwidth of the data processing system and the control loops. The digitization of eight data channels runs with 250 kHz, the DFM fit algorithm uses 100 Hz data and provides therefore actuation signals at the same rate, which limits the bandwidth of the laser and test mass control to approximately 20 Hz. A dedicated FPGA-based phasemeter as developed in [Vor17] can reduce the digitization noise by sampling with higher resolution and the fit algorithm, or a Kalman filter, can be implemented in a system on a chip micro-processor architecture by which the bandwidth of the actuation signals can be increased significantly. The maximum number of eight channels is currently limited by the DAQ card and the processing power of the PC, already using multi-threaded software running on eight CPU cores. The channel count must be increased for optimizing the TMitM readout and for future experiments containing more quadrant sensors and optical heads. This can on the one hand be

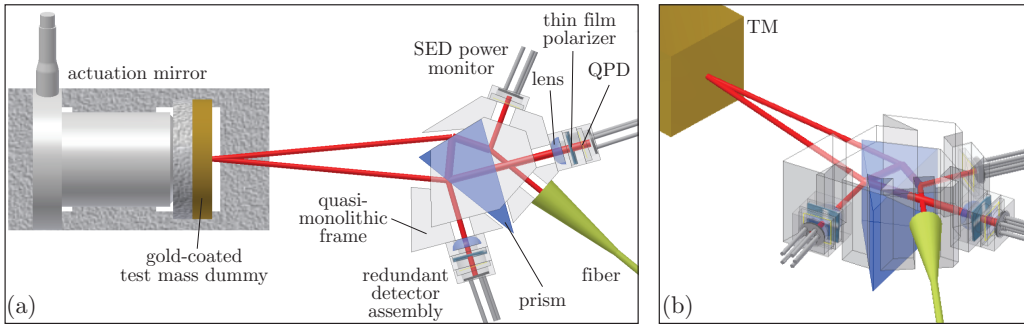


**Fig. 10.3.:** 3D engineering model showing a possible design of a monolithic frame for the prism by which the optical fiber and the photodiodes are connected to the test mass interferometer. View from the top is shown in (a). An angled view from the front is shown in (b) with a cubic test mass in the background.

achieved by replacing the current DAQ-system by a FPGA-based phasemeter, but also the implementation of other phase extracting methods, like a Kalman filter as shown in [Vor17] might be advantageous for future experiments

### 10.3 Future test mass readout with DFMI

One major planned application of DFMI is the readout of a torsion balance that is currently being constructed within the SFB geo-Q project A06. With a torsion pendulum small forces can be observed which makes the instrument ideal for applying and testing multi-channel interferometry. A symmetric four-arm payload will be suspended in a large, complex vacuum chamber from a torsion fiber made from fused silica. As small spurious forces are aimed to be monitored the motion and rotation of the suspended test masses must be very stable. The system is built such that the test mass is nearly free-floating, like a test mass in space, along the torsional DoF. Small rotations are then translated into quasi-free linear motions at the end of each pendulum arm. A more quiet torsion pendulum can be achieved by applying multiple active stabilizations to control the rotational operating point by actuating on the platform. DFMI will be used to read out the motion of all suspended test masses, as shown in Figure 10.2. The accommodation, alignment and cross-talk will still make the application of DFMI in this test-bed challenging. However, this novel interferometer technique provides the most compact optical set-ups available to reach the desired performance. The usage of one-component interferometry simplifies the optical heads significantly in comparison to classic heterodyne LPF-interferometer schemes.

For further reducing the complexity of future optical set-ups a 3D sketch of a monolithic frame made from glass with a low CTE has been designed, that

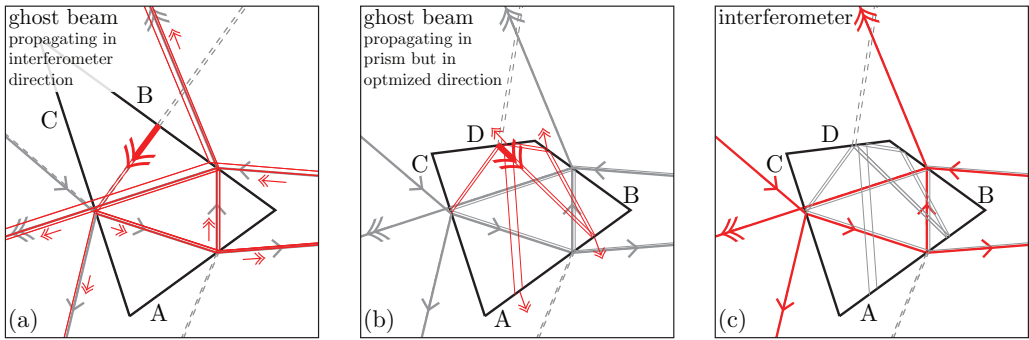


**Fig. 10.4.:** Sketch of a re-worked one-component interferometer design, based on the prism layout. One edge of the classic prism (a) is cut off such that the ghost beam, generated by surface C and initially reflected by surface B, does not enter the interferometer anymore (b). The main interferometer structure and geometry stays the same (c), but without ghost beams traveling collinear to the nominal signals and entering the detectors.

is shown in Figure 10.3. It includes the fiber injection and sensors within one quasi-monolithic assembly which is then bonded to the top, or bottom, of the prism. The sensor assemblies consist of focusing lenses, thin film polarizers and photodiodes that are all angled with respect to the interferometer plane such that eventual backreflections leave the interferometer plane and the coupling of ghost beams can be prevented.

The geometrical shape of the prism can also be improved for preventing the occurrence of ghost beams in the main interferometer axis. Simulations have shown that by using a commercially available isosceles prism the surface C, as illustrated in Figure 10.4a, produces a ghost beam that is reflected by surface B after propagation in opposite direction through the prism. This later reflection causes a critical ghost beam to enter the photodetectors which can be avoided by an enhanced design of the prism. Figure 10.4b shows the propagation of this ghost beam if the edge of the prism is cut off, the overall geometry including the initial beam propagation is kept the same, as shown in 10.4c. Further optical simulations are required for determining the optimal cut-off angle of the prism edge such that the ghost beam power is minimized and its propagation direction is optimized.

Alternative sensor designs might also be advantageous for future multiplexed interferometer set-ups. One example, a multi-core fiber, is shown in Figure 10.5. One fiber core is used for injecting the laser light onto the optical bench, while four additional cores are used for guiding the interfered light towards single element sensors. Owing to the spatial separation of these fiber cores, different optical phases are detected on each diode, depending on the actual wavefront curvature of the measurement and reference beam before they are coupled into the individual fiber ports. This kind of fiber-based DWS sensors allow us to separate the detectors from

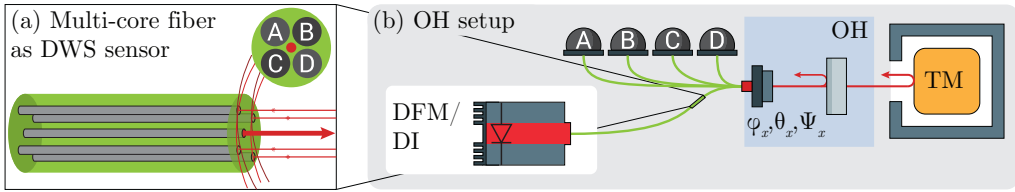


**Fig. 10.5.:** Future DFM-multiplexing-interferometry with DWS by using a multi-core fiber that injects the light to the optical head and guides it also back to some single element sensors. One core in the middle is used for the injection, four others detect differential wavefront signals from the interference at different points.

the optics which might be beneficial for the design of satellite missions or other applications. In addition, existing ranging devices, as demonstrated by [Kis+15], could be improved by DWS technology. The gain factor between optical phase and DWS provides highly sensitive interferometric measurements and apart from displacement changes, also angular tilts in multiple OHs can be measured using a single set of detectors.

# BIBLIOGRAPHY

- [Abb+16] Benjamin P Abbott, Richard Abbott, TD Abbott, et al. „Observation of gravitational waves from a binary black hole merger“. In: *Physical review letters* 116.6 (2016), p. 061102 (cit. on pp. 2, 3).
- [Abb+17] Benjamin P Abbott, R Abbott, TD Abbott, et al. „GW170814: a three-detector observation of gravitational waves from a binary black hole coalescence“. In: *Physical review letters* 119.14 (2017), p. 141101 (cit. on p. 3).
- [Abr74] Milton Abramowitz. *Handbook of Mathematical Functions, With Formulas, Graphs, and Mathematical Tables*, Dover Publications, Incorporated, 1974 (cit. on p. 123).
- [aC13] Karsten Danzmann et. al and eLISA Consortium. „The Gravitational Universe“. In: *ArXiv e-prints* (May 2013). arXiv: 1305.5720 [astro-ph.CO] (cit. on pp. 3, 19–22, 24, 115).
- [Ace+07] F Acernese, P Amico, M Al-Shourbagy, et al. „The Virgo interferometric gravitational antenna“. In: *Optics and lasers in Engineering* 45.4 (2007), pp. 478–487 (cit. on p. 2).
- [Anz+05] S Anza, M Armano, E Balaguer, et al. „The LTP experiment on the LISA Pathfinder mission“. In: *Classical and Quantum Gravity* 22.10 (2005), S125 (cit. on p. 5).
- [Arm+16] Michele Armano, Heather Audley, Gerard Auger, et al. „Sub-femto-g free fall for space-based gravitational wave observatories: LISA pathfinder results“. In: *Physical Review Letters* 116.23 (2016), p. 231101 (cit. on pp. 4, 117).
- [Arm+18] M Armano, H Audley, J Baird, et al. „Beyond the Required LISA Free-Fall Performance: New LISA Pathfinder Results down to  $20 \mu \text{ Hz}$ “. In: *Physical Review Letters* 120.6 (2018), p. 061101 (cit. on pp. 4, 112, 117).
- [Bar15] Simon Barke. „Inter-Spacecraft Frequency Distribution“. PhD thesis. Quest-Leibniz-Forschungsschule der Gottfried Wilhelm Leibniz Universität Hannover, 2015 (cit. on p. 40).



- [Bis15] Lea Bischof. „Aufbau und Charakterisierung der Laservorbereitung für das 3-Backlink-Experiment“. Bachelor thesis. Albert Einstein Institute Max Planck Institute for Gravitational Physics Leibniz Universität Hannover, Institute for Gravitational Physics, 2015 (cit. on pp. 73, 74, 76).
- [Bis18] Lea Bischof. „An optical phase reference for LISA: comparison of different solutions with picometer sensitivity“. MA thesis. Albert Einstein Institute, Max Planck Institute for Gravitational Physics Leibniz Universität Hannover, Institute for Gravitational Physics, 2018 (cit. on pp. 73, 95, 99, 100, 108–110).
- [Bru+17] Christina Brugger, Bernhard Broll, Ewan Fitzsimons, et al. „An experiment to test in-field pointing for Elisa“. In: *International Conference on Space Optics ICSSO 2014*. Vol. 10563. International Society for Optics and Photonics. 2017, p. 105634D (cit. on pp. 4, 23).
- [BW99] Barry C Barish and Rainer Weiss. „LIGO and the detection of gravitational waves“. In: *Physics Today* 52 (1999), p. 44 (cit. on p. 2).
- [Car+12] L Carbone, S M Aston, R M Cutler, et al. „Sensors and actuators for the Advanced LIGO mirror suspensions“. In: *Classical and Quantum Gravity* 29.11 (2012), p. 115005 (cit. on p. 133).
- [CF88] Tony F. Chan and David E. Foulser. „Effectively Well-Conditioned Linear Systems“. In: *SIAM Journal on Scientific and Statistical Computing* 9.6 (1988), pp. 963–969. eprint: <https://doi.org/10.1137/0909067> (cit. on p. 63).
- [Che+05] JL Chen, CR Wilson, JS Famiglietti, and M Rodell. „Spatial sensitivity of the Gravity Recovery and Climate Experiment (GRACE) time-variable gravity observations“. In: *Journal of Geophysical Research: Solid Earth* 110.B8 (2005) (cit. on p. 5).
- [Che+07] JL Chen, CR Wilson, BD Tapley, and S Grand. „GRACE detects coseismic and postseismic deformation from the Sumatra-Andaman earthquake“. In: *Geophysical Research Letters* 34.13 (2007) (cit. on p. 5).
- [Chw+16] M Chwalla, K Danzmann, G Fernández Barranco, et al. „Design and construction of an optical test bed for LISA imaging systems and tilt-to-length coupling“. In: *Classical and Quantum Gravity* 33.24 (2016), p. 245015 (cit. on p. 16).
- [Coh13] Coherent. *Ultra-Narrow Linewidth CW DPSS Laser System Data Sheet*. MC-015-13-1M0113. Coherent. 2013 (cit. on p. 197).
- [Dah+12] K Dahl, G Heinzl, B Willke, et al. „Suspension platform interferometer for the AEI 10 m prototype: concept, design and optical layout“. In: *Classical and Quantum Gravity* 29.9 (2012), p. 095024 (cit. on p. 115).



- [Dan+17] Karsten Danzmann et al. „Laser interferometer space antenna“. In: *arXiv preprint arXiv:1702.00786* (2017) (cit. on pp. 2–4, 22).
- [Deh+12] Marina Dehne, Michael Tröbs, Gerhard Heinzl, and Karsten Danzmann. „Verification of polarising optics for the LISA optical bench“. In: *Opt. Express* 20.25 (2012), pp. 27273–27287 (cit. on pp. 52, 65, 117, 140–142, 193, 199).
- [Deh12] Marina Dehne. „Construction and noise behaviour of ultra-stable optical systems for space interferometers“. PhD thesis. Fakultät für Mathematik und Physik der Gottfried Wilhelm Leibniz Universität Hannover, 2012 (cit. on pp. 112, 117, 199).
- [Die+09] Christian Diekmann, Frank Steier, Benjamin Sheard, Gerhard Heinzl, and Karsten Danzmann. „Analog phase lock between two lasers at LISA power levels“. In: *Journal of Physics: Conference Series*. Vol. 154. 1. IOP Publishing, 2009, p. 012020 (cit. on pp. 75, 86).
- [Die13] Christian Diekmann. „Development of core elements for the LISA optical bench - Electro-optical measurement systems and test devices“. PhD thesis. Fakultät für Mathematik und Physik der Gottfried Wilhelm Leibniz Universität Hannover, 2013 (cit. on pp. 38, 52, 112).
- [Dou+17a] Karim Douch, Hu Wu, Jürgen Müller, and Gerhard Heinzl. „Mapping the time-variable gravity field with satellite gravity gradiometry. In Satellite Geodesy for Climate Studies“. In: *IAG Workshop, Bonn, Germany*. 2017 (cit. on pp. 7, 118).
- [Dou+17b] Karim Douch, Jürgen Müller, Gerhard Heinzl, and Hu Wu. „Recovering the time-variable gravitational field using satellite gradiometry: requirements and gradiometer concept“. In: *EGU General Assembly Conference Abstracts*. Vol. 19. 2017, p. 14875 (cit. on pp. 7, 118).
- [Dou+17c] Karim Douch, Hu Wu, Christian Schubert, Jürgen Müller, and Franck Pereira dos Santos. „Simulation-based evaluation of a cold atom interferometry gradiometer concept for gravity field recovery“. In: *Advances in Space Research* (2017) (cit. on pp. 7, 118).
- [DR03] Karsten Danzmann and Albrecht Rüdiger. „LISA technology—concept, status, prospects“. In: *Classical and Quantum Gravity* 20.10 (2003), S1 (cit. on p. 3).
- [Dri+03] MR Drinkwater, R Floberghagen, R Haagmans, D Muzi, and A Popescu. „GOCE: ESAs first Earth Explorer Core mission“. In: *Earth gravity field from space—From sensors to earth sciences*. Springer, 2003, pp. 419–432 (cit. on p. 6).

- [Dri+06] Mark R Drinkwater, R Haagmans, D Muzi, et al. „The GOCE gravity mission: ESA’s first core Earth explorer“. In: *Proceedings of the 3rd international GOCE user workshop*. European Space Agency Noordwijk, The Netherlands. 2006, pp. 6–8 (cit. on pp. 6, 115).
- [DV+09] Glenn De Vine, David S Rabeling, Bram JJ Slagmolen, et al. „Picometer level displacement metrology with digitally enhanced heterodyne interferometry“. In: *Optics express* 17.2 (2009), pp. 828–837 (cit. on pp. 115, 130).
- [Ein16] Albert Einstein. „Die grundlage der allgemeinen relativitätstheorie“. In: *Annalen der Physik* 354.7 (1916), pp. 769–822 (cit. on pp. 1, 3).
- [ESA18] European Space Agency ESA. *Official Website*. 2018. URL: <http://www.esa.int> (visited on Mar. 24, 2018) (cit. on pp. 5, 116).
- [Fal+09] Konstantinos Falaggis, David P Towers, and Catherine E Towers. „Phase measurement through sinusoidal excitation with application to multi-wavelength interferometry“. In: *Journal of Optics A: Pure and Applied Optics* 11.5 (2009), p. 054008 (cit. on p. 118).
- [Fib] Fibercore. *Zing Polarizing Fiber*. URL: <https://www.fibercore.com/product/zing-polarizing-fiber> (visited on Mar. 8, 2018) (cit. on pp. 92, 93, 215).
- [Fit+13] Ewan D Fitzsimons, Johanna Bogenstahl, James Hough, et al. „Precision absolute positional measurement of laser beams“. In: *Applied optics* 52.12 (2013), pp. 2527–2530 (cit. on pp. 112, 214).
- [Fle+17] Roland Fleddermann, Christian Diekmann, Frank Steier, et al. „Sub-pm/ $\sqrt{\text{Hz}}$  non-reciprocal noise in the LISA backlink fiber“. In: *Classical and Quantum Gravity* (2017) (cit. on pp. 19, 24–26, 36, 52).
- [Fle12] Roland Fleddermann. „Interferometry for a space-based gravitational wave observatory Reciprocity of an optical fiber“. PhD thesis. Fakultät für Mathematik und Physik der Gottfried Wilhelm Leibniz Universität Hannover, 2012 (cit. on pp. 26, 47, 52, 112, 193, 213).
- [Fol01] WM Folkner. „LISA orbit selection and stability“. In: *Classical and Quantum Gravity* 18.19 (2001), p. 4053 (cit. on p. 4).
- [GD08] Peter J de Groot and Leslie L Deck. „New algorithms and error analysis for sinusoidal phase shifting interferometry“. In: *Interferometry XIV: Techniques and Analysis*. Vol. 7063. International Society for Optics and Photonics. 2008, 70630K (cit. on p. 118).

- [Ger+15] Oliver Gerberding, Christian Diekmann, Joachim Kullmann, et al. „Readout for intersatellite laser interferometry: Measuring low frequency phase fluctuations of high-frequency signals with microradian precision“. In: *Review of Scientific Instruments* 86.7 (2015), p. 074501 (cit. on pp. 75, 83, 86, 191, 193).
- [Ger+16] Oliver Gerberding, Katharina-Sophie Isleif, Moritz Mehmet, Karsten Danzmann, and Gerhard Heinzl. „Laser frequency stabilisation via quasi-monolithic, unequal arm-length Mach-Zehnder interferometer with balanced DC readout“. In: *arXiv preprint arXiv:1610.09684* (2016) (cit. on pp. 180, 185, 195, 216).
- [Ger14] Oliver Gerberding. „Phase readout for satellite interferometry“. PhD thesis. Von der Fakultät für Mathematik und Physik der Gottfried Wilhelm Leibniz Universität Hannover, 2014 (cit. on pp. 10, 12, 15, 112, 132).
- [Ger15] Oliver Gerberding. „Deep frequency modulation interferometry“. In: *Optics Express* 23.11 (2015), pp. 14753–14762 (cit. on pp. 115, 119, 121, 124, 188, 189, 216).
- [Gro09] Peter de Groot. „Design of error-compensating algorithms for sinusoidal phase shifting interferometry“. In: *Applied optics* 48.35 (2009), pp. 6788–6796 (cit. on p. 118).
- [Han+04] Shin-Chan Han, Christopher Jekeli, and CK Shum. „Time-variable aliasing effects of ocean tides, atmosphere, and continental water mass on monthly mean GRACE gravity field“. In: *Journal of Geophysical Research: Solid Earth* 109.B4 (2004) (cit. on p. 5).
- [Haw+01] CJ Hawthorn, KP Weber, and RE Scholten. „Littrow configuration tunable external cavity diode laser with fixed direction output beam“. In: *Review of scientific instruments* 72.12 (2001), pp. 4477–4479 (cit. on p. 162).
- [Hei+04] Gerhard Heinzl, Vinzenz Wand, Antonio Garcia, et al. „The LTP interferometer and phasemeter“. In: *Classical and Quantum Gravity* 21.5 (2004), S581 (cit. on pp. 4, 133).
- [Hei+10] Gerhard Heinzl, Felipe Guzmán Cervantes, Antonio F Garcia Marin, et al. „Deep phase modulation interferometry“. In: *Optics express* 18.18 (2010), pp. 19076–19086 (cit. on pp. 115, 119, 121, 123, 124, 131, 169).
- [Hen13] Jan-Simon Hennig. „Mitigation of Stray Light Effects in the LISA Backlink“. MA thesis. Leibniz Universität Hannover, Albert-Einstein-Institut Hannover, Max-Planck-Institut für Gravitationsphysik, 2013 (cit. on p. 25).
- [Hob+10] G Hobbs, A Archibald, Zaven Arzoumanian, et al. „The international pulsar timing array project: using pulsars as a gravitational wave detector“. In: *Classical and Quantum Gravity* 27.8 (2010), p. 084013 (cit. on p. 3).

- [Hof74] Karl Hoffmann. *Applying the wheatstone bridge circuit*. HBM, 1974 (cit. on p. 82).
- [Isl+14] Katharina-S Isleif, Oliver Gerberding, Sina Köhlenbeck, et al. „Highspeed multiplexed heterodyne interferometry“. In: *Optics express* 22.20 (2014), pp. 24689–24696 (cit. on pp. 115, 130, 133).
- [Isl+16a] Katharina-Sophie Isleif, Oliver Gerberding, Moritz Mehmet, et al. „Comparing interferometry techniques for multi-degree of freedom test mass readout“. In: *Journal of Physics: Conference Series* 716.1 (2016), p. 012008 (cit. on pp. 132–134).
- [Isl+16b] Katharina-Sophie Isleif, Oliver Gerberding, Thomas S. Schwarze, et al. „Experimental demonstration of deep frequency modulation interferometry“. In: *Opt. Express* 24.2 (2016), pp. 1676–1684 (cit. on pp. 115, 121, 185, 216).
- [Isl+17] K-S Isleif, O Gerberding, D Penkert, et al. „Suppressing ghost beams: Backlink options for LISA“. In: *Journal of Physics: Conference Series* 840.1 (2017), p. 012016 (cit. on pp. 24, 213).
- [Isl+18] Katharina-Sophie Isleif, Lea Bischof, Stefan Ast, et al. „Towards the LISA Backlink: Experiment design for comparing optical phase reference distribution systems“. In: *Classical and Quantum Gravity* 35.8 (2018), p. 085009 (cit. on pp. 45, 73, 84, 95, 98, 100, 103, 108, 214, 216).
- [Isl13] Katharina-Sophie Isleif. „Development and characterization of a SoC-based phase readout system for deep frequency modulation“. MA thesis. Albert Einstein Institute Max Planck Institute for Gravitational Physics Leibniz Universität Hannover, Institute for Gravitational Physics, 2013 (cit. on p. 130).
- [Jin+91] Wei Jin, Li Ming Zhang, Deepak Uttamchandani, and Brian Culshaw. „Modified J1 ... J4 method for linear readout of dynamic phase changes in a fiber-optic homodyne interferometer“. In: *Appl. Opt.* 30.31 (1991), pp. 4496–4499 (cit. on p. 119).
- [Kil+16] Christian J Killow, Ewan D Fitzsimons, Michael Perreur-Lloyd, et al. „Optical fiber couplers for precision spaceborne metrology“. In: *Applied optics* 55.10 (2016), pp. 2724–2731 (cit. on pp. 46, 199).
- [Kis+13] Thomas Kissinger, Thomas O H Charrett, and Ralph P Tatam. „Fibre segment interferometry using code-division multiplexed optical signal processing for strain sensing applications“. In: *Measurement Science and Technology* 24.9 (2013), p. 094011 (cit. on p. 136).

- [Kis+15] Thomas Kissinger, Thomas OH Charrett, and Ralph P Tatam. „Range-resolved interferometric signal processing using sinusoidal optical frequency modulation“. In: *Optics express* 23.7 (2015), pp. 9415–9431 (cit. on pp. 118, 124, 136, 188, 220).
- [Lig17] Orbits Lightwave. *Eternal™ SlowLight™ Lasers*. Orbits Lightwave. 2017 (cit. on p. 165).
- [Liv+13] Jeffrey C Livas, Petar Arsenovic, John A Crow, et al. „Telescopes for space-based gravitational wave missions“. In: *Optical Engineering* 52.9 (2013), p. 091811 (cit. on p. 23).
- [Liv+17] J Livas, S Sankar, G West, et al. „eLISA Telescope In-field Pointing and Scattered Light Study“. In: *Journal of Physics: Conference Series* 840.1 (2017), p. 012015 (cit. on pp. 4, 23).
- [Lon+13] Di Long, Bridget R Scanlon, Laurent Longuevergne, et al. „GRACE satellite monitoring of large depletion in water storage in response to the 2011 drought in Texas“. In: *Geophysical Research Letters* 40.13 (2013), pp. 3395–3401 (cit. on p. 5).
- [Mar63] Donald W Marquardt. „An algorithm for least-squares estimation of nonlinear parameters“. In: *Journal of the society for Industrial and Applied Mathematics* 11.2 (1963), pp. 431–441 (cit. on p. 124).
- [McN05] Paul W McNamara. „Weak-light phase locking for LISA“. In: *Classical and Quantum Gravity* 22.10 (2005), S243 (cit. on pp. 75, 86).
- [NASa] NASA. *Gravity Anomaly Maps and The Geoid*. URL: <https://earthobservatory.nasa.gov> (visited on Mar. 25, 2018) (cit. on p. 5).
- [NASb] NASA. *Orbiting Stars Flooding Space With Exotic Gravitational Waves*. URL: <https://www.nasa.gov> (visited on Mar. 25, 2018) (cit. on p. 3).
- [New14] Newport. *Model TLB-6800 Vortex Plus Laser System - User’s Manual*. 90059204. Rev. A. Newport Corporation, New Focus. 2014 (cit. on pp. 162, 165).
- [New17a] Newport. *Tunable Diode Lasers*. Newport Corporation, New Focus. 2017 (cit. on p. 163).
- [New17b] Newport. *Velocity 6700 Widely Tunable Lasers*. DS-041104. New Focus, Newport Corporation. 2017 (cit. on pp. 164, 165).
- [New17c] Newport. *Vortex Plus 6800 Precision Tunable Lasers*. DS-051202. New Focus, Newport Corporation. 2017 (cit. on pp. 164, 165).
- [NM65] John A Nelder and Roger Mead. „A simplex method for function minimization“. In: *The computer journal* 7.4 (1965), pp. 308–313 (cit. on p. 124).

- [Ott+12] Markus Otto, Gerhard Heinzel, and Karsten Danzmann. „TDI and clock noise removal for the split interferometry configuration of LISA“. In: *Classical and Quantum Gravity* 29.20 (2012), p. 205003 (cit. on p. 22).
- [Pen16] Daniel Penkert. „Hexagon - An optical three-signal testbed for the LISA metrology chain“. Diploma thesis. Albert Einstein Institute, Max Planck Institute for Gravitational Physics Leibniz Universität Hannover, Institute for Gravitational Physics, 2016 (cit. on pp. 110, 214).
- [Rob+13] DI Robertson, ED Fitzsimons, CJ Killow, et al. „Construction and testing of the optical bench for LISA Pathfinder“. In: *Classical and quantum gravity* 30.8 (2013), p. 085006 (cit. on p. 116).
- [Sal+09] M Sallusti, P Gath, D Weise, M Berger, and H R Schulte. „LISA system design highlights“. In: *Classical and Quantum Gravity* 26.9 (2009), p. 094015 (cit. on p. 21).
- [Sas+87] Osami Sasaki, Hirokazu Okazaki, and Makoto Sakai. „Sinusoidal phase modulating interferometer using the integrating-bucket method“. In: *Applied optics* 26.6 (1987), pp. 1089–1093 (cit. on p. 118).
- [SC93] VS Sudarshanam and Richard O Claus. „Generic J1...J4 method of optical phase detection: accuracy and range enhancement“. In: *Journal of Modern Optics* 40.3 (1993), pp. 483–492 (cit. on p. 119).
- [Sch+09] Thilo Schuldt, Martin Gohlke, Dennis Weise, et al. „Picometer and nanoradian optical heterodyne interferometry for translation and tilt metrology of the LISA gravitational reference sensor“. In: *Classical and Quantum Gravity* 26.8 (2009), p. 085008 (cit. on pp. 65, 180).
- [Sch+14a] Daniel Schütze, Gunnar Stede, Vitali Müller, et al. „Laser beam steering for GRACE Follow-On intersatellite interferometry“. In: *Optics express* 22.20 (2014), pp. 24117–24132 (cit. on pp. 4, 6).
- [Sch+14b] Daniel Schütze, Vitali Müller, and Gerhard Heinzel. „Precision absolute measurement and alignment of laser beam direction and position“. In: *Appl. Opt.* 53.28 (2014), pp. 6503–6507 (cit. on pp. 66, 112, 179, 214).
- [Sch+14c] Thomas S Schwarze, Oliver Gerberding, Felipe Guzmán Cervantes, Gerhard Heinzel, and Karsten Danzmann. „Advanced phasemeter for deep phase modulation interferometry“. In: *Optics express* 22.15 (2014), pp. 18214–18223 (cit. on pp. 115, 119, 131, 133, 168, 191).
- [Sch15] Dennis Schmelzer. „Thermally compensated fiber injectors for the three-backlink and hexagon experiments“. MA thesis. Albert Einstein Institute, Max Planck Institute for Gravitational Physics Leibniz Universität Hannover, Institute for Gravitational Physics, 2015 (cit. on pp. 46, 110, 214).

- [Sch17] Sönke Schuster. „Tilt-to-length coupling and diffraction aspects in satellite interferometry“. PhD thesis. QUEST-Leibniz-Forschungsschule der Gottfried Wilhelm Leibniz Universität Hannover, 2017 (cit. on pp. 13, 14, 16, 125, 155).
- [Sch18] Thomas S. Schwarze. „Phase extraction for laser interferometry in space: read-out schemes and optical testing“. PhD thesis. QUEST-Leibniz-Forschungsschule der Gottfried Wilhelm Leibniz Universität Hannover, 2018 (cit. on pp. 75, 110, 112, 168, 172).
- [Sch99] Bernard F Schutz. „Gravitational wave astronomy“. In: *Classical and Quantum Gravity* 16.12A (1999), A131 (cit. on p. 2).
- [See03] Günter Seeber. *Satellite geodesy: foundations, methods, and applications*. Walter de gruyter, 2003 (cit. on p. 5).
- [Ses16] Alberto Sesana. „Prospects for Multiband Gravitational-Wave Astronomy after GW150914“. In: *Phys. Rev. Lett.* 116 (23 2016), p. 231102 (cit. on p. 3).
- [SH68] John S Steinhart and Stanley R Hart. „Calibration curves for thermistors“. In: *Deep Sea Research and Oceanographic Abstracts*. Vol. 15. 4. Elsevier. 1968, pp. 497–503 (cit. on p. 81).
- [Sha07] Daniel A Shaddock. „Digitally enhanced heterodyne interferometry“. In: *Optics letters* 32.22 (2007), pp. 3355–3357 (cit. on pp. 115, 124, 130).
- [She+12] B. S. Sheard, G. Heinzel, K. Danzmann, et al. „Intersatellite laser ranging instrument for the GRACE follow-on mission“. In: *Journal of Geodesy* 86.12 (2012), pp. 1083–1095 (cit. on pp. 6, 115).
- [Smi+09] DT Smith, JR Pratt, and LP Howard. „A fiber-optic interferometer with subpicometer resolution for dc and low-frequency displacement measurement“. In: *Review of Scientific Instruments* 80.3 (2009), p. 035105 (cit. on p. 133).
- [SO86] Osami Sasaki and Hirokazu Okazaki. „Sinusoidal phase modulating interferometry for surface profile measurement“. In: *Applied optics* 25.18 (1986), pp. 3137–3140 (cit. on p. 118).
- [Som12] Kentaro Somiya. „Detector configuration of KAGRA—the Japanese cryogenic gravitational-wave detector“. In: *Classical and Quantum Gravity* 29.12 (2012), p. 124007 (cit. on p. 2).
- [SS09] Bangalore Suryanarayana Sathyaprakash and Bernard F Schutz. „Physics, astrophysics and cosmology with gravitational waves“. In: *Living Reviews in Relativity* 12.1 (2009), p. 2 (cit. on p. 2).
- [SS89] VS Sudarshanam and K Srinivasan. „Linear readout of dynamic phase change in a fiber-optic homodyne interferometer“. In: *Optics letters* 14.2 (1989), pp. 140–142 (cit. on p. 119).

- [Ste+09] F Steier, R Fleddermann, J Bogenstahl, et al. „Construction of the LISA back-side fibre link interferometer prototype“. In: *Classical and Quantum Gravity* 26.17 (2009), p. 175016 (cit. on p. 24).
- [Sut+12] Andrew J Sutton, Oliver Gerberding, Gerhard Heinzl, and Daniel A Shaddock. „Digitally enhanced homodyne interferometry“. In: *Optics express* 20.20 (2012), pp. 22195–22207 (cit. on pp. 115, 130, 133).
- [Tap+04] Byron D Tapley, S Bettadpur, M Watkins, and Ch Reigber. „The gravity recovery and climate experiment: Mission overview and early results“. In: *Geophysical Research Letters* 31.9 (2004) (cit. on p. 6).
- [TD05] Massimo Tinto and Sanjeev V. Dhurandhar. „Time-delay interferometry“. In: 8 (2005), <http://www.livingreviews.org/lrr-2005-4> cited on 09.09.2005 (cit. on p. 22).
- [Tho] Thorlabs. *Hollow Core Photonic Crystal Fibers*. URL: [https://www.thorlabs.com/newgrouppage9.cfm?objectgroup\\_id=912r](https://www.thorlabs.com/newgrouppage9.cfm?objectgroup_id=912r) (visited on Mar. 20, 2018) (cit. on p. 215).
- [Tou+99] Pierre Touboul, Bernard Foulon, and Eric Willemenot. „Electrostatic space accelerometers for present and future missions“. In: *Acta Astronautica* 45.10 (1999), pp. 605–617 (cit. on p. 115).
- [Trö+12] M Tröbs, L d’Arcio, S Barke, et al. „Testing the LISA optical bench“. In: *LISA Symposium Paris*. 2012 (cit. on pp. 50, 51).
- [Unn13] CS Unnikrishnan. „IndIGO and LIGO-India: Scope and plans for gravitational wave research and precision metrology in India“. In: *International Journal of Modern Physics D* 22.01 (2013), p. 1341010 (cit. on p. 2).
- [Vor17] Christoph Vorndamme. „Development and characterization of a SoC-based phase readout system for deep frequency modulation“. MA thesis. Albert Einstein Institute Max Planck Institute for Gravitational Physics Leibniz Universität Hannover, Institute for Gravitational Physics, 2017 (cit. on pp. 119, 124, 168, 217, 218).
- [VW13] I Velicogna and J Wahr. „Time-variable gravity observations of ice sheet mass balance: Precision and limitations of the GRACE satellite data“. In: *Geophysical Research Letters* 40.12 (2013), pp. 3055–3063 (cit. on p. 5).
- [Wan+12a] Wenbo Wang, Arkady Major, and J. Paliwal. „Grating Stabilized External Cavity Diode Lasers for Raman Spectroscopy – A Review“. In: 47 (Feb. 2012) (cit. on p. 162).



- [Wan+12b] Gudrun Wanner, Gerhard Heinzel, Evgenia Kochkina, et al. „Methods for simulating the readout of lengths and angles in laser interferometers with Gaussian beams“. In: *Optics Communications* 285.24 (2012), pp. 4831–4839 (cit. on pp. 14–16).
- [Wan10] Gudrun Wanner. „Complex optical systems in space: numerical modelling of the heterodyne interferometry of LISA Pathfinder and LISA“. PhD thesis. Der Fakultät für Mathematik und Physik der Gottfried Wilhelm Leibniz Universität Hannover, 2010 (cit. on p. 155).
- [WH14] Gudrun Wanner and Gerhard Heinzel. „Analytical description of interference between two misaligned and mismatched complete Gaussian beams“. In: *Applied optics* 53.14 (2014), pp. 3043–3048 (cit. on p. 33).
- [Wik16] Wikipedia. *Unit Eotvos*. 2016. URL: [https://en.wikipedia.org/wiki/Eotvos\\_\(unit\)](https://en.wikipedia.org/wiki/Eotvos_(unit)) (visited on Jan. 17, 2018) (cit. on p. 7).
- [Wil+02] Benno Willke, Peter Aufmuth, Carsten Aulbert, et al. „The GEO 600 gravitational wave detector“. In: *Classical and Quantum Gravity* 19.7 (2002), p. 1377 (cit. on p. 2).
- [Win17] Michael Winter. „Performance of optical components for the LISA backlink“. MA thesis. Leibniz Universität Hannover, Albert-Einstein-Institut Hannover, Max-Planck-Institut für Gravitationsphysik, 2017 (cit. on pp. 39, 54).
- [Wu03] Chien-ming Wu. „Periodic nonlinearity resulting from ghost reflections in heterodyne interferometry“. In: *Optics communications* 215.1-3 (2003), pp. 17–23 (cit. on p. 26).
- [Xia+10] Yan Xia, GuangYu Li, Gerhard Heinzel, Albrecht Rüdiger, and YongJie Luo. „Orbit design for the Laser Interferometer Space Antenna (LISA)“. In: *Science China Physics, Mechanics and Astronomy* 53.1 (2010), pp. 179–186 (cit. on pp. 4, 20).
- [Zhe05] Jesse Zheng. *Optical frequency-modulated continuous-wave (FMCW) interferometry*. Vol. 107. Springer Science & Business Media, 2005 (cit. on p. 119).



# THREE-BACKLINK PARAMETERS

The propagation directions and origins are simulated with IfoCAD for beams that are relevant for construction of the TBI. These are shown in Table A.1. A complete list of all optical components of the TBI is given in Table A.2 and A.3.

Tab. A.1.: Beam parameter for the alignment process of the TBI plan.

step	beam	origin[cm]			direction			intersection[cm]		
		x	y	z	x	y	z	x	y	z
4	a0	24	4.5	1.5	1	0	0	27	4.5	1.5
	a1	22.3033	18.7966	1.5	0	1	0	22.3033	27	1.5
5	c0	25.5	19.5	1.5	1	0	0	27	19.5	1.5
	c1	25.2816	9.02845	1.5	-1	0	0	0	9.02845	1.5
6	d1	22.3033	20.809	1.5	-1	0	0	0	20.809	1.5
8	h7	18.8508	25.5557	1.5	0	1	0	18.8508	27	1.5
	h8	22.0692	24.7842	1.5	0	1	0	22.0692	27	1.5
	i1	22.0816	24.7966	1.5	0	1	0	22.0816	27	1.5
	i2	18.8632	25.5681	1.5	0	1	0	18.8632	27	1.5
9	l0	14.8157	12.2534	1.5	0	-1	0	14.8157	0	1.5
10	m6	20.7649	2.45945	1.5	0	-1	0	20.7649	0	1.5
	m7	17.5465	1.6879	1.5	0	-1	0	17.5465	0	1.5
	o0	17.5341	1.70033	1.5	0	-1	0	17.5341	0	1.5
	o1	20.7525	2.47188	1.5	0	-1	0	20.7525	0	1.5
11	s0	9.09165	9.5816	1.5	0	1	0	9.09165	27	1.5
12	t10	9.29761	21.3622	1.5	0	1	0	9.29761	27	1.5
	t11	6.07921	20.5906	1.5	0	1	0	6.07921	27	1.5
	w0	6.09165	20.5782	1.5	0	1	0	6.09165	27	1.5
	w1	9.31005	21.3497	1.5	0	1	0	9.31005	27	1.5
13	x2	4.33171	24.04	1.5	0	1	0	4.33171	27	1.5
14	B1	4.35658	4.25586	1.5	0	-1	0	4.35658	0	1.5
	B2	1.23818	5.02741	1.5	0	-1	0	1.23818	0	1.5
	B3	4.33171	24.04	1.5	0	1	0	4.33171	27	1.5

Tab. A.2.: Component positions of the left TBI bench.

name	position(x,y,z) [mm]			direction(nv,nvv,nvh)			refl.(prim,sec)		size [mm]		d [mm]
gr-l	135	135	-18						270	270	36
fios1-l	240	30	15	0	1	0	2e-05	0	16	30	30
fios2-l	115.625	65.1525	15	-1e-15	1	0	2e-05	0	16	30	30
fios3-l	15.385	195.284	15	-2e-16	-1	0	2e-05	0	16	30	30
fios4-l	255	210	15	0	-1	0	2e-05	0	16	30	30
m1-l	222.816	67.7155	10	0.707	0.707	0	0.999	0.001	15	20	7
m2-l	148.157	22.5348	10	0.707	0.707	0	0.999	0.001	15	20	7
m3-l	207.525	24.7188	10	-0.707	-0.707	0	0.999	0.001	15	20	7
m4-l	73.157	47.9658	10	-0.707	0.707	0	0.999	0.001	15	20	7
m5-l	12.2575	50.1498	10	0.707	-0.707	0	0.999	0.001	15	20	7
m6-l	125.441	250.15	10	0.707	-0.707	0	0.999	0.001	15	20	7
m7-l	60.9165	205.782	10	0.707	0.707	0	0.999	0.001	15	20	7
m8-l	220.816	247.966	10	-0.707	0.707	0	0.999	0.001	15	20	7
att1-l	240	45	10	0.707	-0.707	0	0.95	0.001	20	20	7
att2-l	255	195	10	0.707	0.707	0	0.95	0.001	20	20	7
bs1-l	173.157	207.966	10	0.707	-0.707	0	0.5	0.001	15	20	7
bs2-l	173.157	167.966	10	-0.707	0.707	0	0.5	0.001	15	20	7
bs3-l	125.441	210.15	10	0.707	0.707	0	0.5	0.001	15	20	7
bs4-l	175.341	130.25	10	-0.707	0.707	0	0.5	0.001	15	20	7
bs5-l	150.341	130.25	10	0.707	0.707	0	0.5	0.001	15	20	7
bs6-l	177.525	24.7188	10	0.707	0.707	0	0.5	0.001	20	20	7
bs7-l	73.157	167.966	10	0.707	-0.707	0	0.5	0.001	15	20	7
bs9-l	190.816	90.2845	10	0.707	0.707	0	0.5	0.001	15	20	7
bs10-l	93.1005	88.1005	10	0.707	-0.707	0	0.5	0.001	15	20	7
bs11-l	90.9165	205.782	10	-0.707	-0.707	0	0.5	0.001	20	20	7
bs12-l	190.816	247.966	10	0.707	-0.707	0	0.5	0.001	20	20	7
bs8-l	41.2575	50.1498	10	-0.707	0.707	0	0.5	0.001	20	20	7
pbs1-l	237.816	67.7155	10	-0.707	-0.707	0	0.999	0.001	20	20	7
pbs2-l	115.625	128.066	10	0.707	-0.707	0	0.999	0.001	20	20	7
pbs3-l	15.385	90.2845	10	0.707	0.707	0	0.999	0.001	20	20	7
pbs4-l	252.816	90.2845	10	-0.707	0.707	0	0.999	0.001	20	20	7
pbs5-l	43.4414	170.15	10	0.707	0.707	0	0.5	0.001	20	20	7
pbs6-l	223.157	207.966	10	-0.707	-0.707	0	0.999	0.001	20	20	7
act-l	43.4414	270.4	15	0.707	-0.707	0	1	0	33	20	48
hwp1-l	41.2575	147.434	15	-3e-16	1	0	0	0	17	17	10.25
qwp2-l	43.4414	230.15	15	2e-16	-1	0	0	0	17	17	10.25
hwp3-l	223.157	177.716	15	-2e-16	-1	0	0	0	17	17	10.25
l1-l	43.4414	-42.5657	15	-3e-08	1	0	0	0	12.7	12.7	3.9
l2-l	12.2575	0.14978	15	-2e-16	1	0	0	0	12.7	12.7	3.9
l3-l	175.341	-37.9967	15	-8e-16	1	0	0	0	12.7	12.7	3.9
l4-l	207.525	-30.2812	15	-3e-08	1	0	0	0	12.7	12.7	3.9
l5-l	93.1005	298.497	15	3e-08	-1	0	0	0	12.7	12.7	3.9
l6-l	60.9165	310.782	15	0	-1	0	0	0	12.7	12.7	3.9
l7-l	188.632	300.681	15	3e-08	-1	0	0	0	12.7	12.7	3.9
l8-l	220.816	282.966	15	0	-1	0	0	0	12.7	12.7	3.9
fara-l	222.816	122.716	10	-0.035	-0.999	0	0	0	3.3	40	20

Tab. A.3.: Component positions of the right TBI bench.

name	position(x,y,z) [mm]			direction(nv,nvv,nvh)			refl.(prim,sec)		size [mm]		d [mm]
gr-r	465	135	-18						270	270	36
fios1-r	360	30	15	0	1	0	2e-05	0	16	30	30
fios2-r	484.375	65.1525	15	1e-15	1	0	2e-05	0	16	30	30
fios3-r	584.615	195.284	15	2e-16	-1	0	2e-05	0	16	30	30
fios4-r	345	210	15	0	-1	0	2e-05	0	16	30	30
m1-r	377.184	67.7155	10	-0.707	0.707	0	0.999	0.001	15	20	7
m2-r	451.843	22.5348	10	-0.707	0.707	0	0.999	0.001	15	20	7
m3-r	392.475	24.7188	10	0.707	-0.707	0	0.999	0.001	15	20	7
m4-r	526.843	47.9658	10	0.707	0.707	0	0.999	0.001	15	20	7
m5-r	587.743	50.1498	10	-0.707	-0.707	0	0.999	0.001	15	20	7
m6-r	474.559	250.15	10	-0.707	-0.707	0	0.999	0.001	15	20	7
m7-r	539.083	205.782	10	-0.707	0.707	0	0.999	0.001	15	20	7
m8-r	379.184	247.966	10	0.707	0.707	0	0.999	0.001	15	20	7
att1-r	360	45	10	-0.707	-0.707	0	0.95	0.001	20	20	7
att2-r	345	195	10	-0.707	0.707	0	0.95	0.001	20	20	7
bs1-r	426.843	207.966	10	-0.707	-0.707	0	0.5	0.001	15	20	7
bs2-r	426.843	167.966	10	0.707	0.707	0	0.5	0.001	15	20	7
bs3-r	474.559	210.15	10	-0.707	0.707	0	0.5	0.001	15	20	7
bs4-r	424.659	130.25	10	0.707	0.707	0	0.5	0.001	15	20	7
bs5-r	449.659	130.25	10	-0.707	0.707	0	0.5	0.001	15	20	7
bs6-r	422.475	24.7188	10	-0.707	0.707	0	0.5	0.001	20	20	7
bs7-r	526.843	167.966	10	-0.707	-0.707	0	0.5	0.001	15	20	7
bs9-r	409.184	90.2845	10	-0.707	0.707	0	0.5	0.001	15	20	7
bs10-r	506.899	88.1005	10	-0.707	-0.707	0	0.5	0.001	15	20	7
bs11-r	509.083	205.782	10	0.707	-0.707	0	0.5	0.001	20	20	7
bs12-r	409.184	247.966	10	-0.707	-0.707	0	0.5	0.001	20	20	7
bs8-r	558.743	50.1498	10	0.707	0.707	0	0.5	0.001	20	20	7
pbs1-r	362.184	67.7155	10	0.707	-0.707	0	0.999	0.001	20	20	7
pbs2-r	484.375	128.066	10	-0.707	-0.707	0	0.999	0.001	20	20	7
pbs3-r	584.615	90.2845	10	-0.707	0.707	0	0.999	0.001	20	20	7
pbs4-r	347.184	90.2845	10	0.707	0.707	0	0.999	0.001	20	20	7
pbs5-r	556.559	170.15	10	-0.707	0.707	0	0.5	0.001	20	20	7
pbs6-r	376.843	207.966	10	0.707	-0.707	0	0.999	0.001	20	20	7
act-r	556.559	270.4	15	-0.707	-0.707	0	1	0	33	20	48
hwp1-r	558.743	147.434	15	3e-16	1	0	0	0	17	17	10.25
qwp2-r	556.559	230.15	15	-2e-16	-1	0	0	0	17	17	10.25
hwp3-r	376.843	177.716	15	2e-16	-1	0	0	0	17	17	10.25
l1-r	556.559	-42.5657	15	3e-08	1	0	0	0	12.7	12.7	3.9
l2-r	587.743	0.14978	15	2e-16	1	0	0	0	12.7	12.7	3.9
l3-r	424.659	-37.9967	15	8e-16	1	0	0	0	12.7	12.7	3.9
l4-r	392.475	-30.2812	15	3e-08	1	0	0	0	12.7	12.7	3.9
l5-r	506.899	298.497	15	-3e-08	-1	0	0	0	12.7	12.7	3.9
l6-r	539.083	310.782	15	0	-1	0	0	0	12.7	12.7	3.9
l7-r	411.368	300.681	15	-3e-08	-1	0	0	0	12.7	12.7	3.9
l8-r	379.184	282.966	15	0	-1	0	0	0	12.7	12.7	3.9
fara-r	377.184	122.716	10	0.035	-0.999	0	0	0	3.3	40	20



# DEEP FREQUENCY MODULATION

## B.1 Analytic calculation of interferometer signals

We will start the calculation for the following two electric fields of the measurement and the reference beam:

$$E_m = \frac{1}{2} E_{in} \sin \left[ \omega_0 t + \varphi + \frac{\Delta f}{f_{mod}} \sin(2\pi f_{mod} t + \psi) \right], \quad (\text{B.1})$$

$$E_r = \frac{1}{2} E_{in} \sin \left[ \omega_0(t - \tau) + \frac{\Delta f}{f_{mod}} \sin(2\pi f_{mod}(t - \tau) + \psi) \right]. \quad (\text{B.2})$$

The output power on a square-law detector can therefore be written as:

$$P_{out} \propto (E_m + E_r)^2 \quad (\text{B.3})$$

$$= \left( \frac{1}{2} E_{in} \sin \left[ \omega_0 t + \varphi + \frac{\Delta f}{f_{mod}} \sin(2\pi f_{mod} t + \psi) \right] + \frac{1}{2} E_{in} \sin \left[ \omega_0(t - \tau) + \frac{\Delta f}{f_{mod}} \sin(2\pi f_{mod}(t - \tau) + \psi) \right] \right)^2 \quad (\text{B.4})$$

$$= \frac{1}{4} E_{in}^2 \sin^2 \left[ \omega_0 t + \varphi + \frac{\Delta f}{f_{mod}} \sin(2\pi f_{mod} t + \psi) \right] + \frac{1}{4} E_{in}^2 \sin^2 \left[ \omega_0(t - \tau) + \frac{\Delta f}{f_{mod}} \sin(2\pi f_{mod}(t - \tau) + \psi) \right] + 2 \cdot \frac{1}{4} E_{in}^2 \sin \left[ \omega_0 t + \varphi + \frac{\Delta f}{f_{mod}} \sin(2\pi f_{mod} t + \psi) \right] \cdot \sin \left[ \omega_0(t - \tau) + \frac{\Delta f}{f_{mod}} \sin(2\pi f_{mod}(t - \tau) + \psi) \right] \quad (\text{B.5})$$

For the first two lines of the last equation we can apply the trigonometric identity  $\sin^2 x = \frac{1}{2}(1 - \cos 2x)$  and the last expression in Equation (B.5) we can expand via  $\sin x \sin y = \frac{1}{2}(\cos[x - y] - \cos[x + y])$

$$\begin{aligned}
P_{\text{out}} &= \frac{1}{8}E_{\text{in}}^2 \left[ 1 - \cos \left( 2\omega_0 t + 2\varphi + 2\frac{\Delta f}{f_{\text{mod}}} \sin(2\pi f_{\text{mod}} t + \psi) \right) \right] + \\
&\frac{1}{8}E_{\text{in}}^2 \left[ 1 - \cos \left( 2\omega_0(t - \tau) + 2\frac{\Delta f}{f_{\text{mod}}} \sin(2\pi f_{\text{mod}}(t - \tau) + \psi) \right) \right] \\
&\frac{1}{4}E_{\text{in}}^2 \\
&\left[ \cos \left( \omega_0 \tau + \varphi + \frac{\Delta f}{f_{\text{mod}}} \sin(2\pi f_{\text{mod}} t + \psi) - \frac{\Delta f}{f_{\text{mod}}} \sin(2\pi f_{\text{mod}}[t - \tau] + \psi) \right) - \right. \\
&\left. \cos \left( 2\omega_0 t - \omega_0 \tau + \varphi + \frac{\Delta f}{f_{\text{mod}}} \sin(2\pi f_{\text{mod}} t + \psi) + \frac{\Delta f}{f_{\text{mod}}} \sin(2\pi f_{\text{mod}}[t - \tau] + \psi) \right) \right]
\end{aligned}$$

By neglecting all terms of the order of  $2\omega_0$  the last equation can be simplified to

$$\begin{aligned}
P_{\text{out}} &= \frac{1}{8}E_{\text{in}}^2 + \frac{1}{8}E_{\text{in}}^2 \\
&\frac{1}{4}E_{\text{in}}^2 \cos \left( \omega_0 \tau + \varphi + \frac{\Delta f}{f_{\text{mod}}} \sin(2\pi f_{\text{mod}} t + \psi) - \frac{\Delta f}{f_{\text{mod}}} \sin(2\pi f_{\text{mod}}[t - \tau] + \psi) \right) \\
&= \frac{1}{4}E_{\text{in}}^2 \left\{ 1 + \cos \left( \omega_0 \tau + \varphi + \frac{\Delta f}{f_{\text{mod}}} [\sin(2\pi f_{\text{mod}} t + \psi) - \sin(2\pi f_{\text{mod}}(t - \tau) + \psi)] \right) \right\}
\end{aligned}$$

Applying the trigonometric function  $\sin x - \sin y = 2 \cos(\frac{x+y}{2}) \sin(\frac{x-y}{2})$  we achieve the following expression:

$$P_{\text{out}} = \frac{1}{4}E_{\text{in}}^2 \left\{ 1 + \cos \left( \omega_0 \tau + \varphi + 2\frac{\Delta f}{f_{\text{mod}}} \cos[2\pi f_{\text{mod}} t - \pi f_{\text{mod}} \tau + \psi] \sin[\pi f_{\text{mod}} \tau] \right) \right\}$$

With the assumption that the delay is small and  $f_{\text{mod}}\tau \ll 1$ , which is true by using typical values like  $f_{\text{mod}} \approx 1$  kHz and  $\tau \approx 1$  ps, we can rewrite the equation in the first place by neglecting this term in the cosine, and secondly by approaching the sine via  $\sin[\pi f_{\text{mod}} \tau] \approx \pi f_{\text{mod}} \tau$ :

$$\begin{aligned}
P_{\text{out}} &= \frac{1}{4}E_{\text{in}}^2 \left\{ 1 + \cos \left( \varphi + 2\frac{\Delta f}{f_{\text{mod}}} \cos[2\pi f_{\text{mod}} t + \psi] \pi f_{\text{mod}} \tau \right) \right\} \\
&= \frac{1}{4}E_{\text{in}}^2 \{ 1 + \cos(\varphi + 2\pi \Delta f \tau \cos[2\pi f_{\text{mod}} t + \psi]) \} \tag{B.6}
\end{aligned}$$

$$= \frac{1}{2}P_{\text{in}} \{ 1 + \cos(\varphi + m_{\text{DFM}} \cos[2\pi f_{\text{mod}} t + \psi]) \} \tag{B.7}$$



## B.2 Data demodulation

The photodiode power output signal, given by Equation (B.7) can be expanded into its higher harmonics with the usage of Bessel function amplitudes:

$$\begin{aligned} P_{\text{out}} &= \frac{1}{2}P_{\text{in}} [1 + J_0(m) \cos(\varphi)] + \sum_{n=1}^N a_n(m, \varphi) \cos(n[\omega_{\text{mod}}t + \psi_{\text{mod}}]) \\ &= P_{\text{DC}}(\varphi) + P_{\text{AC}}(n, m, \varphi, \omega_{\text{mod}}, \psi_{\text{mod}}) \end{aligned}$$

with

$$\begin{aligned} a_n(m, \varphi) &= kJ_n(m) \cos(\varphi + n\frac{\pi}{2}), \\ P_{\text{DC}}(\varphi) &= \frac{1}{2}P_{\text{in}} [1 + J_0(m) \cos(\varphi)] \end{aligned}$$

where  $k$  is a common amplitude factor and  $J_n(m)$  are the well-known Bessel function amplitudes, shown in Fig. 6.4. The photodiode signal  $P_{\text{out}}$  can be converted into a voltage,  $v_{\text{out}} = v_{\text{DC}}(\varphi) + v_{\text{AC}}(n, m, \varphi, \omega_{\text{mod}}, \psi_{\text{mod}})$ , via a transimpedance amplifier, also consisting of a DC and an AC component. After digitization the signal is demodulated with sine and cosine tones at the relevant harmonics of the modulation frequency and low-pass filtered. This  $IQ$ -demodulation determines the complex amplitudes of the  $n$ -th harmonic in terms of quadrature,  $Q_n$ , and in-phase  $I_n$ :

$$\begin{aligned} Q_n &= \cos(n\omega_{\text{mod}}t) \cdot v_{\text{AC}} \\ &= \cos(n\omega_{\text{mod}}t) \cdot kJ_n(m) \cos\left(\varphi + n\frac{\pi}{2}\right) \cos(n[\omega_{\text{mod}}t + \psi_{\text{mod}}]) \\ &= kJ_n(m) \cos\left(\varphi + n\frac{\pi}{2}\right) \cdot \cos(n\omega_{\text{mod}}t) \cos(n\omega_{\text{mod}}t + n\psi_{\text{mod}}) \\ I_n &= \sin(n\omega_{\text{mod}}t) \cdot v_{\text{AC}} \\ &= \sin(n\omega_{\text{mod}}t) \cdot kJ_n(m) \cos\left(\varphi + n\frac{\pi}{2}\right) \cos(n[\omega_{\text{mod}}t + \psi_{\text{mod}}]) \\ &= kJ_n(m) \cos\left(\varphi + n\frac{\pi}{2}\right) \cdot \sin(n\omega_{\text{mod}}t) \cos(n\omega_{\text{mod}}t + n\psi_{\text{mod}}) \end{aligned}$$

The next step is to use the trigonometric addition theorem  $\cos x \cos y = \frac{1}{2}(\cos[x - y] + \cos[x + y])$  that delivers the following equation for  $Q$ :

$$Q_n = \frac{1}{2}kJ_n(m) \cos(\varphi + n\frac{\pi}{2}) \cdot [\cos(-n\psi_{\text{mod}}) + \cos(2n\omega_{\text{mod}}t + n\psi_{\text{mod}})] \quad (\text{B.8})$$

and  $\sin x \cos y = \frac{1}{2}(\sin[x - y] + \sin[x + y])$  the following equation for  $I_n$ :

$$I_n = \frac{1}{2}kJ_n(m) \cos(\varphi + n\frac{\pi}{2}) \cdot [\sin(-n\psi_{\text{mod}}) + \sin(2n\omega_{\text{mod}}t + n\psi_{\text{mod}})]. \quad (\text{B.9})$$

For both, quadrature and in-phase, a low-pass filter is applied that makes the two variables time-independent:

$$\begin{aligned} Q_n &= \frac{1}{2}kJ_n(m) \cos(\varphi + n\frac{\pi}{2}) \cdot \cos(-n\psi_{\text{mod}}), \\ I_n &= \frac{1}{2}kJ_n(m) \cos(\varphi + n\frac{\pi}{2}) \cdot \sin(-n\psi_{\text{mod}}). \end{aligned}$$

With  $\cos(-x) = \cos x$  and  $\sin(-x) = -\sin x$  it follows:

$$\begin{aligned} Q_n &= \frac{1}{2}kJ_n(m) \cos(\varphi + n\frac{\pi}{2}) \cdot \cos(n\psi_{\text{mod}}), \\ I_n &= -\frac{1}{2}kJ_n(m) \cos(\varphi + n\frac{\pi}{2}) \cdot \sin(n\psi_{\text{mod}}). \end{aligned}$$

# PRISM COATINGS

C

The specific coatings for each prism surface are plotted in Figure C.1 over wavelength. These measurement were provided by the manufacturer Laseroptik Garbsen. Two different AOIs were analyzed, accordingly to the simulated beam geometry in IfoCAD. The perpendicularity between optical surface and ground surface is specified by the manufacturer to be better than  $2''$ .

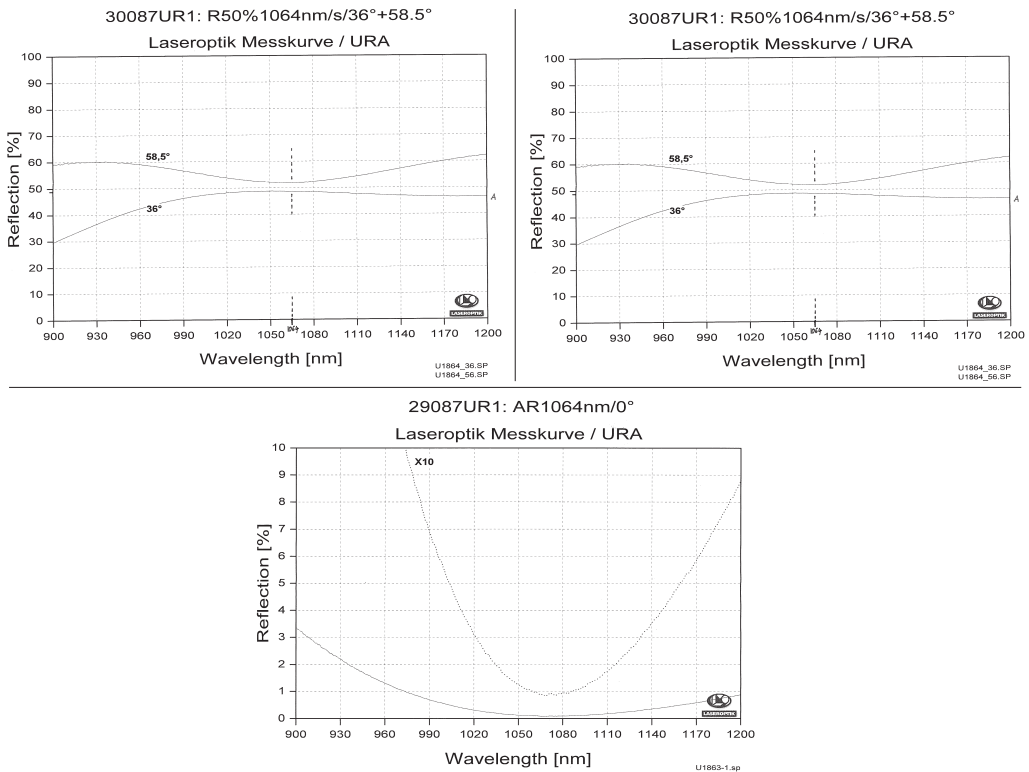


Fig. C.1.: Reflectivities for the prisms measured by Laseroptik Garbsen for different wavelengths and the relevant AOI. Surface A: top left, Surface B: top right, Surface C: bottom.

